UNIVERSITY OF CALIFORNIA SAN DIEGO

Development of photoacoustic and optical techniques for probing disease

A Dissertation submitted in partial satisfaction of the requirements
for the degree Doctor of Philosophy

in

NanoEngineering

by

Colman A. Moore

Committee in charge:

Professor Jesse V. Jokerst, Chair
Professor Ester Kwon
Professor Darren Lipomi
Professor Nisarg Shah
Professor Yingxiao Wang

2022

The Dissertation of Colman A. Moore is approved, and it is acceptable in quality and form for publication on microfilm and electronically.

University of California San Diego

2022

DEDICATION

To my family: John, Charmaine, and Claire,
for their love and encouragement.

EPIGRAPH

"Perfection belongs to narrated events, not to those we live."

—Primo Levi, *The Periodic Table*

"Even bad coffee is better than no coffee at all."

—David Lynch

TABLE OF CONTENTS

LIST OF FIGURES

LIST OF TABLES

ACKNOWLEDGEMENTS

Firstly, I would like to thank my advisor, Professor Jesse Jokerst, for his scientific and professional mentorship over the past five years. I will always be grateful for the training and opportunities he provided me. I would also like to acknowledge the support and guidance of my committee members: Professor Ester Kwon, Professor Darren Lipomi, Professor Nisarg Shah, and Professor Yingxiao (Peter) Wang.

Many people have helped me along the way. I would like to acknowledge Professor Casey Chen and Professor Anthony O'Donoghue for their scientific mentorship and collaborations. In addition, thanks to Ryan Wing and Timothy Pham for their diligent efforts as undergraduate researchers. I am grateful for the assistance and collaborative efforts of numerous others including Dr. Sreenivas Koka, Dr. Paris Sedghizadeh, Moein Mozaffarzadeh, Dr. Jane Law, Dr. Christopher Pham, Dr. Mohammed Hayati, Dr. Kai-Chiao J. Chang, Dr. Pavla Fajtová, and Dr. Natalia Tjokro. I would also like to thank my scientific mentors prior to graduate school: Dr. Melissa Moss, Dr. Andrew Lee, Dr. Zeb Vance, and Dr. Bruce Gao, who generously introduced me to research as a high school student. I must also acknowledge the consistent support and encouragement from my colleagues in the lab, both past and present.

I have been fortunate to receive organizational support of my work as a graduate student. Chronologically, I would like to thank the Charles Lee Powell Foundation and Jacobs School of Engineering for my first-year fellowship. Secondly, I would like to acknowledge the UCSD Interfaces Graduate Training Program in Multi-Scale Biology and Professor Andrew McCulloch with funding from the National Institute of Biomedical Imaging and Bioengineering (NIH 5T32EB009380). Third, I am deeply grateful for the

support of the National Science Foundation through the Graduate Research Fellowship Program (DGE-1650112) and ARCS (Achievement Reward for College Scientists) Foundation. I would also like to acknowledge the Shiley Foundation. These generous investments in my training and career continuously pushed me to work harder in the pursuit of impactful research.

Chapter 1, in full, is a reprint of the material as it appears in Theranostics, vol. 9, 1550-1571, 2019. Moore, Colman; Jokerst, Jesse V. The dissertation author was the primary investigator and author of this paper.

Chapter 2, in full, is a reprint of the material as it appears in Advanced Drug Delivery Reviews, vol. 144, 78-79, 2019. Moore, Colman; Chen, Fang; Wang, Junxin; Jokerst, Jesse V. The dissertation author was the primary investigator and author of this paper.

Chapter 3, in full is a reprint of the material as it appears in Dental Ultrasound in Periodontology and Implantology, Springer Nature Switzerland AG. 215-23, 2020. The dissertation author was the primary investigator and author of this book chapter.

Chapter 4, in full, has been submitted for publication of the material as it may appear in Dentomaxillofacial Radiology, 2022. Moore, Colman; Law, Jane; Pham, Christopher; Chang, Kai-Chiao J.; Chen, Casey; Jokerst, Jesse V. The dissertation author was the primary investigator and author of this paper.

Chapter 5, in full, is a reprint of the material as it appears in Photoacoustics, vol. 12, 67-74, 2018. Moore, Colman; Bai, Yuting; Hariri, Ali; Sanchez, Joan B.; Lin, Ching-Yu; Koka, Sreenivas; Sedghizadeh, Paris; Chen, Casey; Jokerst, Jesse V. The dissertation author was the primary investigator and author of this paper.

Chapter 6, in full, is a reprint of the material as it appears in Biomedical Optics Express, vol. 12, 1543-1558, 2021. Mozaffarzadeh, Moein*; Moore, Colman*; Golmoghani, Erfan*; Mantri, Yash; Hariri, Ali; Jorns, Alec; Fu, Lei; Verweij, Martin D.; Orooji, Mahdi; de Jong, Nico; Jokerst, Jesse V. The dissertation author was the co-primary investigator and co-primary author of this paper.

Chapter 7, in full, is a reprint of the material as it appears in ACS Sensors, vol. 6 (6), 2356-2365, 2021. Moore, Colman; Borum, Raina; Mantri, Yash; Xu, Ming; Fajtová, Pavla; O'Donoghue, Anthony; Jokerst, Jesse V. The dissertation author was the primary investigator and author of this paper.

Chapter 8, in full, has been submitted for publication of the material as it may appear in Angewandte Chemie, 2022. Moore, Colman; Tjokro, Natalia; Zhang, Brendan; Hayati, Mohammed; Cheng, Yong; Chang, Kai Chiao J.; Chen, Casey; Jokerst, J. V. The dissertation author was the primary investigator and author of this paper.

Chapter 9, in full, is a reprint of the material as it appears in Analytical Chemistry, vol. 144, 78-89, 2019. Moore, Colman; Wing, Ryan; Pham, Timothy; Jokerst, Jesse V. The dissertation author was the primary investigator and author of this paper.

VITA

2017 Bachelor of Science in Biomedical Engineering, University of South Carolina

2019 Master of Science in Nanoengineering, University of California San Diego

2022 Doctor of Philosophy in Nanoengineering, University of California San Diego

PUBLICATIONS

1. **Moore, C.**, Tjokro, N., Zhang, B., Hayati, M., Cheng, Y., Chang, K. C., Chen, C., & Jokerst, J. (2022). A photoacoustic-fluorescent imaging probe for proteolytic gingipains expressed by Porphyromonas gingivalis. *ChemRxiv*.

2. **Moore, C.**, Law, J., Pham, C., Chang, K.-C. J., Chen, C., & Jokerst, J. V. (2021). High-resolution ultrasonography of gingival biomarkers for periodontal diagnosis in healthy and diseased subjects. *MedRxiv*.

3. **Moore, C.**, Borum, R., Mantri, Y., Xu, M., Fajtová, P., O'Donoghue, A., & Jokerst, J. (2021). Activatable Carbocyanine Dimers for Photoacoustic and Fluorescent Detection of Protease Activity. *ACS Sensors*, *6* (6), 2356-2365.

4. Mozaffarzadeh, M.*, **Moore, C.***, Golmoghani, E. B.*, Mantri, Y., Hariri, A., Jorns, A., Fu, L., Verweij, M. D., Orooji, M., & de Jong, N. (2021). Motion-compensated noninvasive periodontal health monitoring using handheld and motor-based photoacoustic-ultrasound imaging systems. *Biomedical Optics Express, 12*(3), 1543-1558.

5. **Moore, C.**, Wing, R., Pham, T., & Jokerst, J. V. (2020). Multispectral Nanoparticle Tracking Analysis for the Real-Time and Label-Free Characterization of Amyloid-β Self-Assembly In Vitro. *Analytical Chemistry, 92*(17), 11590-11599.

6. **Moore, C.**, & Jokerst, J. V. (2020). Photoacoustic Ultrasound for Enhanced Contrast in Dental and Periodontal Imaging. In *Dental Ultrasound in Periodontology and Implantology* (pp. 215-230). Springer Nature Switzerland AG.

7. **Moore, C.**, Chen, F., Wang, J., & Jokerst, J. V. (2019). Listening for the therapeutic window: advances in drug delivery utilizing photoacoustic imaging. *Advanced drug delivery reviews, 144*, 78-89.

8. **Moore, C.**, & Jokerst, J. (2019). Strategies for Image-Guided Therapy, Surgery, and Drug Delivery Using Photoacoustic Imaging. *Theranostics, 9*(6), 1550-1571.

9. **Moore, C.**, Bai, Y., Hariri, A., Sanchez, J. B., Lin, C.-Y., Koka, S., Sedghizadeh, P., Chen, C., & Jokerst, J. V. (2018). Photoacoustic imaging for monitoring periodontal health: A first human study. *Photoacoustics, 12*, 67-74.

10. Borum, R. M., **Moore, C.**, Chan, S. K., Steinmetz, N. F., & Jokerst, J. V. (2021). A Photoacoustic

Contrast Agent for miR-21 via NIR Fluorescent Hybridization Chain Reaction. *Bioconjugate Chemistry*.

11. Creyer, M. N., Jin, Z., **Moore, C.**, Yim, W., Zhou, J., & Jokerst, J. V. (2021). Modulation of Gold Nanorod Growth via the Proteolysis of Dithiol Peptides for Enzymatic Biomarker Detection. *ACS Applied Materials & Interfaces, 13*(38), 45236-45243.

12. Cheng, Y., Borum, R. M., Clark, A. E., Jin, Z., **Moore, C.**, Fajtová, P., O'Donoghue, A. J., & Carlin, A. F, & Jokerst, J.V. (2021). A Dual-Color Fluorescent Probe Allows Simultaneous Imaging of Main and Papain-like Proteases of SARS-CoV-2-Infected Cells for Accurate Detection and Rapid Inhibitor Screening. *Angewandte Chemie*.

13. Jin, Z., Mantri, Y., Retout, M., Cheng, Y., Zhou, J., Jorns, A., Fajtova, P., Yim, W., **Moore, C.**, & Xu, M. (2021). A Charge-Switchable Zwitterionic Peptide for Rapid Detection of SARS-CoV-2 Main Protease. *Angewandte Chemie*.

14. Jin, Z., Yeung, J., Zhou, J., Cheng, Y., Li, Y., Mantri, Y., He, T., Yim, W., Xu, M., Wu, Z., Fajtova, P., Creyer, M., **Moore, C**., Fu, L., Penny, W., O'Donoghue, A., and Jokerst, J.V. (2022). Peptidic Sulfhydryl for Interfacing Nanocrystals and Subsequent Sensing of SARS-CoV-2 Protease. *Chemistry of Materials*.

15. Jin, Z., Jorns, A., Yim, W., Wing, R., Mantri, Y., Zhou, J., Zhou, J., Wu, Z., **Moore, C.**, & Penny, W. F. (2021). Mapping Aerosolized Saliva on Face Coverings for Biosensing Applications. *Analytical Chemistry, 93*(31), 11025-11032.

16. Xu, M., Yim, W., Zhou, J., Zhou, J., Jin, Z., **Moore, C.**, Borum, R., Jorns, A., & Jokerst, J. V. (2021). The application of organic nanomaterials for bioimaging, drug delivery, and therapy: spanning various domains. *IEEE Nanotechnology Magazine, 15*(4), 8-28.

17. Yim, W., Zhou, J., Mantri, Y., Creyer, M. N., **Moore, C.** A., & Jokerst, J. V. (2021). Gold nanorod–melanin hybrids for enhanced and prolonged photoacoustic imaging in the near-infrared-II window. *ACS Applied Materials & Interfaces, 13*(13), 14974-14984.

18. Hariri, A., **Moore, C.**, Mantri, Y., & Jokerst, J. V. (2020). Photoacoustic imaging as a tool for assessing hair follicular organization. *Sensors, 20*(20), 5848.

19. Hariri, A., Chen, F., **Moore, C.**, & Jokerst, J. V. (2019). Noninvasive staging of pressure ulcers using photoacoustic imaging. *Wound Repair and Regeneration, 27*(5), 488-496.

20. Naveau, A., Shinmyouzu, K., **Moore, C.**, Avivi-Arber, L., Jokerst, J., & Koka, S. (2019). Etiology and Measurement of Peri-Implant Crestal Bone Loss (CBL). *Journal of Clinical Medicine, 8*(2), 166.

21. Mozaffarzadeh, M., Hariri, A., **Moore, C.**, & Jokerst, J. V. (2018). The double-stage delay-multiply-and-sum image reconstruction method improves imaging quality in a led-based photoacoustic array scanner. *Photoacoustics, 12*, 22-29.

22. Wang, J., Lin, C.-Y., **Moore, C.**, Jhunjhunwala, A., & Jokerst, J. V. (2018). Switchable photoacoustic intensity of methylene blue via sodium dodecyl sulfate micellization. *Langmuir, 34*(1), 359-365

ABSTRACT OF THE DISSERTATION

Development of photoacoustic and optical techniques for probing disease

by

Colman A. Moore

Doctor of Philosophy in NanoEngineering

University of California San Diego, 2022

Professor Jesse V. Jokerst, Chair

Medical imaging requires the perturbation of biological tissues with external radiation. Clinically, acoustic and optical methods (e.g., ultrasonography, fluorescence imaging) are attractive because they are non-ionizing and offer real-time acquisition with high resolution. Photoacoustic imaging is an emerging hybrid modality that combines the

contrast of optics with the penetration of ultrasound. This dissertation presents novel strategies for the detection of aberrant biomarkers through the application of high-frequency ultrasonography, optical methods (i.e., visible/near-infrared absorbance, fluorescence, scattering) and photoacoustic imaging, with primary focuses in periodontal disease and protease detection. First, the preclinical field of photoacoustic imaging is reviewed across various disease areas for image-guided therapy, surgery, and drug delivery. The second chapter describes research advances in photoacoustic imaging specifically for drug delivery. The third chapter reviews progress to date in photoacoustic imaging for dental and oral health applications. In the fourth chapter, the clinical value of high-resolution ultrasonography is demonstrated for noninvasive and chairside measurement of anatomic periodontal metrics in a pilot case control study. Next, this work is extended to imaging the periodontal pocket in a healthy human case study using photoacoustic imaging with a food-grade contrast agent. Chapter six describes the application of a modality-independent algorithmic method for reducing motion artifacts that commonly arise during 3D photoacoustic/ultrasound imaging of the oral environment. Chapter seven describes the chemical development of a modular and activatable contrast agent that produces photoacoustic and fluorescent signal upon proteolytic cleavage by leveraging the intramolecular coupling of dye-peptide conjugates. This work is validated with trypsin as a model protease and subcutaneous photoacoustic imaging of the probe in mice. In chapter eight, the design is honed for targeting proteolytic gingipains secreted by the periodontal pathogen, *Porphyromonas gingivalis*, with demonstrated photoacoustic imaging of the gingipain-activated probe in ex vivo swine jaws and fluorescent activation in gingival crevicular fluid samples collected from human subjects with periodontal disease. In chapter

nine, the dissertation concludes with a foray into the characterization of protein aggregates associated with Alzheimer's disease. It is demonstrated that multispectral nanoparticle tracking analysis can utilize light scattering at multiple wavelengths to measure the nanoscale distribution of amyloid-β aggregates (size and concentration) in vitro, without interfering dyes and in real time.

CHAPTER 1. STRATEGIES FOR IMAGE-GUIDED THERAPY, SURGERY, AND DRUG DELIVERY USING PHOTOACOUSTIC IMAGING

ABSTRACT: Photoacoustic imaging is a rapidly maturing imaging modality in biological research and medicine. This modality uses the photoacoustic effect ("light in, sound out") to combine the contrast and specificity of optical imaging with the high temporal resolution of ultrasound. The primary goal of image-guided therapy, and "theranostics" in general, is to transition from conventional medicine to precision strategies that combine diagnosis with therapy. Photoacoustic imaging is well-suited for noninvasive guidance of many therapies and applications currently being pursued in three broad areas. These include the image-guided resection of diseased tissue, monitoring of disease states, and drug delivery. In this review, we examine the progress and strategies for development of photoacoustics in these three key areas with an emphasis on the value photoacoustics has for image-guided therapy.

1.1. Introduction

1.1.1. History of Photoacoustic Imaging

In the past few decades, photoacoustic imaging (PAI) has emerged as a novel imaging modality with a variety of promising applications in medicine. In contrast to traditional X-ray imaging, positron-emission tomography (PET), and computed tomography (CT), PAI is capable of revealing structural, functional, and molecular information of biological systems without ionizing radiation by integrating optical excitation with ultrasound detection. This hybrid technique relies on the photoacoustic effect—the generation of acoustic waves as light is converted to heat following optical absorption. In the body, PAI can be used to image intrinsic components of tissue such as hemoglobin and melanin, as well as extrinsic contrast agents targeted to biomarkers or specific regions of the body.

Today, PAI is being developed for a wide range of image-guided applications including the monitoring and therapy of disease states, drug delivery, and surgical guidance. A number of review articles on PAI exist in the literature. These range from emphases on contrast agents or specific applications to more general overviews [1-6]. For contrast agents, both broad surveys [7-10] and spotlights on particular types such as ratiometric probes [11], activatable probes [12], inorganic nanomaterials [13-16], photothermal probes [17], NIR-II probes [18, 19], and organic probes [19-23] are recommended to the reader. In addition, applications reviewed include imaging the brain [24, 25], microvasculature [26], cancer [27], and drug delivery [28]. The purpose of this review is to highlight image-guided applications of PAI, assess developments in the technology, and examine progress towards clinical translation.

Alexander Graham Bell first reported the photoacoustic (PA) effect in 1880 following his experiments on the photophone, the world's first wireless communications

device [29]. He described the generation of sound waves by various materials in response to pulses of sunlight [30]. These observations were overlooked for many years, but have since been studied extensively, and the physics of the PA effect were expounded by Rosencwaig and Gersho, of Bell Labs, for photoacoustic spectroscopy [31]. They predicted its utility for biomedical imaging because of its ability to obtain optical absorption spectra for almost all solids and semisolids, its insensitivity to light scattering, and its noninvasive nature. Not long after, a method was developed for acquiring 1D PA signal in synthetic scattering media using a single transducer element following a pulse of ionizing radiation [32]. In the 1990s, non-ionizing light was harnessed for signal propagation, and the technology was extended to 3D imaging in biological tissue, along with theoretical underpinnings of PA ultrasound reconstruction tomography [33-35] and microwave-induced acoustic tomography [36]. Since then, major developments in PAI have included photoacoustic tomography (PAT), photoacoustic computed tomography (PACT), photoacoustic microscopy (PAM), handheld imaging devices, and customized contrast agents [37]. In this review, we provide an overview of the emerging roles these PA technologies are playing in image-guided therapy, surgery, and drug delivery.

1.1.2. Principles of PAI

PAI is a *hybrid* imaging modality because it combines the high contrast and specificity of optical imaging with the strong temporal resolution and increased penetration depth of ultrasound. PAI (sometimes called optoacoustic imaging) takes advantage of the photoacoustic effect and typically uses near-infrared (NIR) or visible light to leverage the optical window— a range of non-ionizing wavelengths that allow for deeper penetration in human tissue [38, 39]. The photoacoustic effect consists of three distinct steps in soft matter [40]:

(1) The target absorbs a photon.

(2) The target increases in temperature, inducing a local pressure increase via thermoelastic expansion.

(3) The pressure perturbation is propagated throughout the surrounding medium by elastic interactions.

The generation of acoustic waves requires thermal expansion to be time variant. To achieve this in PAI, a pulsed laser is used (1-100 ns), or a continuous-wave (CW) laser is intensity modulated to excite a light-absorbing target [41, 42]. Pulsed lasers are the most common because they have a better signal to noise ratio than CW lasers at constant fluence and power [43]. In addition, laser pulses are shorter than the thermal and stress confinement times of absorbers, meaning thermal diffusion and volume expansion can be neglected during illumination [4].

In tissue, the interaction of photons with cellular structures results in elastic scattering. The molecules struck by these scattered photons undergo thermoelastic expansion generating wideband acoustic waves (ultrasonic) in the surrounding medium [44]. These waves are detectable by an array of piezoelectric transducers and images can be generated by measuring the waves' amplitudes and arrival times to reconstruct the initial photoacoustic pressure distribution.

The initial amplitudes of PA waves can be determined according to Equation 1.

$$P_0 = \Gamma \eta_{th} \mu_a F \quad (1)$$

Here, P_0 is the initial local pressure rise (PA amplitude) that initiates ultrasonic wave propagation. The PA efficiency is dictated by the Grüneisen parameter Γ (dimensionless), a thermodynamic property that scales with temperature and differs between absorbing targets,

and η_{th}, the heat conversion efficiency (equivalent to the amount of nonradiative energy decay following the laser pulse, or, 1 minus the fluorescence quantum yield) [4, 28]. Because Γ is temperature dependent, PAI can be used to monitor temperature [45]. The optical absorption coefficient, μ_a (cm^{-1}), is proportional to the concentration of the chromophore target, and F is the local optical fluence (J/m^2). Together, μ_a and F can be understood as the total energy deposition (J/m^3), or absorbed optical energy [6, 28, 40]. Equation 1 shows that the absorption coefficient of an object can be determined from pressure measurements if the optical fluence is known.

1.1.3. PAI Implementation: Tomography, Microscopy, and Endoscopy

The principles of PAI have been primarily adapted in major forms to photoacoustic microscopy (PAM), photoacoustic tomography (PAT), photoacoustic computed tomography (PACT), and photoacoustic endoscopy (PAE) [46]. These configurations are summarized in **Table 1.1**. PAI systems may operate in reflection (backward) mode or transmission (forward) mode [47]. In reflection mode, the irradiation source and transducer are on the same side of the sample. The irradiation source and transducer are typically coupled, making operation similar to B-mode ultrasound imaging. In forward mode, the irradiation source and transducer are on opposite sides of the sample. This mode is usually limited to thin tissue sections or ex vivo samples because of the strong attenuation of light through tissue.

Table 1. 1. Major hardware configurations of PAI with representative performance metrics.

Technique	Full Name	Brief Description	Resolution	Imaging Depth
OR-PAM	Optical Resolution - Photoacoustic Microscopy [48, 49]	A laser is focused to a diffraction-limited spot with a microscope objective and the generated acoustic signal is focused with a concave acoustic lens to be detected by a broadband ultrasound transducer.	~0.5 - 3.0 µm	~1.2 mm
AR-PAM	Acoustic Resolution - Photoacoustic Microscopy [3]	A dark-field ring of light is focused onto tissue and a concave acoustic lens focuses the acoustic signal to a broadband ultrasound transducer.	~45 µm	~5 mm
PAT/PACT	Photoacoustic Tomography / Computed Tomography [5]	A pulsed illumination beam excites a region of interest and a linear or circular transducer array receives acoustic signal for image generation using inverse/back-projection algorithms.	0.1 - 1.0 mm	Multiple centimeters possible
PAE	Photoacoustic Endoscopy [50]	Optical excitation, acoustic transduction, and mechanical scanning components are confined to the distal tip of an endoscope.	31 - 170 µm	1 - 7 mm

PAM is a reflection or transmission mode technique in which a single element transducer raster scans the sample and it is capable of millimeter imaging depths and micron resolutions[51]. In this mode, the optical excitation and acoustic detection create dual foci that are both focused to increase sensitivity [3]. A single laser pulse is capable of returning a 1D ultrasonic signal with resolution axial to the laser. When scanning laterally, the laser transduces these signals across the area of the sample, generating 3D images. Axial

resolution depends on the acoustic time of flight and lateral resolution relies on the distance between foci [3]. PAM is further classified by the modality that governs resolution: OR-PAM (optical resolution) or AR-PAM (acoustic resolution). OR-PAM is limited in depth by the optical diffusion limit (~1.2 mm), but can image cellular and subcellular structures from hundreds of nanometers to a few micrometers [48, 49]. The capabilities of OR-PAM have recently been extended by Lan et al., who reported frame rates of 900 Hz with a wide field of view (12 mm) using a hexagon-mirror scanner [52, 53]. AR-PAM uses dark-field optical excitation, and is capable of penetrating millimeters beyond the diffusion limit (though this depth sacrifices lateral resolution) [54]. A 45-μm lateral resolution and 3-mm imaging depth are achievable values for AR-PAM [3]. PAM systems are typically benchtop configurations that are most conveniently used for *ex vivo* applications; however, they can certainly be used for *in vivo* work. For example, subcutaneous melanomas in mice, oxygen saturation in rats, and total hemoglobin concentration in the human palm have been imaged with PAM [51]. Furthermore, a handheld PAM probe using a waterproof MEMS scanner (total weight: 162 g, diameter: 17 mm), was recently developed and shown to be effective for clinically relevant, *in vivo* applications such as delineating the 3D boundaries of a human mole [55]. These miniaturizations will improve the clinical feasibility of PAM systems.

PAT is a technique that follows the principles described in Section 1.2— it is widely used in research studies and multiple commercial systems are on the market. In focused scanning PAT, a focused ultrasonic transducer mechanically scans the area of the sample. PACT was developed to decrease the long imaging times (tens of minutes for a full mouse body) associated with such raster scanning modes [28]. It implements a wide beam of homogenous light to illuminate the entire region of interest and an array (linear or circular)

of ultrasound detectors for signal acquisition. Back-projection algorithms are then used to pinpoint the ultrasonic sources and reconstruct 2D or 3D images [56]. PACT is faster than scanning PAM and can image more deeply, but typically has lower resolution [28]. In general, tomographic systems have resolutions in the 0.1 – 1.0 mm range but can achieve multiple centimeter imaging depths in soft tissue. Another advantage of tomography is that transducers (e.g. linear arrays) can be handheld, as in conventional ultrasound imaging. A recently published review covers advancements in handheld PAI in detail [57].

PAE has also been developed for imaging in difficult locations such as the gastrointestinal tract, lungs, trachea, and mediastina [58]. These internal organs can be imaged using miniaturized components confined to the tip of an endoscopic probe a few millimeters in diameter [59, 60]. In such cases, typically an apparatus combining the light generator (optical fiber) and ultrasound detector is driven by motors to circumscribe the target resulting in cross-sectional and volumetric images. The size and capabilities of these PAE probes will improve as designs using optically transparent transducer components become more common and are further miniaturized. Intraoperative PAE applications are discussed more in Section 2.1.

1.1.4. Strengths and Limitations of PAI

PAI demonstrates numerous unique features and advantages over traditional imaging techniques. For example, by relying on NIR and visible light, PAI eliminates the risks associated with high-frequency ionizing radiation. It is capable of imaging at multiple scales, resolving single cells, organelles, and capillaries in vivo [61, 62]. In PAM, imaging depths and resolutions can be scaled from the micro to macro regime by tuning the numerical aperture of the objective lens or the central frequency of the transducer [3, 4]. Unlike most optical

imaging techniques, PAI is capable of breaking the optical diffusion limit, which is defined by the transport mean free path (~1 mm in tissue) [63]. Photons scatter ballistically above this depth and diffusely below it. Most optical techniques cannot achieve adequate resolution below this depth, but PAI overcomes this limit by detecting the ultrasonic waves induced by diffuse photons [46]. This fact demonstrates that PA signal is fundamentally based on absorption (and subsequent thermoelastic expansion). In effect, background can be reduced in PAI because non-absorbing objects do not generate PA signal and spectral imaging/signal thresholding can be used to minimize signal from endogenous absorbers.

Both non-fluorescent and fluorescent targets can be imaged, and a number of endogenous chromophores have strong signal such as oxygenated/deoxygenated hemoglobin [64], melanin [65], lipids [66], and water because of their differential absorbance spectra in the NIR. A wide variety of exogenous contrast agents have also been developed and are designed to boost contrast while expanding the range of biological processes that can be imaged. Some examples include small-molecule dyes, metallic and polymeric nanoparticles, up-conversion nanoparticles, carbon nanotubes, microbubbles, quantum dots and numerous others [7, 67, 68]. Because a diverse array of materials and strategies have been investigated as contrast agents, it can be useful to distinguish them according to certain traits: for instance, activatable vs. non-activatable (passive), nanoparticle vs. small-molecule, inorganic vs. organic, or NIR-I absorbing vs. NIR-II absorbing. Activatable probes benefit from higher specificity and signal-to-background ratios than passive ones because they only activate PA signal following a biological stimulus. Nanoparticles are ideal for carrying cargoes and have unique optical properties, but small molecules tend to have better biocompatibility and lower toxicity/faster clearance. Similarly, organic nanomaterials offer

better biodegradability than inorganics, but may have lower absorption coefficients or more complex syntheses.

One important consideration for nanoparticle design is the size: typically, particles < 6 nm will be rapidly cleared by the kidneys, whereas particles > 8 nm cannot undergo glomerular filtration, and sizes between 30-200 nm can achieve long circulation times for enhanced accumulation and retention in tumors [69, 70]. It is also known that for photothermally active gold nanomaterials (e.g. spheres, rods, shells), the magnitude of extinction increases with size (e.g. from 20 to 80 nm for spheres) [71]. Specifically, the contribution of scattering to the total extinction increases relative to absorption. Feis et al. investigated this effect with gold nanoparticles and saw that larger particles at larger wavelengths had lower photoacoustic amplitudes than predicted by the extinction spectrum [72]. This discrepancy was attributed to the insensitivity of PAI to scattering effects. Therefore, the individual contributions of absorption and scattering, which is often size dependent, should also be considered during PA nanoparticle design. Overall, desirable properties for effective contrast agents include high molar absorption coefficients, absorption at long NIR wavelengths (ideally non-overlapping with endogenous absorbers), stability, affordability, targetability, and safety [10].

Using exogenous contrast, imaging depths in PACT have been reported as high as 11.6 cm in chicken breast tissue and 5 cm in the human arm [73]. However, deep imaging (>1 cm) with high resolution still remains a challenge for most PA applications. Specific deep-lying organs that present challenges for PAI because of their location include the heart (location under the rib cage), lungs (beneath rib cage and gas-tissue interface), stomach (a hollow structure and under rib cage), and pancreas (depth) [28]. Penetration depth issues can

be countered, however, with exogenous agents (especially in the second optical window) and unique hardware designs. For example, novel transducers and intraoperative probes have been designed to image trans-vaginally [74], trans-rectally [75, 76], and trans-esophageal [77]. Of course, all hardware designs can be combined with molecular imaging strategies using exogenous contrast agents to maximize performance. Furthermore, one of the emerging trends in recent years has been the increased use of the second optical window (NIR II: 1000-1700 nm) for fluorescence imaging and subsequently PAI [78, 79]. This range is highly attractive for biophotonic applications because of the diminished light-tissue interactions—specifically, scattering and autofluorescence— at longer wavelengths [80]. Compared to the first optical window (650-950 nm), these factors allow imaging at higher penetration depths. Additionally, because these photons have lower energies, the maximum permissible exposure (MPE) is higher for clinical applications which can boost PA performance and reduce signal-to-background ratios. The first NIR-II PA contrast agents explored have been inorganic nanomaterials, such as plasmonic precious metal nanoparticles and copper sulfide nanoparticles [81-83]. However, recent progress has been made in organic NIR-II probes, including semiconducting polymer nanoparticles [22, 79] and small molecules [19]. Still, the second optical window presents new challenges that must be overcome. For example, water has a significant absorption peak at 1450 nm, existing NIR-II agents have low quantum yields, and few organic materials have been reported that can absorb above 1064 nm in the NIR-II [22].

1.2. Metastasis Detection and Surgical Resection

1.2.1. Endogenous Targets for Guided Surgery

A substantial portion of PAI research is devoted to cancer applications. The vast

majority of cancer deaths are caused by metastatic progression of the disease. To mitigate these cases, it is important to determine both the extent of metastasis and the margins of tumors to guide surgical intervention [84]. Intraoperative PAI shows potential to improve upon existing methods (immunohistochemistry, histopathological assessment) by determining these variables in real time. Many groups are investigating the potential for PAI to detect metastasis and enhance tumor imaging. Melanoma is an appropriate target for such studies because melanoma cells contain highly absorbent melanin that acts as an endogenous PA absorber.

Using PAT, Grootendorst et al. compared intraoperative PA images of melanoma metastases from resected, human sentinel lymph nodes (SLN: the first lymph node to which a tumor drains) to hematoxylin-eosin histologic images (the routine method for prognosis that takes days). This showed that intraoperative detection of melanoma was possible although distinctions between malign and benign nodes were not obvious [85]. In order to discriminate between signals from blood versus melanin, the signal from *ex vivo* nodes were characterized spectrally and separated with an unmixing algorithm [86]. However, the accuracy of this method depends entirely on the accuracy of the PA reference spectra measured for blood and melanin. The potential benefit of intraoperative PAI of *ex vivo* SLNs is that detection of metastasis would allow an immediate node dissection and prevent the need for a second surgery. Luke & Emelianov showed that metastasis in lymph nodes from other (non-melanoma) primary tumor types could also be imaged [87]. In a mouse model for oral cancer, they took advantage of the decreased blood oxygen saturation (SO_2) associated with metastatic foci in SLNs and imaged deoxygenated/oxygenated hemoglobin to evaluate the metastasis. The differential absorption between oxygenated and deoxygenated blood

provides one of the most straightforward mechanisms of endogenous PA contrast [64, 88, 89].

To accelerate clinical translation, intraoperative handheld PA probes have been designed that streamline operation of the technology. Xi et al. demonstrated a handheld microelectromechanical systems (MEMS) probe for real time inspection of 3D tumor margins in mice during resection [90]. Here, they used the imaging system at 532 nm to evaluate the completeness of tumor removal following surgery and histologically validated the margins as measured with photoacoustics with < 6.5% error. One issue with using endogenous contrast for resection validation, especially at 532 nm, is the strong absorption of blood, which will produce background during surgeries. Longer wavelengths can mitigate this effect but it is difficult to match the signal to background ratios achievable with exogenous agents.

Neuschmelting et al. evaluated both 2D and 3D handheld MSOT (multispectral optoacoustic tomography) devices developed by iThera Medical by imaging murine brain melanomas at 4 MHz and 700 – 900 nm [91]. The authors implanted B16F10 melanoma cells into the right frontal lobe, where tumors 3.5 – 7.0 mm in diameter grew within 13 days; the size of these tumors were independently measured with MRI. The 2D system was deemed more accurate (bias = 0.24 mm) than the 3D system (bias = 2.35 mm) but was limited to axial tumor depths of 4 mm. The 3D probe was limited by tumor size (< 3.5 mm) in all dimensions, but the acquisition time was shorter. The performance disparity between the 2D and 3D systems was attributed to a non-ideal distribution of diffused light in the transducer array of the 3D system. These handheld systems also showed superior signal to noise ratios and limits of detection and for metastatic melanoma cells (5 cells/uL at 8 mm tissue depths in mice) to PET/CT using fluorine 18 fluorodeoxyglucose [92]. However, this sensitivity would

be difficult to achieve if applied to human lymph nodes located centimeters below the skin. Additionally, to our knowledge, these systems have not yet been used to monitor resection during or after an operation.

Miniaturized and endoscopic probes can offer advantages for image-guided surgeries due to their adaptability and form factor. One example is radical prostatectomy, a common treatment for prostate cancer in which the prostate and seminal vesicles are fully removed [93]. Oncological success (full tumor elimination) must be balanced with minimizing functional damage (e.g. incontinence and impotence). A recent study was conducted to determine the best scanning geometry for intraoperative PA prostate imaging [94]. It was demonstrated through simulation and experiment (using phantoms) that a convex, "pick-up" transducer (28 mm width, 10 MHz) controlled by a da Vinci robot was a promising approach for prostate imaging. In this setup, the transducer is located anterior to the prostate and can form a cylindrical detection surface while conformally scanning the prostate to generate a 3D image. The integration of PAI with a da Vinci robot for guided surgery was also investigated by Gandhi et al [95]. They used phantom studies to show that by connecting an optical fiber (powered by a pulsed laser diode) to a surgical arm of the robot, and a transducer to another arm, that the system could distinguish separation distances blood vessels and nerves in real-time while also visualizing the tool tip itself[96]. These technologies are still in their early stages but show promise for improving patient outcomes during future *in vivo* and human studies.

PAE applications have been studied for over a decade but miniaturizing the hardware while maintaining high image quality is a challenge. Nevertheless, systems have been proposed and constructed for detection of atherosclerotic plaques in cardiovascular disease

[97-100], esophageal imaging [101], and gastrointestinal diseases [59]. However, many of these designs take a side-viewing approach, whereby a single element transducer is attached to the distal end of an optical fiber and generates a field of view perpendicular to the fiber axis. This approach is not as desirable as a forward-viewing design, which is more useful for image-guided intraoperative procedures [102]. For PAE, this presents a design challenge because forward-viewing necessitates either lateral scanning of the transducer head (which is more challenging then rotational scanning of a side-view design), or the use of a 2-D array of transducer elements. Unfortunately, traditional ultrasound transducer elements are opaque to light; therefore, they need to be offset from the light source which increases the overall probe size.

To solve this issue, optically transparent ultrasound elements can be used. Dong et al. used a polymeric microring resonator ultrasound sensor and demonstrated phantom imaging with sub-10- μm axial resolution and 15.7 μm tangential resolution but retained a side-view design [103]. Furthermore, Ansari et al. recently demonstrated a novel, forward-view PAE system with a 3.2 mm diameter footprint that uses a Fabry-Pérot polymer film sensor, capable of resolving microvascular anatomy in impressive detail [50]. The sensor acts as a high-density transducer array with 50,000 individual elements and allows transmission of light with 45-170 μm on-axis lateral resolution, 31 μm vertical resolution, and 1-7 mm imaging depths. While still in its early stages, this new class of instrumentation shows promise for accelerating the use of PAE in image-guided laparoscopies and surgeries.

1.2.2. Exogenous Contrast Agents for Guided Surgery

Many exogenous contrast agents have been designed to accumulate at target sites and enhance the photoacoustic signal of diseased tissues. These are typically small molecules

or nano-scale agents injected into the bloodstream, but they can be administered via other routes. This section highlights some of the vehicles used specifically for tumor identification and resection (**Table 1.2**).

Variations of gold nanoparticles are popular because of their strong optical absorption (orders of magnitude greater than organic dyes), and geometry-dependent resonant frequencies that exploit the NIR window [13, 14]. Gold nanorods were employed in 2012 as dual PA/Raman contrast agents for passive targeting of ovarian xenografts in mice [104]. Here, maximum PA signal was observed after 3 h (persisting for 48 h). The detection limit was 0.40 nM, and the margins between tumor and normal tissue were clearly visualized. Silica-coated gold nanoparticles coated with Raman and MRI-active layers have also been developed as triple modality (PA/MRI/Raman) contrast agents for glioblastoma tagging and resection [105]. They exhibited optical absorbance coefficients 200-fold higher than previously studied carbon nanotubes, allowing for 3D imaging of deep-lying tumor tissue (via PA) in conjunction with the Raman modality's high sensitivity to microscopic tumor deposits. Guan et al. combined gold nanorods with indocyanine green dye (ICG, a NIR absorbing fluorescent dye) to integrate fluorescent imaging and photoacoustics with utility for liver cancer diagnosis [106].

Table 1. 2. Representative exogenous contrast agents used for applications in PA-image guided surgery.

Photoacoustic Agent	Description	Wavelength (nm)	Target	Image-Guided Outcome	Reference
B7-H3-ICG	Anti-B7-H3 conjugated with Indocyanine Green	800-825	Breast Tumor	*In vivo* murine tumor delineation	Wilson et al. 2017 [107]
Gold Nanorods	Gold nanorods coated with PEG, 41 nm x 12 nm, 3.5 aspect ratio	756	Ovarian Tumor	*In vivo* murine tumor delineation and resection guidance	Jokerst et al. 2012 [104]
Iron Oxide NPs (Endorem®)	Superparamagnetic Iron Oxide NPs (80-150 nm diameter)	720	Lymphoma	Nodal staging of resected human lymph nodes	Grootendorst et al. 2013 [108]
Coomassie Blue Polyacrylamide NPs	Polyacrylamide hydrogel nanoparticles crosslinked with Coomassie-Blue dye (80 nm diameter)	590	Brain Tumor	*Ex vivo* murine tumor delineation	Ray et al. 2011 [109]
ICG-Coated Gold Nanorods	Gold nanorods coated with liposomal indocyanine green, 31 nm x 10 nm, 3.1 aspect ratio	795	Liver Tumor	Pre-operative PA detection and intraoperative fluorescence-guide resection	Guan et al. 2017 [106]
Black Hole Quencher 3-Fluorescein-labeled Trastuzumab	Chemotheraeutic trastuzumab dual-labeled with BHQ3 (photoacoustic) and fluorescein (fluorescence)	700	Breast Tumor	Pre-operative PA detection and post-operative fluorescence-guided resection validation	Maeda et al. 2015 [110]
Silica-coated gold nanoparticles with Raman/MRI-active layers	Gold nanoparticles (60 nm) coated with trans-1,2-bis(4-pyridyl)-ethylene (Raman), silica, and DOTA-Gadolinium (MRI)	532	Brain Tumor	Intra-operative PA and Raman-guided resection	Kircher et al. 2012 [105]

A variety of other nanoparticles for PA-based tumor tagging have been studied as well [8]. Magnetic iron oxide nanoparticles (IONPs) are biodegradable with low toxicity and

have been used previously in humans in conjunction with MRI [111]. They enhance PA signal in lymph nodes following uptake by nodal macrophages although metastatic versus benign tissue could not be distinguished [108]. However, Xi et al. reported the successful imaging of breast cancers with IONPs conjugated with NIR-dye labeled peptide fragments in a murine model [112]. Other groups have reported tumor targeting antibodies labeled with PA contrast agents (such as the Black Hole Quencher 3 dye) [110] and self-assembling nanovesicles containing lipid-based dyes (J-aggregates) [113].

One challenge in PAI is differentiating the signal from the contrast agents from that of endogenous photoabsorbers. With spectroscopic photoacoustic imaging (sPA), it is possible to reduce noise from background photoabsorbers using knowledge of their wavelength-specific absorption spectra and relative tissue concentrations to isolate the signal of the exogenous agent [114, 115]. Wilson et al. used sPA and an ICG-labeled antibody to target and image a novel breast cancer surface receptor, B7-H3 [107]. They could distinguish agent that had located and penetrated the target cells because of the spectral shift in absorption following its endocytosis and degradation by malignant cells.

1.3. Monitoring Drug Delivery

1.3.1. Nanocarriers and Co-Loaded Contrast Agents

A major challenge in drug delivery is the noninvasive and real-time monitoring of biodistribution and pharmacokinetics. In humans, radiotracers in conjunction with PET/CT scanning can be used [116]. In animals, pharmacokinetics are usually determined via radiolabeling followed by dissection or imaging for biodistribution analysis [117]. PAI shows potential in small animals for both localized drug monitoring and whole-body imaging in a non-invasive format without ionizing radiation [118]. Unfortunately, very few clinically

prescribed drugs, if any, exhibit intrinsic absorption in the NIR—an important trait for PAI [28]. This shortcoming can be overcome, however, with the use of co-loaded contrast agents and nanocarriers and that act as vehicles for drugs. Furthermore, some of these materials can act therapeutically themselves, in the case of photothermal and photodynamic therapies. Examples of contrast agents discussed in this section are highlighted in **Table 1.3**.

Table 1. 3. Representative exogenous PA contrast agents with applications in drug delivery and monitoring.

Photoacoustic Agent	Description	Wavelength (nm)	Target	Image-Guided Outcome	Reference
Semiconducting Polymer Nanoparticles	Photothermal SPNs doped with fullerene	750	Breast Tumor	Photothermal therapy	Lyu et al. 2016 [119]
Nanonaps	Frozen micelles of hydrophobic, napthalocyanine dyes (~20 nm diameter)	600, 707, 793, 863 (Tunable)	Intestine	Diagnosis/treatment of intestinal motility disorders	Zhang et al. 2014 [120]
MoS_2 Nanosheets	PEGylated, 2-D nanosheets loaded with photodynamic Ce6	800	Breast Tumor	Photothermal therapy, photodynamic therapy	Liu et al. 2014 [121]
Rb_xWO_3 Nanorods	Rubidium tungsten bronze nanorods with doxorubicin payload, 20-40 nm x 5 nm	808	Breast Tumor	Combined chemo/photo-thermal therapy	Tian et al. 2014 [122]
Gold Nanocages	Gold nanocages loaded with 1-tetradecanol (phase-change) and organic dyes	750	Non-specific	HIFU/Temperature-triggered drug release and monitoring	Moon et al. 2011 [123]
Fucoidan Capped Gold Nanoparticles	Gold nanoparticles coated with fucoidan and doxorubicin	566	Breast Tumor	Chemotherapy	Manivasagan et al. 2016 [124]
Perfluorocarbon Nanodroplets	Perfluorocarbon nanodroplets loaded with gold nanorods and paclitaxel	770	Cervical Tumor	Combined chemo/photo-acoustic therapy	Zhong et al. 2016 [125]
Porphyrinoid-Loaded PLGA Nanoparticles	Poly(lactic-co-glycolic) acid nanoparticles loaded with porphyrinoid macrocycles	910	Uranium	Quantification of in vivo uranium exposure	Ho et al. 2015 [126]
Optode Nanosensors	Intradermal injectable nanosensor containing a crown ether ionophore and a chromoionophore	515, 660	Lithium	Drug monitoring of systemic lithium dose	Cash et al. 2015 [127]
Methylene Blue or Nile Blue	Cellulose-based, PEG-infused substrates containing Nile Blue	680	Heparin	Drug monitoring of systemic heparin dose	Jeevarathinam et al. 2018 [128]

In 2011, hollow gold nanocages were loaded with a phase change material (1-tetradecanol) and either methylene blue (44 g/L solubility in H_2O) or Rhodamine 6G (20 g/L solubility in H_2O) to demonstrate a controlled release drug delivery system that can be monitored with PAI [123]. 1-Tetradecanol has a melting temperature of 38°C and the authors showed that high-intensity focused ultrasound (HIFU) or heating could melt the material, allowing both the hydrophilic methylene blue and 2-fold less hydrophilic Rhodamine 6G to leak from pores in the nanocages at a controllable rate. Another group has shown that the hydrophobic cancer drug, doxorubicin, can be loaded with fucoidan capped gold nanoparticles for PA imaging of anti-tumor therapy in breast cancer cell lines [124]. However, it was not demonstrated in vivo. One interesting approach is to use the pulsed NIR excitation itself as a stimulus for drug release—e.g. using a low laser fluence for imaging and a higher fluence for triggered release. Wilson et al. first developed this platform by loading phase-change particles (perfluorocarbon droplets) with gold nanorods (for optical absorption), showing that both US and PA signal could be drastically boosted following the vaporization of the particles; the technique was then extended by Zhong et al. who incorporated paclitaxel for an activatable release mechanism at a laser fluence of 14 mJ/cm^2 [125, 129]. Organic vesicle-forming carriers also show potential for drug delivery imaging via their capacity for passive loading and biodegradability. Supra-molecular assemblies of the highly absorbent porphyrin (porphysomes and porphyrin shell microbubbles) can accumulate in tumors of xenograft-bearing mice while exhibiting high contrast [130, 131]. Ho et al. showed that polymeric nanoparticles containing porphyrinoids could boost PA signal upon complexing with uranyl ions, demonstrating a path towards sensitive and specific imaging of radioactive isotopes in vivo [126].

Another promising method for direct PA drug monitoring was demonstrated by Cash et al. in 2015 [127]. They developed a nanosensor capable of detecting systemic lithium. Upon recognition by a crown ether ionophore, a lithium cation deprotonates a chromoionophore of the nanosensor, changing its absorption, PA, and fluorescence properties. This injectable nanosensor allows for the continuous PA and fluorescence monitoring of lithium, which has both a narrow therapeutic window and low toxic dose. An injectable nanosensor has also been developed for cell permeable calcium ion imaging [132]. This group synthesized a metallochromic compound based on fura-2, a fluorescent indicator for calcium, but replaced the chromophore with a semi-cyanine chromophore to shift the absorption to longer wavelengths while maintaining a photoinduced charge transfer mechanism. Furthermore, the first application of photoacoustics for non-invasive imaging of the ubiquitous anticoagulant, heparin, was recently reported [128, 133, 134]. Currently, heparin concentrations in patients undergoing surgery are monitored with the activated partial thromboplastin time (aPTT) per nomogram, an in vitro surrogate test for the deactivation of clotting factors [135]. Here, the concentration of heparin was monitored in blood using the FDA approved dye methylene blue, a method that benefits from a fast turnaround time, strong sensitivity to heparin, and correlation to the aPTT. Methylene blue is an attractive PA agent because of its clinical approval [136, 137]— it has previously been used for PAI of sentinel lymph nodes [138] and has also demonstrated PA lifetime and intensity shifts via self-quenching and interactions with micelles [139, 140].

Non-IR-absorbing carriers can be used for drug monitoring if the payload includes fluorescent/PA-active dyes. Multispectral Optoacoustic Tomography (MSOT) was developed to image fluorescent proteins in vivo. It can track, at high speeds, the

biodistribution of fluorescent agents (e.g. ICG, carboxylate dyes) through circulation and uptake in the liver, gallbladder, and kidneys [141, 142]. These agents are commonly loaded within delivery vehicles to boost contrast. Perfluorocarbon (PFC) nano-droplets have been loaded with ICG to enable photoacoustic and ultrasound imaging; signal is enhanced by the optically triggered phase transition of the droplets to generate PFC microbubbles [143]. This controlled event also allows for drug release. Another unique example is the use of PAT with micelle-forming naphthalocyanines, "nanonaps", to address the challenges of non-invasive GI tract imaging [120]. These hydrophobic chromophores self-assemble in biocompatible surfactant (PEO-PPO-PEO) to form 20 nm spheres with high PA signal. Organic dyes are promising in PAI for their biocompatibility, multimodal nature, small size, and general stability. Current efforts devoted to synthesizing new fluorophores for optical imaging in the deep NIR (second optical window) will also have significant utility for PAI [144] For the time being, payload strategies that incorporate already FDA approved dyes such as methylene blue and ICG may have the quickest path to clinical approval. However, much work remains towards demonstrating the full potential of PAI for drug delivery and monitoring. In humans, because penetration depths are heavily surface-weighted and tissue-transducer coupling is required, it is likely that drug monitoring applications will continue to take the form of localized imaging and monitoring approaches rather than full-body biodistributions.

1.3.2. Photothermal Contrast Agents

Certain nanocarriers can exert their own therapeutic effects by exciting them via NIR laser radiation to release heat. Photothermal therapy (PTT) refers to the use of these photothermal agents for targeted tissue ablation. In recent decades, thermal ablation has been

used to destroy diseased tissue using radiofrequencies [145] and lasers without contrast agents [146]. Recently, dual contrast/PTT agents have become attractive for their ability to combine diagnostic and therapeutic capabilities into a single agent [147]. Desirable traits for these agents include the ability to locate and identify tumor margins, monitor the treatment in real time, and determine post-treatment effectiveness afterwards. Photoacoustic imaging is particularly suited for monitoring these tasks.

In 2006, gold nanorods functionalized with antibody were shown to selectively target malignant cells *in vitro* [148]. Photothermal destruction of the cells could be triggered using an 800 nm NIR laser, and malignant cells (with higher nanorod uptake) required half the laser power of non-malignant cells to cause necrosis. It was subsequently shown that PTT could be integrated with PAI using agents such as quantum dots [149], graphene [150], gold nanoshelled microcapsules [151], gold nanovesicles [152], iron oxide-polydopamine nanocomposites [153] porphysomes [130, 154], and semiconducting polymers [119]. Quantum dots extended their application in fluorescent imaging to PAI/PTT, but their absorption spectra marginally overlapped with that of blood. In contrast, nanographene sheets (coated with polyethylene glycol, "PEGylated") showed excellent NIR absorption and passive targeting of tumors, while requiring a relatively low laser power density for effective ablation.

Transitional metal dichalcogenides (TMDCs) are another noteworthy class of 2D nanomaterials; they have gained popularity in electronics and energy storage because of their unique optical and electronic properties. These materials are now being studied for their utility in medicine. In one such example, PEGylated WS_2 nanosheets passively targeted tumors while maintaining strong photothermal activity. This enabled tumor ablation via NIR light-activation [155]. Both groups hypothesized that the 2D geometries of nanosheets are well

suited to take advantage of the experimentally observed enhanced permeability and retention (EPR) effect of growing tumors.

Organic carriers can also be useful in PTT for their biocompatibility and capacity for drug loading. Porphysomes have passive tumor targeting and PA signal while also being photothermally active [130, 154]. Some polymer carriers have been combined with inorganic components: gold-nanoshelled microcapsules, for example, consist of poly-lactic acid cores coated with gold nanoparticles to impart both photoacoustic and photothermal functionality with drug-loading capabilities. Recently, semiconducting polymer nanoparticles, engineered at the molecular orbital level to favor photoinduced electron transfer, were shown to localize in tumors while increasing photoacoustic signal and PTT efficiency [119].

In 2017, the temperature responsive polymer poly(N-isospropylacrylamide) (PNIPAM), was loaded with photothermally active gold nanorods to achieve sensitive PA monitoring of photothermal therapy [156]. PNIPAM shrinks when heated, allowing the gold nanorods to approach one another and shift their NIR absorbance (and PA signal) via plasmonic coupling. These dynamic constructs were used to selectively monitor photothermal activation in murine prostate tumors while negating background from blood. Overall, these advances in PTT demonstrate practical ways that PAI can be leveraged with synergistic contrast agents to both deliver and monitor drugs in real time.

1.3.3. Photosensitizers and Photodynamic Therapy

Photodynamic therapy (PDT) is another therapeutic approach that can work in tandem with PAI. PDT was the first drug-device combination to be approved by the FDA over two decades ago [157]. It has been used clinically to address a wide range of conditions, such as acne [158], microbial infections [159], and macular degeneration [160]. Currently,

researchers are showing the potential for PDT to address a number of unmet needs in cancer therapy [161]. It requires light, oxygen, and a photosensitizer, an agent that can absorb light and initiate a photochemical reaction to generate the highly reactive singlet oxygen, a type of reactive oxygen species (ROS). Singlet oxygen is characterized by the opposite spin of a pair of its electrons, reducing its stability and lending it cytotoxic effects. During the procedure, a photosensitizer is systemically or locally administered, localizing in a neoplastic region, followed by irradiation from a light source. Because NIR light penetrates tissue deeper than other optical wavelengths, ideal photosensitizers would be strong absorbers in the NIR range.

PAI also uses NIR absorbing agents, and some photosensitizers exhibit PA contrast in vivo. This allows the monitoring of therapy in real time [162]. Ho et al. demonstrated the photoacoustic activity of five photosensitizers— the most promising molecule, zinc phthalocyanine, localized in tumors within 10 min, peaked at 1 h, and cleared after 24 h. Unfortunately, the activation absorption spectrum of many photosensitizers is in the visible range. In order to extend the usable depth of these agents in human tissue, it is possible to convert deep penetrating NIR light to visible wavelengths while enabling activation of the photosensitizers. Idris et al. accomplished this using mesoporous-silica-coated upconverting fluorescent nanoparticles that functioned as "nanotransducers" to convert NIR light to visible in vivo [163]. Creative strategies such as this one will be required to enable PDT in deep-tissue applications. Alternatively, because 1) PDT requires oxygen to generate ROS and 2) PAI can be used to image oxygen saturation (via the ratiometric absorption of oxygenated and deoxygenated hemoglobin), the efficacy of PDT can be monitored label-free. Shao et al. used AR-PAM to image SO_2 in the microvasculature of a rat ear following

tail vein injection of the photosensitizer Verteporfin with 80 mW/cm^2 light irradiance for 60 min [164]. They observed an initial decrease in oxygenation followed by a gradual recovery during the treatment course; however, the data was limited to a sample size of n = 3. Nevertheless, this study showed the potential for PDT monitoring with endogenous contrast.

As with other PA applications, the therapeutic agent does not strictly require inherent contrast. The active agent (the photosensitizer, in PDT) can be loaded into NIR-absorbing vehicles to enable PA signal. Srivatsan et al. showed that the photosensitizer HPPH could be loaded onto the surface of gold nanocages via non-covalent entrapment with a PEG monolayer [165]. These conjugates were stable in saline and began to degrade in protein solutions. This allowed for slow release of HPPH under biological conditions. PAI was harnessed to track the progress of delivery and suppressed tumor growth in mice—likely because of the passive targeting of the nanocages and generation of singlet oxygen at tumor sites by HPPH. Similarly, gold nanovesicles loaded with the photosensitizer Ce6 have been shown to infiltrate tumors in xenograft-bearing mice while drastically reducing the growth of tumors after 14 d [166]. This study highlights the synergistic effects of agents that allow for both thermal ablation (PTT) and ROS generation (PDT). In fact, TMDC nanosheets, previously discussed for their photothermal applications, have also been employed for PDT. Liu et al. took advantage of the high surface area of MoS_2 nanosheets to load Ce6, which then passively targeted and suppressed tumors via ROS generation and photothermal ablation [121]. One more strategy for synergistic therapy is to use a multifunctional material such as $Cu_2(OH)PO_4$ quantum dots to achieve a "one-for-all" technique for PAI-guided PTT/PDT [167]. Notably, these particles absorb well into the second optical window (up to 1700 nm). In the clinic, these could be implemented for image-guided therapy by delivering

the agent to the site of a tumor, imaging the distribution of the agent for treatment guidance, and then pulsing NIR light for PTT/PDT therapy followed by PAI for short and long-term monitoring. However, the toxicological effects of quantum dots vary widely and more work is needed to establish their potential utility in humans [168].

1.4. Monitoring Disease States and Therapeutic Effects

Diseases are multi-scale processes that exert effects from the molecular to the visible. Diseases often begin with a molecular event and gradually cascade as larger macroscopic effects emerge. As a molecular imaging modality, PAI is capable of revealing the early stages of pathogenesis. Early detection of these pre-disease states is critical when the therapeutic intervention can have the greatest impact. Importantly, by imaging changes in specific aberrations characteristic of disease—such as hemodynamics or ROS generation—the utility of PAI can extend beyond initial diagnosis to monitoring the results of therapeutic intervention. This section covers applications that use both endogenous and exogenous contrast, and examples are highlighted in **Table 1.4**.

Table 1. 4. Representative endogenous and exogenous targets used for PA monitoring of therapies and disease states.

Endogenous/Exogenous PA Target	Description	Wavelength (nm)	Image-Guided Outcome	Reference
Hemoglobin	Label-free 3D monitoring of colorectal xenografts in response to vascular disruptor Oxi4503	600, 640, 758	Evaluation of anti-angiogenic therapy	Laufer et al. 2012 [169]
Hemoglobin	Label-free 3D monitoring of orthotopic ovarian tumors following trebananib treatment	757, 797, 837	Evaluation of anti-angiogenic therapy	Bohndiek et al. 2015 [170]
Circulating Tumor Cells	Label-free, real-time monitoring of flow rate and distribution of melanoma CTCs in the mouse brain	680	Tracking of metastatic cancer cell fate for malignancy indication	Li et al. 2017 [118]
Organic Semiconducting Nanoprobes (OSNs)	Boronate-caged boron-dipyrromethane dyes were doped with bulky boranes for imaging peroxynitrite	675	ROS monitoring	Zhang et al. 2017 [171]
Silver-Coated Gold Nanorods	Au/AgNRs were etched by ROS at sites of bacterial infection for Ag ion release and PA imaging	800	ROS monitoring and anti-bacterial treatment	Kim et al. 2018 [172]
Lipid Rich Plaques	Atheromatous lesions of human aortas were spectrally distinguished from healthy areas	970, 1210	Vulnerable plaque identification for atherosclerosis	Allen et al. 2012 [66]
J-Aggregating Nanoparticles	Light-harvesting porphyrins were intercalated with phospholipids to form PA-active nanovesicles sensitive to temperature	680, 824	Monitoring thermal therapy of tumors	Ng et al. 2014 [173]
Oligomerizable Fluorescent Peptide Probes	Furin substrates were linked with an Atto740 fluorophore and cleaved to form aggregated, PA active nanostructures	740	Monitoring proteolytic furin and furin-like activity in tumors	Dragulescu-Andras et al. 2013 [174]

1.4.1. Blood and Vasculature

PAI is well suited for vascular imaging because it is optically sensitive to oxygen saturation of hemoglobin at visible and NIR wavelengths, and it can operate at length scales from a few microns to millimeters. PAI can improve upon current methods for vascular imaging, which have various drawbacks including the use of ionizing radiation (CT), requisite contrast agents (pulse-echo US, MRI, CT), minimum flow velocities (speckle variance tracking), and low penetration depths (optical methods).

Angiogenesis refers to the growth of new blood vessel networks and is often correlated to the progression of a tumor. Laufer et al. used a PA scanner and a time-reversal image reconstruction program to create accurate 3D images of angiogenesis in vivo at depths of nearly 10 mm and with sub-100 μm spatial resolution [169]. Tumor margins were clearly visualized while showing dynamic changes such as the recruitment of feeding vessels from surrounding tissue and vessel tortuosity. In addition, by administering the targeted vascular disrupting agent, OXi4503, PA images showed that features of necrosis associated with this agent could be tracked longitudinally. Trebanabib is another drug that disrupts angiogenesis. Bohndiek and colleagues showed that PAT could be used to monitor the antiangiogenic efficacy of trebanabib by monitoring the tumor hemoglobin concentration and oxygenation in an orthotopic mouse model of ovarian cancer [170].

In 2014, a handheld system was developed that could provide volumetric imaging of spectrally resolved vascular parameters in real time [175]. In a healthy human wrist, the spectral signals from melanin, oxygenated hemoglobin, and deoxygenated hemoglobin were separated and imaged within a few seconds. In mice, favorably low concentrations (10 nM) of the dye ICG were employed to boost contrast and monitor perfusion in the brain, allowing

for an overall improvement of sensitivity in deep tissue while using less agent. The application of PAI to functional brain imaging was further developed by Yao et al., who were able to image blood oxygenation, flow, vascular morphology, and O_2 metabolism using PAM [62]. They achieved capillary level resolution while imaging through the intact mouse skull.

Very recently, Li et al. reported the development of a novel PA system, Single-Impulse Panoramic Photoacoustic Computed Tomography (SIP-PACT), which has already been used to image the full mouse body, brain functional connectivity, and track circulating tumor cells in the living vasculature. This scheme improves upon many of the issues encountered with PACT thus far, especially low spatiotemporal resolution beyond 10 mm depths caused by multiplexed signal acquisition, partial spatial sampling, and gaps in acoustic detection space. In its current form, SIP-PACT is designed and optimized for full body imaging of the mouse, combining a ring shaped, 512-element transducer array with multi-source, confocal laser propagation, providing frame rates of 50 Hz and the ability to image vasculature, organs, and sub-organ structures at high spatiotemporal resolution. The team ultimately aims to use it to resolve individual action potentials throughout the brain, which will require even greater advances in spatiotemporal resolution as well as contrast agents sensitive to voltage. It should be understood, however, that full body imaging requires a water bath for coupling, which limits the design at this stage to small animals.

1.4.2. Reactive Oxygen Species

ROS are highly reactive molecules formed by the reaction of molecular oxygen with electrons and include O_2-, H_2O_2, $^{\cdot}OH$, and $^1O_2$ (singlet oxygen) [176]. They have been implicated in the etiology of dozens of disease states as well as normal biological functions

[177-179]. Because their presence can be linked to both the onset and progression of many diseases, they are powerful targets for monitoring pathogenesis in real-time and measuring therapeutic effects.

In 2014, initial steps were taken to develop real-time probes of pathogenesis in the form of semiconducting π-conjugated polymer nanoparticles (SPNs) [180]. These agents are NIR-active nanoparticles capable of generating bright PA signal. Because of their stability towards ROS, they were conjugated to a cyanine dye (IR775S), sensitive to oxidation by ROS, allowing for spectral differentiation between various ROS. It was shown in murine macrophage cells that activated SPNs could return to their normal state when their environment was no longer saturated with ROS illustrating the real-time monitoring potential for these agents. The SPNs were subsequently proven to highlight regions of increased ROS production in murine models of acute edema. Importantly, these agents could undergo signal evolution following a molecular event, making them activatable. An example of a ROS-sensitive, activatable nanoparticle was demonstrated in 2018— here, a silver-coated gold nanorod was used for simultaneous imaging and treatment of bacterial infection [172]. In this strategy, the PA signal from gold was initially quenched while coated with silver, but was gradually turned on as the silver was etched and released by ROS into sites of infection, exerting bactericidal effects. Activatable probes differentiate themselves from many of the agents used for guided surgeries, which are typically based on accumulation at a target site (relying on the EPR effect) with signal-to-noise ratios proportional to their concentration differences between target and background tissue.

Another activatable probe was recently developed for peroxynitrite. Peroxynitrite ($ONOO^-$) is a particularly reactive species, capable of nitrating numerous amino acids,

leading to mutation of protein function. It has also shown to play an important role in the immunosuppression of the tumor microenvironment, making it a highly desirable target for understanding the mechanisms that protect tumors from the host immune system and developing effective therapies [181]. Recently, Zhang et al. employed organic semiconducting nanoprobes doped with bulky boranes to enable ratiometric detection of $ONOO^-$ in murine tumors with PAI [171]. In short, this strategy allowed the ROS-sensitive component, a NIR-active dye, to shift its absorption upon reaction with $ONOO^-$ (enabling imaging), while the bulky borane prevented reaction with unwanted ROS and maintained a favorable pH in the local environment.

1.4.3. Lipids

Lipids are essential for many biological functions (energy storage, membrane structure, cell signaling, regulation) but can also perform destructive roles. Unfortunately, existing methods are lacking in their ability to image and quantitatively track lipid molecules in living cells [182]. Cardiovascular health in particular would benefit from such a method. There are currently no reliable techniques to detect vulnerable or unstable arterial plaques prone to rupture (leading to stroke or heart attack) [183]. One of the early studies in biomedical PAI showed that atheromatous (lipid rich) arterial tissue could be distinguished from healthy tissue using wavelengths in the visible range [184]. The characteristic spectra associated with lipids are generated by the overtones of the stretching vibration mode of C-H bonds abundant in their structures [66]. These spectral profiles of lipids are easily distinguished from other vascular constituents, such as collagen, elastin and water [185]. However, visible wavelengths are weakly penetrating and interfere with the absorbance of hemoglobin. Photoacoustic catheter designs can be used to mitigate this issue [186]. Another approach is to use the upper

wavelength range of the second NIR window [144] to penetrate tissue more deeply [187], where lipids have peaks around 1200, 1400, and 1700 nm [188].

In 2012, Allen et al. used NIR wavelengths around 1210 nm to image the entire thickness (3 mm) of an atheromatous region of aorta differentiating it from healthy tissue [66]. In addition, they demonstrated the feasibility of imaging through ~3 mm of blood, increasing the ease of use for intravascular implementation. Detection of atheroma in its early stages would allow for therapeutic and lifestyle interventions to prevent the onset of fully staged cardiovascular disease. Similarly, Wang et al. developed a rotational, catheter-based intravascular PA probe for the detection of lipid deposits within plaques of the aorta of rabbits [97]. Their data suggested that imaging of lipids at 1720 nm provided superior contrast to 1210 nm while also requiring lower laser output energy. The imaging speed was limited, however, to about 50 s per frame. To address this limitation, another group constructed a 2-kHz master oscillator power amplifier -pumped, barium nitrite Raman laser [189]. Because of its high repetition rate, pulse-to-pulse stability, and beam quality, this laser was able to image two orders of magnitude faster than prior reports (1.0 s per frame). These developments in intravascular lipid imaging, especially in concert with improvements in PAE probes, will likely continue to facilitate clinical translation.

1.4.4. Temperature and pH

Standard thermometers and pH meters can both be used for intravital readings but they cannot obtain precise spatiotemporal data. PAI is fundamentally sensitive to temperature (Equation 1) and can serve as a non-invasive approach for *in vivo* temperature mapping. Additionally, contrast agents for enhanced sensitivity can be used to obtain highly localized measurements of temperature/pH gradients as well as long term temporal

monitoring [190]. In comparison to their optical counterparts, PA probes are well-suited for this application because of their deeper penetration depths in tissue and ability to overlap with ultrasound anatomy.

In order to detect temperature changes in tissue following thermal therapy, Ng et al. developed a probe capable of spectral shifting via phase transition [173]. Photosynthetic organisms show a remarkable ability to optimize light absorption using ordered arrangements of pigment molecules within lipid and protein scaffolds. By mimicking this phenomenon with lipid-conjugated, light-absorbing porphyrins, the group assembled aggregates (nanovesicles) with tunable temperature thresholds, allowing for the generation of spatial maps of temperature thresholds to monitor heat therapy with PAI. The exploited mechanism of reversible dye coupling (J-aggregation) can also apply to biological stimuli beyond temperature, such as enzyme and pH detection.

Advancements have also been made in label-free temperature mapping and thermal detection of flow speeds. Typically, it is assumed that a linear correlation exists between temperature and the Grüneisen parameter, and that the temperature is independent from optical fluence [191, 192]. This allows relative temperature mapping based either on calibration measurements or ratiometric changes in PA signals, and avoids quantifying optical tissue parameters [193]. Recently, however, in order to achieve absolute temperature mapping, a multi-illumination PAT method was proposed and simulated that obtains optical parameters, such as the fluence, using multiple illumination sources and an optical diffusion model to quantify temperature directly [194]. This technique achieved relative errors between 10.6-15.7%, but has not yet been applied beyond simulation. Another interesting temperature-based PA technique was demonstrated by Liu et al., who developed a flowmetry method

based on OR-PAM that uses a pulsed light source for both “thermal tagging” and photoacoustic excitation [195]. It leverages the correlation between the Grüneisen parameter and local temperature to measure thermal dynamics and flow speed of homogenous or nonhomogeneous media. The authors were able to measure flow speeds (e.g. 2.55, 0.96, 0.99 mm/s) in the microvasculature of a mouse ear based on thermal fluctuations.

Aberrations in physiological parameters such as pH are associated with a number of conditions and diseases, including ischemia, inflammation, cancer, chronic obstructive pulmonary disease, and kidney failure [196]. Existing methods for in vivo pH detection rely primarily on dye fluorescence, which is hindered by light scattering, cytosolic leakage, and varying photostabilities [197]. In 2016, Miao et al. developed an activatable probe for the detection of pH, combining a semiconducting oligomer matrix (for PA signal) with a boron-dipyrromethene dye (for pH indication and PA enhancement) [198]. The dye backbone contained hydroxyl groups allowing for protonation upon exposure to acids, endowing the probe with sensitivity to pH. The researchers showed that in mice, a dose of 25 μg was sufficient for real time, ratiometric mapping of pH in tumors.

In 2013, PAI was used to monitor and image enzyme activity. Dragulescu-Andrasi et al. targeted the protease, furin, which plays a role in tumor regulation and normal cell function [174]. They devised an enzyme-sensitive oligomerizable reactive PA probe consisting of a peptide substrate, two pro-reactive moieties, and the NIR active PA molecule Atto740, sensitive even in deep tissue. The ability to image furin activity was shown in mice, and the probe could be theoretically adapted to interrogate other enzymes of interest. In another enzyme-responsive system, Chen et. al developed a micellar probe combining indocyanine green with an alkaline phosphatase-specific peptide for combination PAI and PTT. Here, the

probes had prolonged circulation/tumor accumulation and could convert to a nanofiber morphology once the peptides were phosphorylated by alkaline phosphatase in the tumor microenvironment [199]. In this form, the probes had 25-fold higher tumor uptake than free indocyanine green at 4 h after injection, while facilitating PTT (0.8 W/cm^2, 5 min) with high therapeutic efficacy. Enzyme-sensitive contrast agents hold significant biological interest but PA applications are still in their early stages. It is likely that strategies from other imaging modalities can be borrowed; for example, FRET-based mechanisms, responsive hydrogels, and assembly/disassembly of micelles [200]. However, some challenges include honing the specificity of engineered probes for their target enzymes (especially against members of the same enzyme family, e.g. matrix metalloproteinases), and choosing feasible targets that do not require deep tissue penetration.

1.5. Outlook And Future Developments

The applications and capabilities of photoacoustic technology are growing at a rapid pace. The development of novel PA systems such as SIP-PACT (Section 4.1), forward-viewing PAE (Section 2.1), and handheld PAM (Section 1.3) are promising examples of hardware innovations [50, 55, 118]. These advances are pushing the state of the art toward finer resolutions and new areas of application. It is feasible that the spatial resolutions of PAI will continue to improve as transducer elements become more affordable and image reconstruction algorithms are refined to address problems such as the heterogeneity of the speed of sound through various tissues [201]. Additionally, lower cost systems with excitation sources such as laser diodes [202] and light emitting diodes (LEDs) [203, 204], which are more stable, may increase the accessibility of PAI for researchers and clinicians alike. Furthermore, contrast agents with absorbance maxima at longer wavelengths in the second

optical window will be increasingly developed to improve the depths at which PAI is effective. This will likely mirror the recent progress in fluorescence imaging, where new NIR-II fluorophores have been pushing the field forward [18, 205, 206]. Analogous PA materials should become more common as the chemistry develops. Fortunately, PA systems do not need to implement expensive, high quantum efficiency detectors (InGaAs or HgCdTe) that are required for fluorescence imaging in the second optical window [19]. Instead, however, they must implement longer wavelength lasers—e.g., the commercial Vevo LAZR-X includes a 1200-2000 nm laser in addition to a 680-970 nm source (though this combination excludes the 1000-1200 nm range) [18, 79]. In the short-term, we believe that biodegradable contrast agents, small molecule dyes (especially those with existing FDA approval), and techniques that do not require intravenous injection will have the shortest paths to the clinic.

As the technology itself continues to develop, so does the application space. Work is underway by numerous groups on alternative transducer designs for specialized applications, including through-needle imaging for guided surgery [207], PA-guided surgical drilling [96], and human finger joint imaging [208]. "Wearable" PA devices are another example. The concept was recently demonstrated for dental imaging, specifically, non-invasive periodontal pocket depth measurements for early gum disease diagnosis. Here, a contrast agent derived from food-grade cuttlefish ink (rich in melanin nanoparticles) was used with PAT to image the pockets between gum and teeth, showing potential for a PA mouthpiece device [209, 210].

It is also worth recognizing progress in Magneto-Acoustic Imaging (MAI), a technique similar to PAI, but in which magnetic contrast agents are used to label tissue, whereafter a pulsed magnetic field is used to induce motion of the agents within the tissue, detectable by ultrasound [211]. Such a technique would circumvent the need for optical

penetration. Proof-of-concept has been demonstrated in cells and tissue phantoms and MAI remains in its early stages, but may see progress in the near future that parallels the recent growth of photoacoustics [212].

PAI will likely never become as widespread as MRI or CT, but it is highly complementary to ultrasound, already one of the most widely available imaging tools in medicine. While ultrasound generates anatomical images, PAI adds to this the molecular and functional contrast that is normally associated with optical imaging techniques. The clinical appeal of this combination will be a driving force for the continued growth of photoacoustic imaging.

1.6. Acknowledgements

Chapter 1, in full, is a reprint of the material as it appears in Theranostics, vol. 9, 1550-1571, 2019. Moore, Colman; Jokerst, Jesse V. The dissertation author was the primary investigator and author of this paper.

CHAPTER 2: LISTENING FOR THE THERAPEUTIC WINDOW: ADVANCES IN DRUG DELIVERY UTILIZING PHOTOACOUSTIC IMAGING

ABSTRACT: The preclinical landscape of photoacoustic imaging has experienced tremendous growth in the past decade. This non-invasive imaging modality augments the spatiotemporal capabilities of ultrasound with optical contrast. While it has principally been investigated for diagnostic applications, many recent reports have described theranostic delivery systems and drug monitoring strategies using photoacoustics. Here, we provide an overview of the of the progress to date while highlighting work in three specific areas: theranostic nanoparticles, real-time drug monitoring, and stem cell ("living drug") tracking. Additionally, we discuss the challenges that remain to be addressed in this burgeoning field.

2.1. Introduction

One of the fundamental goals of drug delivery research is to maximize the efficacy of therapeutics while minimizing their side effects. In many cases, this is achieved by delivering a high concentration of drug to a diseased tissue site or region of interest (e.g. tumor, infection, or organ). Therefore, in both research and clinical settings, it is critical to quantify biodistribution and pharmacokinetic parameters with high precision and accuracy. Increasingly, imaging modalities are being used to obtain these measurements because they can obtain *in vivo* data in a non-invasive format with good temporal and spatial resolution. Furthermore, they can be used in concert with delivery vehicles that simultaneously carry both imaging and therapeutic agents.

Ultrasound, magnetic resonance imaging (MRI), positron emission tomography (PET), and single photon emission computed tomography (SPECT) are all currently used in the clinic for pre- and post-treatment evaluation [213]. These have recently been pursued pre-clinically as molecular imaging tools to monitor therapies in real time [214, 215]. For example, numerous theranostic nanoparticles for MRI have been developed [216-218] that can co-deliver materials that boost T1 or T2 contrast (such as gadolinium [219], manganese [220] and iron oxide [221]) with therapeutic molecules. Similarly, radionuclides are commonly conjugated to biomolecules or drugs for probing biological processes (e.g. 2-deoxy-2-[^{18}F]fluoro-D-glucose for monitoring glucose metabolism [222]) or pharmacokinetics using the gamma radiation detectable with PET and SPECT [223-225]. Ultrasound can harness the cavitation of microbubbles to increase contrast [226].

These modalities are powerful tools but face a variety of drawbacks. One of the main challenges in imaging local tissue distributions of drug molecules is achieving sensitivity to

micromolar concentrations. PET, SPECT, and optical techniques are capable of this, but PET and SPECT have low resolutions (~1.5 mm), cannot provide anatomical information without CT pairing, and require ionizing radiation [227]; meanwhile, optical imaging is limited by shallow penetration depths and low clinical deployment [228]. MRI has high spatial resolution (<100 μm) but is limited in sensitivity (millimolar) without amplification strategies [229]. Finally, ultrasound can offer high spatiotemporal resolution but has low contrast—it is most commonly used in drug delivery as a tool to improve delivery via heat or cavitation [230].

While ultrasound can image structure in real-time, it can only distinguish tissue interfaces via differences in the speed of sound. In recent years, photoacoustic imaging has emerged as a technique that extends the contrast of ultrasound from the anatomical to the molecular—it augments the spatiotemporal resolution of ultrasound with the spectral contrast of optics [3]. This promising combination has spurred growth in the field over the past decade, with researchers pursuing applications in photoacoustic diagnostics/theranostics, surgery, and drug delivery [37, 67, 231].

This technique relies on the photoacoustic effect—energy from light is absorbed by a material and released as an acoustic vibration [232]. In a typical imaging event, a near-infrared (NIR) laser source is used to pulse light (1-100 ns) onto a tissue target [5]. At a molecular level, the target undergoes thermoelastic expansion which generates broadband acoustic waves detectable by conventional ultrasound transducers [4]. To date, it has been implemented in numerous hardware configurations: photoacoustic tomography and photoacoustic microscopy are the most widely used for research applications [3]. Microscopy offers excellent

spatial resolution but limited depth; tomography has better penetration but less spatial resolution.

Contrast can arise from both endogenous and exogenous sources. The main sources of endogenous contrast in photoacoustic imaging are strongly absorbing molecules such as oxygenated and deoxygenated hemoglobin [64], melanin [233], lipids [97], and water. These targets have often been used to image hemodynamics [52], blood oxygen saturation [89], and cancers [27]. However, a wide variety of exogenous contrast agents—often small-molecules or nanoparticles—have also been developed for both boosting contrast and probing specific biomarkers or disease states [7,234]. From a materials perspective, the current landscape of these agents primarily consists of organic small molecules [19], inorganic nanomaterials [15], and organic nanoparticles [20,235].

2.2. Photothermal and Photodynamic Contrast Agents

Photothermal and photodynamic therapy are two techniques for cancer therapy that rely on NIR irradiation. For this reason, they have frequently been combined with photoacoustic imaging so that the NIR excitation can be used for both imaging and therapy. In photothermal therapy, nanoparticles with a high photothermal conversion efficiency are excited with a pulsed or continuous-wave laser and the generated heat is harnessed for local tissue ablation.

One of the first examples of photothermal therapy performed with nanoparticles was published by Hirsch *et al*. in 2003 [236]. They found that solid tumors treated with gold nanoshells would undergo irreversible tissue damage ($\Delta T = 37°C$) within 4-6 minutes of 820 nm laser exposure (4 W/cm^2). Since then, a large body of work has been conducted on photothermal therapy with nanoparticles [237]. Furthermore, many of these particles have been

used in tandem with photoacoustic imaging: Gold nanovesicles [238], quantum dots [149], graphene oxide [239], porphysomes [240], semiconducting polymer nanoparticles [119], iron oxide-polydopamine [241], and bimetallic oxide (MoMnOX) nanorods [242] are a few examples.

One unique example was demonstrated by Chen *et al*. in 2017; here, they synthesized nanoparticles from the temperature sensitive polymer, poly(N-isopropylacrylamide) (PNIPAM) and loaded them with gold nanorods [156]. PNIPAM shrinks when heated above its lower critical solution temperature. Therefore, when the constructs were raised above this temperature, the gold nanorods were brought closer together, resulting in plasmon coupling and a shifted absorption spectrum. When these particles were localized to subcutaneous tumors of mice, they could then be used to photoacoustically monitor photothermal therapy in real-time while reducing background from hemoglobin. Though photothermal agents are most commonly metallic, certain organic materials can also be used. These typically benefit from enhanced biocompatibility or degradability. For example, Lyu *et al*. recently developed a method for increasing three key properties of semiconducting polymer nanoparticles [243]. They used polymer chemistry to introduce vinylene bonds to the polymer backbone that are cleavable by peroxidase, highly expressed in immune cells. This enhanced the biodegradability in addition to the absorption coefficient (1.3-fold) and the photothermal conversion efficiency (2.4-fold).

Photodynamic therapy is an FDA-approved procedure with a track record in the clinic for treating a variety of conditions including acne [158], bacterial infections [159], and macular degeneration [160]. In the past decade, it has been increasingly studied as a cancer therapy [161, 244]. Generally, the mechanism is as follows: A near infrared laser source is used to excite a photosensitizer molecule, which initiates a photochemical reaction with oxygen

to produce a singlet oxygen molecule. This molecule is an unstable reactive oxygen species (ROS), possessing an opposite spin pair of electrons that make it highly destructive and cytotoxic to its local environment.

Some photosensitizers possess intrinsic photoacoustic contrast, which can allow real-time treatment monitoring. Ho *et al*. studied the photoacoustic behavior of five well-known photosensitizers, and found that zinc phthalocyanine produced the highest signal [245]. They subsequently showed that its localization and biodistribution could be monitored with photoacoustics in mice, revealing a peak tumor concentration at 1 hour and clearing within 24 hours. However, many photosensitizers do not absorb in the near infrared which limits penetration depth and compatibility with photoacoustic imaging. To address this issue, it is possible to use upconverting particles that absorb near infrared light and emit visible. Using this strategy, Idris *et al*. loaded mesoporous-silica-coated upconversion fluorescent particles with multiple photosensitizers for enhanced photodynamic efficacy in melanoma-bearing mice [246].

Interestingly, it is also possible to monitor photodynamic efficacy with photoacoustics by simply harnessing the endogenous contrast of blood. It is well-established that blood oxygen saturation can be directly imaged with photoacoustics via the ratiometric absorbance of oxygenated and deoxygenated hemoglobin; therefore, because photodynamic therapy requires oxygen for ROS generation, the consumption of oxygen can be monitored in real-time via the decrease in blood oxygen saturation. Shao *et al*. demonstrated this technique in the mouse ear vasculature using AR-PAM after tail vein injection of the photosensitizer, Verteporfin [247]. After irradiation with 80 mW/cm^2, they observed an initial decrease in the oxygen saturation followed by a gradual recovery to baseline.

Photosensitizers can also be conjugated to or loaded into photoacoustically active nanocarriers. 2-[1-hexyloxyethyl]-2-devinyl pyropheophorbide-a (HPPH) is a hydrophobic photosensitizer that has been functionalized to the surfaces of gold nanocages using a poly ethylene glycol layer; these conjugates allowed the slow release of the photosensitizer in protein-containing solutions [165]. After injection into tumor-bearing mice, the progress of delivery was monitored with photoacoustic imaging and reduction in tumor volume was observed. It is also possible for agents to be used for both photothermal and photodynamic therapy; MoS_2 nanosheets [121] and $Cu_2(OH)PO_4$ quantum dots [248] have both been investigated on this front. These quantum dots actually absorb within the second optical window (~1700 nm) making them attractive for deep tissue applications [19]. The clinical utility of these photothermal/photodynamic agents could be local administration or systemic administration to target a disease site followed by activation and treatment monitoring using near infrared excitation via photoacoustic imaging [249].

2.3. Nanocarriers and Co-Loaded Contrast Agents

The clinical state of the art for imaging pharmacokinetics is PET/CT with drug conjugated or co-loaded radiotracers [250]. In the preclinical space, photoacoustic imaging is being used for monitoring drug release and localized measurements of delivery. These applications require the use of *in vivo* sensors or co-loaded contrast agents because most small-molecule drugs do not absorb NIR light—a prerequisite for photoacoustic contrast in the body. However, it is possible for some materials such as gold nanomaterials to act therapeutically (e.g. photothermal/photodynamic therapy) while intrinsically generating photoacoustic signal. This section surveys progress in theranostic nanoparticles and materials that can act both diagnostically and therapeutically.

Gold nanomaterials are a well-studied class of photoacoustic contrast agent due to their intense plasmon resonance in the near infrared [72]. In a study by Moon *et al*., hollow gold nanocages were used to encapsulate 1-tetradecanol—a material that undergoes solid to liquid transition at 38 °C (i.e., a phase-change material) [123]. The gold nanocages generated photoacoustic contrast, while external heating or high frequency ultrasound could be applied to melt the 1-tetradecanol, allowing it to diffuse out of the particles. Both methylene blue and Rhodamine 6G were dissolved in the 1-tetradecanol and shown to release from the particles at a controllable rate using this mechanism.

In 2012, Wilson *et al*. took advantage of perfluoropentane phase-change material to form nanodroplets that encapsulated gold nanorods for NIR absorption [129]. This is analogous to the strategy used by Hannah *et al*., who used perfluorocarbons to encapsulate the small molecule indocyanine green rather than nanorods [143]. Both groups found that ultrasound and photoacoustic signal could be drastically boosted following the vaporization of the droplets. Later, a group incorporated paclitaxel into the nanorod design for an activatable release scheme at laser fluence values of 14 mJ/cm^2 [125]. Zhong *et al*. found that indocyanine green, in addition to generating photoacoustic contrast, could act therapeutically by generating strong mechanical waves when loaded in a phospholipid-polyethylene glycol nanoparticle and exposed to constant laser fluence. They used this system for imaging and destroying cancer cells [251]. Gold and paclitaxel have also been integrated by Manivasagan *et al*., who synthesized chitosan oligosaccharide gold nanospheres and loaded their surfaces with paclitaxel [252]. These showed efficacy against MDA-MB-231 cells by generating reactive oxygen species and disturbing the mitochondrial membrane potential.

Doxorubicin is another cancer drug that has been investigated by numerous groups for co-delivery with photoacoustic contrast agents. In 2014, Tian *et al*. synthesized rubidium tungsten nanorods, a type of transition-metal oxide nanostructure with a size dependent plasmon resonance, and loaded them with doxorubicin [253]. These particles were able to exert both chemo- and photothermal therapy (photothermal conversion efficiency: 17.8%), generating a burst drug release and localized heating following 808 nm laser exposure (1 W/cm^2) for 10 minutes. They were used for photoacoustic imaging and treatment of pancreatic cancer (Pance-1 tumor model) in nude mice. Other transition-metal nanomaterials that have been pursued for photoacoustic drug delivery are molybdenum oxide nanospheres; these were stabilized with polyethylene glycol and loaded with camptothecin, a cancer drug that could be controllably released in a mouse model of pancreatic cancer [254]. Cobalt selenide nanoplates have also been reported as chalcogenide based theranostics, exhibiting high photothermal conversion efficiency (26°C temperature increase following 808 nm exposure for 10 min at 1 W/cm^2), low toxicity, and significant absorbance in the near infrared [255]. One of the main benefits of most metallic carriers is their ability for synergistic chemo- and photo-thermal therapy.

Table 2. 1. Examples of nanoparticle-based exogenous contrast agents for photoacoustic theranostics and drug monitoring.

Description	Contrast Mechanism	Imaging Wavelength (nm)	Therapeutic or Target	Model	Reference
Perfluorocarbon Encapsulated Gold Nanorods	Heat-induced phase transition (liquid to gas) of nanodroplets	770	Paclitaxel	Subcutaneous HeLA tumors in Balb/c mice	Zhong et al. 2016
Chitosan Oligosaccharide Stabilized Gold Nanoparticles	Thermal expansion at the peak plasmon resonance of 60 nm gold nanoparticles	532	Paclitaxel	MDA-MB-213 adenocarcinoma cells	Manivasagan et al. 2016
Porphyrinoid-Loaded PLGA Nanoparticles	Complexation of porphyrinoid macrocycles with uranyl cations to impart aromaticity	910	Uranium	Healthy mice with subcutaneous complexed nanoparticles	Ho et al. 2015
Rb_xWO_3 Nanorods	Thermal expansion of rubidium tungsten nanorods (20-40 x 5 nm)	808	Doxorubicin	Pance-1 tumor-bearing mice	Tian et al. 2014
MoS_2 Nanosheets	Thermal expansion of MoS_2 nanosheets	800	Ce6 (Photosensitizer)	Subcutaneous 4T1 tumors in Balb/c mice	Liu et al. 2014
Mesoporous Silica/Quantum Dot Coated Gold Nanorods	Thermal expansion of gold nanorods, leading to release of drug payload through silica layer	800	Doxurubin, p53	Subcutaneous glioma C6 tumors in Balb/c nude mice	Duan et al. 2016
Gold Nanocages Loaded with 1-Tetradecanol (Phase Change)	Thermal expansion at the peak plasmon resonance of gold nanocages (60 nm side length)	750	Methylene Blue, Rhodamine 6G	Controlled release study only	Moon et al. 2011
Fucoidan/Doxorubicin Capped Gold Nanoparticles	Thermal expansion at plasmon resonance of 82 nm gold nanoparticles	532	Doxorubicin	MDA-MB-213 adenocarcinoma cells	Manivasagan et al. 2016
Intradermal Optode Nanosensors Containing Crown Ether Ionophores	Shifted optical absorbance following binding of lithium to chromoionophore	515, 660	Lithium	Athymic nude mice	Cash et al. 2015
Single Wall Carbon Nanotubes with Mesoporous Silica/Doxorubicin	Thermal expansion of nanotubes via near infrared absorbance	808	Doxorubicin	4T1-tumor bearing mice	Liu et al. 2014

During the same year, Liu *et al*. loaded single wall carbon nanotubes with mesoporous silica and doxorubicin [256]. The goal was to leverage the loading and release capacity of mesoporous silica with the near infrared absorbance and photothermal

conversion efficiency of the nanotubes. The researchers found that the tumor surface temperature could be increased to 48°C when irradiated with 808 nm light at 0.5 W/cm^2 for 20 min. Again, this technique showed synergistic chemo-/photothermal effects against cancer in nude mice with 4T1 tumors. Similar efficacy and imaging traits were noted when the nanotubes were replaced with reduced graphene oxide, though the photothermal conversion efficiency is lower [257]. More recently, doxorubicin was delivered both via surface conjugation with fucoidan capped gold nanoparticles [124] and mesoporous silica-quantum dot functionalized gold nanorods [258]. This last example is particularly interesting because it included the delivery of p53 pDNA, a mechanism for gene therapy. These multi-mechanistic particles were capable of photoacoustic/magnetic resonance/computed tomography, and synergistic gene/chemo-/photothermal therapy. They could be magnetically guided to the tumor site under magnetic resonance imaging, and could be verified with photoacoustic imaging followed by activatable release via laser fluence or pH. The authors showed effective eradication and suppression of 4T1 tumors in nude mice with this system.

2.4. Therapeutic Drug Monitoring

The high temporal resolution and contrast of photoacoustic imaging offers the potential for real-time monitoring and maintenance of drug concentrations within the therapeutic window. Therefore, there is growing interest in developing new materials in tandem with photoacoustic imaging for therapeutic assays. For example, lithium is an effective treatment for bipolar disorder between 0.6-1.2 mM [259], but can be toxic at high doses above 2 mM [260]. Cash *et al*. developed a lithium ionophore-based nanoparticle to measure lithium concentrations in 15 seconds using photoacoustic imaging; the binding and release of lithium cations shifted the absorption and subsequently the photoacoustic intensity

of the nanoparticle [127]. This work demonstrated a novel and safe concept for chronic bipolar disorder management. In another case, porphyrinoid-containing nanoparticles were used to detect uranium ion concentrations in the parts per billion range [126]. In this case, uranium ions, though toxic rather than therapeutic, are analogous to a drug that is being monitored. Finally, photoacoustic imaging can indirectly monitor therapeutics via genetic indicators. For example, the tyrosinase-based reporter gene can catalyze the production of endogenous melanin, a strong near infrared absorber [261]. Zheng *et al*. found that microRNA-9, a potential gene therapy [262], could silence the translation of tyrosinase and reduce the photoacoustic signal. [263] Therefore, the photoacoustic shift could be correlated to the concentration of microRNA-9 in the cells.

To extend the capabilities of photoacoustics for monitoring drug dosing, our group has developed a photoacoustic imaging method to detect heparin. Heparin is an indispensable surgical and cardiovascular anticoagulant with more than 500 million doses given annually in the world [264]. However, it is difficult to maintain safe and efficacious heparin concentrations because it has a variable molecular weight and a narrow therapeutic window [265]. Furthermore, the current heparin measurement methods, such as the activated partial thromboplastin time (aPTT) [266], anti-Xa analysis [267], thromboelastography [268], and activated clotting time [269], require lab processing and thus a long turnaround time. The maintenance of inaccurate heparin dosing due to the belated measurement results can cause severe side effects including hemorrhage and embolism [270]. Photoacoustic imaging has the potential to address this problem by rapidly and longitudinally sampling blood samples. However, the hemoglobin and deoxyhemoglobin in blood are endogenous absorbers, meaning an exogenous contrast agent is required to differentiate heparin from blood [271].

In 2016, we described a simple photoacoustic method for real-time heparin measurement in human blood [133,272]. The method employed the Federal Drug Administration (FDA)-approved dye methylene blue as the contrast agent. It generated 31-fold enhanced photoacoustic signal when it was bound to 10 U/mL heparin. This high contrast overcame the noise caused by other components in blood and was strongly correlated to the heparin concentrations with a logarithmic regression of $R^2 > 0.97$ and a detection limit of 0.28 U/mL. This concentration was lower than the clinical dose of heparin used in common applications including thromboembolism (7–8 U/mL), acute myocardial infarction (2.5 U/mL), and cardiopulmonary bypass (5.6 U/mL), suggesting a broad clinical potential.

The rapid and sensitive photoacoustic enhancement of methylene blue to heparin unlocked the opportunity for developing a bed-side heparin and clotting assay. Therefore, we developed a nanosensor to immobilize methylene blue on the outer surface of a peripheral venous catheter for clinical applications [133]. The nanosensor was a silica nanoparticle/agarose hydrogel. However, simply conjugating methylene blue to the silica nanoparticle decreased the sensitivity of the photoacoustic enhancement. This was because the strong negative charges on the silica nanoparticle surface hindered the electrostatic association of methylene blue with the negative charged heparin. The photoacoustic signal could be reduced by the addition of protamine—the known antagonist of heparin.

Recently, we extended this work using the methylene blue derivative Nile Blue A infused in cellulose to measure heparin in blood samples. The cellulose sensor was a Whatman filter paper modified with polyethylene glycol for increased hydrophilicity. The Nile Blue A in the cellulose (0.6 nanomoles per mg of cellulose) had low solubility (< 10 ng/ml) in 0.01 M phosphate buffer saline due to ionic strength and pH, yet was highly

sensitive to heparin with a detection limit of 0.28 U/mL in plasma and 0.29 U/mL in human blood [128]. After analyzing the 78 blood samples from 16 patients that underwent cardiac ablations and received various doses of heparin, we found that the photoacoustic intensity of the cellulose sensor had strong linearity with the cumulative heparin dose (Pearson's r=0.85) and the activated clotting time (Pearson's r=0.87). These results suggested that the photoacoustic assay could potentially serve as a point-of-care testing method for heparin and clotting time measurement. Future work will be devoted to the development of an intravenous sensor for real-time heparin detection.

In another example, our lab used photoacoustic imaging to monitor Ag^+ delivered therapeutically. Ag^+ are a well-known antibacterial agent, and Ag nanoparticles can be a reservoir of Ag^+ for targeted therapy of bacterial infections. However, there are no tools to measure Ag^+ in vivo or trigger Ag^+ release from Ag nanoparticles. Our group recently used photoacoustic imaging with gold nanorods to monitor Ag^+ release [172]. The strategy coated the gold nanorods with Ag for hybrid nanoparticles. This coating decreased their photoacoustic signal. The as-prepared, Ag-coated Au nanorods (Au/AgNRs) are stable under ambient conditions, but the addition of exogenous ferricyanide (1 mM) or endogenous reactive oxygen species results in oxidative etching of the silver shell. The photoacoustic contrast is simultaneously recovered as the silver is released, and this photoacoustic signal offers noninvasive monitoring of localized release of Ag^+.

The released Ag^+ ions showed a strong bactericidal efficacy similar to equivalent free Ag^+, and the nanoparticles killed >99.99% of both (Gram-positive) methicillin-resistant Staphylococcus aureus (MRSA, 32 μM Ag^+ equivalent) and (Gram-negative) Escherichia coli (8 μM Ag^+ equivalent). The potential of these nanoparticles was further demonstrated in

a pilot rodent study. There was a 730% increase in the photoacoustic signal ($p<0.01$) pre- and post- etching, and the bacterial counts in infected tissues of the treated group were reduced by 1000-fold (log CFU/g = 4.15 vs 7.75) relative to the untreated cohort.

2.5 Stem Cell Delivery

Ultrasound imaging has strong potential for guiding the injection of therapeutic stem cells ("living drugs") to specific regions because it is a real-time imaging modality and the needle tip in soft tissues can be clearly visualized under the ultrasound transducers. In 2005, Springer and Rodriguez-Porcel *et al*. from two separate research groups described ultrasound imaging-guided percutaneous injections of cells into a mouse infarct model [273, 274]. This approach is also applicable to large animals [275]. The ultrasound-guided procedure is less invasive and significantly more accurate than open-chest injections. However, it is difficult to visualize and track injected therapeutic cells with ultrasound imaging because these cells have poor ultrasound contrast relative to the local tissues [276]. Moreover, the guided catheter position does not guarantee sufficient cell delivery at the desired location [277].

The inability to track stem cells leads to blindness of delivery efficiency and retention in patients [278]. However, cell tracking *in vivo* is essential to understanding the cell fate, therapeutic efficacy, and safety issues related to the injected cells [278]. Therefore, it is important to develop *in vivo* cell tracking techniques. Based on the already-existing imaging modalities, novel contrast agents can help better visualize injected cells. While contrast agents for other imaging modalities have been investigated [279], the development of ultrasound/photoacoustic contrast agents for *in vivo* stem cell tracking is more attractive given the convenience, low cost, and safety of ultrasound/photoacoustic imaging [280, 281].

The most common ultrasound contrast agents are microbubbles. Cui *et al*. demonstrated that microbubbles could track neural progenitor cells *in vivo* [282]. An ultrasound frequency of 7 MHz could detect a single microbubble-labeled neural progenitor cell. However, the elevated ultrasound signal was only maintained for up to 7 days, close to the upper limit for microbubbles. Due to their large size and instability, microbubbles are incapable of long-term tracking for therapeutic cells *in vivo* [283].

Because microbubbles are limited in their utility for stem cell tracking by their short lifetimes, we have investigated silica nanoparticles as ultrasound contrast agents for therapeutic stem cell delivery and tracking; these particles are generally biocompatible and have high impedance mismatch with soft tissues.

Our group has studied the echogenicity of solid silica nanoparticles (SiNPs) [277] and MCM-41 typed mesoporous silica nanoparticles (MSNs) as therapeutic ultrasound contrast agents [284]. Both nanoparticles increased the ultrasound signal of human mesenchymal stem cells (hMSCs). The SiNP aggregated within the stem cells to amplify the ultrasound backscatter. The ultrasound contrast of SiNP-labeled hMSCs was 6 times higher than unlabeled cells. The detection limit of SiNP-labeled hMSCs in cardiac tissue of rodents was 70,000 *via* ultrasound imaging. The MSNs enhanced the ultrasound signal of hMSCs and increased the stem cell survival *via* sustained release of pro-survival agents. The detection limit of MSNs-labeled hMSCs at this concentration was near 9000 cells via ultrasound imaging. Moreover, the MSNs could degrade in cells and were cleared in approximately 3 weeks.

Later, the effect of particle morphology on echogenicity was studied for four types of silica nanoparticles including Stöber silica nanoparticles (SSN), MCM-41 mesoporous

silica nanoparticles (MSN), mesocellular foam silica nanoparticles (MCF), and novel exosome-like silica nanoparticles (ELS) that are reminiscent of the shape of exosomes [285]. The porous silica nanoparticles showed stronger echogenicity than solid nanoparticles with similar diameter when their mass concentrations were kept constant. In addition, all silica nanoparticles were biocompatible with hMSCs when the labeling concentrations were no higher than 500 μg/mL. The ELS nanoparticles showed the highest cellular uptake and increased the echogenicity of hMSCs the most.

Another type of inorganic nanoparticle for ultrasound contrast that has been used for cell tracking are glass nanospheres. Foroutan *et al*. developed glass nanospheres to increase the ultrasound signal of therapeutic stem cells [286]. The nanospheres are biocompatible and biodegradable, and thus they can be easily metabolized in the body. The glass nanosphere-labeled MSCs could be measured with ultrasound imaging with cell counts as low as 4000.

One limit of these nanoparticles-based ultrasound contrast agents is that the ultrasound signal does not reflect information about cell death. However, research involving gene editing makes it possible to specifically track live cells via ultrasound. Kuliszewski *et al*. programmed therapeutic stem cells to produce a specific cell surface protein H-2Hk, which is the target of the injected microbubbles [287]. Hence, only cells that have the unique cell marker will show strong ultrasound signal. Shapiro's group reported biogenic gas nanostructures as ultrasonic molecular reporters [288-290]. However, this method has only been applied in microorganisms up to this point.

While the ultrasound intensity of therapeutic cells can be enhanced by novel contrast agents, the modality still suffers from low signal-to-noise due to the lack of spectral contrast. To combat this, photoacoustic imaging combines the benefits of ultrasound and optical

imaging, providing spectral contrast between targets (e.g. labeled stem cells) and local tissues [281]. Thus, photoacoustic imaging for therapeutic stem cell tracking has been more broadly investigated than traditional ultrasound imaging [287, 291-293].

Gold nanoparticles are some of the most popular photoacoustic contrast agents due to their high absorption cross sections and multiplexable absorption peaks [281]. Jokerst *et al*. labeled MSCs with silica-coated gold nanorods and could track the labeled MSCs via photoacoustic imaging [291]. The silica shells stabilized the photoacoustic signal of gold nanorods and increased cellular uptake. The simultaneous ultrasound and photoacoustic imaging provided clearly defined anatomic features and localization of implanted labeled MSCs. Nam *et al*. labeled stem cells with gold nanotracers and could track these cells via ultrasound/photoacoustic imaging after injection into the lateral gastrocnemius muscle of a rat 5 mm under the skin [294]. The same group labeled therapeutic stem cells with gold nanoparticles for treatment of neurodegenerative diseases. The detection limit of these labeled stem cells in the spinal cord was 1000 cells [293].

Prussian blue nanoparticles are another emerging class of photoacoustic contrast agents due to their strong optical absorption in the near-infrared region. We developed poly-L-Lysine (PLL)-coated Prussian blue nanocubes to label hMSCs [295]. The PLL coating reduced the negative charge of the Prussian blue nanocubes and facilitated cell internalization. The labeled hMSCs showed strong photoacoustic contrast when imaged at 730 nm, which allowed photoacoustic imaging-guided delivery of these therapeutic cells into the desired locations. The labeled hMSCs were still detectable with photoacoustic imaging two weeks after cell implantation. The detection limit of these labeled hMSCs through the skulls of rodents was 200 cells/μL.

Organic nanoparticles have also been investigated as cellular photoacoustic contrast agents. For example, we developed an iron oxide- and 1,1′-dioctadecyl-3,3,3′,3′-tetramethylindotricarbocyanine iodide (DiR)-loaded poly(lactic-co-glycolic acid) (PLGA) nanobubble for trimodal ultrasound/MRI/photoacoustic imaging [296]. These nanobubble-labeled hMSCs had a 3.8-fold ultrasound and 10.2-fold photoacoustic contrast in cardiac tissue compared to unlabeled hMSCs. These nanobubbles were also visible with magnetic particle imaging, an emerging imaging modality.

Melanin nanoparticles are another class of promising photoacoustic contrast agents. These particles have great potential in translation because they are natural components of food-grade cuttlefish ink [297]. We recently reported synthetic melanin nanoparticles as photoacoustic contrast agents for therapeutic stem cell imaging [298]. The photoacoustic intensity at 720 nm of these nanoparticles could be enhanced up to 40-fold by gadolinium doping. These nanoparticles were biocompatible and could be internalized and with hMSCs. The nanoparticles-labeled hMSCs had a detection limit of 23,000 cells *in vitro*.

To increase the penetration depth of photoacoustic imaging, Yin *et al*. developed organic semiconducting polymer nanoparticles for photoacoustic tracking of therapeutic stem cells in the second near-infrared window [299]. The signal-to-noise ratio was increased compared to excitation in the first near-infrared window. These polymer nanoparticle-labeled hMSCs showed 40.6- and 21.7-fold higher photoacoustic intensity in subcutaneous and brain imaging than unlabeled hMSCs.

Researchers have developed many ultrasound/photoacoustic contrast agents for therapeutic cells delivery. However, most reported contrast agents can only provide information about the location of the implanted labeled cells with limited information about

the cell number *in vivo*. It is possible that photoacoustic reporter gene techniques may overcome some of the existing limitations, especially ones that leverage dyes with existing FDA approval [300]. Nevertheless, tremendous and revolutionary research on multiple imaging modalities and contrast agents is still needed to fully understand the therapeutic efficacy and cell fate of stem cell therapies [278].

2.6. Perspective and Concluding Remarks

One of the remaining challenges for theranostic photoacoustic delivery systems is to improve the signal-to-background ratio. For many of these systems, the signal does not change if the drug is released or not. The ability to quantify released vs. unreleased drug *in vivo* would be a highly valuable tool for researchers and clinicians alike. Future strategies will likely use activatable probes to address these questions [301]. When it comes to clinical deployment of nanoparticle contrast agents, the distinctions between inorganic and organic particles must also be considered. Inorganics have useful optical and magnetic properties that can be tuned by adjusting their size, morphology, and chemical composition [15]. Furthermore, their surfaces can be functionalized with both targeting and drug molecules. Due to effects such as plasmon resonance, they can drastically enhance contrast relative to most organic molecules and particles. However, organic nanoparticles (such as liposomes, micelles, and polymeric nanoparticles) offer better biodegradability; they are also ideal for encapsulating drug and targeting molecules [302]. In addition, recent progress suggests that certain semiconducting nanoparticles may match or even exceed the optical advantages of inorganics [20, 119, 243].

Both types of these particles have recently been explored for imaging in the second optical window ("NIR-II", 1000-1700 nm), a promising strategy that has followed the

developments of NIR-II optical imaging [302]. These longer wavelengths can penetrate more deeply through tissue due to reduced scattering and autofluorescence [303]. In addition, the lower energy photons can be used with higher fluence, which is dictated clinically by the maximum permissible exposure (MPE) [304]. Some initial materials for NIR-II photoacoustics have included plasmonic metal nanoparticles, copper sulfide particles, semiconducting polymer nanoparticles, and small molecules [82, 83, 305, 306]. Still, certain challenges must be overcome: For example, photoacoustic imaging systems must implement longer wavelength lasers, the absorbance of water at 1450 must be avoided, and few existing organic compounds absorb above 1064 nm. Nevertheless, we will likely continue to see progress in the second optical window (1000 – 1700 nm) for increased penetration depths. This trend has already emerged in the field of optical imaging [303, 307].

Photoacoustic stem cell delivery may benefit in the future from genetically encodable chromophores; these can allow direct visualization with extremely high specificity [308]. Bacterial reporters such as bacteriochlorophyll *a*, which change their spectral signature in response to cellular activity, may also prove useful in the future for photoacoustic monitoring of gene/drug delivery [309]. At this stage, much work is still required to reveal the full potential of photoacoustics for theranostic drug delivery. For the near future, it is likely that strategies that are (1) surface-weighted and (2) leverage molecules with existing FDA approval, such as methylene blue and indocyanine green, will have the least regulatory burden for clinical translation. Finally, photoacoustic imaging may never become as prevalent as PET/CT for biodistribution and pharmacokinetics; however, it is highly adaptable for localized imaging and measurements without requiring any ionizing radiation. It drastically increases the

contrast and potential for molecular imaging of ultrasound, which is already one of the most common modalities in medicine.

2.7. Acknowledgements

Chapter 2, in full, is a reprint of the material as it appears in Advanced Drug Delivery Reviews, vol. 144, 78-79, 2019. Moore, Colman; Chen, Fang; Wang, Junxin; Jokerst, Jesse V. The dissertation author was the primary investigator and author of this paper.

CHAPTER 3. PHOTOACOUSTIC ULTRASOUND FOR ENHANCED CONTRAST IN DENTAL AND PERIODONTAL IMAGING

ABSTRACT: Ultrasound is one of the most widely accessible imaging modalities but has yet to be adopted in clinical dentistry. Its utility for real-time analysis of soft and hard tissue interfaces can be augmented with optical excitation for photoacoustic ultrasound. Optical excitation enables contrast based on the characteristic absorption properties of tissue. This diagnostic technique is currently being investigated for a number of potential oral applications: detection of caries, determination of pulp vitality, measurement of periodontal pockets, and monitoring implant status. This chapter introduces the imaging modality for a dental readership while reviewing the progress to date and discussing the future development of this field.

3.1. Introduction

Ultrasound is a long-standing tool in medical diagnosis. Its benefits include affordability, high spatiotemporal resolution, sensitivity, and safety—it is ideally suited for imaging soft tissue and bone surfaces simultaneously. Despite these advantages, it is surprisingly uncommon in clinical dentistry. Nevertheless, a variety of reports have been published on oral applications of ultrasound; for an overview of the field to date, we recommend previously published reviews on this topic as well as the other chapters in this textbook [310-317]. Briefly, the scope of ultrasound applications include visualization of dental and gingival anatomy, the detection of caries, dental fractures and cracks, gingival thickness measurements, periapical lesions, maxillofacial fractures, periodontal bony defects, muscle thickness, temporomandibular disorders, and implant dentistry [318].

Ultrasound imaging systems use piezoelectric transducers to transmit high frequency (1-50 MHz) pulses through target tissue and detect the reflected waves. Because sound waves are mechanical vibrations, the speed of sound through a particular medium depends on the acoustic impedance of the material. At interfaces between tissue types with distinct acoustic impedances, a fraction of the ultrasonic pulse is backscattered while the other part is transmitted. The magnitude of the reflected pulse (echo) scales with the impedance mismatch at the boundary. Therefore, the intensity of the returning echo and the time it takes to reach the transducer are the two main components used to reconstruct images.

However, one of the main drawbacks of ultrasound is its limited contrast. The modality can resolve anatomical features but cannot probe *molecular* components of disease (nucleic acids, proteins, enzymes, etc.). Recent progress has been made in activatable ultrasound contrast agents, but these still can only boost the grayscale intensity in a given

region; they cannot produce spectrally unique signal. Fortunately, *photoacoustic ultrasound* has emerged as a fast-growing and promising technique for augmenting conventional ultrasound with the spectral contrast of optical imaging.

Photoacoustic ultrasound harnesses the photoacoustic effect— a phenomenon first observed by Alexander Graham Bell that occurs when the energy from light is absorbed by a material and released as an acoustic vibration. For imaging, a near-infrared (NIR) light source is used to pulse photons (1-100 ns) onto an absorbing target or tissue. NIR light is used because it can propagate through tissue better than blue or green wavelengths. The tissue being irradiated by the NIR absorbs the light and experiences brief (nanosecond) thermoelastic expansion. This expansion generates broadband acoustic waves that can be detected with conventional ultrasound transducers. Importantly, there is no bulk heating of the tissue. This is because the incident laser pulse is shorter than the thermal and stress relaxation times of the target; thus, the system becomes mechanically and thermally confined and the fractional volume expansion of the target can be neglected[319]. Therefore, the initial pressure rise (i.e. the generated photoacoustic wave) is proportional to the optical fluence and absorption coefficient of the material. The resulting photoacoustic wave propagates in three dimensions and is detected by either a single element ultrasound transducer or an array of transducer elements. From here, if the fluence is assumed to be locally homogenous, an image can be reconstructed based primarily upon differences in the absorption coefficient of tissue components effectively mapping the pressure wave distribution.

A variety of hardware configurations are commonly used in research applications: These primarily include photoacoustic tomography, photoacoustic microscopy, and photoacoustic endoscopy [320]. The body possesses a number of endogenous absorbers but

exogenous contrast agents can also be used. The main sources of endogenous contrast are NIR-absorbing molecules such as oxygenated and deoxygenated hemoglobin, melanin, lipids, and water [44]. These targets have often been used to image hemodynamics [321], blood oxygen saturation [64, 322], and cancers [27, 323]. However, a wide variety of exogenous contrast agents—often small-molecules or nanoparticles—have also been developed to boost contrast and probe specific biomarkers or disease states [231]. From a materials perspective, the current landscape of these agents primarily consists of organic small molecules[324], inorganic nanomaterials[325, 326], and organic nanoparticles[23, 327].

The preclinical applications of photoacoustic imaging for oral health have been growing in the past decade. Early work on this topic was focused on optical and photoacoustic spectroscopic measurements of oral tissue. The induced temperature distributions of photoacoustic excitations and the absorbing/scattering behavior of incident light have also been characterized. Following this, investigations have proceeded on dental pulp characterization as well as enamel/dentin imaging for early detection of caries and cracks. Recently, the field has expanded into characterization of the periodontium via non-invasive imaging of the periodontal pocket. Here, we review the developments in oral photoacoustics to date and offer perspectives on future progress in this burgeoning field.

3.2. Optical And Photoacoustic Characterization Of Oral Tissues

Early investigations into dental applications of photoacoustics largely focused on the determination of optical and photoacoustic properties of oral tissue within the optical window. In medical imaging modalities, the optical window refers to a range of wavelengths between 650-900 nm in which tissue absorbance and scattering are reduced relative to other wavelengths [328]. Imaging modalities typically operate in this range to maximize resolution,

contrast, and penetration depths. The optical properties of tissue that govern these parameters, primarily absorption and scattering, vary between tissue types; therefore, the investigation of these properties preceded imaging applications. Furthermore, they are relevant to both photoacoustic imaging and optical coherence tomography—another modality that has seen recent growth in oral diagnostic research.

Initial work focused on understanding the absorption and scattering properties of NIR light in healthy and carious/demineralized enamel [329-331]. For many years, dental caries have been diagnosed with visual, tactile, and radiographic exams; however, a significant level of variation exists between examiners. Healthy enamel is primarily composed of hydroxyapatite ($Ca_{10}(PO_4)_6(OH)_2$) and is highly transparent to NIR light. During demineralization and decay, individual mineral crystals dissolve which causes micropores to form in carious lesions [332]. These pores strongly scatter visible and NIR light [333]. Darling et al. found that the porosity of these lesions increased the scattering coefficient one to two orders of magnitude above healthy enamel. Indeed, the interactions of NIR light with enamel are dominated by scattering rather than absorption making absorption properties difficult to measure using optical methods[334]. Nevertheless, because photoacoustic intensity is proportional to optical absorption, photoacoustic ultrasound can measure relative absorption coefficients as well as true values if the light fluence is known quantitatively [335].

One of the earliest studies of photoacoustics for dentistry used a pulsed Nd:YAG (neodymium-doped yttrium aluminum garnet) laser to study the absorption and ablation properties of 1064 nm light on dentin and enamel [334]. The authors found that enamel absorbs poorly at 1064 nm so the photoacoustic signal is low. However, it increases with caries due to the presence of melanin from pigmented anaerobic bacteria and their metabolites. In

addition, the pulsed laser could be used for ablation of caries lesions, which could be monitored due to the higher photoacoustic signal from ablation (rapid expansion of vaporized organic material) compared to non-pigmented tissue. The acoustic properties of teeth following laser irradiation have also been studied to elucidate the acoustic differences between healthy and decayed teeth. El-Sharkawy et al. used an interferometric detection scheme for measuring surface acoustic waves, which propagate parallel to surfaces of irradiated teeth[336,337]. The system could differentiate healthy and decayed teeth by calculating the longitudinal speed of sound, optical penetration depth, and Gruneisen coefficient for each sample—this photoacoustic spectroscopy scheme suggests the potential of automated caries diagnosis if used with pattern recognition algorithms.

In 2006, Kim et al. extended the concept of detecting early-stage caries using photoacoustics [338]. They used a Nd: YAG laser (15-ns pulse width at 100 mJ, 10 Hz, 1064/532 nm) and an unfocused single-element transducer (12 MHz) to analyze extracted human molars split into three groups (healthy, incipient caries, and advanced caries) as determined visually and radiographically. Here, incipient caries only affected the enamel while advanced caries penetrated to the dentin. They found that the photoacoustic signal at 1064 nm was significantly stronger from regions of teeth with incipient caries than normal regions. This signal was further elevated for teeth with advanced caries. There was elevated signal between regions of teeth with incipient caries and normal teeth at 532 nm; importantly, the signal did not increase for advanced caries. This work was an important proof-of-concept but full photoacoustic imaging was not possible because the data acquisition was limited to one-dimension, i.e., only spectroscopic data.

3.3. Dentin And Enamel Imaging For Caries And Crack Detection

The photoacoustic technique was extended for imaging of dental caries in 2D and 3D in 2010 by Li et al. [339, 340]. They used a Q-Switched Nd:YAG laser (8-ns pulse width at 6 mJ, 2Hz, 1064 nm) with a needle hydrophone aligned with an optical fiber for acoustic transduction. To acquire images, the probe was raster scanned using step motors. They also performed temperature and pressure field simulations in teeth to validate the safety of laser excitation. The 2D finite element modelling results suggested that the maximum local temperature change would be below 1° C (where ≥ 5° C is required for pulpal necrosis). In addition, the modeled pressure change in the dentin was ≤ 0.7 MPa, much less than its fatigue limit of 20 MPa. The authors could image both an extracted healthy tooth and one with caries.

Photoacoustic tomography has been further investigated for early detection of dental lesions [341, 342]. Cheng et al. used a similar imaging system (8-ns pulse width, 10 Hz, 11 mJ/cm^2, 532 nm with 4.39 MHz ultrasound center frequency) to study extracted teeth with white spot enamel caries and artificially induced cracks. They used both typical B-mode photoacoustic tomography (contrast is proportional to the relative optical absorption in tissue) and "S-mode" tomography (where contrast is determined by the spectral slope of the photoacoustic signal). This S-mode exploits the spectral profile of the photoacoustic echo rather than just its time-domain properties; it has shown potential for better differentiation of tissue types based on physical properties (such as the Young's modulus) than conventional photoacoustic imaging [343]. These authors found that the conventional B-mode technique was useful for imaging the structure of teeth including the enamel, dentin, and pulp. However, their images could not distinguish early enamel lesions. This limitation was primarily

attributed to insufficient changes in optical absorption. Nevertheless, S-mode imaging could correlate differences in photoacoustic spectral slope to differences in stiffness between enamel and dentin as well as early enamel lesions.

Rao et al. improved the resolution and contrast of these techniques with photoacoustic *microscopy* [344]. Photoacoustic microscopy is a form of photoacoustic imaging that can drastically improve resolution by using lenses to focus the excitation light analogous to traditional optical microscopy. There are two primary forms, and they are classified by the property that limits resolution: optical-resolution photoacoustic microscopy (OR-PAM) and acoustic-resolution photoacoustic microscopy (AR-PAM). In OR-PAM, the optical excitation and acoustic detection (single element ultrasound transducer) are co-focused to create dual foci that increase sensitivity. OR-PAM can generally achieve 0.5-3.0 μm resolutions with imaging depths of 1.2 mm. In AR-PAM, a cone of light is used for dark-field excitation of tissue and offers ~45 μm resolutions with 5 mm imaging depths. Both of these modalities have been used to image extracted teeth. The authors found that the darkened color characteristic of dental decay was correlated with increased photoacoustic intensity. Furthermore, healthy vs. decayed teeth showed significantly different intensities under AR-PAM; of course, longitudinal tracking would be required to reliably quantify the progression of dental decay. One challenge noted by Periyasamy et al. is that photoacoustic signal from metal fillings can dominate the signal generated by the tooth itself introducing undesirable background when looking for dental lesions [345].

Hughes el al. also utilized photoacoustic microscopy in an all-optical configuration for early stage detection of dental caries [346]. They showed that the optically generated ultrasonic signal in one-dimension alone could differentiate pre-caries lesions from healthy

enamel; in addition, the sample could be scanned to acquire depth-resolved images revealing the extent of the sub-surface lesion (confirmed with histology). The authors noted that error in the measurement of enamel lesion thickness was about 3%, which they attributed to variation in the speed of sound caused by the lesions themselves. A larger error (30%) was present when measurements were made closer to the enamel dentine junction possibly due to the higher depth. Perhaps the largest limitation of photoacoustic microscopy is that it is not suited for *in vivo* imaging. To this end, a handheld PAM probe was recently reported, but it has not yet been demonstrated for dental applications [347].

3.4. Imaging Dental Pulp, Implants, And Periodontal Features

Accurate assessment of the pulp status is critical for the diagnosis of a number of conditions such as reversible/irreversible pulpitis, acute/chronic abscess, and necrosis. However, the objective measurement and characterization of pulp vitality remains a significant challenge in dental practice. The clinical gold standard is to perform sensitivity tests: these primarily refer to thermal testing (assessment of the response to hot and cold stimuli) and electric pulp testing, which is used to assess the status of pulpal nerve fibers. Unfortunately, these techniques are painful for the patient and do not necessarily reflect the status of the vascular supply. An ideal diagnostic tool would supply an objective, reproducible, non-painful, and accurate method for quantifying the vascular supply of a tooth. Some optical techniques such as pulse oximetry and laser Doppler flowmetry have been applied to probing pulpal blood oxygen saturation; however, these are primarily limited by the high scattering and absorption coefficients of the surrounding hard dental tissues.

Yamada et al. conducted an early feasibility study on photoacoustic imaging of dental pulp in 2016 [348]. They investigated both 532 nm and 1064 nm wavelengths (100 Hz

repetition rate, 1.2 ns pulsewidth, 1 mJ pulse energy, 4.6 MHz central frequency) for imaging extracted teeth. First, they imaged teeth split in half. In the first case, the root canal was filled with water and in the second case it was filled with 3% hemoglobin solution. At 532 nm, the water and the hemoglobin filled samples could not be distinguished, primarily due to the strong scattering by the enamel and dentin. However, at 1064 nm, high frequency vibrations could be detected in the photoacoustic waveform of the hemoglobin-filled tooth that were not present in the water-filled tooth. Furthermore, the intensity of the high frequency signals had a linear correlation to the hemoglobin concentration. Unfortunately, the differences in frequency spectra between hemoglobin and water-filled whole teeth were much less significant than in split teeth. Photoacoustic imaging for diagnosis of pulp vitality is an attractive concept but is still largely unexplored. The intense reflection, scattering, and absorption of dentin and enamel will pose the largest challenge going forward.

Another interesting application is in implant dentistry. Ultrasound has recently been growing as a promising tool for evaluating implant status across multiple stages of treatment, and we recommend a recent review for a systematic discussion of this topic [310]. One of its limitations, however, is the lack of molecular contrast, which can be desirable for diagnosis and quantification of peri-implantitis. Peri-implantitis is an umbrella term for "destructive inflammatory processes around osseointegrated implants" that contribute to pocket deepening and crestal/alveolar bone loss [349,350]. Lee et al. conducted initial work on this topic with photoacoustic imaging using porcine jaws *ex vivo* [351,352]. They used a 532/1064 nm Q-switched Nd:YAG laser with a tunable (680-950 nm) OPO laser at 17.7 mJ/cm^2 for excitation with both an AR-PAM system (5 MHz central frequency) and a commercial US system (3-12 MHz central frequency) for detection. They then imaged a titanium implant

with abutment and fixture both under chicken breast of varying thickness (10 – 20 mm) and after implantation at the site of the molar in an extracted porcine jawbone. The authors found that the structure of the jawbone and internal position of the implant could be easily visualized with both systems. Of course, the entire bone structure could not be resolved as in radiographic techniques because the optical illumination and ultrasonic emission cannot penetrate through bone like X-rays. Nevertheless, they could determine the angle and length of the position under the jawbone in addition to the depth of the layer of soft tissue above it.

Finally, resolving the periodontal anatomy, especially the pocket depth, is of significant interest to clinical practice. Periodontal disease is currently and has historically been diagnosed by a combination of factors: pocket (probing) depth, attachment loss, mobility, bone loss, and degree of inflammation. The periodontal probe is often used for physically measuring the extent of apical epithelial attachment relative to the gingival margin. However, it is a highly variable technique that is time consuming and uncomfortable for patients; furthermore, the threads of dental implants often impede the physical probe measurements [353]. A facile imaging technique could potentially address these issues and improve the poor clinical rate of pocket depth charting [354, 355]. Optical coherence tomography is one option that has recently been explored for imaging the gingiva and periodontal structures in high resolution [356, 357]. This technique can resolve tissue microstructures and capillary vasculature with impressive detail, but unfortunately is limited to penetration depths of 2 mm due to optical tissue scattering. Though photoacoustic ultrasound cannot significantly improve the penetration depth through hard tissues, it can penetrate through centimeters of soft tissue (e.g. gingiva) because even diffuse photons can generate acoustic waves.

Our group has recently leveraged this ability for imaging the periodontal pocket in both swine jaws *ex vivo* [358] and the human mouth *in vivo* [210]. This work used a commercial, tomographic photoacoustic-ultrasound system (16-40 MHz central frequency, 680-970 nm, 5-ns pulse width at 20 Hz) along with a food-grade contrast agent derived from cuttlefish ink. The spatial resolution of this system was roughly 300 μm in the photoacoustic mode and 100 μm in the ultrasound-only mode. The contrast agent contained melanin nanoparticles with broad absorption in the NIR and was used to irrigate the gingival sulcus using a micropipette tip or oral gavage, thereby enabling visualization of the pocket with photoacoustics. This contrast media was chosen for its broad NIR absorbance, food-grade biocompatibility, and simple formulation. The technique was first conducted on 39 porcine teeth in extracted swine jaws, both with natural and artificially deepened pockets, and was validated with the conventional Williams probe (bias values < ±0.25 mm, <11% variance). Shallow (1.65 mm), intermediate (2.04 mm), deep (4.45 mm), and artificially deep pockets (4.60 mm) were successfully measured. The ultrasound mode was also leveraged to measure 45 gingival thicknesses and compared to measurement with a needle. These measurements were only 0.07 mm larger than invasive examination. This bias could potentially be accounted for by the pressure generated by the needle during physical measurement. The contrast agent was also easily removed following rinsing with water (applied via a 5-mL syringe without needle) and normal tooth brushing.

Subsequently, this application was extended to a case study in a healthy adult subject. The relative standard deviation of five replicate measurements for a mandibular incisor was 10%. The depths measured by imaging agreed with conventional probing. Of note, all measurements were ≤ 2 mm because the imaging site was healthy incisors. One of the

benefits of this approach was that the whole pocket could be mapped as opposed to single positions (e.g. mesiobuccal, central buccal, and distobuccal) at a time. Additionally, the contrast agent was easily removed by rinsing with water and brushing the teeth as in the *ex vivo* porcine model. Current efforts are focused on streamlining the post-processing steps and miniaturizing the imaging hardware for improved access to distal teeth.

3.5. Outlook And Practical Considerations

One of the main advantages of ultrasound for dentistry is its ability to image the gingiva, which is mostly transparent to the common dental imaging modalities such as X-ray and cone beam computed tomography. In addition, it can resolve the surfaces and contours of hard tissues (e.g. tooth, bone) and integrate these with the depth-resolved data from the gingiva. It follows, however, that the major limitations are its relative inability to image through tooth/bone and its limited grayscale contrast. Photoacoustic imaging can improve upon these limitations by shifting the contrast mechanism to the absorption of light rather than differences in refractive index and extending penetration depths from the ballistic to the diffusive regime. Nevertheless, research to date suggests that photoacoustic analysis of teeth alone will probably be restricted to their surfaces (enamel and cementum).

Currently, a handful of practical challenges face the translation of photoacoustics to dentistry but we believe these are largely solvable. One example is the form factor of existing photoacoustic hardware. Most research-grade systems are meant for general purpose applications and utilize relatively large transducers that can only access the anterior teeth. Furthermore, the laser is housed separately. However, new hardware can be envisioned for the specific purpose of imaging within the oral cavity. These designs could potentially take the form of a mouthpiece transducer with coupled optical excitation or a handheld “hockey-

stick" transducer for reaching the posterior teeth [359]. Another consideration for eventual clinical adoption is the price: Ultrasound is an inexpensive technique but the laser associated with photoacoustic imaging raises the cost significantly. It is possible, however, for systems to harness LED excitation sources that drastically reduce both the cost and overall footprint [203].

When taking 3-D scans with a linear array transducer, it is necessary for the head of the subject to remain still. Otherwise, artifacts from minor movements will distort the final image. To combat this, a clinical setup would likely use a head immobilizer similar to those used for dental radiographs. Post-processing algorithms can also be employed to minimize these effects. Furthermore, since ultrasound waves do not propagate through air, the choice of coupling agent between oral surfaces and the transducer requires some consideration. Ultrasound gel is functional but requires re-sterilization of the transducer between patients in a clinical setting. Single-use materials for dry coupling may be useful in this context.

Photoacoustic imaging is a young technology but is developing at a rapid pace due to its optical contrast, good spatial resolution, and real-time imaging. Dental-specific investigations are still in their very early stages, but they show potential for caries detection, analysis of tooth surface integrity (crack detection), implant imaging, and characterization of the periodontium. With the growing availability of commercial photoacoustic systems, and the prevalence of custom preclinical systems, it is likely that photoacoustic imaging will continue to complement the developments in ultrasound techniques for dental applications.

3.6. Acknowledgements

Chapter 3, in full is a reprint of the material as it appears in Dental Ultrasound in Periodontology and Implantology, Springer Nature Switzerland AG. 215-23, 2020. The dissertation author was the primary investigator and author of this book chapter.

CHAPTER 4. HIGH-RESOLUTION ULTRASONOGRAPHY OF GINGIVAL BIOMARKERS FOR PERIODONTAL DIAGNOSIS IN HEALTHY AND DISEASED SUBJECTS

ABSTRACT: Periodontal examination via physical probing provides critical metrics such as pocket depth, clinical attachment level, and gingival recession; however, this practice is time consuming, variable, and often causes discomfort. Ultrasonography is painless, non-ionizing, and can resolve hard and soft tissues simultaneously. In this study, a set of 16 subjects were identified from patients scheduled to receive dental care and clinically classified as periodontally healthy (n = 10) or diseased (n = 6). A 40-MHz ultrasound system was used to measure gingival recession, gingival height, alveolar bone level, and gingival thickness from 66 teeth for comparison to probing measurements of pocket depth and clinical attachment level. Gingival recession and its risk in non-recessed patients were assessed via ultrasonographic measurement of the supra- and subgingival cementoenamel junction relative to the gingival margin. Interexaminer bias for ultrasound image analysis was negligible (<0.1 mm) for gingival height measurements and 0.45 mm for alveolar bone level measurements. Ultrasound measurements of gingival height and alveolar bone level were equivalent to clinical measurements of probing pocket depth and clinical attachment level for disease classification (1.57-mm bias and 0.25-mm bias, respectively). Overall, ultrasonography possessed equivalent diagnostic capacity as gold-standard probing for periodontal metrics while resolving the subgingival anatomy.

4.1. Introduction

Nearly 50% of Americans have periodontitis [360] resulting in pain, tooth loss [361, 362], reduced quality of life [363-366] and even systemic effects like cardiovascular disease [367], but tools to diagnose/monitor periodontitis have major limitations. Clinical assessment (by periodontal examination) and radiography are currently the standard of care but are time-consuming for the clinician, uncomfortable for the patient, and subject to large errors—inter-operator variation in probing can be >40% [368]. Moreover, clinical assessment and radiographic examination may not capture all clinical information (e.g., gingival thickness and inflammation).

The periodontal examination provides critical information such as probing pocket depth (PPD; current periodontal health) and clinical attachment level (CAL; cumulative destruction) [369]. PPD, CAL, and other clinical parameters form the basis of periodontal diagnosis. Radiography offers excellent sensitivity to hard tissue (bone, enamel, etc.) but cannot discriminate between healthy and diseased gingiva or map disease within soft tissue; it also has a small but non-negligible dose of ionizing radiation. Ultrasound imaging has the benefits of being a portable and low-cost alternative to radiography that is noninvasive and free of ionizing radiation[370]. It can measure the thickness of the gingiva—this is difficult for radiographic imaging modalities.

Locating the CEJ is important for determining metrics of periodontal health such as gingival recession and (CAL). The CEJ is typically covered by the gingiva (subgingival), its exact location is difficult to determine via physical probing and can be subject to significant error: In midbuccal sites, Vandana et al. reported over- or underestimation of the CEJ by trained periodontists for 74% (34/46) of measured teeth [371]. More recently, ultrasound

imaging has been used to resolve dental and periodontal structures—especially for alveolar bone and the cementoenamel junction [372-379]. It has also been used for imaging peri-implantitis, the topography of edentulous crestal bone, and the bone-implant interface [380-383]. We and others have previously evaluated these techniques via ex vivo models and human case studies but higher-powered studies in human subjects using healthy and diseased cohorts are relatively rare [210, 358, 384].

Here, we extend this concept via 40-MHz ultrasound to locate the CEJ in relation to other anatomical markers for image-based calculation of periodontal metrics that could serve as surrogate measurements for physical probing. While existing work has evaluated the accuracy of ultrasound for imaging periodontal structures, the integration of these biomarkers into diagnostic measurements and their performance for staging disease is relatively unexplored. Therefore, the study objective was to evaluate high frequency ultrasound in clinical periodontology for potential replacement of probing by comparing performance of the two techniques in healthy and diseased subjects. This goal was achieved by identifying and evaluating imaging biomarkers and comparing these biomarkers to established clinical metrics of periodontal health.

4.2. Methods

4.2.1. Materials

A high-frequency, commercially available imaging ultrasound system was employed (Vevo LAZR, Visualsonics, Toronto CA) with a 40-MHz linear array transducer (LZ-550). Disposable tegaderm films were used as sterile transducer sleeves (3M, Minnesota, USA). Periodontal probing measurements were conducted with a Williams and Marquis probe. Extracted swine jaws were provided by Sierra for Medical Science, Inc. Whittier, CA.

4.2.2. Subject Recruitment and Clinical Examination

The study protocol was approved by the USC and UCSD Institutional Review Boards and was in accordance with STROBE and the ethical guidelines for human subjects research established by the Helsinki Declaration of 1975. The study subjects were identified from patients seeking dental care at the Herman Ostrow School of Dentistry. As part of the clinical protocol, the patients received extra- and intra-oral examinations, medical and dental history review, a set of full-mouth radiographs, periodontal examination, periodontal diagnosis, and treatment planning. Eligible subjects were healthy adults who weighed at least 110 pounds with one quadrant with at least upper and lower anterior teeth. Subjects were excluded if they had bloodborne pathogen infections, bleeding disorders, acute oral infections, or were pregnant or lactating women. Two subject groups were recruited based on the periodontal diagnosis described in the 2017 World Workshop on the Classification of Periodontal and Peri-implant Diseases and Conditions [385]. The first group (n = 10) comprised subjects with the following diagnosis: periodontal health in intact or reduced periodontium in stable periodontitis patients, or dental biofilm-induced gingivitis in the intact or reduced periodontium. The second group (n = 6) comprised subjects diagnosed with periodontitis (Stage II-IV and Grade B or C) with localized or generalized involvement.

The periodontal diagnosis was given by a board-certified periodontist faculty (K.C.J.C.) and a resident (J.L.). Six maxillary or mandibular anterior teeth were then selected for the study. We could not access molars because of the size of the transducer. Periodontal probing depth was determined with a Williams and Marquis probe at six sites per tooth (mesio-labial, mid-labial, disto-labial, mesio-lingual, mid-lingual, and disto-lingual). Tooth mobility was determined as Class 1: mobility of up to 1 mm in an axial direction, Class 2:

mobility of greater than 1 mm in an axial direction, and Class 3: mobility in an apico-coronal direction (depressible tooth). Bleeding on probing (BOP) provoked by applying a probe to the bottom of a sulcus/pocket was recorded. Gingival recession was recorded by measuring the distance between the CEJ to the top of the gingival margin in the mid-labial aspect of the tooth with a periodontal probe. Clinical attachment level (CAL) was determined from CEJ to the bottom of the pocket. The gingival phenotype was determined by inserting the periodontal probe into the mid-labial surface of the tooth. A thin gingival phenotype was assigned if the probe was visible through the gingival tissue.

4.2.3. Periodontal Ultrasound Imaging

Subjects were seated in the supine position in the dental chair and imaged with a handheld, linear array transducer by a clinician. A disposable transparent sleeve was used to wrap the transducer in addition to sterile ultrasound coupling gel. Imaging was performed manually by positioning the transducer parallel to the long axis of the tooth along the buccal midline. A layer of ultrasound coupling gel ~5 mm thick was placed between the contact areas and the transducer to achieve good coupling and optimum resolution. Freehand scans of each tooth were exported as a video file consisting of at least 1,000 frames.

4.2.4. Image Analysis

All images had to meet specific quality criteria prior to measurement. These were: 1) clear resolution of the GM, (2) clear resolution of the ABC, and (3) a lack of interfering artifacts coincident with the relevant anatomy. If these conditions were met, then further image analysis was performed (**Table 4.1**). All imaging measurements were performed in duplicate by two individuals blinded to data collection. These raters assessed human variation in the identification of anatomical biomarkers. The first was a clinician with no

ultrasound experience (Analyst 1) while the second was an ultrasound researcher with no clinical experience (Analyst 2). Imaging measurements were performed digitally in the VisualSonics software and ImageJ [210, 386]. The distance from the gingival margin (GM) to the alveolar bone crest (ABC) was defined as the image-based gingival height (iGH). Similarly, the distance from the CEJ to the ABC was defined as the image-based alveolar bone level (iABL). The image-based gingival thickness (iGT) was measured at the midpoint of the ABC and GM.

4.3. Results

A high-frequency, commercially available imaging system was used for chairside imaging of subjects (**Figure 4.1A**). The handheld linear array transducer (40 MHz, **Figure 4.1B**) permitted access to the maxillary/mandibular incisors and cuspids (teeth 6-11 and 22-27, **Figure 4.1C**). B-mode images (2D ultrasound cross-sectional images) were collected in the sagittal plane at the midbuccal site of each tooth. The anatomy of the imaged region is depicted in **Figure 4.1D** for comparison to a representative B-mode image in **Figure 4.1E**. In general, six anatomical markers were consistently identified and used to orient the imaging operator/analyst: the alveolar bone, the gingiva, ABC, GM, CEJ, and the tooth surface (**Figure 4.1D-E**).

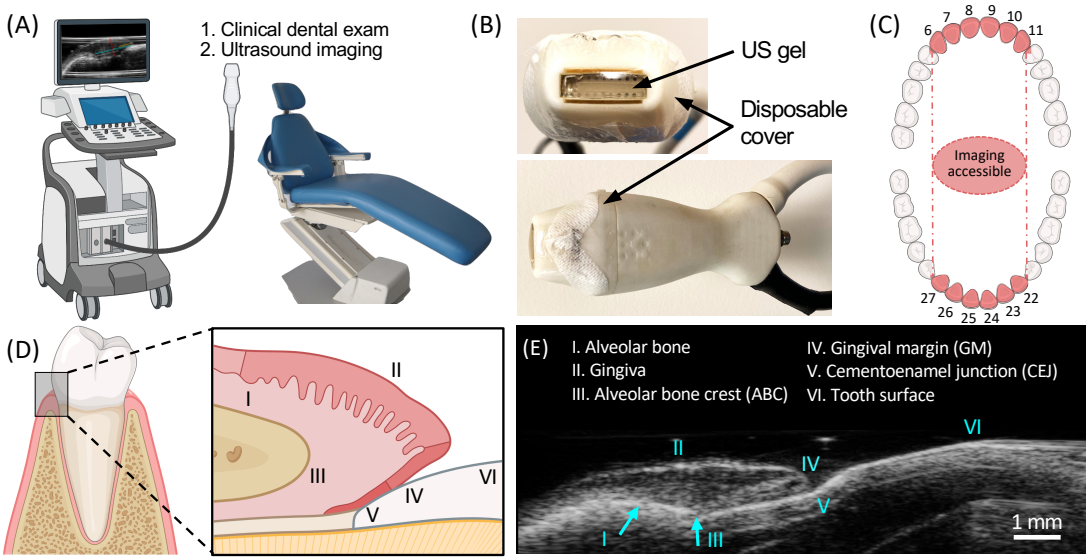

Figure 4. 1. Overview of periodontal ultrasound imaging.
(**A**) Schematic of chairside ultrasound imaging during routine dental examination. (**B**) Photograph of the commercial 40-MHz transducer with coupling gel and sterile sleeve used for subject imaging. (**B**) Dental chart with teeth highlighted (6-11, 22-27) that could be physically accessed by the ultrasound transducer. (**C**) Diagram of the periodontal anatomy surrounding the gingival sulcus with magnification of the sagittal plane. Roman numerals denote the I: alveolar bone, II: gingiva, III: alveolar bone crest (ABC), IV: gingival margin (GM), V: cementoenamel (CEJ), VI: tooth surface. (**D**) B-mode ultrasound image of the region in (C) for the central mandibular incisor (#25) of a patient with anatomical markers labeled.

First, we confirmed that our ultrasound system could resolve the CEJ in cadaver swine jaws (**Figure 4.5**). This was achieved by imaging each tooth (**Figure 4.5A**), measuring the CEJ with image analysis (**Figure 4.5B-E**), and comparing the values to tactile probing measurements following gum flap resection (**Figure 4.5F-G**) and measurement by a clinician (**Figure 4.5H**). These measurements are restricted to integers but represent the gold standard and showed good agreement with imaging (<1.0 mm difference between GM-CEJ values and <0.5 mm difference between GM-ABC values) (**Figure 4.5I**). In humans, 79 B-mode images were acquired from 16 subjects comprising 43 teeth clinically diagnosed as healthy and 36 diagnosed with periodontal disease via physical measurements and examination. Of these images, 66 (84%) met quality criteria and were used for analysis. All

image quality metrics, image measurements, and clinical measurements are included in **Table 4.1.**

One simple periodontal measurement is the distance between the CEJ and GM: This was used to track gingival migration (recession or overgrowth). **Figure 4.2** demonstrates varying positions of the CEJ relative to the GM for six different subjects. The CEJ has as an angled disruption in the echogenicity of the tooth surface between the GM and ABC. For subjects in **Figure 4.2A-C**, the CEJ is apical to the GM (typically, a positive health marker) showing subgingival CEJ-GM distances of -4.0 mm, -1.3 mm, and -0.6 mm. The CEJ and GM are coincident in **Figure 4.2D**. The last two cases have gingival recession (**Figure 4.2E-F):** The GM is apical to the CEJ (0.6 mm and 1.1 mm respectively).

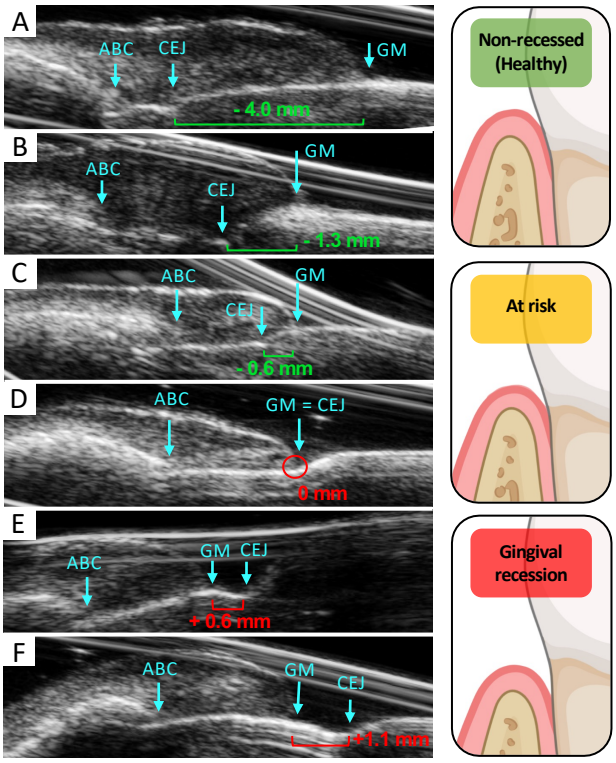

Figure 4. 2. B-mode images in six subjects demonstrating ultrasound monitoring of gingival recession via periodontal landmarks.
Clinically, the distance between the CEJ and GM defines the extent of gingival recession and is used to determine CAL. Panels **A-F** show teeth from subjects with increasing levels of gingival recession. (**A-C**) Images from subjects with the CEJ apical to the GM (i.e., non-recessed). These measurements are represented as negative values (green). (**D**) Image from a subject where the GM is coincident with the CEJ (i.e., PPD = CAL). (**E-F**) Images from subjects with the GM apical to the CEJ (i.e., recessed). Recessed measurements are represented as positive values (red).

All image-based measurements including iGH, iABL, iGR (image-based gingival recession), and iGT (image-based gingival thickness) are depicted for a representative tooth site in **Figure 4.3A.** To determine the iGH and iABL values in this study, two blinded analysts (one clinician and one researcher) independently measured each frame, and their values were averaged. Bias between raters was < 0.1 mm for iGH (**Figure 4.3B**) and 0.45 mm for iABL (**Figure 4.3C**). The increased variance for iABL reflected differences between the raters in assigning the CEJ, which can be a less obvious feature than the ABC or GM.

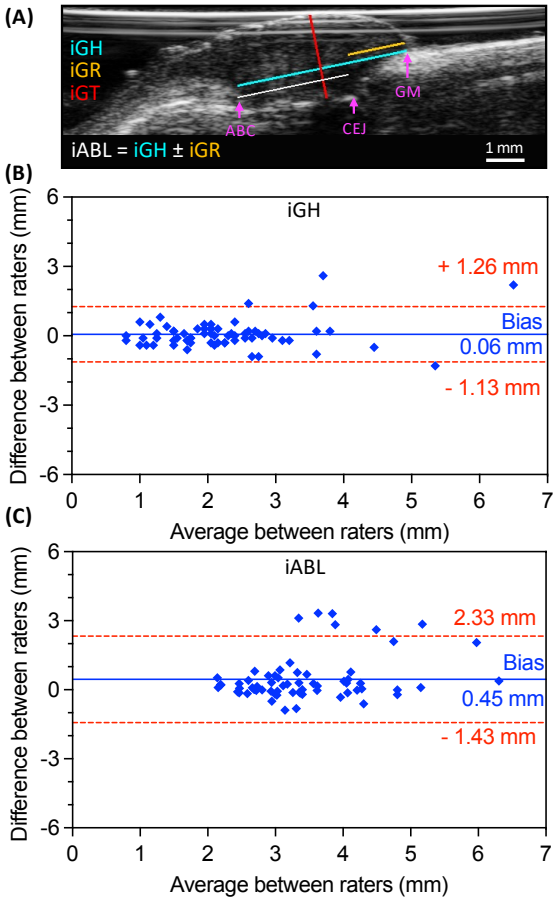

Figure 4. 3. Ultrasound for diagnostic measurements and interrater variability for ultrasound image-based measurements of pocket depth (iPD) and clinical attachment level (iCAL).
(**A**) B-mode image with manual annotations showing the extraction of iGH (teal), iABL (white), iGR (yellow), and iGT (red) for a representative subject. The iGH is defined as the distance from the ABC to the GM. (**B-C**) Bland-Altman plots comparing the iGH and iABL measurements from two blinded image analysts for the same image set (n = 66 teeth). The increased variance (bias) between analysts for iABL (0.45 ± 0.96 mm) relative to iGH (0.06 ± 0.61 mm) was due to differences in identification of the CEJ between the two image analysts.

The average iGH and iABL values for teeth from healthy/diseased subjects were compared to clinical PPD and CAL measurements, respectively (**Figure 4.4**). The average PPD measurements were 1.68 mm for healthy subjects and 2.25 mm for diseased subjects (**Figure 4.4A**). A similar increase was observed for iGH measurements: 3.19 mm for healthy subjects and 3.67 mm for diseased subjects. In both cases, measurements in diseased subjects were significantly higher than in healthy subjects (unpaired, two-tailed t-test, p = 0.0142 for PPD, p = 0.0286 for iGH). Expectedly, iGH values were larger than PPD values (1.57 mm

Bland-Altman bias, on average) because the iGH measurements terminated at the ABC rather than the gingival sulcus (**Figure 4.4B**). As with the PPD measurements, CAL measurements were significantly higher for diseased than healthy subjects: 1.68 mm in the healthy group and 2.56 mm in the diseased group (unpaired, two-tailed t-test, $p = 0.0003$, **Figure 4.4C**). For iABL, the healthy average was 1.80 mm, and the diseased average was 2.74 mm—this difference between groups was even more significant than the CAL measurements ($p < 0.0001$, **Figure 4.4C**). Bland-Altman analysis revealed a minor 0.25-mm magnitude bias toward the iABL measurements (**Figure 4.4D**). Lastly, iGT was compared to gingival biotype: 93.5% of the associated gingiva for measured teeth possessed a thick biotype, and there was no correlation to disease status (**Figure 4.6A**). Accordingly, the iGT measurements (taken from the midpoint of the ABC and GM) were not significantly different for healthy versus diseased patients (**Figure 4.6B**).

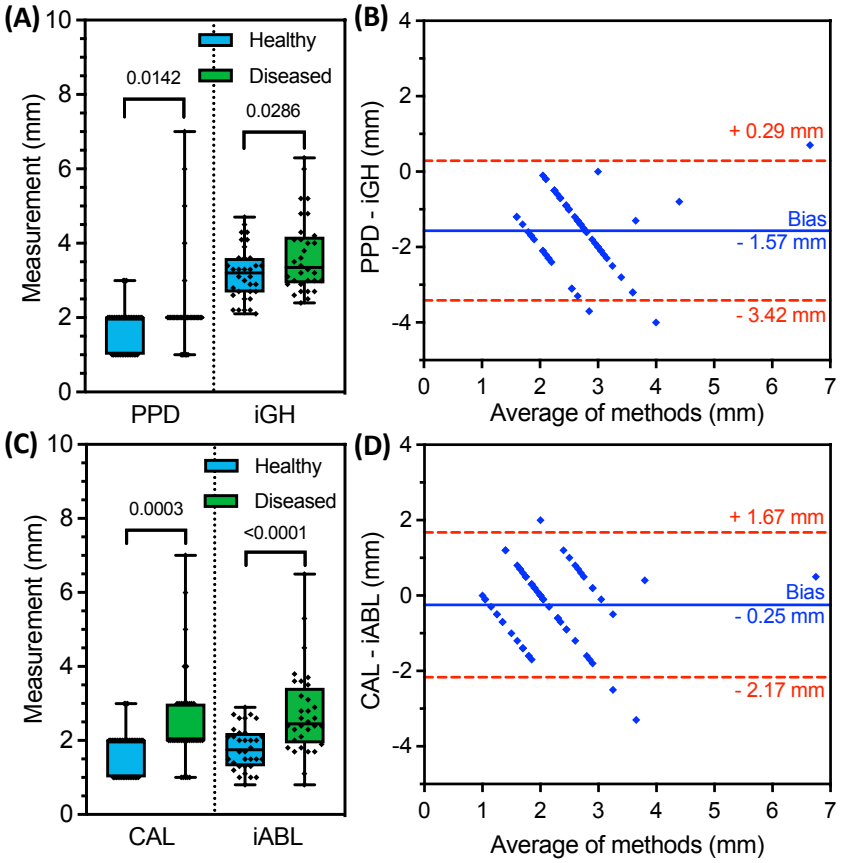

Figure 4. 4. Comparison between ultrasound image-based measurements (iGH, iABL) and clinical probing measurements (PPD, CAL) for individual teeth (n = 66) of patients with healthy or diseased clinical diagnoses.
(**A**) Box-and-whisker plots for PPD and iGH both indicate significantly higher measurements in the diseased group (n = 32) than the healthy group (n = 34); PPD values are limited to integers. Pairwise comparison values are p-values (unpaired, two-tailed t-test). (**B**) Bland-Altman analysis between the measurement methods shows a 1.57 ± 0.95 mm bias toward iGH measurements averaged from all teeth– these values are larger because—while both measurements begin at the GM—the iGH is measured to the ABC rather than the terminus of the gingival sulcus. This difference, due to the connective tissue and junctional epithelium between the ABC and gingival sulcus, has been described as the "biological width"[387]. (**C**) Box-and-whisker plots for iABL and CAL indicate significantly higher values for teeth in the diseased group than the healthy group. CAL values are limited to integers. Pairwise comparison values are p-values (unpaired, two-tailed t-test). (**D**) Bland-Altman analysis between the iABL/CAL measurement methods reveal a 0.25 ± 0.98 mm bias toward the iABL measurements indicating a minimal difference between the two methods.

4.4. Discussion

The CEJ and the GM are two of the most prominent features in ultrasound images at midbuccal sites (**Figure 4.1E**). These can be used to precisely measure the extent of gingival recession or procession (**Figure 4.2**). Though useful for longitudinal monitoring, the position

of the CEJ in relation to the GM (gingival recession) at any single timepoint is insufficient for diagnosing periodontal health because gingival recession is often multifactorial in origin [388, 389]. Therefore, we evaluated the diagnostic value of measurements derived from the ABC, CEJ, and GM (**Figure 4.3A**). Specifically, we measured image-based alveolar bone level (iABL) and image-based gingival height (iGH) for each tooth site and compared them to clinically measured PPD and CAL values. We also compared the magnitudes of these values after classifying patient images into healthy or diseased groups corresponding to their clinical diagnosis.

We compared iGH to PPD and iABL to CAL because these measurements are physically equivalent except for their termini—that is, the iGH and iABL terminate at the ABC while the PPD and CAL terminate at the apex of the gingival sulcus. This difference, the distance between the ABC and the terminus of the gingival sulcus (corresponding to connective tissue and junctional epithelium), has been described as the biologic width [390]. Therefore, if known, the biologic width should be subtracted as a correction factor to calculate an image-based pocket depth (iPD) from the iGH as well as an image-based clinical attachment level (iCAL) from the iABL. Thus, iPD should approximate PPD and correlate with iGH. This correction factor is useful to help correlate these novel imaging biomarkers to conventional metrics of periodontal health; however, it is possible to imagine these novel imaging biomarkers being used to stratify oral health independent of conventional probing depths.

In this dataset, the average difference between iGH and PPD measurements was 1.57 mm (**Figure 4.4B**). If this value is defined as the average biologic width and subtracted from each iGH measurement, then we obtain a set of iPD values after rounding to the nearest

integer similar to rounding done when measuring the PPD. Likewise, we obtain a set of iCAL values after performing the same subtraction from the iABL data. This analysis suggested 83% agreement between iPD and PPD values, and 49% agreement between iCAL and CAL values, where agreement was defined as ≤ 1 mm difference between paired measurements. While our measured estimate for the biologic width falls within the range of mean values reported in a systematic meta-analysis (between 1.15- 3.95 mm), disease state, tooth type, probing depth, and attachment loss can all affect the biological width [387]. The combination of these variables and the lack of precision in locating the subgingival CEJ with a periodontal probe are likely reasons for the relatively low agreement between iCAL and CAL values. Indeed, this limitation of physical probing for CEJ identification reduces the value of this comparison. Given the higher accuracy of physical probing for PPD measurements, the comparison between iPD and PPD is both more reliable and promising.

Importantly, while recapitulating the PPD values via imaging has value, the iGH is simpler and more straightforward to measure (non-invasive). It also does not require *a priori* knowledge of the biological width. More importantly, we show here that iGH correlates to disease as well as if not better than PPD and thus we suggest that it could be a standalone metric of periodontal health. Of course, the true value will need to be validated with larger cohorts including molars that could not be accessed here due to the large size of the transducer.

Ultrasound can also measure gingival thickness with a high degree of precision and accuracy—while iGT alone does not reflect periodontal health, it is an important metric in the context of operations such as gum grafts and periodontal flap surgeries. Currently, biotype is a binary evaluation performed by inserting the periodontal probe into the gingival

sulcus and assessing probe visibility. A visible probe corresponds to a "thin" biotype and an invisible probe corresponds to a "thick" biotype. Actual values for thin and thick biotypes have been proposed as < 1.0 mm GT and > 1.0 mm GT, respectively [391]. We did not observe a statistical difference between GT or iGT measurements in healthy and diseased patients (**Figure 4.6**). Though imaging is significantly more precise than the probe visibility method, this comparison served as assurance that iGT measurements were not biased by the health status of the patient.

Our technique does have some limitations. Many images possessed reflection artifacts generated by the ultrasound sleeve. These artifacts are generated by the specific geometry of the transducer, i.e., the ~ 0.5-mm gap between the transducer elements and the subject/imaging target. Most transducers do not have this gap. Another limitation of the transducer was its size. This restricted imaging to the buccal surfaces of teeth 6-11 and 22-27. The ideal transducer could access the buccal and lingual surfaces of the full dentition. Practical clinical deployment will also need to integrate computational techniques to automatically extract imaging biomarkers [372, 378, 392, 393]. Nevertheless, ultrasound may have significant clinical value for longitudinal monitoring of periodontal health. Unlike other oral imaging modalities, ultrasonography offers details of both hard and soft tissues, thus facilitating the measurement of periodontal metrics that require the resolution of both hard (ABC, CEJ) and soft (GM, GT) features. It is non-ionizing, painless, and can be operated chairside with minimal training.

4.5. Conclusions

We investigated the use of high-frequency ultrasound in 10 healthy subjects (34 teeth) and 6 subjects with periodontal disease (32 teeth) for measuring critical metrics of

periodontal health, including probing pocket depth, clinical attachment level, gingival recession, and gingival thickness at mid-buccal sites. Image-based measurements of gingival height extended from the gingival margin to the alveolar bone crest and were comparable to probing pocket depth (1.57-mm magnitude bias) with functional equivalence for assessing disease status. Identification of the cementoenamel junction by human operators also allowed image-based measurement of alveolar bone level and gingival recession. Inter-operator bias was negligible (<0.1 mm) for gingival height and 0.45 mm for alveolar bone level measurements. Image-based alveolar bone level measurements were equivalent to clinical attachment level for staging disease (0.25-mm magnitude bias). Overall, ultrasonographic metrics in this patient group had at least an equivalent diagnostic capacity as gold-standard physical probing while offering more detailed anatomical information and painless operation. We anticipate that advances in the form factor of ultrasound hardware will facilitate the further translation of this technology into the dental clinic.

4.6. Acknowledgements

Chapter 4, in part, has been submitted for publication of the material as it may appear in Dentomaxillofacial Radiology, 2022. Moore, Colman; Law, Jane; Pham, Christopher; Chang, Kai-Chiao J.; Chen, Casey; Jokerst, Jesse V. The dissertation author was the primary investigator and author of this paper.

Table 4. 1. Image quality metrics and clinical measurements.

Image index and quality							Clinical measurements		
Patient (n)	Clinical diagnosis	Tooth number	GM Identified?	ABC Identified?	Free of interfering artifacts?	Image Quality (0-3)	Gingival Biotype	PPD (mm)	CAL (mm)
1	Healthy	6	X	✓	X	1	Thick	3	3
		7	X	✓	X	1	Thick	2	2
		8	✓	✓	✓	3	Thick	2	2
		9	✓	✓	✓	3	Thick	2	2
		10	✓	✓	✓	3	-	1	1
		11	X	X	X	0	-	1	1
2	Healthy	7	✓	✓	✓	3	-	-	-
		8	✓	✓	✓	3	-	-	-
		9	✓	✓	✓	3	-	-	-
3	Healthy	6	✓	✓	✓	3	Thick	1	1
		7	✓	X	X	1	Thick	1	1
		8	✓	✓	✓	3	Thick	2	2
		9	✓	✓	✓	3	Thick	2	2
		10	✓	✓	✓	3	Thick	2	2
		11	✓	✓	✓	3	Thick	2	2
4	Healthy	6	✓	✓	✓	3	Thick	1	1
		7	✓	✓	✓	3	Thick	2	2
		8	✓	✓	✓	3	Thick	2	2
		9	✓	✓	✓	3	Thick	2	2
		10	✓	✓	✓	3	Thick	2	2
		11	✓	✓	✓	3	Thick	2	2
5	Healthy	6	✓	✓	✓	3	Thick	2	2
		9	✓	✓	✓	3	Thick	2	2
		10	✓	X	X	1	Thick	2	2
		11	✓	✓	✓	3	Thick	3	3
6	Healthy	7	✓	✓	X	2	Thick	2	2
		8	✓	✓	✓	3	Thick	2	2
7	Healthy	7	✓	✓	✓	3	Thick	1	1
		8	✓	✓	✓	3	Thick	1	1
		9	✓	✓	✓	3	Thick	1	1
		10	✓	✓	✓	3	Thick	1	1
8	Healthy	7	✓	✓	✓	3	Thick	3	3
		8	✓	✓	✓	3	Thick	1	1
		9	✓	X	✓	2	Thick	1	1
		10	✓	X	✓	2	Thick	1	1
9	Healthy	7	X	✓	X	1	Thick	1	1
		8	✓	✓	✓	3	Thick	1	1
		9	✓	✓	✓	3	Thick	1	1
		10	✓	✓	✓	3	Thick	1	1
10	Healthy	7	✓	✓	✓	3	Thick	2	2
		8	✓	✓	✓	3	Thick	2	2
		9	✓	✓	✓	3	Thick	2	2
		10	✓	✓	✓	3	Thick	2	2
11	Diseased	22	✓	✓	✓	3	Thick	2	3
		23	✓	X	✓	2	Thick	3	4
		24	✓	✓	✓	3	Thick	1	2
		25	✓	✓	✓	3	Thick	2	3

Table 4. 2. Image quality metrics and clinical measurements.

Image index and quality							Clinical measurements		
Patient (n)	Clinical diagnosis	Tooth number	GM Identified?	ABC Identified?	Free of interfering artifacts?	Image Quality (0-3)	Gingival Biotype	PPD (mm)	CAL (mm)
		26	✓	✓	✓	3	Thick	2	2
		27	✓	✓	✓	3	Thick	2	2
12	Diseased	6	✓	✓	✓	3	Thick	2	3
		7	✓	✓	✓	3	Thick	2	3
		8	✓	X	✓	2	Thick	2	2
		9	✓	✓	✓	3	Thick	2	3
		10	✓	✓	✓	3	Thick	2	3
		11	✓	✓	✓	3	Thick	2	3
13	Diseased	6	✓	✓	✓	3	Thick	1	1
		7	✓	✓	✓	3	Thin	1	1
		8	✓	✓	✓	3	Thin	4	4
		9	✓	✓	✓	3	Thin	7	7
		10	✓	✓	✓	3	Thin	2	2
		11	✓	X	X	1	Thin	6	6
14	Diseased	22	✓	✓	✓	3	Thick	2	2
		23	✓	✓	✓	3	Thick	1	1
		24	✓	✓	✓	3	Thick	2	2
		25	✓	✓	✓	3	Thick	2	2
		26	✓	✓	✓	3	Thick	2	2
		27	✓	✓	✓	3	Thick	1	1
15	Diseased	22	✓	✓	✓	3	Thick	2	2
		23	✓	✓	✓	3	Thick	2	2
		24	✓	✓	X	2	Thick	5	5
		25	✓	✓	✓	3	Thick	2	2
		26	✓	✓	✓	3	Thick	2	2
		27	✓	✓	✓	3	Thick	2	2
16	Diseased	22	✓	✓	✓	3	Thick	2	2
		23	✓	✓	✓	3	Thick	2	3
		24	✓	✓	✓	3	Thick	2	3
		25	✓	✓	✓	3	Thick	1	1
		26	✓	✓	✓	3	Thick	2	2
		27	✓	✓	✓	3	Thick	2	2

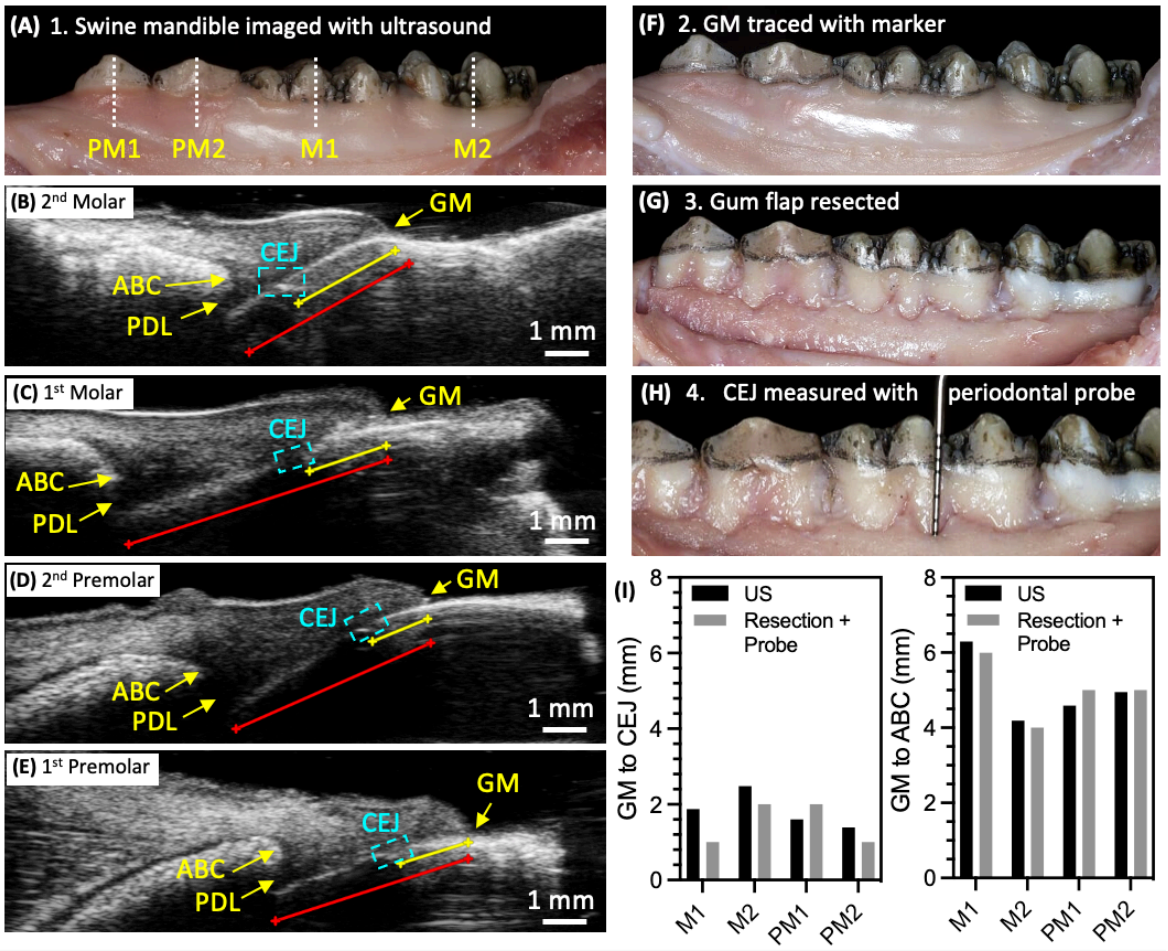

Figure 4. 5. Comparison of ultrasound to physical examination for an extracted swine mandible following gum flap resection and periodontal measurement with physical probing.
(**A**) Photograph of the 2nd molar (M2), 1st molar (M1), 2nd premolar (PM2), 1st premolar (PM1), and the imaging plane for each tooth (white dashed lines). (**B-E**) Visualization of the cementoenamel junction (CEJ) relative to the alveolar bone crest (ABC) and gingival margin (GM) for the (**B**) 2nd molar, (**C**) 1st molar, (**D**) 2nd premolar, and (**E**) first premolar. The CEJ is consistently resolvable as a change in the echogenicity of the tooth surface between the GM and the ABC. The image-based measurements of the GM to CEJ (yellow lines) were M2 = 2.53, M1 =1.88, PM2 = 1.39 mm, PM1 = 1.60 mm. The corresponding GM to AC measurements (red lines) were M2 = 4.19 mm, M1 = 6.30 mm, PM2 = 4.95 mm, PM1 = 4.59 mm. (**F**) Following imaging, the GM was traced along the teeth using black ink from marker. (**G**) The gingiva (gum flap) was resected to reveal the roots of the teeth. (**H**) The distances from GM to CEJ and GM to ABC were measured by a clinician using physical probing. (**I**) These values were plotted and compared to the image-based measurements (<1.0 mm difference between GM-CEJ values (mean percent difference = 34%) and <0.5 mm difference between GM-ABC values (mean percent difference = 4.8%)). All resection + probe values were restricted to integers.

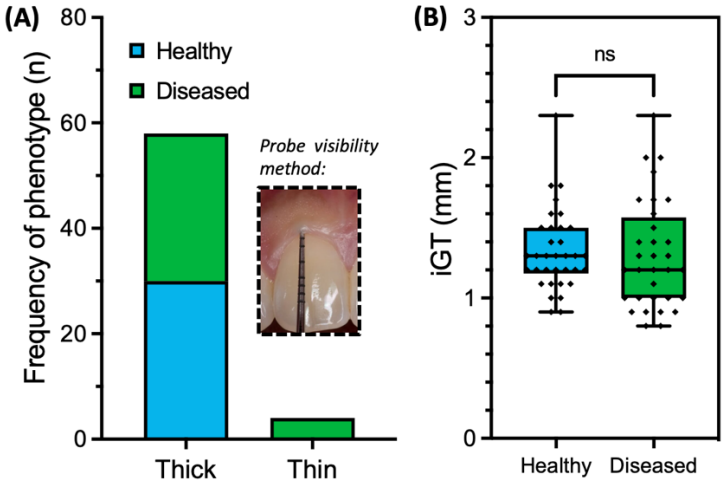

Figure 4. 6. Comparison between clinically assigned biotype and US image-based measurements of gingival thickness (iGT).

(**A**) Teeth from healthy and diseased groups were classified as a thick or thin biotype according to the conventional probe-visibility method. Photographic inset: example of a thick biotype. (**B**) The imaged gingival thickness (iGT) can provide significantly more quantitative assessment (< 0.1 mm precision over the full cross-sectional area) than probe-based biotyping. As expected, no significant difference was observed between iGT for the healthy and diseased groups. Here, the iGT was measured from the midpoint between the ABC and GM.

CHAPTER 5. PHOTOACOUSTIC IMAGING FOR MONITORING PERIODONTAL HEALTH: A FIRST HUMAN STUDY

ABSTRACT: The gold-standard periodontal probe is an aging tool that can detect periodontitis and monitor gingival health but is highly error-prone, does not fully characterize the periodontal pocket, and causes pain. Photoacoustic imaging is a noninvasive technique that can address these limitations. Here, a range of ultrasound frequencies between 16-40 MHz were used to image the periodontium and a contrast medium based on cuttlefish ink was used to label the pockets. A 40 MHz ultrasound frequency could spatially resolve the periodontal anatomy, including tooth, gum, gingival margin, and gingival thickness of tooth numbers 7-10 and 22-27. The photoacoustic-ultrasound measurements were more precise (0.01 mm) than those taken with physical probes by a dental hygienist. Furthermore, the full geometry of the pockets could be visualized with relative standard deviations of 10% (n = 5). This study shows the potential for non-invasive monitoring of periodontal health with photoacoustic-ultrasound imaging in the dental clinic.

5.1. Introduction

Periodontitis affects nearly 50% of Americans and exerts both local and systemic effects on the body [394, 395]. These range from mild discomfort to debilitating pain, tooth loss, and excessive activation of the immune system [396-398]. In fact, studies have identified the chronic inflammation from periodontitis as a risk factor for conditions such as cardiovascular disease [367, 399, 400], cancer [401], and dementia [402, 403]. Thus, it is critical to diagnose periodontal disease early while the symptoms are mild and reversible [404].

The current metrics for monitoring periodontal health include attachment level, probing depth, bone loss, mobility, recession, and degree of inflammation [405]. The gold standard for quantifying periodontitis progression is measurement of pocket depths with a periodontal probe. This tool provides a numerical metric that reflects the degree of apical epithelial attachment measured from the gingival margin and is critical for disease staging [406].

However, the periodontal probe is a relatively unsophisticated tool that suffers from poor reproducibility [368, 406]. These errors are attributed to the significant variation in probing force between operators, which can vary across multiple orders of magnitude [407]. Physical probing can penetrate inflamed tissue leading to patient discomfort, bleeding, and inaccurate measurements [398, 408]. The probe can also only measure depth at the point of insertion—with no information on the full width or contour of the pocket. Furthermore, the benefit of traditional probing around dental implants is abrogated due to the implant threads that impede probe penetration along the implant surface [409, 410]. This limits clinical assessment of these tissues potentially leading to peri-implantitis [411, 412].

We recently described an approach that uses photoacoustic imaging to potentially address these issues [413]. Photoacoustic imaging is a hybrid imaging modality that combines visible and near infrared excitation with acoustic detection [44, 67, 320, 414]. It extends the utility of ultrasound by enabling contrast based on optical absorption [415, 416]. Traditional ultrasound operates under the principle of "sound in, sound out", but photoacoustic imaging shifts this concept to "light in, sound out" [37]. Here, a near infrared laser excites a light-absorbing target. The target then undergoes spatially confined heating followed by thermoelastic expansion. This generates wideband acoustic waves that can be detected with ultrasound transducers for image generation. The clinical applications of photoacoustic imaging are growing; some recent examples include endogenous imaging of inflammatory arthritis, noninvasive assessment of Crohn's Disease, and diagnosis of vascular malformations [27, 417-421]. Though photoacoustic-ultrasound (PA-US) signal can be limited by tissue penetration, it has two significant advantages over radiography, the most common dental imaging modality [422]: (1) it can image soft tissue; and (2) it does not use ionizing radiation. Additionally, the surfaces of hard tissues such as bone [423] and teeth [424] can be imaged.

Our previous report demonstrated the first application of photoacoustics for periodontal health and used a biocompatible oral contrast agent based on food-grade cuttlefish ink [413]. That work utilized swine models and imaged nearly 40 teeth to validate the method. While bias values relative to gold standard were low (<0.2 mm), unresolved questions remained about its clinical utility. Here, we show that photoacoustic-ultrasound can image both the full depths and geometries of pockets in healthy human adults for non-invasive monitoring of gingival health after local irrigation of the pocket with contrast media.

5.2. Methods

5.2.1. Reagents and Equipment

Cuttlefish ink was purchased from Conservas de Cambados and contained ink, water, salt, and sodium carboxymethyl cellulose. Phosphate-buffered saline tablets were purchased from Sigma-Aldrich. Ultrasound gel was obtained from Next Medical Products. PA-US images were taken with a laser-integrated high frequency ultrasound system from Visualsonics (Vevo LAZR). A medical head immobilizer was purchased from DealMed. Disposable dental cheek retractors were obtained from Url Dental.

Contrast agent solutions were prepared individually from stock solutions of cuttlefish ink for each imaging experiment. Stock cuttlefish ink solutions (50% w/v in 0.1 M PBS) were aliquoted and refrigerated. To prepare the contrast agent, an aliquot was diluted and mixed with corn starch to a final solution containing 5% ink w/v and 2% corn starch. It was briefly heated to boiling to achieve homogeneity. The spherical melanin nanoparticles within the contrast agent were previously characterized with transmission electron microscopy, which indicated a mean particle size of 125 nm from 500 nanoparticles; and dynamic light scattering, which showed a hydrodynamic radius of 266 nm with a polydispersity index of 0.116 [413]. It is a food-grade material and was approved for human use by the Institutional Review Board (IRB). Human subject exclusion criteria included a shellfish allergy or a kosher diet.

5.2.2. Volunteer Recruitment

This case study enrolled a healthy 22-year old adult female with good oral hygiene. All work with human subjects was approved by the UCSD IRB and conducted according the

ethical standards set forth by the IRB and the Helsinki Declaration of 1975. The participant gave written informed consent and teeth 7-10, 22-27 were imaged.

5.2.3. Periodontal Probe Measurements

Pockets were measured with the Williams and Marquis probes [425] by a licensed periodontist. The measurements were performed at the distobuccal, mesiobuccal, and buccal sites according to clinical convention [426]. For distal and mesial measurements, the probe was inserted at a 10° angle at the interproximal space between adjacent teeth. The buccal measurements were collected at the deepest point observed after walking the probe across the width of the pocket. Per standard clinical practice, measurements were rounded up to the nearest integer. For the Williams probe, all measurements <2 mm were recorded as 2 mm. For the Marquis probe, readings within the 3 mm intervals were estimated to be either in the lower 1.5 mm or upper 1.5 mm range and then rounded up to the nearest integer.

5.2.4. Pocket Labeling

The subgingival pockets were labelled with ~8 μL of contrast agent per tooth. A micropipette with a sterile 2-20 μL tip was placed in contact with the gingival sulcus and used to irrigate the region with contrast agent. Following imaging, the contrast agent was removed from the pockets by rinsing the mouth with water or gentle tooth brushing (< 10 s).

5.2.5. Imaging Procedure

Photoacoustic imaging was performed by pulsing light through two optical fiber bundles integrated with both sides of a rectangular, linear array transducer. The laser excitation (Q-switched Nd:YAG) used 5 ns pulses at 20 Hz (6 Hz frame rate). The ultrasound resolution was controlled by changing between three transducers: LZ-201 (center frequency = 16 MHz), LZ-250 (center frequency = 21 MHz), and LZ-550 (center frequency = 40 MHz).

Typical gains were 15 dB for photoacoustic signal and 10 dB for ultrasound. The subject and operator both wore near-infrared protective laser goggles during experiments. The subject was seated in front of the imaging system and rested their chin on a flat surface in front of the transducer. The subject wore dental cheek retractors and a medical head immobilizer to reduce movements that contribute to motion-based imaging artifacts. A layer of ultrasound gel was applied to the transducer, which was adjusted to 1 cm from the tooth. The 680 nm laser was initialized, and the stepper motor was scanned 17 mm (0.076 mm step size) to obtain a 3D PA-US image via maximum intensity projection [427].

5.2.6. Image Analysis and Statistics

Following raw data acquisition, sagittal cross-sections were examined in ImageJ to determine the penetration of contrast agent and quantify pocket depths. First, images were converted to 8-bit images and exported as two files: one that displayed only the photoacoustic signal and another that displayed only the ultrasound. For these images, a line profile was manually drawn parallel to the gingival margin through both images (**Figure 5.7**). From this, the pixel intensity could be plotted with respect to the position along the line for both the photoacoustic and ultrasound images. Then, a minimum pixel intensity (10% of the maximum intensity in the image) was chosen as a threshold, above which signal was considered significant. If both signals were above the threshold at a given position, then that point was considered part of the pocket depth. Taken together, all of these points formed a length and its magnitude was recorded as the pocket depth.

To avoid bias during quantitative comparison to physical probing, sagittal planes were chosen the same way each time: for distobuccal and mesiobuccal sites, we chose the first 8 sagittal planes (0.6 mm-wide sections) with a measurable pocket depth on each lateral

side of the tooth. These sections mimicked the diameters of the physical probes. For the buccal sites, we selected 0.6 mm-wide sections from the images at the deepest part of the pocket. This dimension mimicked the diameter of the physical probes and the typical procedure of recording the lowest number obtained by walking the probe across the pocket width. For replicate measurements, images were collected on nonconsecutive days across two weeks.

The buccal contours of the pocket geometry were mapped by averaging five separate imaging events. The width of the pocket consisted of dozens of sagittal planes. For each plane, two measurements were taken: the distance from the crown of the tooth to the gingival margin, and the distance from the gingival margin to the edge of photoacoustic signal (the subgingival terminus). Together, these measurements determined the top and bottom of the pocket for that plane. Once these measurements were taken for all planes, they were used to reconstruct a full map of the pocket to overlap on top of the ultrasound image.

5.3. Results

5.3.1. High-Resolution Ultrasound Imaging of Teeth and Soft Tissues

Photoacoustic and ultrasound images were collected by adapting a commercial PA-US system for human operation (**Figure 5.1**). Ultrasound imaging was used to generate frontal and sagittal cross-sections of 10 teeth (tooth numbers 7-10, 22-27) and their associated soft tissues from a healthy volunteer (**Figure 5.2**). They were labelled with the numbering system used by the American Dental Association [428]. These anterior teeth were imaged because the size of the transducer limited access to the posterior region of the oral cavity.

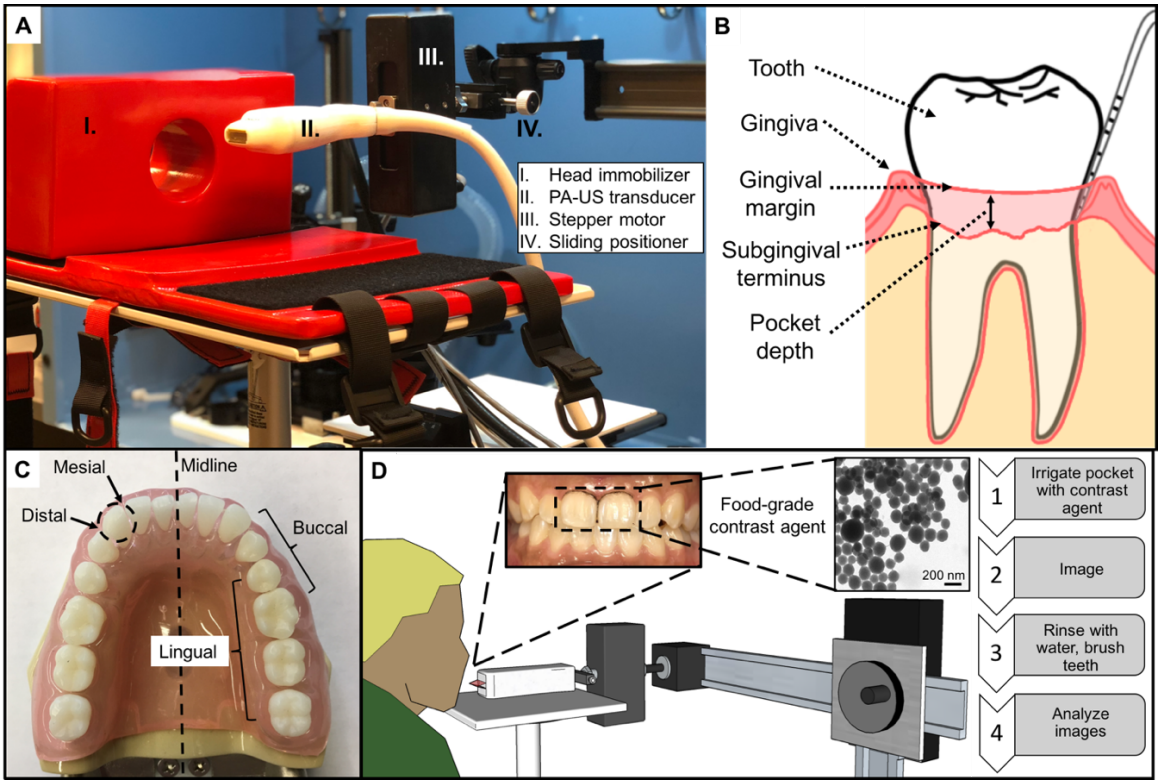

Figure 5. 1. Overview of the human photoacoustic imaging setup, periodontal anatomy, and workflow.
(**A**) The PA-US transducer was connected to a stepper motor for axial scanning and a sliding positioner for lateral control—these components were attached to a larger frame for general positioning. The head immobilizer (cross-section shown) rested on a flat surface. (**B**) The simplified diagram shows a tooth, gingiva, gingival margin, subgingival terminus, and pocket depth for an arbitrary cross-section. (**C**) Anatomical terms for periodontal reference: Mesial refers to a location on a tooth that is closer to the midline while distal refers to one that is further. Lingual refers to the side of a tooth facing the tongue while buccal refers to the side facing the cheek. For example, mesiobuccal and distobuccal refer to the areas of the buccal face of a tooth that are closer to and farther from the midline of the mouth, respectively. (**D**) Experimental workflow. Briefly, a contrast agent containing melanin nanoparticles (TEM inset) derived from cuttlefish ink was used to irrigate the pocket of a target tooth followed by photoacoustic imaging. The pocket could be rinsed with water and then images could be analyzed to measure pocket depths.

Increasing the ultrasound transducer frequency (**Figure 5.2A**) significantly improved our ability to identify the gingival margin. The spatial resolution of the ultrasound mode was approximately 100 μm at 40 MHz and 300 μm for the photoacoustic mode [413, 429]. At 15 and 21 MHz, the gingival-tooth interface and subgingival tooth could not be identified. These features were clearly resolved at 40 MHz, and we used this frequency for all subsequent

images. Frontal views captured surface features of the teeth and tissue, while sagittal views revealed the gingival margin, gingival thickness, and surface topology (**Figure 5.2B**).

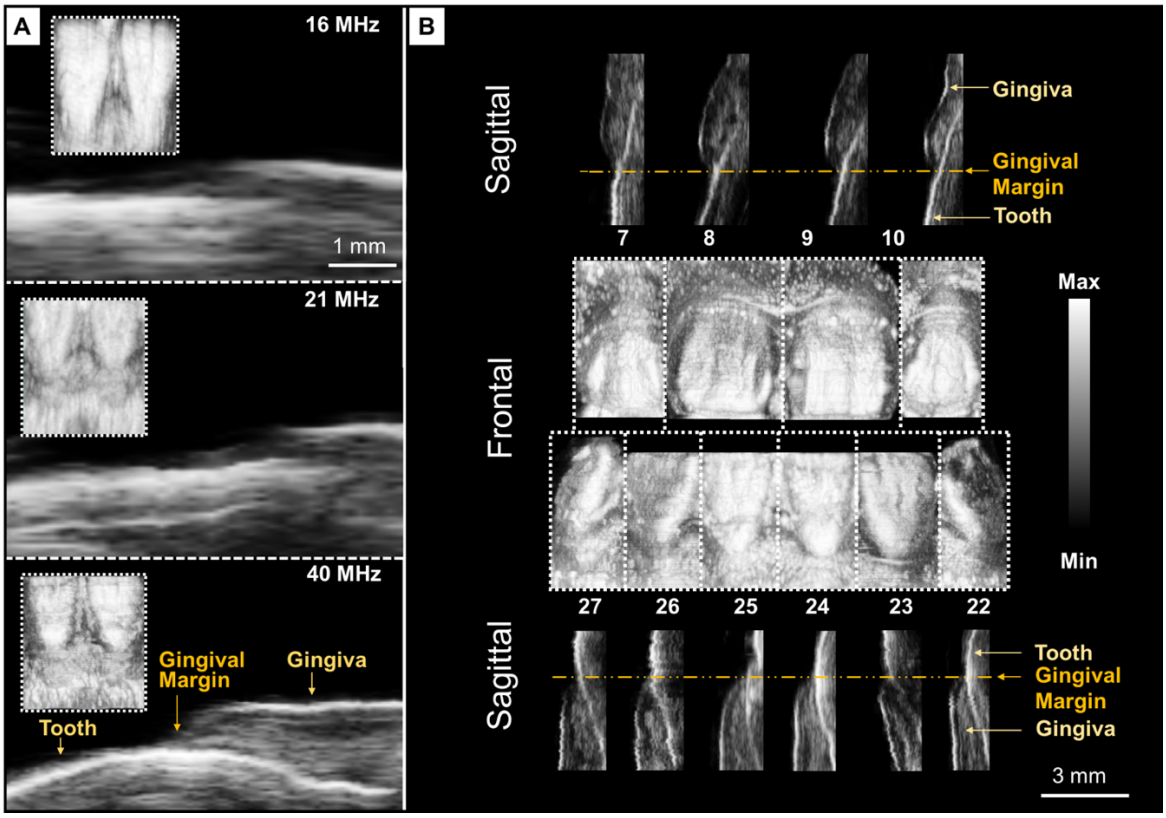

Figure 5. 2. US images of ten teeth acquired from one subject at 40 MHz and comparison to images at lower frequencies.
(**A**) Frontal and sagittal images of the bottom front incisors (24 and 25) at increasing US frequencies. Frontal images are inset within the magnified sagittal images of tooth 25 at the gingival margin. Scale bars are 1 mm and apply to all frequencies for the sagittal images. (**B**) Frontal and sagittal cross-sections of teeth 7-10 and 22-27. The frontal and sagittal views are composites of planes from ten separate scans. The gingiva, gingival margin, and tooth are resolved in each sagittal image. The 3-mm scale bar is for sagittal images.

5.3.2. Periodontal Labeling and Photoacoustic Imaging

The contrast agent possessed broad photoacoustic absorption from 680 to 970 nm due to the presence of melanin nanoparticles (**Figure 5.6**) [413,430,431]. Following administration of contrast agent, we collected PA-US images and overlaid the 680-nm signal on ultrasound to measure the periodontal pocket depths. Frontal and sagittal views of the lower central incisors in **Figure 5.3A-D** show the signal from the mid-buccal pocket after applying the

contrast agent and imaging. The mid-buccal pocket depth of tooth number 25 was 1.31 mm (**Figure 5.3D**); signal from the supragingival surface of the tooth did not contribute to the measurement. The gingival thickness could also be quantified. When measured at the mid-buccal plane, 2 mm below the gingival margin, the gingival thickness was 1.01 ± 0.05 mm for tooth 25 and 0.97 ± 0.04 mm for tooth 24 (n = 5). These values matched the average thickness reported for a 16-24 year old age group [432].

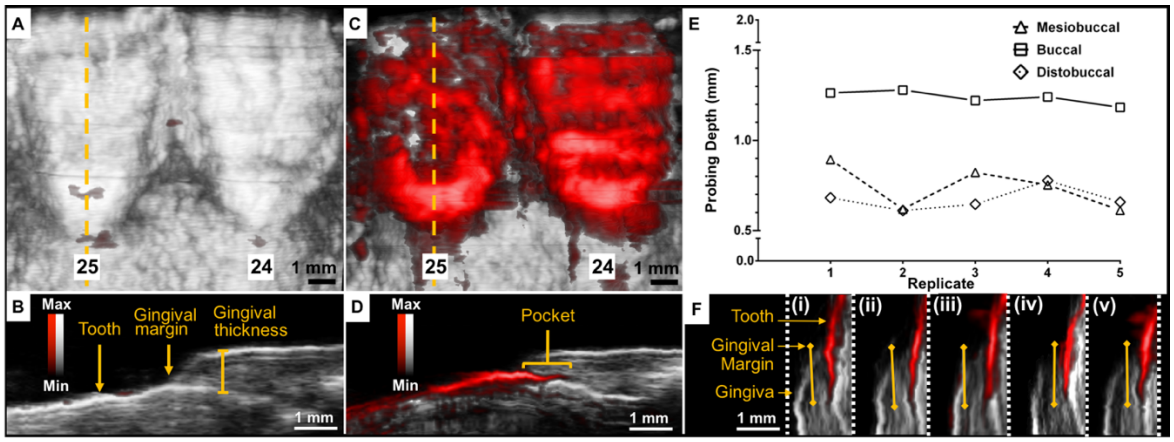

Figure 5. 3. Photoacoustic-ultrasound images of the bottom front incisors (24, 25) before and after administration of contrast agent with demonstrated reproducibility.
(**A**) Frontal cross-section of teeth 24 and 25 with photoacoustic signal overlaid on ultrasound prior to administration of contrast agent. (**B**) Sagittal cross-section of tooth 25, indicated by the dashed yellow line in Panel **A**, with tooth, gingival margin, and gingival thickness labelled. (**C**) Frontal cross-section of teeth 24 and 25 with photoacoustic signal overlaid on ultrasound after administration of contrast agent. (**D**) The sagittal cross-section of tooth 25 (dashed yellow line in Panel **C**) shows the soft-hard tissue interface and pocket revealed by the photoacoustic contrast agent below the gingival margin. (**E, F**) Reproducibility of measurements for representative sagittal planes at mesiobuccal, central buccal, and distobuccal probing locations across five replicates in tooth 25; labeling and imaging procedures were performed independently from beginning to end. Each PA-US image in **F** corresponds to the mesiobuccal probing depth measurement (squares) for its given replicate number on the x-axis in **E**. Light yellow lines show the pocket measurements. White: ultrasound, red: photoacoustic.

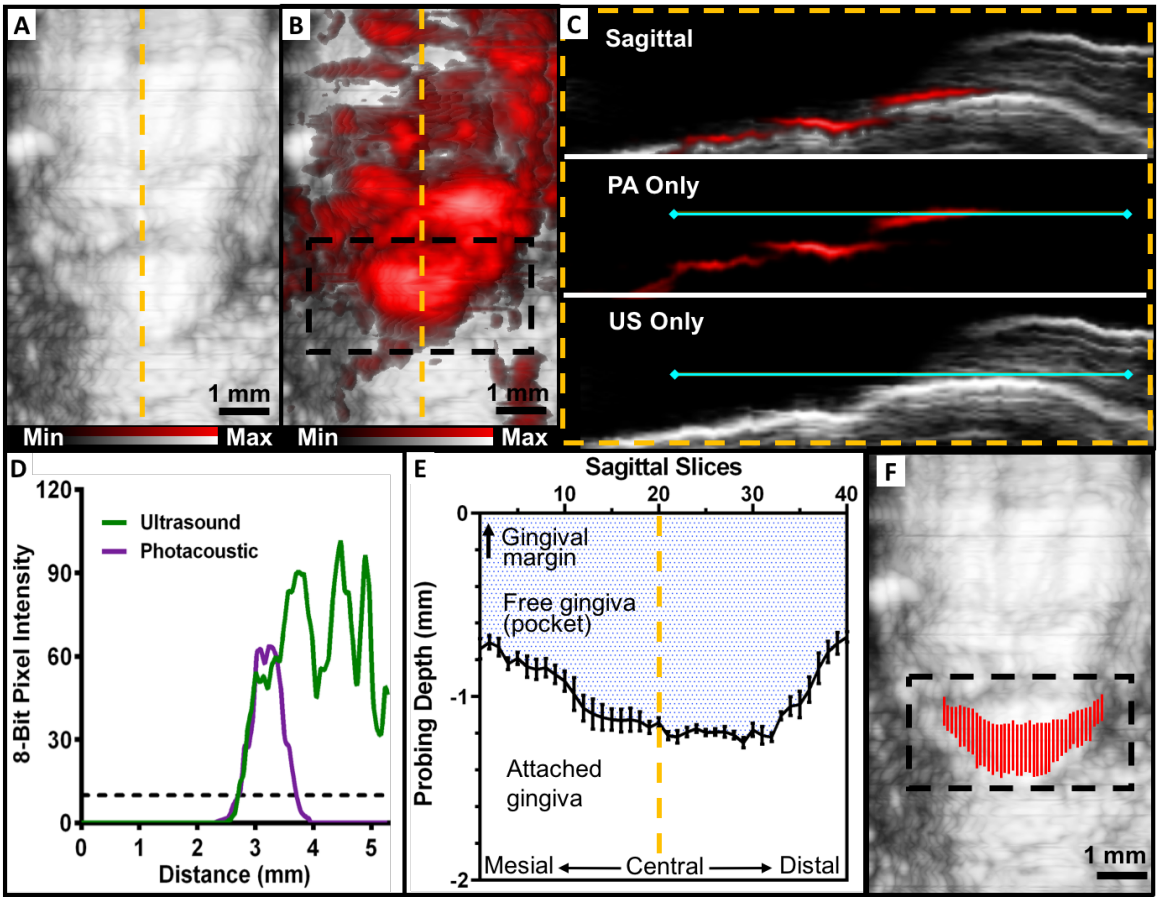

Figure 5. 4. Procedure for mapping the full width and contours of the periodontal pocket. (**A**) US frontal image of tooth 25 prior to administration of contrast agent. (**B**) PA-US frontal image of the same tooth following contrast agent with the subgingival region of interest highlighted by a black box, prior to image processing. (**C**) A sagittal view of the tooth at the yellow dashed line from (A) and (B) used for image processing. The top of panel C is an overlay and the lower panels are ultrasound and photoacoustic layers. A line (solid turquoise) was manually drawn parallel to the gingival margin for both of the layers using ImageJ. (**D**) The 8-bit pixel intensities of the ultrasound and photoacoustic signal along the line were plotted with respect to the length of the line. A minimum intensity threshold (dashed line) of 10% relative to the maximum was chosen to minimize the influence of background signal, and the pocket depth was taken as the total length for which the photoacoustic and ultrasound signals were both higher than the threshold, i.e., from 2.5 mm to 3.8 mm. (**E**) Pocket measurements for every sagittal plane across the full buccal width of the tooth– a total of 40 planes were measured. The x-axis represents each sagittal slice across the width of the tooth. The shaded region represents the geometry of the pocket and the white region represents the normal area of attachment between tooth and epithelia. Error bars show the standard error of the mean for five replicates (n = 5). (**F**) The final mapping of the pocket generated by our photoacoustic method. It was generated by taking the measurements for each sagittal slice from (**E**) and overlaying them on the ultrasound image. This step removes the non-specific photoacoustic signal from (**B**).

To demonstrate reproducibility, we conducted five independent replicates by performing the entire labelling, imaging, cleaning, and processing procedure from start to

finish on different days (**Figure 5.7**). In **Figure 5.3E-F**, the pocket depths are plotted across these replicates for buccal, mesiobuccal, and distobuccal planes. The means and standard deviations for these locations were 1.24 ± 0.04 mm, 0.74 ± 0.12 mm, and 0.68 ± 0.06 mm respectively. These corresponded to relative standard deviations of 3%, 16%, and 9%.

The pocket depth could be determined for a single plane, a region of planes, or the full buccal width of the pocket. The distance between each plane was 0.076 mm, corresponding to roughly 50-120 measurements per tooth. **Figure 5.4** shows the steps to construct a visualization of the full pocket overlaid on a frontal US image of the tooth. The measurements for these steps were performed five times (n=5) on a lower central incisor across its measurable width (**Figure 5.4A-B**). The total mean for the full pocket width was 1.02 ± 0.21 mm. The mean standard deviation of these measurements, i.e. the average of the standard deviations for every measurement plane across five replicates, was 0.104 mm, resulting in a relative standard deviation of 10.2% (**Figure 5.4E**). Furthermore, the range of the measurements was 0.57 mm, reflecting the variation in pocket depth according to probing location. The distobuccal, buccal, and mesiobuccal regions of planes (0.6 mm wide each) had measurements of 0.84 ± 0.17 mm, 1.15 ± 0.05, and 0.79 ± 0.05. **Figure 5.4C** shows a sagittal plane from **Figure 5.4B** split into photoacoustic and ultrasound signal only with a line profile drawn parallel to the gingival margin. **Figure 5.4D** quantifies the intensity of each signal along the line profile, which indicates a pocket depth of 1.10 mm for the plane using a 10% signal threshold. The final mapping of the pocket geometry is shown overlaid on the ultrasound image in **Figure 5.4F**.

We evaluated the persistence of contrast agent in the pockets following oral rinses with water as well as brushing (**Figure 5.5**). The reduction of pocket measurements was

averaged from six representative planes across teeth 24 and 25 following 15 s rinsing, 30 s rinsing, and brushing; these steps resulted in 12.5%, 25.2%, and 100% reductions respectively when averaged across five replicates.

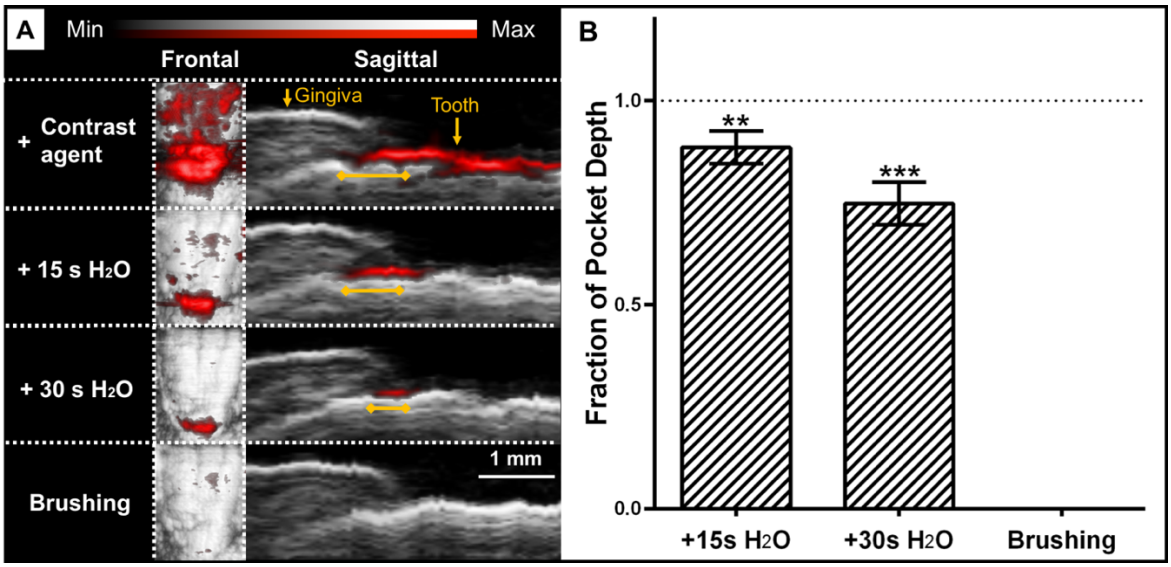

Figure 5. 5. Removal of contrast agent following oral rinsing with water and teeth brushing. (**A**) Representative PA-US images show the reduction in photoacoustic signal/pocket measurement following oral rinsing with water for 15 s, 30 s, and brushing. Yellow lines indicate the pocket measurements. (**B**) Fraction of original measurement following washing steps for five representative sagittal planes taken from teeth 24 and 25. The dotted line indicates the original measurement and error bars show SEM (n = 5). Asterisks denote significant difference from original measurement (unpaired t-test), ** ($P \leq 0.01$), *** ($P \leq 0.001$).

Finally, we compared our pocket measurements with the gold standard (Williams and Marquis) probes. The lowest possible measurement from the probes, as determined by a periodontist, was 2 mm (any lower values were rounded up); this value was recorded for the buccal pockets of teeth 24 and 25 with both probes. We measured 1.34 mm and 1.15 mm (n = 5) for teeth numbers 24 and 25 with PA-US, respectively, which agreed with the gold standard measurements while providing more precision.

5.4. Discussion

We report the first application of PA imaging for monitoring dental and periodontal health in humans by using a food-grade contrast agent. This technique is ideal for imaging periodontal pockets, gingival soft tissue and thickness, and the surfaces of teeth. These features could be distinguished both by visual inspection— ultrasound signal from tooth is brighter than tissue— and more quantitatively with line profiles of photoacoustic and ultrasound pixel intensities (**Figure 5.4D**, **Figure 5.7**). We determined that a 40 MHz ultrasound frequency provided sufficient resolution for discerning these features without sacrificing the requisite penetration depth. The US-only mode is particularly suited for applications that require knowledge of how a tooth is situated within the gingiva—one potential example would be diagnosis and monitoring of patients with delayed tooth eruption [433].

The flow of contrast agent into the gingival sulcus allowed the imaging and measurement of pocket depths, eliminating the need for probing. In the case of patients with peri-implantitis, this technique has potential to allow pocket depth measurements when physical probing is risky or impossible due to threading along the implant surface and tissue sensitivity. It was common for the agent to coat the majority of the tooth surface even when it was locally administered to the gingival margin (**Figure 5.3A**); however, this did not adversely affect measurements. The beginning of the pocket could always be identified by overlaying the ultrasound image to reveal the gingival margin and gingival thickness (**Figure 5.3B**). The imaging procedure took roughly 5 minutes per tooth but could be greatly improved with a mouthpiece transducer capable of scanning all teeth at once.

The PA imaging technique is highly reproducible (**Figure 5.3E, Figure 5.4E**) with relative standard deviations of 10%. This precision offers a major improvement over the Williams probe, which can only record integer values for pocket depths and has inter-operator error of up to 40% [434]. The periodontal pocket is a dynamic structure due to the constant battle between bacterial invasion and the immune response [435], and integers are a poor reflection of this process. In a typical oral exam, six measurements are taken per tooth (distolingual, lingual, mesiolingual, distobuccal, buccal, and mesiobuccal) to approximate the full profile of the pocket [406]. We show that photoacoustic imaging can be used to reveal the entirety of the buccal pocket with sub-millimeter (0.01 mm) precision (**Figure 5.4**). The overlay in **Figure 5.4F** was created manually but it represents a convenient visualization tool for clinicians; in the future, the conversion from raw data to final image with highlighted pocket would be performed by automated algorithms [436]. Imaging the whole pocket over the patients' lifetimes has previously been impossible and could supersede periodontal charting— this practice could reveal the development of abnormalities that would otherwise be overlooked.

We observed that contrast agent could be easily removed from the gingival sulcus after imaging (**Figure 5.5**). Oral rinsing with water reduced the contrast agent both on the surface of the teeth and within the sulcus; a few seconds of normal brushing completely removed the agent. We saw that our PA-US measurements (#24 = 1.34 mm, #25 = 1.17 mm) were in good agreement with those acquired by the Williams and Marquis probes, which recorded 2 mm for both lower central incisors. The probes were not capable of distinguishing any values lower than 2 mm; in addition, they could only record integers and relied on

subjective estimation. PA-US imaging lowers ambiguity and improves the precision of measurements.

We recognize some limitations in this study. Due to the size of the PA-US transducer, only anterior teeth could be imaged. In principle, all 32 teeth and the periodontium can be imaged with this technique but the geometry of our PA-US transducer physically limited access. Fortunately, several groups have reported custom transducer geometries, and future work includes development of a mouthpiece-shaped device to overcome this limitation [76, 77, 437]. A mouthpiece transducer would also reduce imaging artifacts caused by motion from the subject during scanning because the subject could bite down on the device. Partial penetration of contrast agent into the sulcus is also a possibility but the extent of penetration is consistent across irrigation and scanning events (**Figure 5.3C**). The subject of the study had good oral hygiene and did not have deep (≥ 4 mm) pockets indicative of periodontal disease. However, we previously showed that deep pockets could be imaged in swine, a good model of the human gingiva [438]. Finally, because the periodontal pocket is a dynamic structure, imaging and probing across different days may have contributed to small variations in measurements.

5.5. Conclusion

This work demonstrates the first use of photoacoustic imaging for monitoring periodontal health in humans by quantitating pocket depths. The measurements acquired with this technique agreed with those acquired by a trained periodontist, while providing significantly more spatial information and precision. The gold-standard periodontal probe is an established but limited tool. This technique presents an opportunity for dental clinicians to move away from manual probing and toward photoacoustic image-guided diagnostics.

Ultimately, we envision the development of a compact, PA-US mouthpiece as a platform for fast, non-invasive collection of critical periodontal metrics.

5.6. Acknowledgements

Chapter 5, in full, is a reprint of the material as it appears in Photoacoustics, vol. 12, 67-74, 2018. Moore, Colman; Bai, Yuting; Hariri, Ali; Sanchez, Joan B.; Lin, Ching-Yu; Koka, Sreenivas; Sedghizadeh, Paris; Chen, Casey; Jokerst, Jesse V. The dissertation author was the primary investigator and author of this paper.

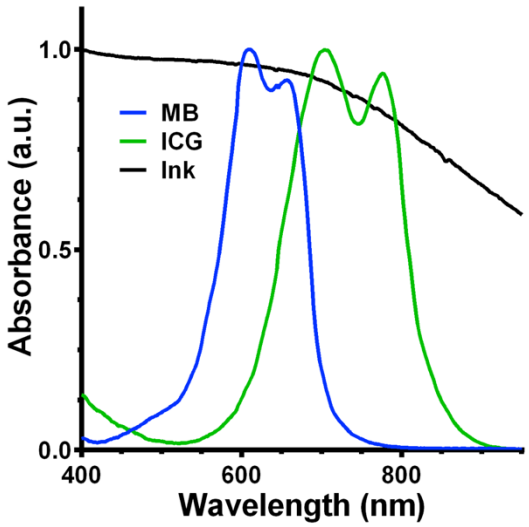

Figure 5. 6. Normalized absorbance spectrum of the cuttlefish ink contrast agent compared to methylene blue (MB) and indocyanine green (ICG).
The contrast agent solution contained 5% (w/v) cuttlefish ink and 2% cornstarch in PBS (pH 7.0). It absorbs across the near infrared in contrast to MB, ICG, and blood, which has endogenous peaks determined by the hemoglobin oxygenation [51].

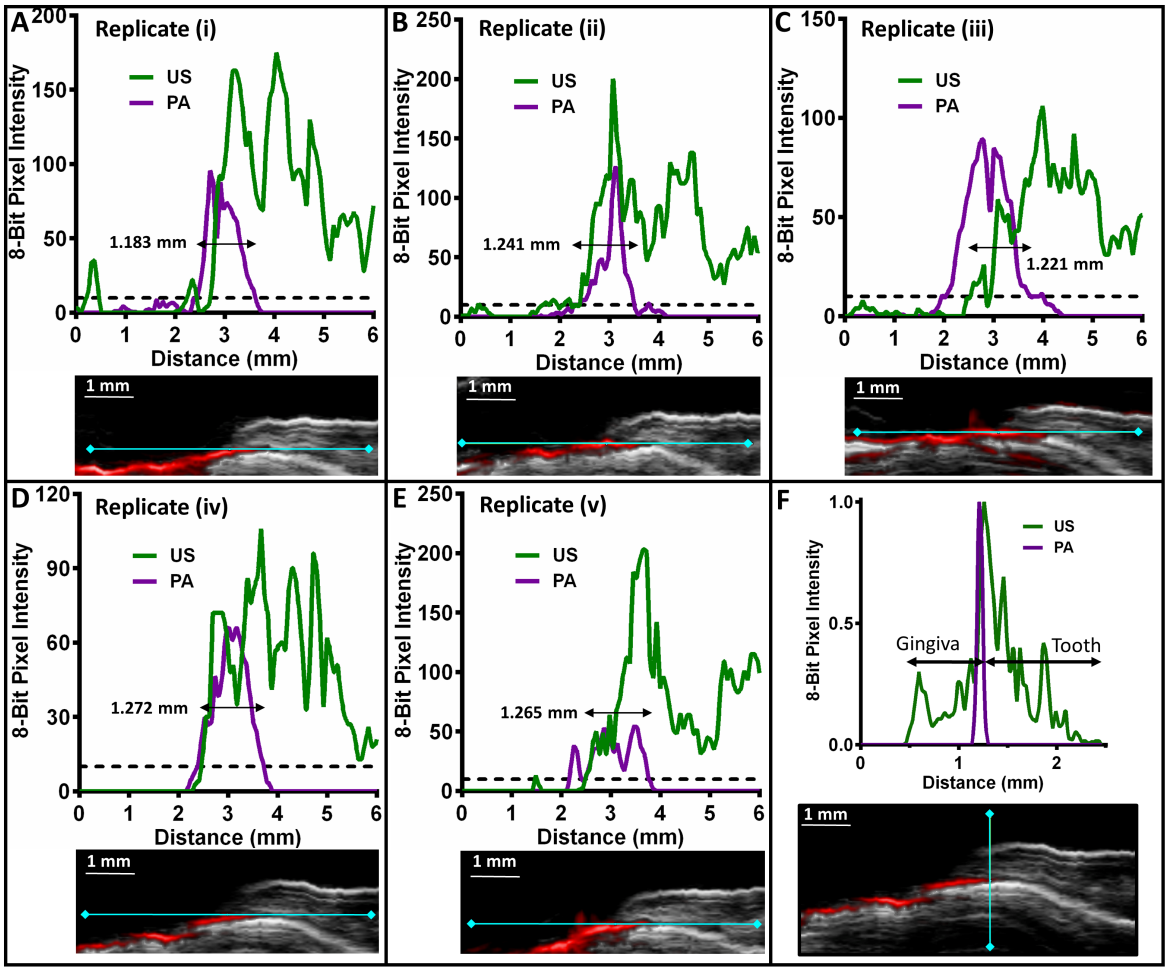

Figure 5. 7. Measurements used to determine pocket depths and differentiate pockets from adjacent tissue.

These data are line profile analyses of the image-based approach. We show replicate experiments of a single tooth (#25). Panels A-E are the replicates, and each contains a line profile and the raw imaging data. First a line profile is drawn across the acoustic data. This is the teal line in the insets of the panels and it quantitates the ultrasound (grayscale) and photoacoustic (red) data. The photoacoustic and ultrasound intensity along that line profile is then plotted (A-E). The ultrasound is in green and details the tooth and the gingiva. The photoacoustic data is in purple and details the sulcus/pocket. This overlap region is used to measure the pocket depth. The variation in the pocket depth for the replicates studies is <10%. This is repeated for five replicates similar to Figure 3 in the main text (A-E). Panel F is a line profile drawn perpendicular to the tissue surface which could be used for differentiation of tooth from gingiva. The PA peak produced by the contrast agent serves as a clear delineator between US signal from gingiva versus tooth. The plot indicates that the first 0.8 mm of tissue are gingiva (from the beginning of US signal to end of PA), while the remaining image depth is tooth.

CHAPTER 6. MOTION-COMPENSATED NONINVASIVE PERIODONTAL HEALTH MONITORING USING HANDHELD AND MOTOR-BASED PHOTOACOUSTIC-ULTRASOUND IMAGING SYSTEMS

ABSTRACT: Simultaneous visualization of the teeth and periodontium is of significant clinical interest for image-based monitoring of periodontal health. We recently reported the application of a dual-modality photoacoustic-ultrasound (PA-US) imaging system for resolving periodontal anatomy and periodontal pocket depths in humans. This work utilized a linear array transducer attached to a stepper motor to generate 3D images via maximum intensity projection. This prior work also used a medical head immobilizer to reduce artifacts during volume rendering caused by motion from the subject (e.g., breathing, minor head movements). However, this solution does not completely eliminate motion artifacts while also complicating the imaging procedure and causing patient discomfort. To address this issue, we report the implementation of an image registration technique to correctly align B-mode PA-US images and generate artifact-free 2D cross-sections. Application of the deshaking technique to PA phantoms revealed 80% similarity to the ground truth when shaking was intentionally applied during stepper motor scans. Images from handheld sweeps could also be deshaken using an LED PA-US scanner. In *ex vivo* porcine mandibles, pigmentation of the enamel was well-estimated within 0.1 mm error. The pocket depth measured in a healthy human subject was also in good agreement with our prior study. This report demonstrates that a modality-independent registration technique can be applied to clinically relevant PA-US scans of the periodontium to reduce operator burden of skill and subject discomfort while showing potential for handheld clinical periodontal imaging.

6.1 Introduction

Periodontitis affects nearly 50% of Americans exerting systemic effects on the body [394]. Chronic inflammation from periodontitis has been implicated as a risk factor for cardiovascular diseases [399, 400, 439], cancer [401], and dementia [402]. Thus, tools to diagnose periodontal disease at an early stage and the development of new measurement techniques are urgently needed [440].

Ultrasound (US) imaging systems with frequencies ≤20 MHz have previously been used to image facial crestal bone or the cementoenamel junction but lack spatial resolution and contrast [441, 442]. The integration of optical excitation via photoacoustic imaging significantly increases the potential applications in oral health [443]. We recently utilized a dual-modality photoacoustic-ultrasound (PA-US) system to non-invasively image the pocket depth and geometry [210, 358]. This approach offered 0.01 mm precision and provided a full contour of the pocket. Even though promising results were obtained, larger-scale clinical translation of this approach is limited by shaking artifacts caused by motion from the subject and operator. In prior work, a medical head immobilizer was used to stabilize the subject, but this failed to completely eliminate motion artifacts while also causing some discomfort to subjects [210, 358].

To address these issues, we implement here an image registration technique for deshaking periodontal PA-US images. Image registration methods try to align two or more images of a specific scene. In general, there are two methods for registration: interactive and automated [444]. In the interactive method, a set of landmarks is manually selected and used to estimate the transformation models between the two images. This method requires an experienced and accurate operator. The work can be tedious, repetitive, and time-consuming.

Consequently, automated registration methods are essential, and various methods have been proposed in this field [445] including the Harris-Laplacian, scale invariant feature transform (SIFT), speeded up robust features (SURF), maximally stable extremal regions (MSER), and modality independent neighborhood descriptor (MIND).

Automated methods typically have at least three steps: feature detection, feature matching, and model estimation [446]. Most of the differences in image registration algorithms are related to feature detection. The Harris-Laplacian algorithm looks for corners as features [447]. It is invariant to scale changes and rotation. The SIFT algorithm extracts key points through a pyramid structure that is invariant to scale, rotation, and brightness [448]. However, the number of these points is undesirable, and it takes a long time to create the vector describing the features. SURF is also invariant to scale and rotation, and its performance is acceptable in terms of speed [447]. MSER uses regional features and is independent of geometric and radiometric changes [449]. MIND [450] is based on a concept called self-similarity. It can be used for linear and deformable registration processes. This algorithm uses edges, corner points, and texture for features. Of these algorithms, we applied MIND for deshaking because it provides more sensitivity to the structural information of images [450].

In this paper, we report on the results obtained with a stepper-motor and handheld PA-US for noninvasive profiling of dental and periodontal anatomy. Our approach uses an image registration method based on MIND to correct for shaking artifacts produced by irregular hand movements during handheld scanning and subject motion during motor-based scanning. Phantom, *ex vivo*, and human data were collected and compared for qualitative and quantitative evaluation. Our results demonstrate that shaking artifacts from 3D PA-US images of the periodontal anatomy, enamel pigmentation, and pocket depth can be

algorithmically removed to allow for accurate measurement and visualization of periodontal features in clinically relevant imaging scenarios.

6.2. Methods

6.2.1. Equipment and imaging setup

This study used three imaging systems. Two commercial photoacoustic-ultrasound (PA-US) systems both capable of simultaneous ultrasound and photoacoustic data acquisition were employed: a laser-integrated, high-frequency system (**Figure 6.1A**, Vevo LAZR, Visualsonics] and an LED-based system (**Figure 6.1B**, AcousticX, Cyberdyne Inc.). The Vevo system was used with a linear array transducer: LZ-550 (Fc = 40 MHz, FOV = 10 × 14 mm (d × w)) and a Q-switched Nd:YAG laser (4-6 ns pulsewidth) followed by an optical parametric oscillator (OPO) laser operating from 680 – 970 nm. The LZ-550 was used for swine and human mandible imaging. The framerate was 5 Hz. The position of the transducer was controlled with a stepper motor (scan distance = 17 mm, step size = 0.054 mm). The AcousticX system utilized a 128-element linear array transducer (Fc = 10 MHz, FOV = 4 cm × 3.5 cm (d × w)) coupled with two 690-nm LED linear arrays. The LED repetition rate was 4K Hz and the framerate was 30 Hz. The scan distance for phantoms was 25 mm and 40 mm for the forearm epidermis imaging (step size = 0.081 mm). We also used a commercial ultrasound data acquisition system named Vantage (**Figure 6.1C,** Verasonics, Inc.) for ultrasound imaging of the depth phantom and swine jaw. This system can collect signal from 256 channels simultaneously with a sampling frequency of 62.5 MHz— here, we used a Verasonics L22-14 vX linear array transducer (20.2 MHz, 128 elements). The FOV was 12.8 × 19.12 mm (d × w), with a frame rate of 11 Hz.

The goal of this study was to validate the correction of motion artifacts for PA-US imaging conditions in which a common stepper motor was used or 3D sweeping was performed completely by hand. Freehand scanning is common and requires shaking corrections as does motor-based scanning when subject immobilization is imperfect [210]. Thus, we experimentally induced shaking motion artifacts by manually perturbing the stepper motor with periodic lateral force as the motor advanced (**Figure 6.1D**); this also caused shaking in the elevation and axial directions. This was done with varying intensities while maintaining similar periodicity to evaluate the tolerance of the algorithm to shaking amplitude. We also performed fully handheld scanning in which the operator's elbow was stabilized but was otherwise subject to imperfect motion (i.e. not strictly 1-dimensional). The operator mimicked the scanning speed of the motor during imaging.

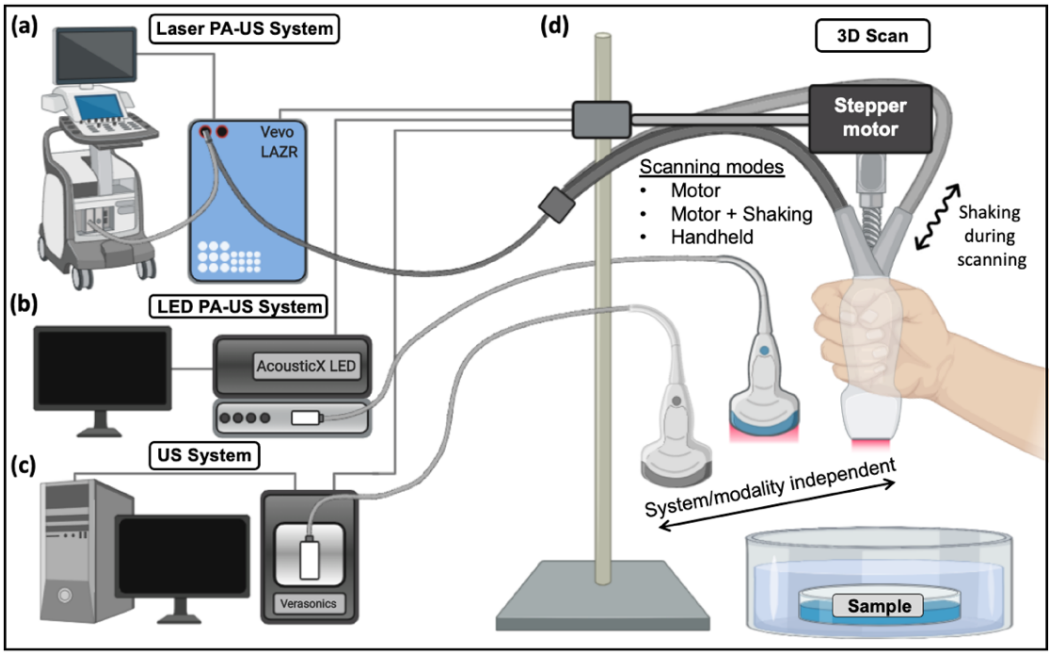

Figure 6.1. Photoacoustic-ultrasound systems and experimental setup.
(A) A laser-integrated photoacoustic-ultrasound system (Vevo LAZR, VisualSonics Inc.), an (B) LED-integrated photoacoustic ultrasound system (AcousticX, Cyberdyne Inc.), or (C) an ultrasound-only system (Vantage, Verasonics, Inc.) was used to collect 3D images by scanning each system's linear array transducer via stepper motor and by hand. (D) Samples were first laterally scanned by a stepper motor as commonly performed. To induce motion artifacts in the motor-based imaging, the scan was repeated but the motor was perturbed by hand with lateral force at various intensities mimicking an imaging setup with imperfect subject-scanner immobilization. Samples were then manually scanned by hand to mimic the most convenient clinical imaging scenario.

6.2.2. Phantom and ex vivo sample preparation

A photoacoustic depth phantom was prepared by 3D-printing (i3 MK3S, Prusa Research) a sample holder from polylactic acid (PLA) with holes for cylindrical samples at increasing depths (**Figure 6.2A-B**, depth spacing: 2 mm, lateral spacing: 1.8 mm). The holes were filled with 0.8 mm graphite cylinders. A photoacoustic lateral resolution phantom was prepared by first inkjet printing six parallel lines (130 µm thickness) at increasing spacing on optically transparent film (**Figure 6.2C**). The spacing distance (**Figure 6.2D**) was doubled between each sequential line (i.e., d1 = 560 µm, d2 = 1120 µm, d3 = 2240 µm, d4 = 4480 µm, and d5 = 8960 µm). This film was then embedded in 1% (w/v) agarose gel in a 5.5-cm petri dish

(**Figure 6.2C-D**). The phantoms were immersed in a water bath atop a height-adjustable stage.

Fresh swine jaws were acquired from an abattoir and prepared as previously described [358]. Briefly, the porcine head was sliced sagittally and the mandible was separated from the maxilla with a saw. The teeth and periodontal tissues were used as provided and immersed in a water bath for imaging (**Figure 6.2F**).

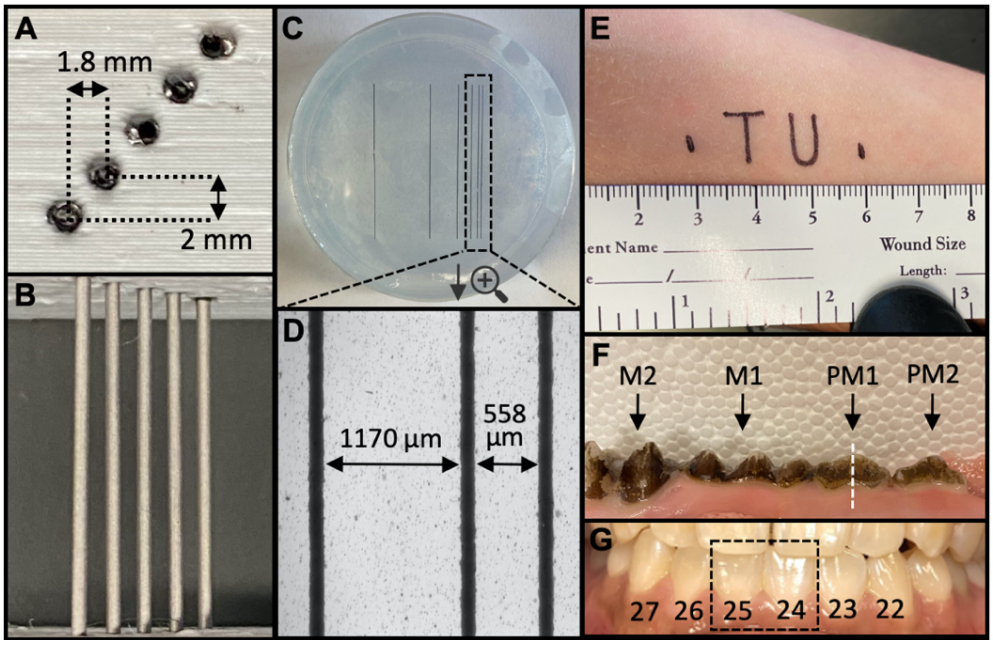

Figure 6.2. Imaging phantoms and targets.
(A) Photographic cross-section of depth phantom 3D-printed from PLA. The holes are 1-mm diameter and filled with 0.8 mm graphite pencil lead. The lateral spacing is 1.8 mm and the axial spacing is 2 mm. (B) Top-down photograph of depth phantom. (C) Top-down photograph of lateral resolution phantom, consisting of inkjet-printed lines on transparent film embedded in 1% agar within a 5.5-cm petri dish. The spacing between each line (width = 130 µm) doubles sequentially and was measured with brightfield microscopy. From right to left, d1 = 560 µm, d2 = 1120 µm, d3 = 2240 µm, d4 = 4480 µm, d5 = 8960 µm. (D) Spacing between the right-most (closest) lines is shown with brightfield microscopy. (E) Text printed with permanent marker on the supinated forearm to evaluate algorithm performance for a non-linear target. The total feature length was 3 cm. (F) Photograph of the *ex vivo* swine maxilla with teeth labeled: M2 (2nd molar), M1 (1st molar), PM1 (1st premolar), PM2 (2nd premolar). The white dashed line indicates the sagittal imaging plane generated from transverse B-mode images. (G) Photograph of the teeth and gingiva imaged in a healthy human subject labeled with the universal numbering system—the dashed box shows teeth imaged for deshaking.

6.2.3. Human periodontal and epidermal imaging

The study enrolled one male and one female healthy adult. These subjects provided written informed consent and all work was conducted with approval from the UCSD Institutional Review Board and was in accordance with the ethical guidelines for human subject research set forth by the Helsinki Declaration of 1975. To evaluate a non-linear imaging target, a fine-tip permanent marker was used to inscribe the text "TU" on the supinated forearm of the male subject (**Figure 6.2E**); this is called the "TU experiment" throughout the paper. The forearm was immersed in a water bath and imaging was performed as described above.

PA-US images of the periodontium were collected from a healthy female subject as previously described [210]. Briefly, the subject was seated in front of the laser-based PA-US system and the subject's head was immobilized upon a chin-level platform using a medical grade head immobilizer. The 40-MHz transducer was positioned at the gingiva perpendicular to the long axes of the central mandibular incisors. Sterile US gel was used for coupling. The stepper motor was then initiated to collect frames spanning the gingiva to the apical edge of teeth 24 and 25 (**Figure 6.2G**, universal numbering system).

6.2.4. Image registration

In this paper, the reconstructed images are deshaken by the method introduced in [451] where computed tomography (CT) and magnetic resonance images MRI images of lungs were registered. It is based on the self-similarity concept used for noise removal [452]. The noise removal equation is as follows:

$$NL[v](i) = \sum_{j \in I} \omega(i, j) v(j)$$

where ω is the weight of each pixel (voxel in 3D) and the criterion for self-similarity, v is the is the noisy image, and NL is the denoised image [451]. First, a descriptor insensitive to the imaging modality (e.g., CT and MRI) and noise are defined, as follows:

$$MIND(I,x,r)=\frac{1}{n}\exp\left(-\frac{D_p\left(I,x,x+r\right)}{V\left(I,x\right)}\right)\quad r\in R$$

Here, we need to consider a search area of R in which the distance between the patch (i.e., sub-image) I centered at x and another patch centered at $x+r$ is denoted by D_P. Term n is a constant coefficient to normalize the equation, V is the variance of the patch, and $MIND$ is the modality independent neighborhood descriptor used for registration.

After finding the descriptor for each pixel of the images, the similarity term for each pixel in both the patches (I and J) are calculated as follows:

$$S(x)=\frac{1}{|R|}\sum_{r\in R}\left|MIND(I,x,r)-MIND(J,x,r)\right|$$

The metric S can be adapted in any image registration algorithm. To obtain a better convergence, the Gauss–Newton optimization technique was used in this study. Readers are referred to [451, 452] for more information. We refer to the deshaking technique by MIND through the rest of the paper.

6.3. Results

6.3.1. Phantom experiments

The maximum intensity projections (MIPs) of the reconstructed images using the depth phantom are shown in **Figure 6.3**. The intensity decreases from the target 1 to 5 due to a lower laser fluence in depth. The effects of the shaking caused by the tapping (in three levels) and movement of the hand can be seen in **Figure 6.3B-E**; the peak-to-peak distance

(PPD) of the most intense target in **Figure 6.3B-D** is 0.7 mm, 1.9 mm, and 3.9 mm, respectively. MIND fails to correct the shaking in **Figure 6.3H** because the level of shaking is too high (**Figure 6.3D**). For the other two levels and also the handheld sweeping, MIND compensates for the shaking and leads to an image visually close to the ground truth (**Figure 6.3A**). We expect no shaking artifacts in the ground truth because the phantom is stable and the minor shaking of the motor in such an ideal condition can be ignored.

The structural similarity index (SSIM) was used to quantitatively evaluate the performance of MIND [453]. The Structural Similarity Index (SSIM) is a metric for evaluating the similarity between two images. It works structurally and does not perform any point-to-point comparison. The maximum value of this index is 1 and occurs when the two images are exactly the same. This metric is available via the ssim command in Matlab. The calculated SSIMs for the tubes in **Figure 6.4A** are higher than those in **Figure 6.4B** because the level of shaking in **Figure 6.3B** is lower than that of **Figure 6.3C.** The MIND algorithm corrects the movements and results in a SSIM of about 0.8 in average for both the shaking levels and handheld scenario (see **Figure 6.4A-C**). The high shaking image presented in **Figure 6.3D** was not evaluated because MIND failed to correct the shakiness (**Figure 6.3H**). We also evaluated the contrast of these images: The ratio of brightness between a region on the most intense line and the background is 15.3 for both the shaky and processed MIP images.

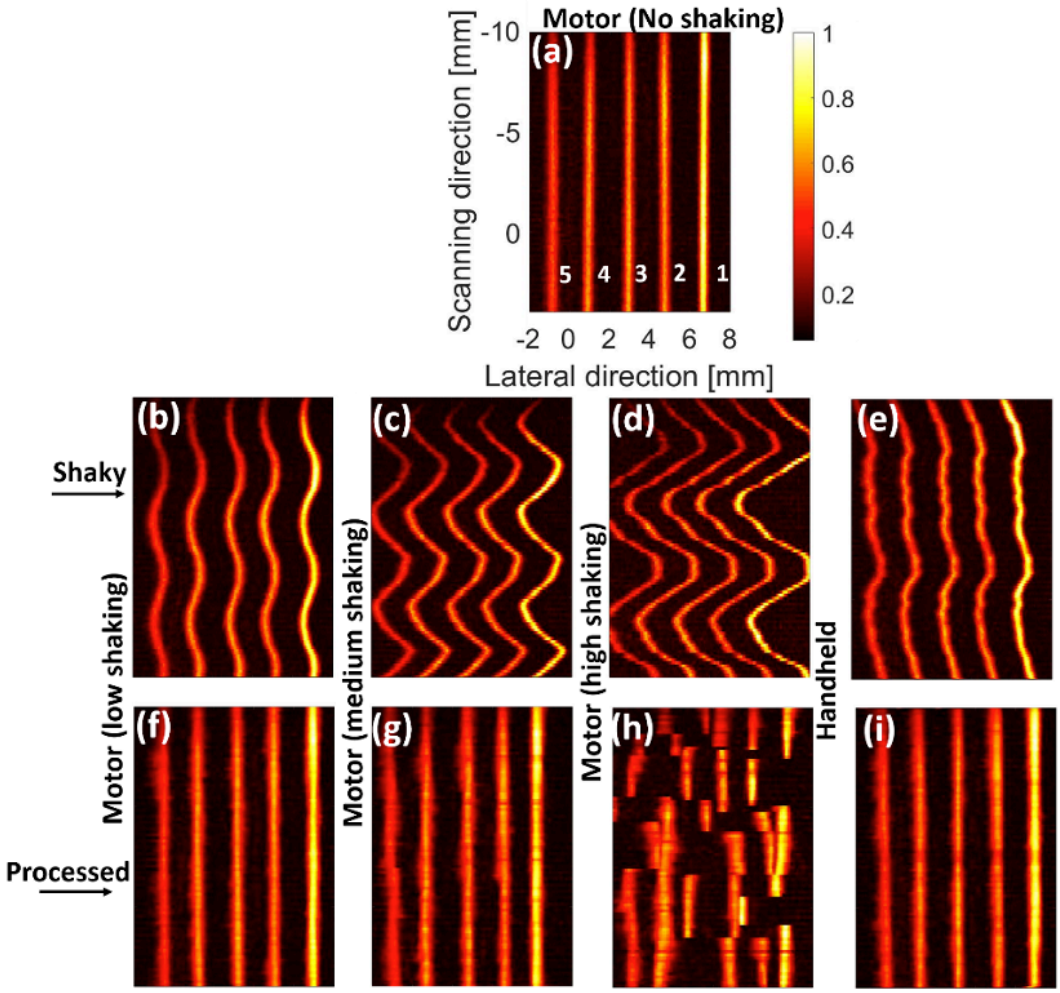

Figure 6. 3. Raw and processed photoacoustic images of a depth phantom with shaking. (A-D) The photoacoustic maximum intensity projection (MIP) of the depth phantom generated by motor with no, low, medium, and high shaking, respectively, as well as (e) hand sweeping. (E-I) The processed (i.e., deshaken) MIPs of (b-e), respectively. The processing was performed on the B-mode images and the MIPs were then generated. The LED-based imaging system was used for data acquisition.

The same experiment was conducted with the Verasonics system, and the results are presented in **Figure 6.5**. Even though a higher frequency probe was used for imaging, MIND could correct the shaky images with an average SSIM of 0.83.

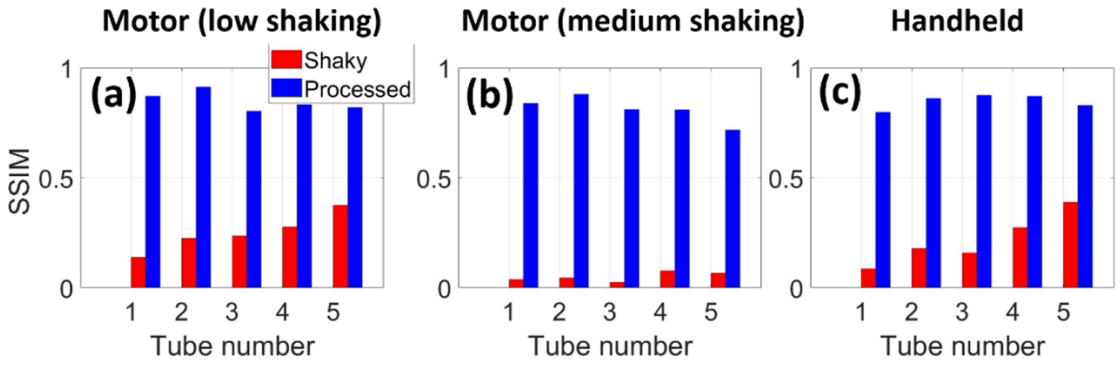

Figure 6. 4. Structural similarity index for photoacoustic images of a depth phantom. (A-B) The structural similarity index (SSIM) for measuring the image quality of motor-based imaging with low and medium shaking, respectively, and (C) handheld sweeping. The results obtained with the depth phantom (presented in Figure 6.3) were used.

The photoacoustic MIPs of the lateral resolution phantom with the LED-based system are presented in **Figure 6.6**. Even though we used low, medium and high level of shaking in both **Figure 6.3** and **Figure 6.6**, it does not mean that the applied forces to the motor were exactly the same in these figures. The PPD caused by the shaking is about 1 mm, 1.7 mm and 2.4 mm for **Figure 6.6B-D**, respectively. The first two lines from right side (see **Figure 6.2D**) were not detected in the MIP images due to the resolution of the imaging system. The intensity of all the targets is the same due to the same laser fluence incident on the targets positioned at the same depth. Shaking causes the tubes to spatially mix together (see **Figure 6.6D**; more specifically, the first two lines in the right side). However, MIND still compensates for the motion artifacts and leads to MIPs (see **Figure 6.6C-G**) that are structurally close to the ground truth (**Figure 6.6A**). It should be noted that the even though a high shaking was applied in **Figure 6.6D**, its PPD is still 1.5 mm lower than **Figure 6.3D**, which is why a reasonable image is obtained in **Figure 6.6G**. Even though the structure of the lines are preserved with MIND, there are some discontinuities (see the blue arrows) in the deshaken images (also visible in **Figure 6.6A** at the scanning distance of 2 mm). These

issues could be due to the combined effects of the step motor shaking, inhomogeneities in the laser fluence, and lower performance of the MIND on those regions.

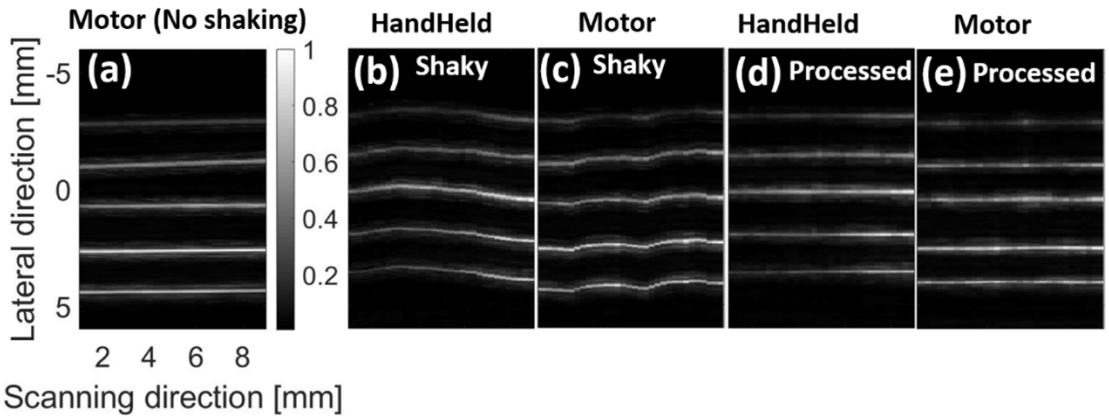

Figure 6. 5. Raw and processed ultrasound images of a depth phantom with shaking and handheld sweeping.
(A-C) The ultrasound maximum intensity projection (MIP) of the depth phantom generated by (a-c) motor with and without the shaking and hand sweeping, respectively. (D-E) The processed MIPs of (B, C), respectively. The processing was performed on the B-mode images and the MIPs were then generated. The Verasonics imaging system was used for data acquisition.

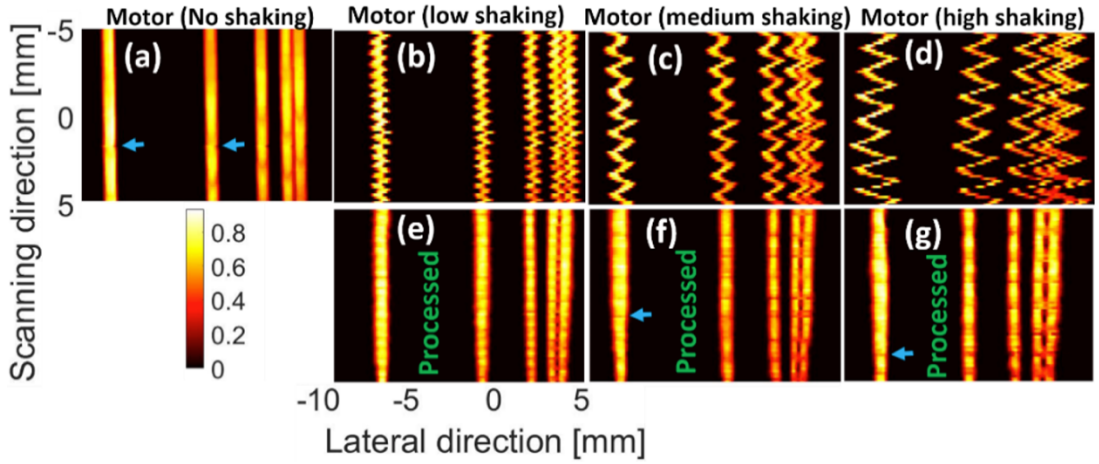

Figure 6. 6. Photoacoustic images of a resolution phantom with shaking.
(A-D) The photoacoustic maximum intensity projection (MIP) of the lateral resolution phantom generated by motor with no, low, medium, and high shaking, respectively. (E-G) The processed MIPs of (b-d), respectively. The processing was performed on the B-mode images and then the MIPs were generated. The LED-based imaging system was used for data acquisition.

The MIPs of the TU experiment are provided in **Figure 6.7** where the shaking reduces the image quality in **Figure 6.7B**, but the deshaken image (**Figure 6.7C**) has a

quality comparable with **Figure 6.7A** where no shaking was applied. **Figure 6.7B** shows that the shaking causes up to 1 mm error in the lateral and scanning directions. The lateral size of some structures (such as what is shown with the blue arrows in **Figure 6.7A** are not even measurable in **Figure 6.7B**. MIND reduces the error to about 0.1 mm and 0.25 mm in the lateral and scanning directions, respectively (compare **Figure 6.7A** and **Figure 6.7C**). **Figure 6.7A** has mild existing distortions (tilting) due to the movement and relative direction of the hand in our experiment: This contributed to the tilting in the processed images in **Figure 6.7B-C**.

6.3.2. Ex vivo swine experiments

The MIPs of the ultrasound images generated by the ex vivo swine experiments are provided in **Figure 6.8**. The effects of motor shaking are visible in **Figure 6.8B-C**. MIND provides better and more accurate structural information (compare the green and red dashed-ovals). **Table 6.1** indicates that SSIM of the processed MIP images are higher than the shaky ones (the mean SSIM for the regions indicated by the green and red dashed circles are presented).

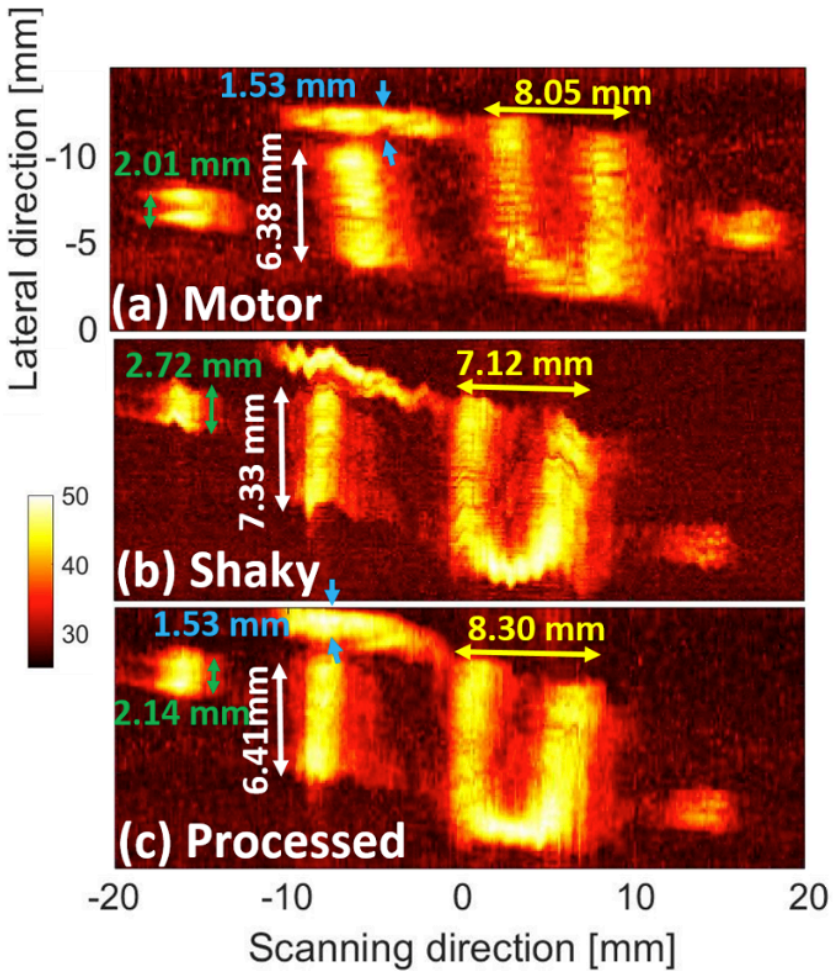

Figure 6. 7. Raw and processed photoacoustic images of marker-printed text on a hand. The photoacoustic maximum intensity projection (MIP) of the TU experiment generated by (a) motor (no shaking), (b) handheld without processing, and (c) handheld with processing. The processing was performed on the B-mode images and then the MIPs were generated. The LED-based imaging system was used for data acquisition.

To better understand the improvements, the sagittal planes of the MIP images (the red dashed line in **Figure 6.8A**) are presented in **Figure 6.9** where the extent of enamel staining is measured by the photoacoustic imaging modality. The gray and red colormaps indicate the ultrasound and photoacoustic images, respectively. The image generated with the motor without shaking (**Figure 6.9A**) was given to the MIND to evaluate the bias of the deshaking method. In the deshaken version (**Figure 6.9A**, second column), the image is

smooth compared to the **Figure 6.9A**, first column. However, the calculus depth is estimated at 4.9 mm in both images, which proves the accuracy of our deshaking method.

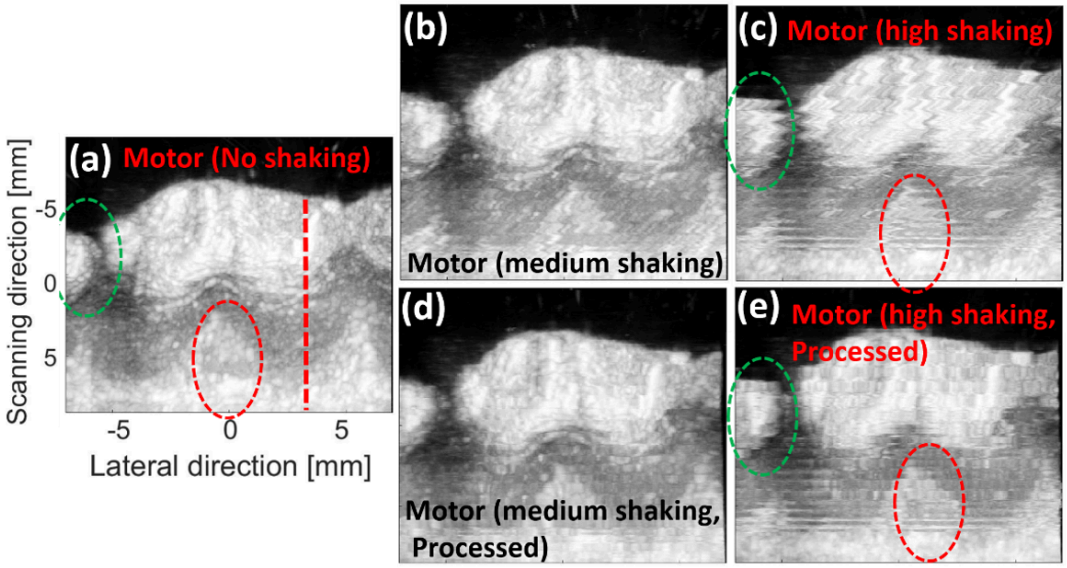

Figure 6. 8. Raw and processed ultrasound images of an ex vivo swine molar.
The ultrasound maximum intensity projection (MIP) of the ex vivo experiments generated by (a-c) motor with no, medium, and high shaking, respectively. (d,e) The processed MIPs of (b,c), respectively. The processing was performed on the B-mode images, and the MIPs were then generated. The Vevo imaging system was used for data acquisition.

For the low-shaking dataset, there is no difference in the calculus depth measured by the two images (see **Figure 6.9B**). In the medium and high shaking levels, the calculus depth is over and under-estimated by about 0.3 mm and 0.5 mm, respectively, but the MIND lowers the measurement error to 0.1 mm. For all levels of shaking, better structural information is obtained with MIND (compare the dotted-boxes in the left and right side of **Figure 6.9**).

Table 6. 1. SSIM measurement for the shaky and processed images with two levels of shaking (presented in Figure 6.8).

	SSIM (%)	
Motion artifact level	Shaky	Processed
Medium	19	50
High	15	47

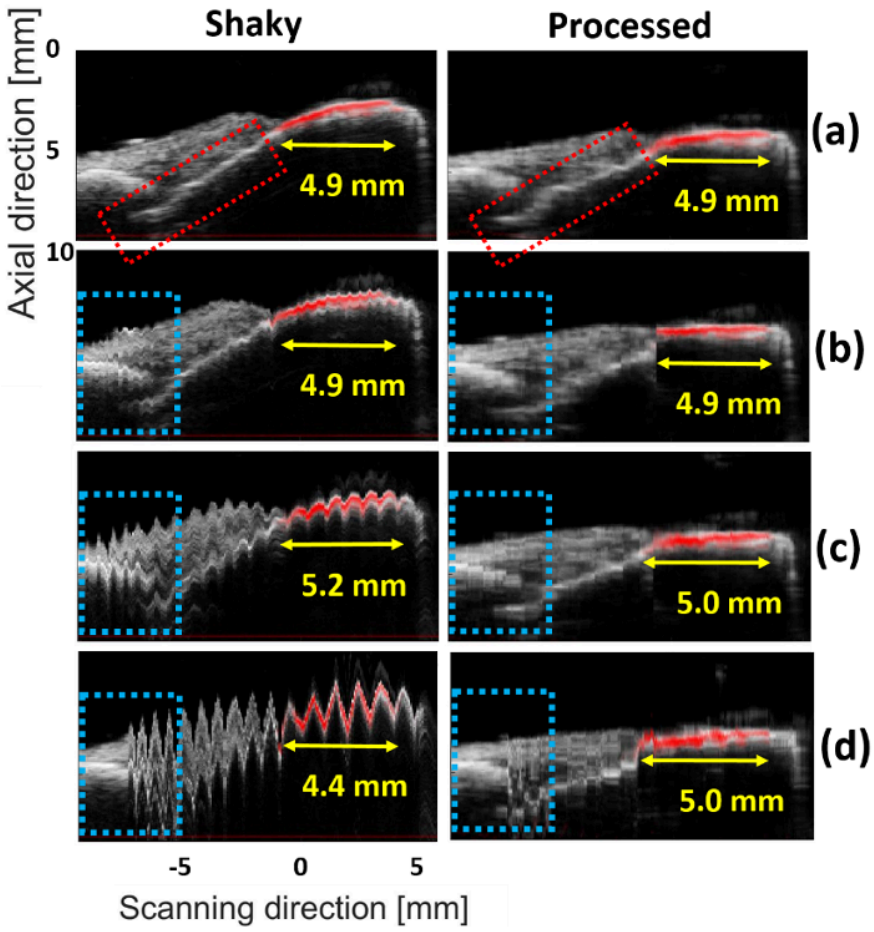

Figure 6. 9. Raw and processed photoacoustic-ultrasound, cross-sectional images of the swine molar with shaking.
The sagittal view of the images generated for the ex vivo experiment: (a) motor with no, low, medium and high shaking, respectively. The right-hand side images show the processed (i.e., deshaken) MIPs. The yellow arrows show the extent of the staining. The blue and red dotted-boxes can be used for comparison of the structural information. The US and PA images are shown in gray and hot colormaps, respectively.

6.3.3. In vivo human experiments

The results obtained for the in vivo experiment are presented in **Figure 6.10**. In **Figure 6.10A**, no intentional motion artifact was applied. However, we expect to see motion artifacts (the dashed boxes in **Figure 6.10A**) due to the movement of the subject (e.g., breathing and minor head movements). These artifacts are addressed in **Figure 6.10B** with MIND (compare the boxes in **Figure 6.10A** and **Figure 6.10B**).

US and PA imaging modalities were used to detect the gingival margin and pocket depth, respectively (**Figure 6.10F** and inset). **Figure 6.10D-E** shows the sagittal cross-section indicated with the blue and green dashed-lines in **Figure 6.10C**, respectively, where the shaking reduces the image quality. **Figure 6.10F-G** shows sagittal cross-section of the processed MIPs where the images are deshaken, and the pocket depth is well estimated in agreement with our prior study [210].

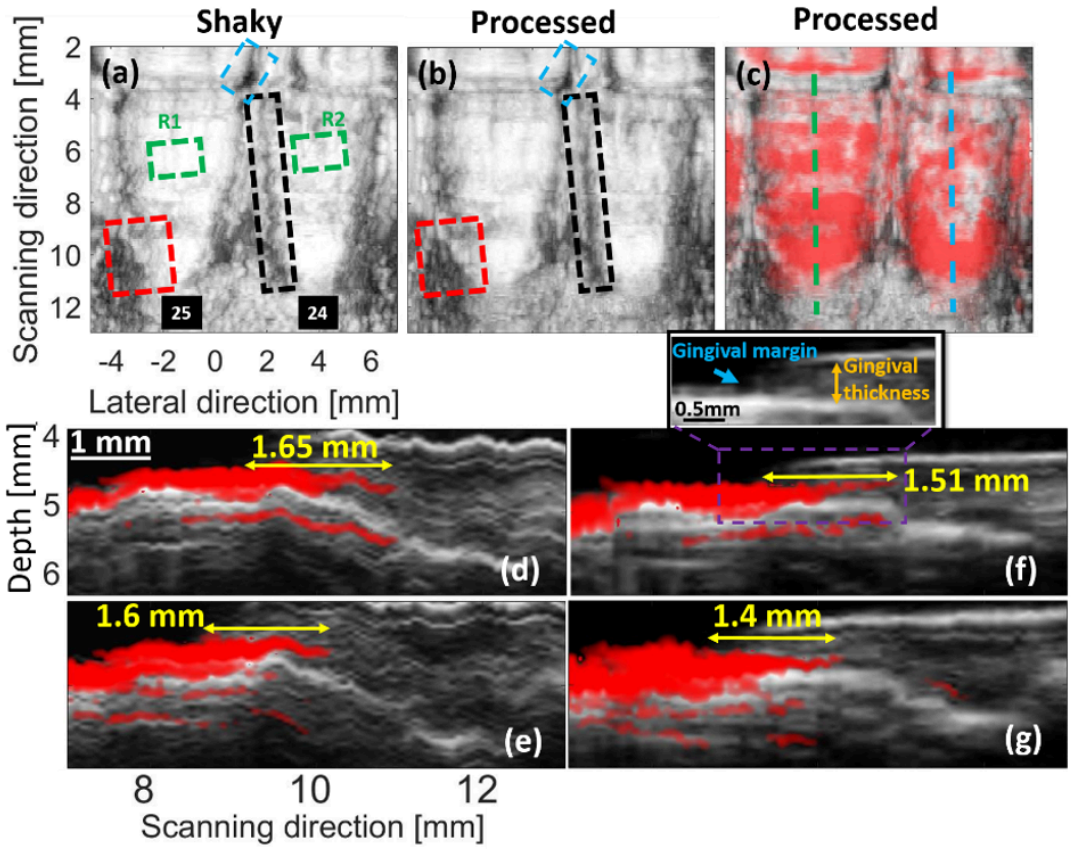

Figure 6. 10. Raw and processed photoacoustic-ultrasound images of human mandibular incisors with shaking.
(a) The MIP generated with multiple shaky US B-mode images. (b) Processed (i.e., deshaken) version of (a). (c) The overlapped processed US-PA MIPs. The sagittal cross section shown with the blue and green dashed-lines in (c) are presented in (d,e) and (f,g), respectively, where (e,g) are the processed version of (d,f), respectively. The blue, black and red dashed-boxes can be used for comparison of the structural information. The green box is used for statistical brightness analysis (R stands for region). The yellow arrows indicate the pocket depth. The US and PA images are shown in gray and hot colormaps, respectively. The Vevo imaging system was used here for data acquisition.

Figure 6.11 shows the statistical brightness analysis conducted on R1 and R2 (**Figure 6.10A**); R, P and S refer to region, processed and shaky, respectively. The mean brightness reduces about 3%, which could be due to displacement of pixels within the regions. The proposed deshaking method does not modify the brightness of pixels and only uses brightness as one of the features to detect similarities.

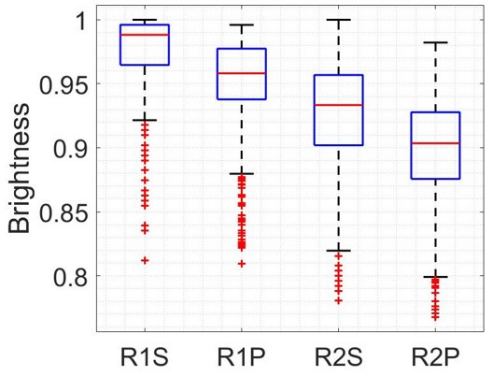

Figure 6. 11. The statistical brightness analysis for R1 and R2 in Figure 6.10
R, P and S refer to region, processed and shaky, respectively. The US images were used for this comparison.

6.4. Discussion

The availability of a noninvasive imaging method to comprehensively profile oral anatomy is potentially of great value for monitoring periodontal health. The feasibility of a dual modality PA-US imaging system to this end was previously presented by our group [210, 358]. In this follow up study, we aimed to improve our imaging system. Different central frequencies will be used for different imaging scales, and the experiments described here were conducted with four probes with different central frequencies (i.e., 10, 20.2 and 40 MHz). Motion artifacts were induced by hand in different levels. An image registration algorithm based on MIND was used to deshake the images and provide more accurate structural information. The images of the depth phantom were deshaken with 80% similarity to the ground truth. The structural errors of about 1 mm were reduced to 0.1 mm and 0.25

mm in the lateral and scanning directions, respectively. Finally, the extent of enamel staining was measured with 0.1 mm error, and the *in vivo* results agreed with our prior study [454].

To deshake the images, the first image is defined as the reference, and image i+1 is registered on the image i. If registering and aligning error occurs between image i and i+1, then it affects all the subsequent steps. For applications with many images to be registered (e.g., our application), this makes the image deshaking very critical. Here, the MIND algorithm was used mainly due to the its simultaneous sensitivity to corners, textures, and edge features as well as its capability to perform deformable registration. Another advantage of this algorithm is that it operates regionally, which increases the processing speed and reduces the incidence of fundamental errors. The direction of the motion artifact does not influence MIND as discussed in [451].

The SSIM calculated for the experiments conducted with Vantage (F0=20.2 MHz) and AcousticX (F0=10 MHz) systems were almost the same (about 80%). This analogy can be used to generalize the error reduction obtained with MIND in AcousticX (0.1 mm and 0.25 mm in the lateral and scanning directions, respectively) to the Vantage system. The measurement error in the Vevo system (F0=40 MHz) was also reduced to 0.1 mm. Therefore, a measurement error of about 0.1 mm can be expected in all the three investigated central frequencies. The performance of the proposed deshaking method might be independent of the central frequency of the probe, but further study is needed to confirm this.

Even though there is no shaking applied in **Figure 6.9A**, MIND smoothens some of the structural variation, especially the region of the calculus depth (PA signal). It is not conclusive whether this is due to the minor internal shaking caused by the step motor or bias from the processing itself. The structures indicated by the red dotted-box are not smoothened

in the second column of **Figure 6.9A**, and we hypothesize that it is due to the minor internal shaking of the step motor. This of course needs further investigation, but if biased, one future direction would be to use machine learning with different, larger datasets to teach MIND to prevent the smoothening of real structural variation. The extent of enamel staining measured in **Figure 6.9A** does not change after applying the MIND, which demonstrates the general preservation of the structural information after deshaking.

The beamformer used for image formation and the contrast of the images along with the signal-to-noise (SNR) affect the performance of deshaking. In our study, a delay-and-sum (DAS) beamformer was used for image formation. More advanced image formation techniques ([454-458]) can be used to improve the contrast of the image and improve the performance of MIND because it locally processes features and sidelobes that might add unrealistic features. Machine learning and deep learning can further improve the performance of the deshaking by providing a better SNR [459, 460]. The number of pixels used in the reconstruction of each image could also affect the performance of the MIND. Our investigation (not presented in this paper) showed that a higher the number of pixels lead to a lower deshaking error.

In the *ex vivo* and *in vivo* experiments, the ultrasound probe was horizontal, and vertical scanning was conducted. To measure the staining, we could perform the imaging with a vertically-held transducer, which would provide an artifact-free sagittal plane of the tooth. However, if a complete profile of the tooth is needed, then image deshaking is necessary to correctly align the sagittal planes and provide an artifact-free image. In our study, the reconstructed B-mode images were used as the input of our deshaking method. This makes our method suitable to be coupled with commercial US/PA imaging systems

without any need for RF data. This is an advantage as RF data is only available in research-based imaging systems, which are expensive to be used in clinics. The proposed motion compensation technique could be used in other applications such as imaging spinal curvatures [461], wound staging [462], carotid imaging [463-465] and generally free-hand imaging systems [466, 467] where the 1D ultrasound probe is used handheld (without any sensor to track the trajectory of the hand) for sweeping the imaging medium and making 3D images.

Care must be taken to set the parameters of the deshaking method properly for different imaging scenarios. The PPD was a key parameter in our application and could be controlled by to the level of applied force to the motor in our study. A higher value of the PPD led to a higher possibility of failure. Our method failed in **Figure 6.3H** mainly due to a large PPD (about 3.9 mm at the central frequency of 10 MHz). Following the fact that the same measurement error of 0.1 mm was obtained in different frequencies (10, 20 and 40 MHz), a PPD of 3.9 mm most probably led to failure in other frequencies as well. Our evaluation showed that the maximum PPD that our deshaking method can handle is 3.6 mm.

One solution to this failure is to increase the search region (parameter R in (2)). However, if a large R is selected, then more complex images such as those presented in the original work [450] might fail due to non-rigid deformation leading to poor image quality. Here, R was equal to 4, but using an R of 48 could still deshake **Figure 6.3H** with a high similarity to the ground truth. Of course, all other results would be different as well.

A larger R also imposes a higher computational complexity. The boundary at which the MIND algorithm fails is not entirely clear and was also not discussed in prior work [450]. However, the clinicians using this approach have fine motor skills and are likely to sweep the probe in a relatively straight trajectory. Thus, the expected tolerance of the hand will be

well within the capacity of the proposed deshaking algorithm to improve the images; this was demonstrated in **Figure 6.3E,I** and **Figure 6.5B,D**.

6.5. Conclusions

In this follow up study, we used an image registration technique to correctly align different B-mode PA-US images and create an artifact-free 2D profile of the tooth and its periodontium. The experimental results obtained with the depth phantom showed that 80% similarity to ground truth could be obtained. An error of about 1 mm in the TU experiment was reduced to 0.1 mm and 0.25 mm in the lateral and scanning directions, respectively. The results of the *ex vivo* experiment showed that the depth of calculus could be measured with 0.1 mm error. The deshaking technique shows potential for clinical collection of motion artifact-free oral PA-US images in both stepper motor and handheld configurations. This reduces the burden of technical skill on the operator and the need for stringent head immobilization.

6.6. Acknowledgements

Chapter 6, in full, is a reprint of the material as it appears in Biomedical Optics Express, vol. 12, 1543-1558, 2021. Mozaffarzadeh, Moein*; Moore, Colman*; Golmoghani, Erfan*; Mantri, Yash; Hariri, Ali; Jorns, Alec; Fu, Lei; Verweij, Martin D.; Orooji, Mahdi; de Jong, Nico; Jokerst, Jesse V. The dissertation author was the co-primary investigator and co-primary author of this paper.

CHAPTER 7. ACTIVATABLE CARBOCYANINE DIMERS FOR PHOTOACOUSTIC AND FLUORESCENT DETECTION OF PROTEASE ACTIVITY

ABSTRACT: Activatable contrast agents are of ongoing research interest because they offer low background and high specificity to the imaging target. Engineered sensitivity to protease activity is particularly desirable because proteases are critical biomarkers in cancer, infectious disease, inflammatory disorders, etc. Herein, we developed and characterized a set of peptide-linked cyanine conjugates for dual modal detection of protease activity via photoacoustic and fluorescence imaging. The peptide-dye conjugates were designed to undergo contact quenching via intramolecular dimerization and contained n dyes (n = 2, 3, or 4) with n – 1 cleavable peptide substrates. The absorption peaks of the conjugates were blue-shifted 50 nm relative to free dye and had quenched fluorescence. This effect was sensitive to solvent polarity and could be reversed by solvent switching from water to dimethyl sulfoxide. Employing trypsin as a model protease, we observed 2.5-fold recovery of the peak absorbance, 330 - 4600-fold fluorescent enhancement, and picomolar detection limits following proteolysis. The dimer probe was further characterized for photoacoustic activation. Proteolysis released single dye-peptide fragments that produced a 5-fold photoacoustic enhancement through increased absorption at 680 nm with nanomolar sensitivity to trypsin. The peptide substrate could also be tuned for protease selectivity; as a proof-of-concept, we detected the main protease (M^{pro}) associated with viral replication in SARS-CoV-2 infection. Lastly, activated probe was imaged subcutaneously in mice and signal was linearly correlated to cleaved probe. Overall, these results demonstrate a tunable scaffold for photoacoustic molecular imaging of protease activity with potential value in areas such as disease monitoring, tumor imaging, intraoperative imaging, in vitro diagnostics, and point-of-care sensing.

7.1. Introduction

Photoacoustic-ultrasound (PA-US) imaging is a fast-growing imaging modality that combines near infrared (NIR) optical excitation with ultrasonic detection [468, 469]. This technique relies on the photoacoustic (PA) effect—the generation of ultrasound waves by an absorbing molecule following optical absorption and thermoelastic expansion [470]. While conventional ultrasound can image anatomical structures in real time, it can only generate contrast from tissue interfaces that differ in their acoustic impedance (i.e., attenuation of the speed of sound). This constraint has motivated the development of ultrasound contrast agents [471, 472] but also highlights a benefit of PA-US: the enhancement of contrast through the dependence of PA signal on optical absorption [473-475]. In vivo, PA contrast is determined by endogenous molecules with high absorption coefficients in the NIR such as melanin, oxy- and deoxyhemoglobin, and lipids [322, 476, 477].

Endogenous PA contrast enables a variety of clinical applications that are under active development [478-480], but the range of imaging applications can be further extended with activatable contrast agents that modulate their optical absorbance [12, 481, 482]. The targets of molecular imaging agents can include cells, nucleic acids, proteins, and other biological molecules; among these, enzymes are particularly attractive due to their critical role in many diseases [483]. Proteases often possess highly specific activity and are implicated in cancer, Alzheimer's disease, cardiovascular diseases, infections, and inflammatory diseases [484, 485]. Matrix metalloproteases, for example, have been widely studied in this area and motivated the cell-penetrating peptide strategy developed by Tsien and coworkers for fluorescence imaging [486]. While fluorescence molecular imaging has proved tremendously valuable, particularly for image-guided surgery/resection and in vitro studies, its poor penetration

depth restricts it to surface-weighted applications. In contrast, PA imaging can achieve deep tissue imaging, though it commonly sacrifices sensitivity relative to fluorescence.

The primary challenge for PA detection of activity is efficient generation of an enzyme-specific PA signal [487]. These probes can take many forms—one general approach that has been explored involves the self-assembly or aggregation of absorbers following enzymatic cleavage [488]. These approaches leverage the macrocyclization of dye molecules or the aggregation of nanomaterials [174, 489-491]. Another strategy is the use of dual-absorber conjugates, e.g., nanoparticle-dye or dye-quencher systems [492-494]. In these designs, two spectrally unique absorbers are linked by a cleavable peptide substrate. These have primarily relied upon one half of the probe retaining at the target site (e.g., intratumoral or intracellular) after proteolysis, while the other half diffuses away. Though powerful, this technique is limited to applications in which the cleaved fragment can quickly and efficiently diffuse out of the imaging plane. One motivation for this work was to develop a simple probe scaffold with activatable PA signal that does not rely upon in vivo clearance of one of the probe components. Some initial efforts in this area validated the difference in photoacoustic lifetime contrast between methylene blue monomers/dimers and proposed an enzyme activatable mechanism [139, 495].

Our work uses cyanine dyes because of their utility in chemical detection [496-500]. These dyes offer high absorption coefficients, tunable fluorescence quantum yields, and long excitation and emission wavelengths. In biological settings, they have exhibited excellent biocompatibility and low toxicity— indocyanine green, a cyanine derivative, has been in clinical use for over 60 years [501]. These favorable properties have driven their integration into a wide variety of chemosensors that can undergo colorimetric and fluorescence changes

for measurement of inorganic ions, pH, small molecules, and biological macromolecules [497, 502-504].

A fundamental property of cyanine dyes is their propensity to aggregate under concentration-dependent conditions in solution [504]. This underpins the well-known formation of H-aggregates and J-aggregates [505]. These molecular assemblies differ according to the relative orientations of the transition dipole moments of their constituent molecules whereby H-aggregates maintain a "side-by-side" orientation and J-aggregates maintain a "head-to-tail" orientation [506]. Spectroscopically, H-aggregates exhibit a hypsochromic shift in their peak absorbance (blue shift) relative to monomeric dye while J-aggregates exhibit a bathochromic shift (red shift) [507]. In addition to the blue shift, H-aggregate dimers undergo complete fluorescent quenching. The quenching is due to rapid internal conversion from the upper to lower exciton singlet state followed by intersystem crossing to the triplet state (radiative transitions from the lower exciton state are formally forbidden) [508]. This characteristic previously informed designs on scaffolds that enabled fluorescent monitoring of protein binding or enzyme activity [509, 510]. However, PA signal is a function of absorbance, and thus our interest here was modulation of the absorbance spectrum following proteolysis. Recently, this property was leveraged in a DNA nanosensor for PA detection of interferon gamma via J-aggregate forming phthalocyanine dyes [511]. In this work, we investigated a set of pentamethine cyanine dye-peptide scaffolds as a platform for PA-based protease activity measurement with tandem fluorescence via proteolytic conversion of H-aggregate dimers to monomers.

7.2. Methods

7.2.1. Reagents

Cy5.5-NHS Ester was purchased from Lumiprobe Inc. (Maryland, USA). Peptides (ArgArgLys, ArgArgLysArgArgLys, ArgArgLysArgArgLysArgArgLys, GlyHisLys, GlyThrSerAlaValLeuGlnSerGlyPheArgLys) were purchased from Genscript Inc. (New Jersey, USA). Pooled human saliva was purchased from Lee Biosolutions (Maryland Heights, MO). Dimethyl sulfoxide, triethylamine, trypsin from porcine pancreas, leupeptin, phosphate buffered saline, sodium chloride, and ammonium bicarbonate were purchased from Sigma-Aldrich (Missouri, USA).

7.2.2. Expression and Purification of M^{pro}

The SARS-CoV-2 M^{pro} plasmid was provided by Rolf Hilgenfeld, University of Lübeck, Germany [512] and transformed into *E.coli* strain BL21-Gold (DE3). Expression and purification of the protein has been described in detail previously [513]. Briefly, cells were lysed by homogenization in 20 mM Tris-HCl, pH 7.8, 150 mM NaCl, 0.25 mM DTT, 5 % glycerol and the lysate was cleared by centrifugation followed by filtration through a 0.45 µM membrane. Soluble M^{pro} was purified by Ni^{2+} chelation chromatography (HisTrap FF, GE Healthcare Life Sciences) and the eluted protein was processed by PreScission protease (GenScript) to remove C-terminal His-tag. M^{pro} was separated from the PreScission protease and His-tag using GSTrap FF and HisTrap FF column (GE Healthcare Life Sciences). Active fractions from the flow-through were pooled and stored at -80°C in 20 mM Tris-HCl, pH 8.0, 150 mM NaCl, 1 mM DTT, 5 % glycerol.

7.2.3. Synthesis Of Dye-Peptide Conjugates

Dye-peptide conjugates were synthesized via the amide linkage of succinimidyl ester (NHS)-activated dyes with the primary amines of peptides at an equimolar ratio of dye: amine. For a representative reaction, RRK (0.4 mg, 0.87 μmol) was mixed with Cy5.5-NHS (1.3 mg, 1.74 μmol) in anhydrous DMSO (200 μL) with a 1.5-fold molar excess of triethylamine (TEA, 1.30 μmol). Reactions were stirred in the dark at 300 rpm for 12 h at 30°C. The reaction mixture was dried under vacuum centrifugation using a Vacufuge Plus (Eppendorf, Hamburg) at 60 °C for 2 – 3 h.

7.2.4. Purification

Crude reaction pellets were resuspended in MeCN/H_2O (50:50 v/v) and purified via analytical RP-HPLC with a Shimadzu LC-40 on a Shim-pack GIS C18 column (5 μm). Crude reaction mixtures were separated with a 50% to 95% B gradient (A: H_2O (0.05% TFA), B: MeCN (0.05% TFA) over 45 min. Fractions were collected and diluted to 90% (v/v) MeOH before analysis with ESI-MS in positive mode (centroid scan) on a Micromass Quattro Ultima Triple Quadrupole mass spectrometer. Products were concentrated via vacuum centrifugation or lyophilization and stored in the dark.

7.2.5. Absorbance and Fluorescence Spectroscopy

Absorbance and fluorescence spectra were measured with a BioTek Synergy H1 plate reader. Samples were measured at 100-μL scale in 96-well plates. Unless otherwise noted, absorbance scans were collected from 500 – 850 nm and fluorescence emission scans were collected with an excitation wavelength of 600 nm and an emission range of 660 – 860 nm in 2-nm increments.

7.2.6. Nuclear magnetic resonance spectroscopy

Dry compound was dissolved in deuterated solvent and ^{1}H-NMR spectra were collected in mixtures of D_2O/DMSO-d_6 with a 300-MHz Bruker spectrometer. Solvent mixtures were varied by drying the compound between scans and then resuspending with different D_2O/DMSO-d_6 ratios.

7.2.7. Photoacoustic imaging

Photoacoustic images of in vitro samples were acquired with a Vevo 2100 LAZR (VisualSonics) using a 21-MHz transducer (LZ-250). Samples (20 μL) were loaded into individual 0.86 mm polyethylene tubes and fixed in parallel within a 3D-printed holder 1 cm below the transducer in a vessel filled with water [234]. Single wavelength scans were operated at 680 nm with a repetition rate of 20 Hz (pulse width = 4-6 ns, ~45 mJ/pulse at source) [514]. To generate 3D images, the transducer was scanned with a stepper motor (step size = 0.054 mm) along the axial dimension of the tubes and B-mode frames were registered via maximum intensity projection. Photoacoustic spectra were measured from 680 nm to 900 nm (2-nm step size). Whole human blood was collected in citrate tubes from a healthy male donor according to institutional guidelines. All animal experiments were performed in accordance with NIH guidelines approved by the Institutional Animal Care and Use Committee (IACUC) under protocol S15050 at the University of California, San Diego. Nude mice (NU/J) were anesthetized with isoflurane and injected subcutaneously with 100 μL of probe or buffer in 50% (v/v) Matrigel. Mice were imaged with a 40-MHz photoacoustic/ultrasound transducer (LZ-550).

7.3. Results and discussion

7.3.1. Synthesis of dye-peptide conjugates

The goal of this study was to synthesize and optically characterize a set of peptide-dye conjugates for their utility in photoacoustic detection of proteolysis (**Figure 7.1A**). The ideal molecular scaffold could be generalizable and repurposed to a variety of target proteases by tuning its cleavable sequence. Here, we studied the utility of carbocyanine dimers formed via forced proximity with peptide linkers and assayed using the representative protease trypsin. Peptide-dye conjugates were synthesized via the reaction of succinimidyl ester activated dyes with the N-terminal primary amines and C-terminal lysine side chains of the peptides reported herein (**Figure 7.8**, **7.9**). The primary scaffold we studied was $[Cy5.5]_2[RRK]_1$; Cy5.5 was chosen for its absorbance in the NIR and arginine residues were included for recognition and cleavage by trypsin, a readily available and well-understood protease.

Our utilization of a tripeptide linker stemmed from two design goals: (1) maximizing the likelihood of contact quenching between the dyes, and (2) minimizing the likelihood of non-specific cleavage by off-target proteases. Though RRK can be cleaved at its first or second peptide bond, both cleavage sites were included to mitigate against the possibility of steric hindrance by the dyes. These conjugates were purified with RP-HPLC (**Figure 7.1B**) and validated with electrospray ionization mass spectrometry (ESI-MS) (**Figure 7.1C**). In order to explore the effect of multiple cleavage sites and dye molecules, we also synthesized conjugates with multiple dye-peptide subunits, i.e., a dye trimer, $[Cy5.5]_3[RRK]_2$, and a dye tetramer, $[Cy5.5]_4[RRK]_3$. The column retention times of these conjugates increased with the addition of peptide-dye subunits: 10.1 min, 10.3 min, and 10.8 min for $[Cy5.5]_2[RRK]_1$,

$[Cy5.5]_3[RRK]_2$, and $[Cy5.5]_4[RRK]_3$, respectively. We also synthesized $[Cy5.5]_2[GHK]_1$ as a negative-control probe for trypsin proteolysis.

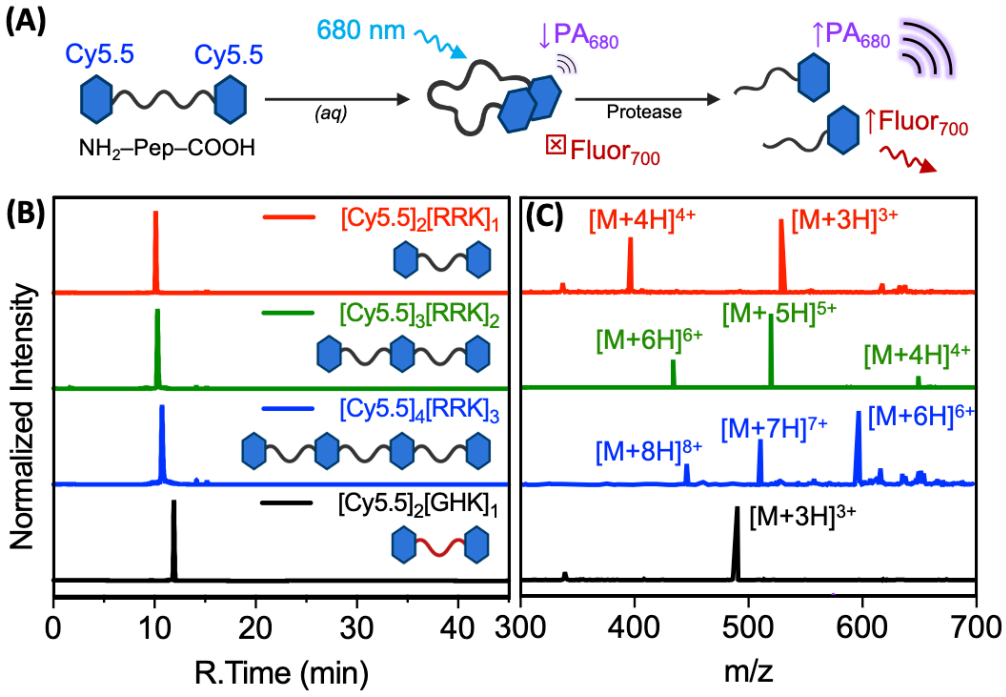

Figure 7.1. RP-HPLC and ESI-MS of protease-responsive cyanine-peptide conjugates. (**A**) Schematic of probe design. (**B**) Liquid chromatograms of purified $[Cy5.5]_2[RRK]_1$ (96.7%), $[Cy5.5]_3[RRK]_2$ (91.5%), $[Cy5.5]_4[RRK]_3$ (96.5%), and $[Cy5.5]_2[GHK]_1$ (97.2%) monitored via HPLC. The retention times were 10.1 min, 10.3 min, 10.8 min, 11.9 min, and 12.7 min, respectively. Samples were dissolved in 25% acetonitrile and eluted at 1 mL/min with a 25 min gradient from 25% to 95% B (A: water (0.05% TFA), B: acetonitrile (0.05% TFA)). The gradient was held at 95% B for 10 min and reduced to 25% B over the next 10 min (total time: 45 min). (**C**) ESI-MS of the respective conjugates. $[Cy5.5]_2[RRK]_1$ expected $[M+4H]^{4+}$: 398.0, detected: 398.1, expected $[M+3H]^{3+}$: 530.3, detected: 530.5 (**Figure 7. S2**). $[Cy5.5]_3[RRK]_2$ expected $[M+6H]^{6+}$: 433.1, detected: 433.3, expected $[M+5H]^{5+}$: 519.5, detected: 519.8, expected $[M+4H]^{4+}$: 649.1, detected: 649.5 (**Figure 7. S3**). $[Cy5.5]_4[RRK]_3$ expected $[M+8H]^{8+}$: 450.8, detected: 450.9, expected $[M+7H]^{7+}$: 515.0, detected: 515.2, expected $[M+6H]^{6+}$: 600.7, detected: 600.9 (**Figure 7. S4**). $[Cy5.5]_2[GHK]_1$ expected $[M+3H]^{3+}$: 490.9, detected: 490.9 (**Figure 7. S5**).

7.3.2. Solvatochromic Properties of Conjugates

It is well known that cyanine dyes in aqueous solution exhibit intermolecular interactions observable as shifts in their peak absorbance wavelength (λ_{max}). Here, we used peptide linkers to facilitate these dimerizing interactions intramolecularly, i.e., between two or more dye structures within a single conjugate (e.g., the covalent dimer, $[Cy5.5]_2[RRK]_1$).

We also synthesized $[Cy5.5]_3[RRK]_2$ and $[Cy5.5]_4[RRK]_3$ conjugates, which are referred throughout as trimers and tetramers, respectively.

In order to assess optical differences in these molecules, we first suspended them in DMSO to solubilize the dyes, favoring the monomeric state, and titrated their concentrations to an equivalent λ_{max}. One might expect solubilization of these molecules in DMSO to fully neutralize the dye-dye interactions. However, the absorbance spectra of these molecules revealed a minor increase in the ratio of OD_{640}/OD_{686} relative to free dye (**Figure 7.2A**), and this ratio increased with respect to the number of dye moieties. This trend corresponded to increased fluorescence quenching (**Figure 7.2B**). However, the absorbance shift and fluorescence quenching were significantly more prominent when the conjugates were suspended in water (1% DMSO, **Figure 7.2C-D**). The λ_{max} shifted from 676 nm for free dye to 624 nm for $[Cy5.5]_2[RRK]_1$, 616 nm for $[Cy5.5]_3[RRK]_2$, and 612 nm for $[Cy5.5]_4[RRK]_3$ (**Figure 7.2C**). These shifts were accompanied by intensity reductions of the hypsochromic peak and peak broadening with increasing dye units; the total area under the curve remained relatively constant (< 1% RSD). Significant changes in absorption at the monomeric peak (676 nm) were not observed between the three conjugates. Fluorescence quenching efficiencies (QE) of the molecules in water relative to DMSO were greater than 98% for $[Cy5.5]_2[RRK]_1$, $[Cy5.5]_3[RRK]_2$, and $[Cy5.5]_4[RRK]_3$ (**Figure 7.2D**). When compared to the free dye QE (69.5%), which is due to aggregation-associated intermolecular quenching, these values reveal the significant effect of intramolecular quenching. We confirmed the role of π–π stacking and hydrophobic effects in the absorbance peak shift and fluorescence quenching for $[Cy5.5]_2[RRK]_1$ by monitoring the upfield shift of its aromatic hydrogens after water addition via ^{1}H-NMR (**Figure 7.14**) [515, 516].

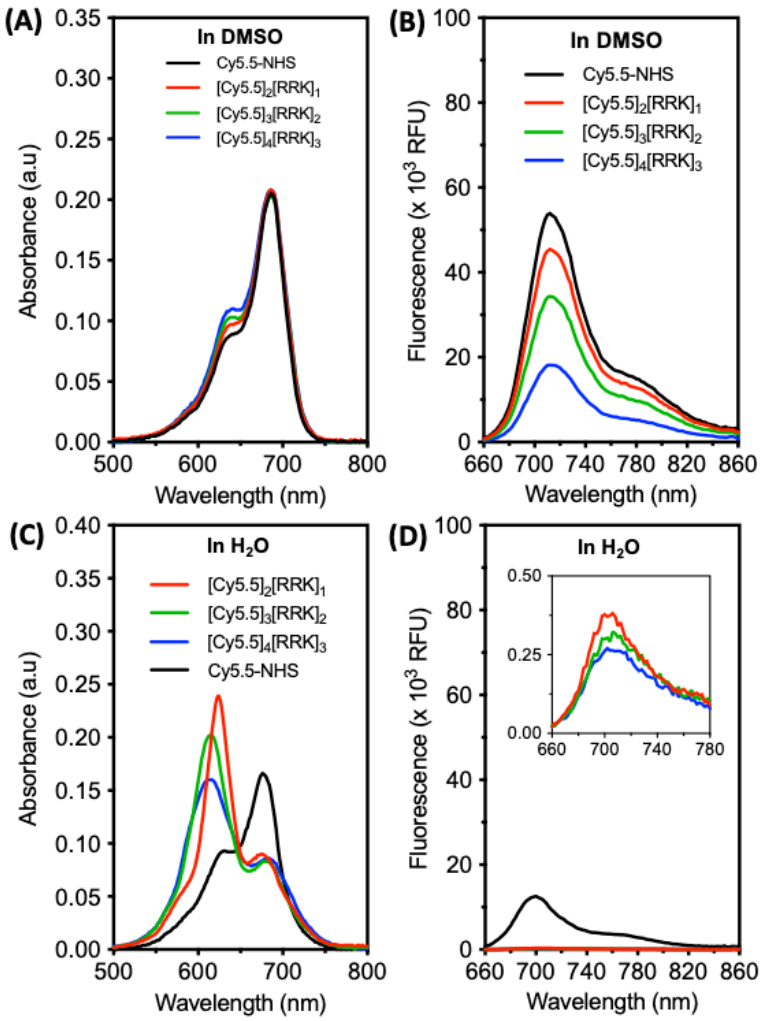

Figure 7.2. Absorbance and fluorescence spectra of cyanine-peptide conjugates are modulated by the self-association of their dye moieties.
(**A**) Absorbance spectra of free dye, dimer, trimer, and tetramer conjugates after suspension in DMSO at an equimolar concentration of dye moieties. This was done by titrating each solution to an equivalent λ_{max} corresponding to the absorbance maximum of Cy5.5-NHS ($OD_{686} = 0.21$). (**B**) The emission spectra in DMSO revealed a decrease in fluorescence from dimer to trimer to tetramer, indicating more persistent $\pi - \pi$ interactions in the higher-order species (ex: 600 nm, em: 660 – 860 nm). (**C**) Absorbance spectra of the conjugates diluted to the same concentrations in water (1% v/v, DMSO/H_2O) reveal significant blue shifts in each case and peak broadening for the trimers and tetramers. (**D**) The emission spectra in water show > 98% fluorescence quenching for all conjugates (inset: magnification reveals minor relative differences in quenching efficiencies).

7.3.3. Absorbance and Fluorescence-Based Activity Measurements

The absorbance spectra of probes at equimolar concentrations were monitored before and after addition of trypsin in ammonium bicarbonate buffer. In buffer, charge screening

induced by the higher ionic strength favors dye aggregation and reduces the intensity of absorption peaks observed in **Figure 7. 3A**. Nevertheless, the area under the curve (AUC) of the probes increased from dimer to trimer to tetramer indicative of increasing dye content across the three conjugates. The ability for trypsin to cleave these probes was first confirmed for $[Cy5.5]_2[RRK]_1$ using HPLC and ESI-MS (**Figure 7.15**). The intact probe eluted at 9 minutes; after incubation with trypsin, new peaks were observed at 6.5 min, 6.9 min, 8.2 min, and 8.3 min. The latter two peaks were collected as a single fraction, and it contained Cy5.5-R measured via ESI-MS. The 6.9-min fraction contained RK-Cy5.5. A non-cleavable sequence was used to synthesize the control probe, $[Cy5.5]_2[GHK]_1$, which did not exhibit trypsin-catalyzed activation (**Figure 7.16**). This confirmed the specificity of the synthesized probes.

After proteolysis, the monomeric spectroscopic peak shape of the probes was regained with relatively similar ΔOD_{676} values between pre- and post-cleaved conjugates of 2.46, 2.64, and 2.51 for the dimer, trimer, and tetramer, respectively (**Figure 7.3B**). Prior to proteolysis, fluorescence intensities at 700 nm were 92, 14, and 9 RFU for dimer, trimer, and tetramer (**Figure 7.3C**). These increased 332-fold, 2436-fold, and 4652-fold, respectively, after 30 min incubation in 5 μM trypsin (**Figure 7.3D**). It is interesting to note that fluorescence contrast increased with higher dye content, but ΔOD_{676} remained relatively constant between probes. For spectral comparison, the absorbance and fluorescence of free dye (Cy5.5-NHS) were also measured. It is clear that the free dye does not enhance absorbance or fluorescence after incubation with trypsin. Instead, we observed some broadening of the absorbance and reduction in fluorescence over the measurement period due to hydrolysis of activated dye, contributing to self-association of the dye monomers and

gradual precipitation (leading to contact quenching). There is also a possibility that some activated dye bound to exposed lysine residues on trypsin. Nevertheless, we conclude that the observed optical enhancements of the probes (red-shifting and turn-on fluorescence) were not caused by nonspecific interaction of the dyes with trypsin. This is further supported by the lack of red-shifting and fluorescence for the non-cleavable $[Cy5.5]_2[GHK]_1$ control probe upon incubation with trypsin (**Figure 7.17**).

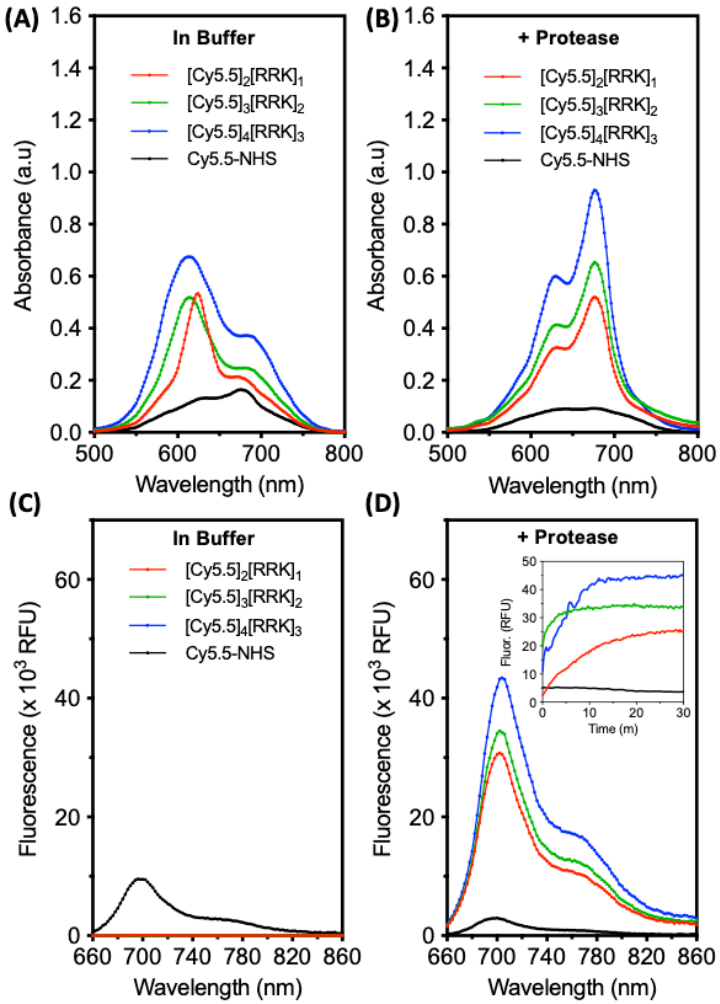

Figure 7.3. Proteolysis of cyanine-peptide conjugates in buffer induces a red shift and fluorescent activation.
(A) Absorbance spectra of free dye, dimer, trimer, and tetramer conjugates at 7 µM in buffer (10 mM NH_4HCO_3, 1% DMSO, pH 8.0). **(B)** Absorbance spectra of the molecules after incubation with 5 µM trypsin (30 min, 37° C). **(C)** Fluorescence spectra of the molecules in buffer (ex: 600 nm); inset: kinetic monitoring of fluorescence after addition of 5 µM trypsin. **(D)** Florescence spectra after 30-min incubation with trypsin. Inset: fluorescence activation from 0 – 30 min.

7.3.4. Fluorescence Sensitivity and Kinetics

According to fluorescence kinetics, $[Cy5.5]_2[RRK]_1$ exhibited maximum activity at approximately 7 μM (**Figure 7.4A**). Initial rate decreased at higher concentrations, likely due to decreasing solubility at these values. The concentrations for peak activity were slightly lower for the trimer and tetramer, though rate appeared to increase proportionally to the number of peptide-dye subunits (**Figure 7.4A**). The increase in signal magnitude was logical since the trimer and tetramer have 1.5 times and 2 times more dye content than dimer.

We also calculated and compared the fluorescent limits of detection (LOD) for trypsin of the three conjugates at equimolar probe concentration (**Figure 7.4B**). Representative spectral titrations are included for $[Cy5.5]_2[RRK]_1$ (**Figure 7.17A**), $[Cy5.5]_3[RRK]_2$ (**Figure 7.17B**), and $[Cy5.5]_4[RRK]_3$ (**Figure 7.17C**). The LODs were calculated based on the linear ranges from 0.05 – 158 nM ($R^2 = 0.9297$) for $[Cy5.5]_2[RRK]_1$, 0.0005 – 3.9 nM ($R^2 = 0.9210$) for $[Cy5.5]_3[RRK]_2$, and 23 – 834 nM ($R^2 = 0.9929$) for $[Cy5.5]_4[RRK]_3$ according to the method described by Armbruster et al [517]. The LODs were 1.2 nM, 51 pM, and 43 nM, respectively. By comparison, the best fluorescent LODs reported for trypsin probes are in the low picomolar range [518].

One possible explanation for the differences in sensitivity is the fact that addition of [RRK][Cy5.5] subunits increases the total charge (z) of the molecule increasing its affinity for the negatively charged catalytic pocket. However, it also decreases the solubility as evidenced by the longer LC retention times (**Figure 7.1B**). The increased affinity hypothesis is supported by comparison of the initial rates of activation for each probe (**Figure 7.4A**). Indeed, the average rate of product formation increased from dimer (z = +4) to trimer (z = +7) to tetramer (z = +10). Due to the higher rate of ES formation (k_f), it would be reasonable

for $[Cy5.5]_3[RRK]_2$ to have a lower LOD than $[Cy5.5]_2[RRK]_1$. However, increasing the charge further (z = +10 for $[Cy5.5]_4[RRK]_3$) proved to be detrimental to the sensitivity of the probe to low trypsin concentrations.

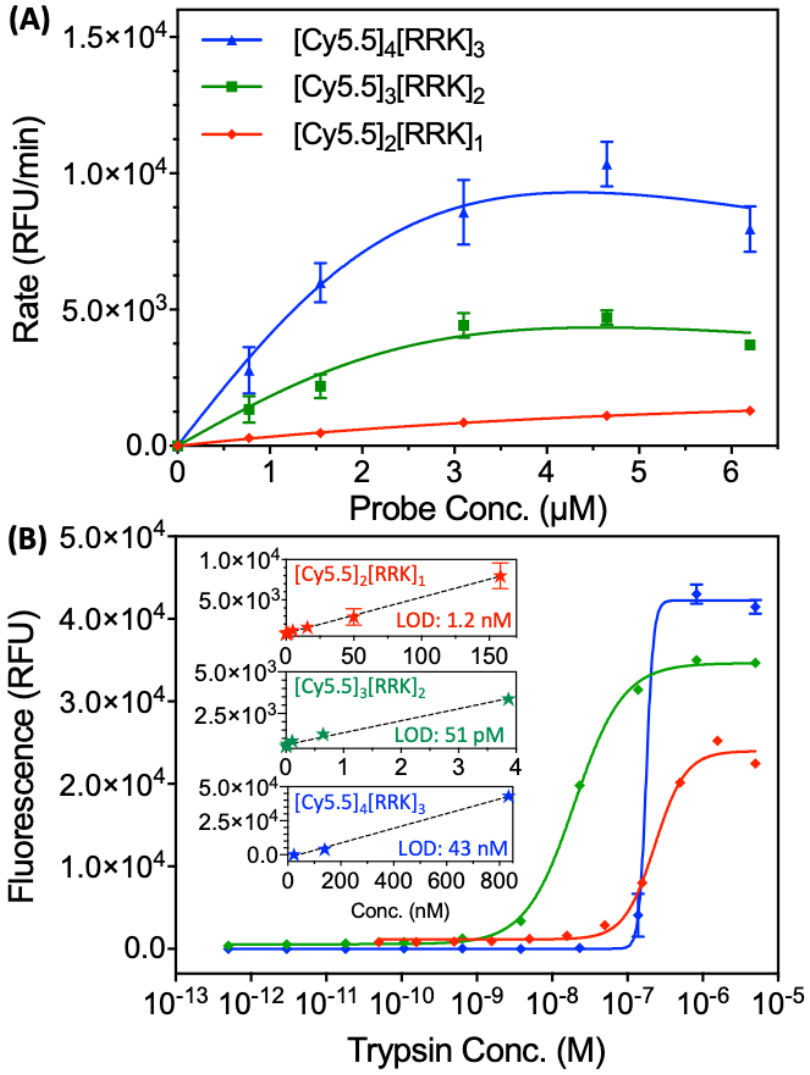

Figure 7.4. Kinetic measurements and fluorescent limits of detection for [Cy5.5]2[RRK]1, [Cy5.5]3[RRK]2, and [Cy5.5]4[RRK]3.
(A) Probe concentration versus initial rate for $[Cy5.5]_2[RRK]_1$, $[Cy5.5]_3[RRK]_2$, and $[Cy5.5]_4[RRK]_3$ with 5 μM trypsin (ex: 600, em: 700). Higher concentrations were not included due to low aqueous solubility of the $[Cy5.5]_3[RRK]_2$ and $[Cy5.5]_4[RRK]_3$ probes at these values. Measurements were performed in triplicate (error bars = standard error of the mean). (**B**) Fluorescent limits of detection for all probes at 7 μM incubated with a trypsin gradient in 10 mM NH_4HCO_3 and 1% DMSO for 1 h at 37 ° C (ex: 600 nm). LODs were calculated to be 1.2 nM for $[Cy5.5]_2[RRK]_1$, 51 pM for $[Cy5.5]_3[RRK]_2$, and 43 nM for $[Cy5.5]_4[RRK]3$. Insets show the linear regions used to calculate LODs. Measurements were performed in triplicate (error bars = standard deviation).

For this bulky and highly charged probe, unfavorable steric or electrostatic interactions with enzyme residues adjacent to the active site could potentially increase $k_r > k_{cat}$. Another possibility is that the lower solubility of the tetramer led to gradual aggregation and reduction of the number of accessible cleavage sites as the probe incubated, causing poor sensitivity to low concentrations of trypsin. Nevertheless, at protease concentrations well above the LOD, the rate of probe activation was proportional to the number of peptide-dye subunits. Kinetic constants for the probes were not extracted due to low aqueous solubilities at higher concentrations.

7.3.5. Photoacoustic characterization of conjugates

A range of probe concentrations were incubated with equimolar trypsin to determine the minimum probe concentration required for imaging, i.e., that would maximize the PA signal to background ratio (SBR) (**Figure 7.18, Figure 7.5**). Concentrations between 1 – 4.5 μM were insufficient for strong contrast between cleaved and uncleaved probe because noise-free PA images could not be collected (**Figure 7.18**). Cleaved probe at 1.12 and 2.25 μM showed no significant difference in PA intensity and 4.50 μM had low contrast. However, concentrations between 6.75 – 11.25 μM had significant contrast and were therefore suitable for PA imaging (**Figure 7.5E-F**). Of note, the fold-differences quantitated in **Figure 7.5F** are underestimated because white pixels in **Figure 7.5E** are saturated pixels.

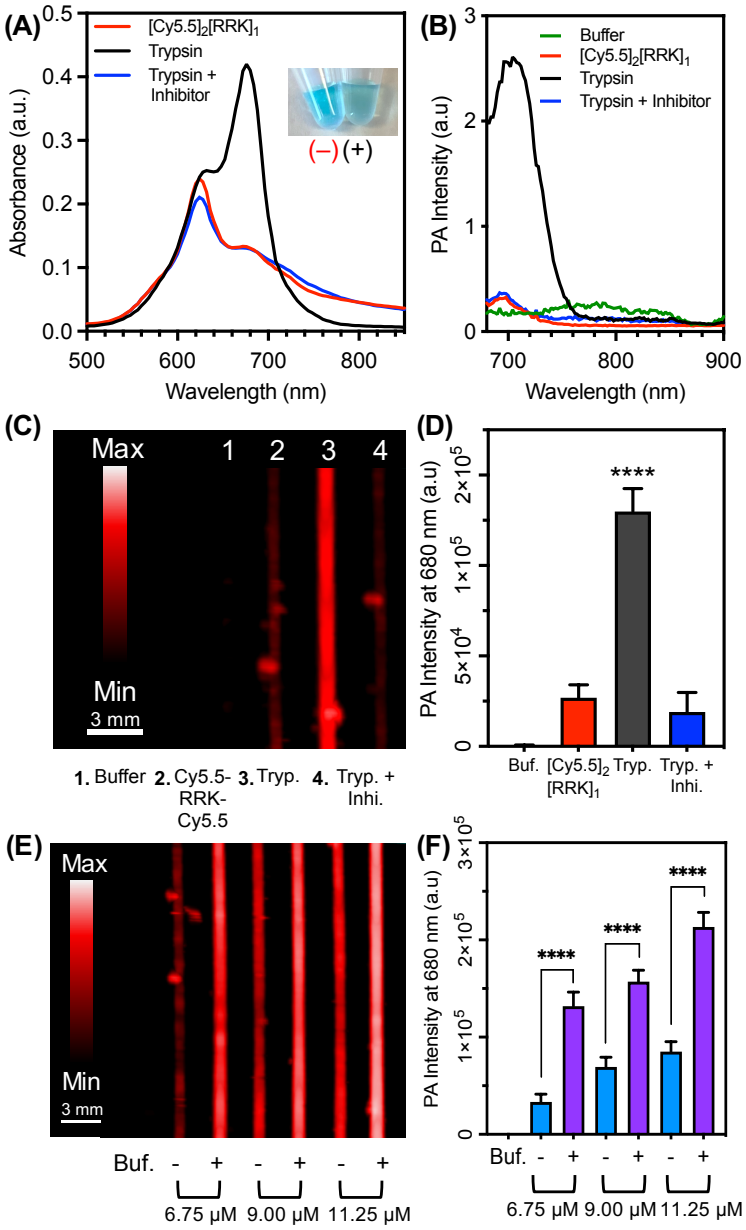

Figure 7.5. Photoacoustic imaging of protease-dependent $[Cy5.5]_2[RRK]_1$ activation.
(**A**) Absorbance spectra of $[Cy5.5]_2[RRK]_1$ (7 µM) with trypsin (5 µM) and trypsin/inhibitor (50 µM leupeptin) after 1 h incubation in 100 mM NH_5CO_3 (1% DMSO) at 37 ° C. Photographic inset shows probe before (-) and after (+) cleavage by trypsin. The color dims due to the increased contribution of longer wavelength absorption. (**B**) Photoacoustic spectra of the same samples, showing signal activation only in the probe + trypsin sample. Units of photoacoustic intensity are arbitrary. (**C**) Photoacoustic image of the samples at 680 nm. (**D**) Quantitation of (C) via integrated pixel density. Asterisks denote significant difference between $[Cy5.5]_2[RRK]_1$ and trypsin and trypsin with inhibitor (unpaired t-test, p-value < 0.0001, n = 8 regions of interest, error bars = SD). (**E**) Photoacoustic image of $[Cy5.5]_2[RRK]_1$ at three concentrations before (-) and after (+) incubation with trypsin. (**F**) Quantitation of (E) via integrated pixel intensity. Asterisks denote significant difference (unpaired t-test, p-value < 0.0001, n = 8 regions of interest, error bars = SD).

The specificity of the probe was verified by further examining the absorbance and fluorescence in parallel to photoacoustics with trypsin alone and trypsin inhibited by the small molecule, leupeptin (**Figure 7.5**) [519]. Following cleavage by trypsin, the probe increased absorbance at 680 nm leading to a noticeable color change (**Figure 7.5A**) and activation of fluorescence (**Figure 7.19**). The PA spectrum followed a similar trend as the absorbance (**Figure 7.5B**); this correlation is generally predicted from the principle that PA signal intensity of a molecule is determined by the amount of light it absorbs. Indeed, validation of this hypothesis for a peptide linked cyanine dye pair was a primary goal of this investigation. Single-wavelength PA scans at 680 nm showed significant contrast between inactivated and cleaved probe (**Figure 7.5C**). The signal enhancement between these two species was about 5-fold (**Figure 7.5D**). Additionally, mixtures of probe, trypsin, and inhibitor did not lead to photoacoustic activation. The photoacoustic sensitivity of $[Cy5.5]_2[RRK]_1$ to enzyme was lower than its fluorescence and absorbance-based sensitivity (**Figure 7.20**). The absorbance spectra for the probe with 0 - 5 μM trypsin revealed an increase in the ratio of OD_{680}/OD_{624} at increasing protease concentration (**Figure 7.20A**), with distinct intensities. Fluorescent activation at 700 nm showed a similar trend (**Figure 7.20B**). Photoacoustic imaging at 680 nm was unable to resolve the difference between 0 and 40 nM enzyme after 1 h, however, the higher tested concentrations were readily detectable (**Figure 7.20C-D**). Overall, this difference in sensitivity was not surprising, as PA imaging commonly involves a trade-off between sensitivity and the ability to perform real-time imaging with high penetration depths.

To validate the tunability of the probe scaffold for other protease targets, we synthesized a variation of the homodimer by exchanging the RRK peptide to

GTSAVLQSGFRK (**Figure 7.21**). The peptide sequence AVLQSGFR is a previously reported substrate for cleavage at Q/S by the main protease (M^{pro}, or $3CL^{pro}$) involved in the replication of SARS-CoV-2 during viral infection[512, 520]. This has motivated the development of both inhibitors and other sensors targeting M^{pro} [521]. After synthesis and purification of the probe $[Cy5.5]_2[GTSAVLQSGFRK]_1$, we used HPLC and ESI-MS to validate the cleavage of the probe with recombinant M^{pro} and observed the expected fragments (Cy5.5-GTSAVLQ and SGFRK-Cy5.5) after incubation of the probe with 100 nM M^{pro} for 1 hour (**Figure 7.21A-B**). We measured an approximate K_m of 3.5 μM (**Figure 7.6A**) via fluorescence and used this probe concentration for titration with M^{pro} (0 – 200 nM). Similar enhancements of absorbance, fluorescence, and photoacoustic intensity were observed (**Figure 7.6B-F**) as with $[Cy5.5]_2[RRK]_1$ and trypsin. We detected a lower limit of 50 nM M^{pro} in buffer with photoacoustics. Aside from the difference in the amino acids used, the major difference was the length of peptide linker (12 vs. 3 residues). We attribute the retained activity to the flexibility of the peptide backbone enabling intramolecular dimerization to occur even with a longer linker. To the best of our knowledge, this is the first demonstration of a PA sensor for a SARS-CoV-2 biomarker. Nevertheless, more work is required to demonstrate its value in preclinical models of disease or clinical samples.

One challenge for the signal-to-background ratio (SBR) of the probe is the presence of exogeneous absorbers such as hemoglobin. While we do not envision this probe design for applications involving intravenous delivery, we measured the PA intensity of the molecule (30 μM) in 25% and 50% whole blood and found that the signal was enhanced relative to blood alone (**Figure 7.22A-C**). We also observed that blood improves the photostability of the probes, which normally have a photoacoustic half-life of only a few

minutes due to the photobleaching of the carbocyanine dyes (**Figure 7.22D**). Unfortunately, cleaved probe was not readily distinguished from uncleaved in solution with 25 and 50% blood. We attribute this difficulty to the significant absorption of hemoglobin, which has a concentration of ~15 g/dL in whole blood [522]. In human tissue, the average concentration of hemoglobin is actually much lower, ranging from ~0.18 g/dL in healthy tissue to ~0.58 g/dL in cancerous tissue [523]. Alternatively, there may be background activation in blood for the "uncleaved" samples. Follow-up work will explore the efficacy of the probe design in such conditions.

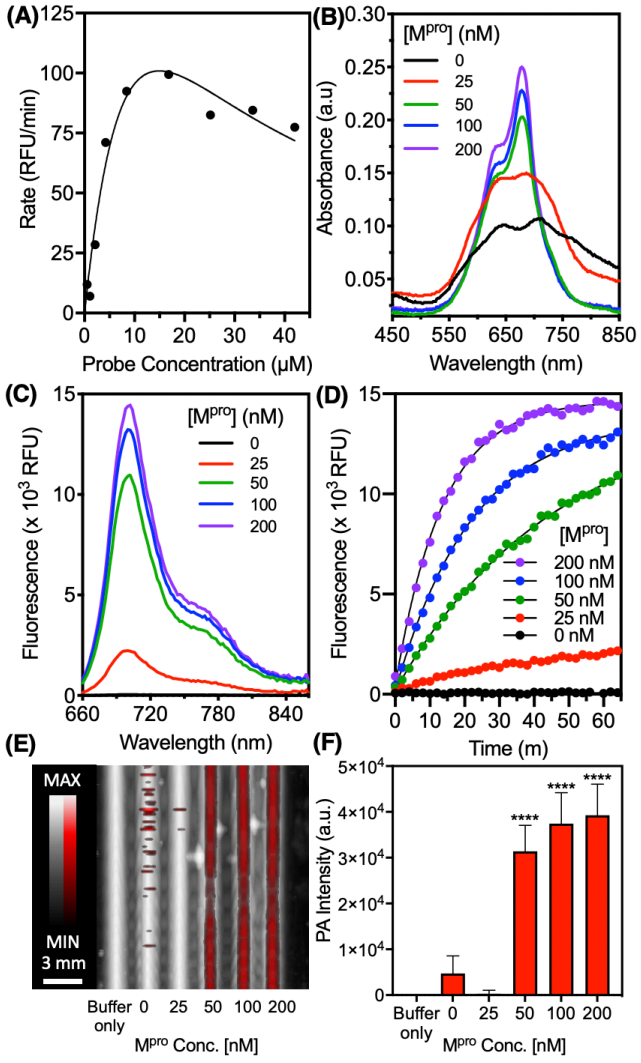

Figure 7.6. Optical and photoacoustic properties of M^{pro}-responsive probe [Cy5.5]$_2$[GTSAVLQSGFRK]$_1$.
(A) Concentration dependent probe activity. The probe was incubated at different concentrations with 50 nM M^{pro} (20 mM Tris, 150 mM NaCl, pH 8.0) at 37° C and the initial rate of fluorescent activation was recorded. (**B**) The probe (3.5 μM) was incubated with increasing concentrations of M^{pro} and the absorbance spectra were recorded after 1 h, showing enhancement at 680 nm. (**C**) Fluorescence spectra after 1 h and (**D**) fluorescence kinetics were recorded (ex: 600 nm, em: 700 nm). (**E**) Dual photoacoustic-ultrasound image of the samples excited at 680 nm. Photoacoustic signal (red) is overlaid on ultrasound (white). (**F**) Quantitation of Panel E via raw integrated density of photoacoustic signal (n = 8 regions of interest, error bars = SD, asterisks denote significant difference from probe-only (unpaired t-test, $p < 0.05$).

Activatable imaging was achieved in saliva (**Figure 7.23**)—a biofluid that contains numerous proteases associated with oral disease. For example, gingipains are a class of trypsin-like protease expressed by the periodontal pathogen *P. gingivalis* and have been

found in the gingival sulcus at micromolar concentrations [524]. After spiking 50% saliva with trypsin, we observed a 2-fold increase in PA intensity between cleaved and uncleaved probe and inhibition of the signal in the presence of inhibitor (leupeptin). Activatable probes may be of use for diagnostic imaging in future PA-based dental applications[210, 384, 474].

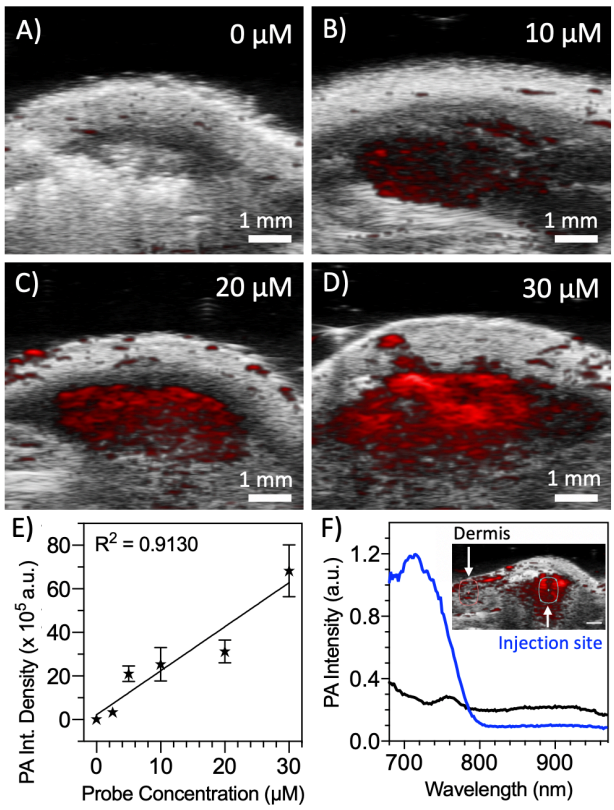

Figure 7. 7. Photoacoustic imaging of activated [Cy5.5]2[RRK]1 in vivo via subcutaneous injection.
A stock solution of $[Cy5.5]_2[RRK]_1$ (40 µM) was incubated with 5 µM trypsin for 1 h in NH_5CO_3 buffer and diluted to five lower concentrations for subcutaneous injection in nude mice (n = 3) after mixture with 50% v/v Matrigel: probe. Representative B-mode PA/US images are shown for (**A**) vehicle only, (**B**) 10 µM probe, (**C**) 20 µM, and (**D**) 30 µM probe. (**E**) Regions of subcutaneous PA intensity were quantitated via integrated pixel density and plotted versus probe concentration to determine the limit of detection of cleaved probe ($y = 20206*x + 21848$, $R^2 = 0.9130$, LOD = 0.3 µM, n = 3, error bars = SD). (**F**) Photoacoustic spectra of the injection site for 20 µM probe showed a peak corresponding to $[Cy5.5]_2[RRK]_1$, distinguishing it from the relatively flat signal from the dermis (inset: photoacoustic-ultrasound image with ROIs for spectral analysis).

Lastly, we characterized the in vivo photoacoustic intensity and limit of detection for activated $[Cy5.5]_2[RRK]_1$ via subcutaneous injection in nude mice (**Figure 7.7**). First, the

probe was cleaved in solution via incubation with trypsin and titrated across a range of concentrations (**Figure 7.24**). Absorbance red shifts, fluorescence enhancement, and PA enhancement were observed for each of the tested concentrations. While first demonstrating the efficacy of the probe across a range of concentrations, this data also confirmed that intramolecular interactions were not surpassed by intermolecular interactions even at higher concentrations. After subcutaneous injection, PA intensity was quantified via integrated density (**Figure 7.25**) and these values correlated with probe concentration for the tested range between 0 – 30 μM (**Figure 7.7A-D**). The minimum amount of detectable probe was determined to be 0.3 μM (**Figure 7.7E**); of course, higher concentrations (e.g., 10 – 30 μM) would provide a higher SBR in tissue for further applications of this scaffold. Nevertheless, for surface-weighted imaging applications, we found that injected probe could be spectrally distinguished from background signal in the surrounding dermis and tissue— this spectral acoustic imaging is a key strength of the PA imaging modality (**Figure 7.7F**).

Quantitative protease imaging in vivo is a challenge—many factors can influence the measured photoacoustic intensity at any given time. These may include differences in optical fluence due to tissue variation, laser fluctuations, inflammation contributing to changes in blood perfusion (and total hemoglobin), photostability, and changes in local concentration of the probe. One approach to improve the quantitative ability of the probes in vivo is to engineer a ratiometric signal. Future efforts will investigate the coupling of more red-shifted dyes to potentially leverage ratiometric photoacoustic imaging in the excitable range of existing photoacoustic scanners (e.g., 680 – 970 nm).

7.4. Conclusions

We investigated the performance of a peptide-linked cyanine dimer, $[Cy5.5]_2[RRK]_1$, for simultaneous photoacoustic imaging and fluorescent monitoring of enzyme activity. The dyes were attached to the N-terminus and C-terminal lysine of a trypsin cleavable peptide [RRK] via amide linkage. This conjugate exploited the intramolecular association of cyanine dyes to blue-shift its peak absorbance by >50 nm and undergo contact quenching, achieving an off state. Following cleavage of the peptide substrate, the dyes were separated, and photoacoustic and fluorescent signals were activated. We compared the cleavable dimer to a trimer and tetramer, such that $n - 1$ peptide spacers [RRK] were linked between n cyanine dyes. A 2.5-fold recovery of the peak absorbance was observed for all conjugates. Fluorescent detection limits of trypsin were 1.2 nM for the dimer, 51 pM for the trimer, and 43 nM for the tetramer. Photoacoustic imaging of the dimer revealed 5-fold signal enhancement at 680 nm with nanomolar sensitivity to trypsin. The activated probe scaffold was imaged subcutaneously in mice and its signal was linearly correlated to concentration. The probe could be tuned for other protease targets by changing the peptide substrate, and we demonstrated photoacoustic detection of M^{pro} associated with SARS-Cov-2 using $[Cy5.5]_2[GTSAVLQSGFRK]_1$. The performance of this dye-peptide scaffold demonstrates a readily synthesized and tunable platform for photoacoustic/fluorescence monitoring of protease activity with potential value in areas such as disease monitoring, tumor imaging, intraoperative imaging, in vitro diagnostics, and point-of-care sensing.

7.5. Acknowledgements

Chapter 7, in full, is a reprint of the material as it appears in ACS Sensors, vol. 6 (6), 2356-2365, 2021. Moore, Colman; Borum, Raina; Mantri, Yash; Xu, Ming; Fajtová, Pavla; O'Donoghue, Anthony; Jokerst, Jesse V. The dissertation author was the primary investigator and author of this paper.

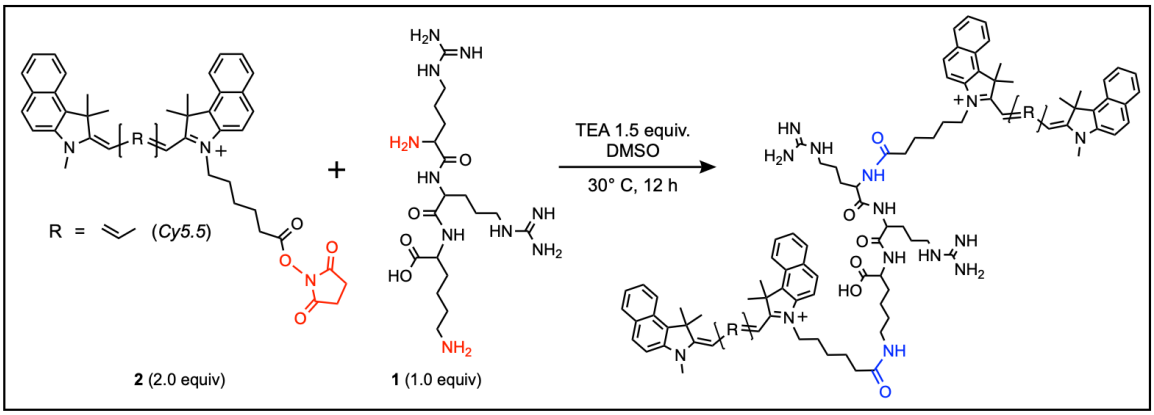

Figure 7.8. Synthetic scheme for dye-peptide conjugates.
For brevity, only the RRK peptide is illustrated. Succinimidyl ester activated dyes (Cy5.5-NHS) were reacted with the N-terminal amines and lysine side chains of the peptides (RRK, RRKRRK, RRKRRKRRK, GHK, GTSAVLQSGFRK) to form amide linkages.

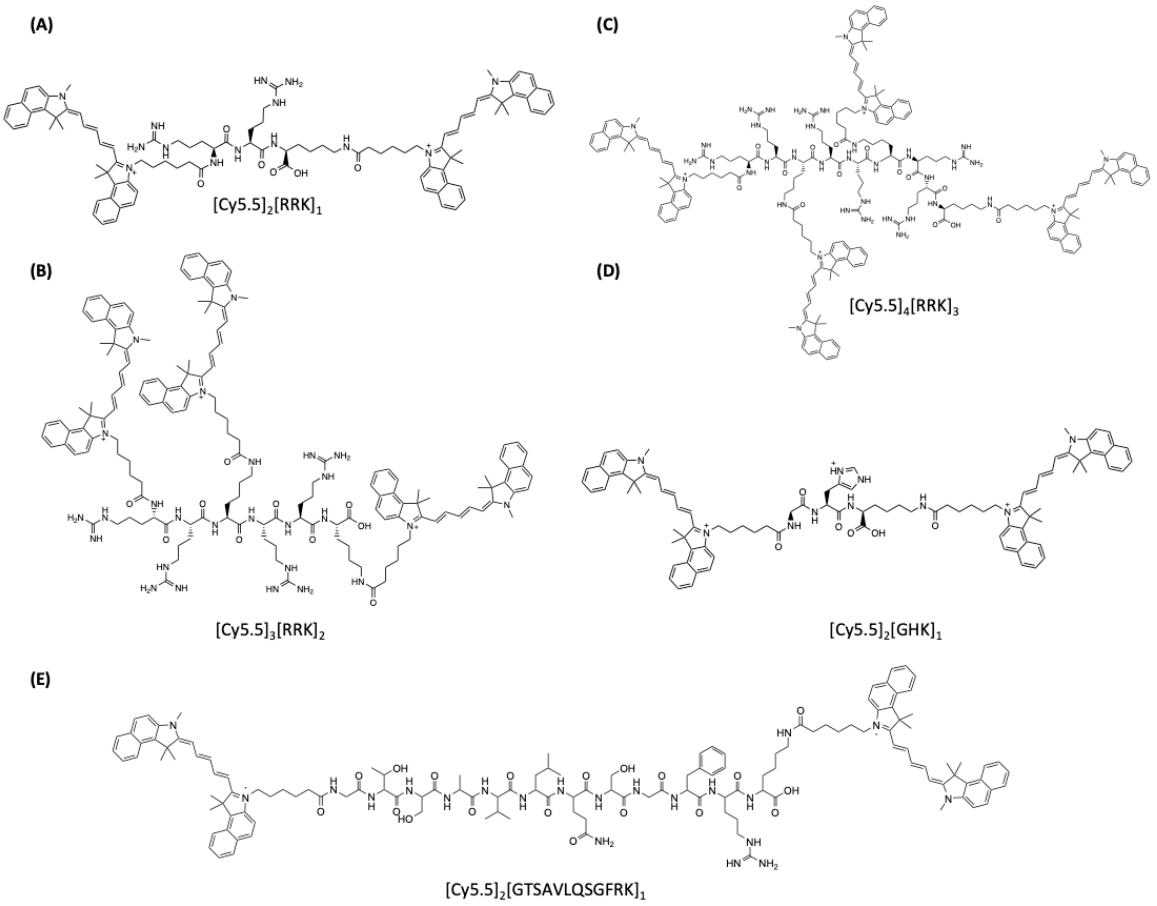

Figure 7.9. Structures of synthesized dye-peptide conjugates.
(**A**) $[Cy5.5]_2[RRK]_1$, (**B**) $[Cy5.5]_3[RRK]_2$, (**C**) $[Cy5.5]_4[RRK]_3$, (**D**) $[Cy5.5]_2[GHK]_1$, and (**E**) $[Cy5.5]_2[GTSAVLQSGFRK]_1$.

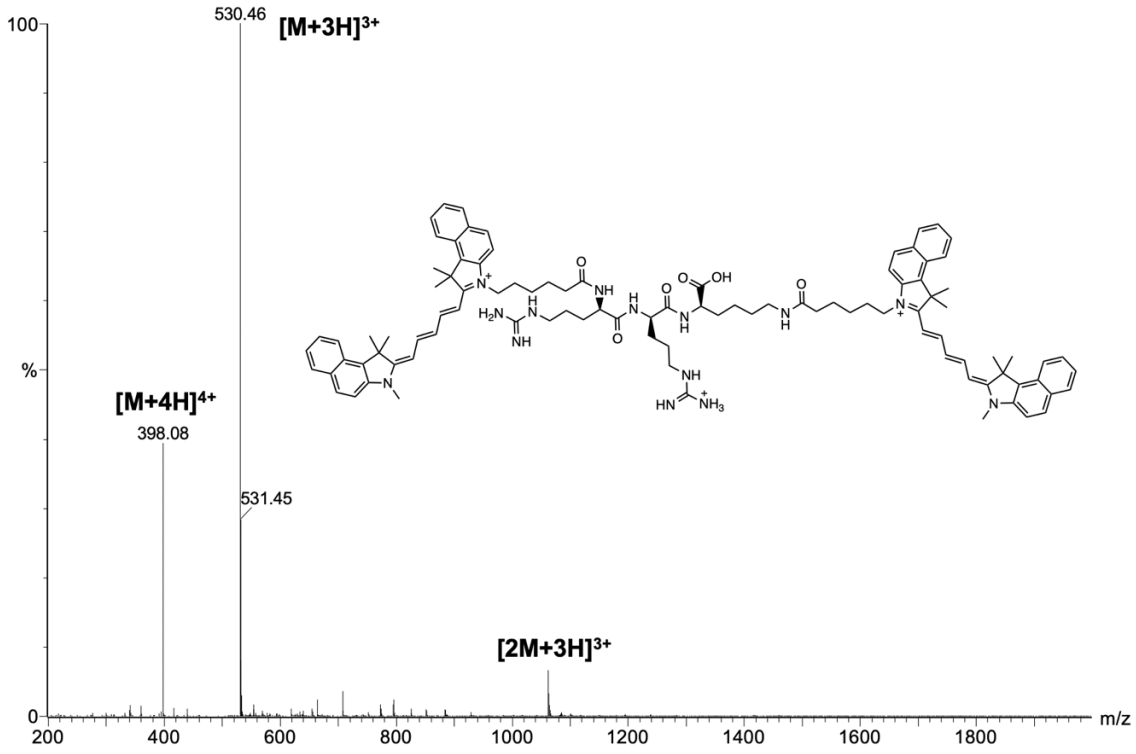

Figure 7.10. ESI-MS spectrum of $[Cy5.5]_2[RRK]_1$ in positive mode.

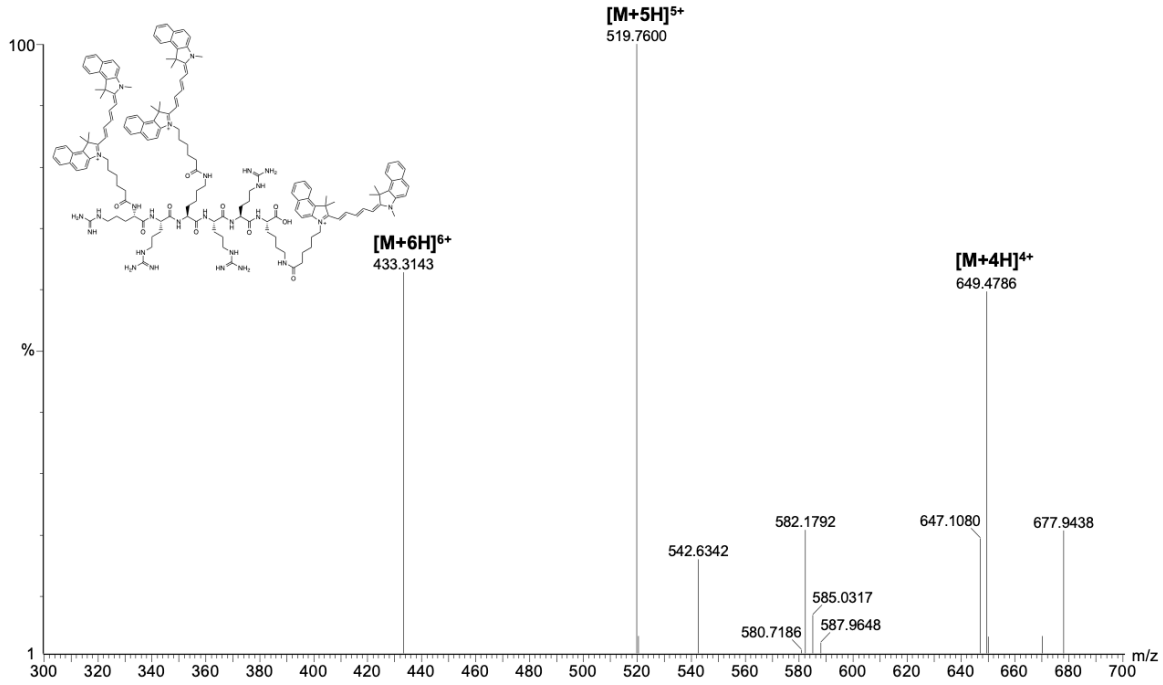

Figure 7.11. ESI-MS spectrum of $[Cy5.5]_3[RRK]_2$ in positive mode.

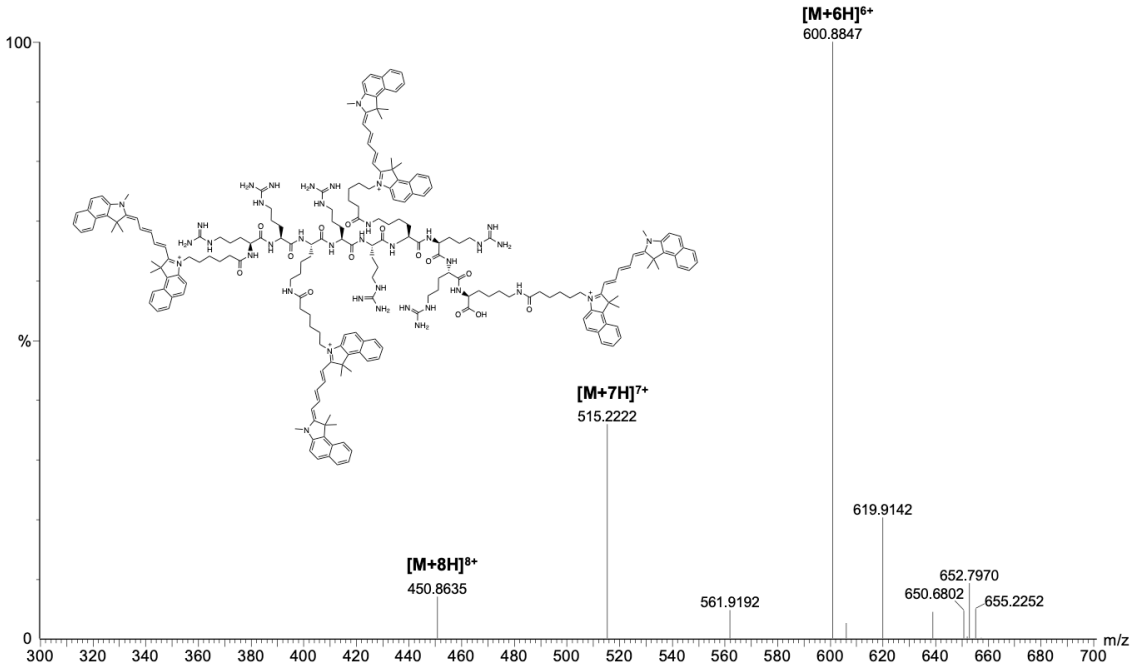

Figure 7.12. ESI-MS spectrum of $[Cy5.5]_4[RRK]_3$ in positive mode.

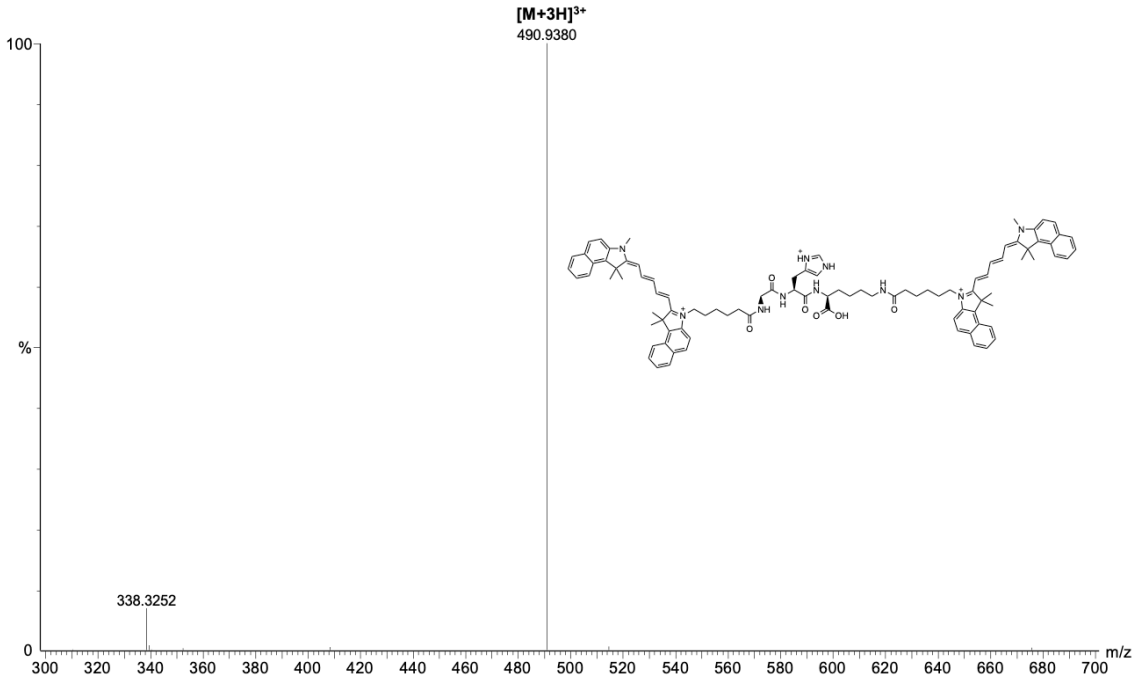

Figure 7.13. ESI-MS spectrum of $[Cy5.5]_2[GHK]_1$ in positive mode.

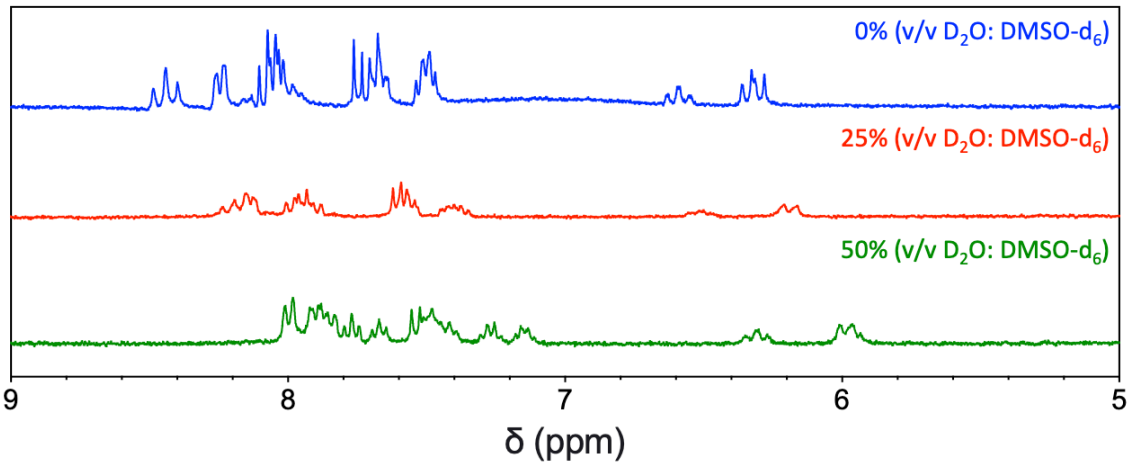

Figure 7.14. 1H-NMR spectra (300 MHz) of $[Cy5.5]_2[RRK]_1$ in increasing ratios of D2O/DMSO-d6.

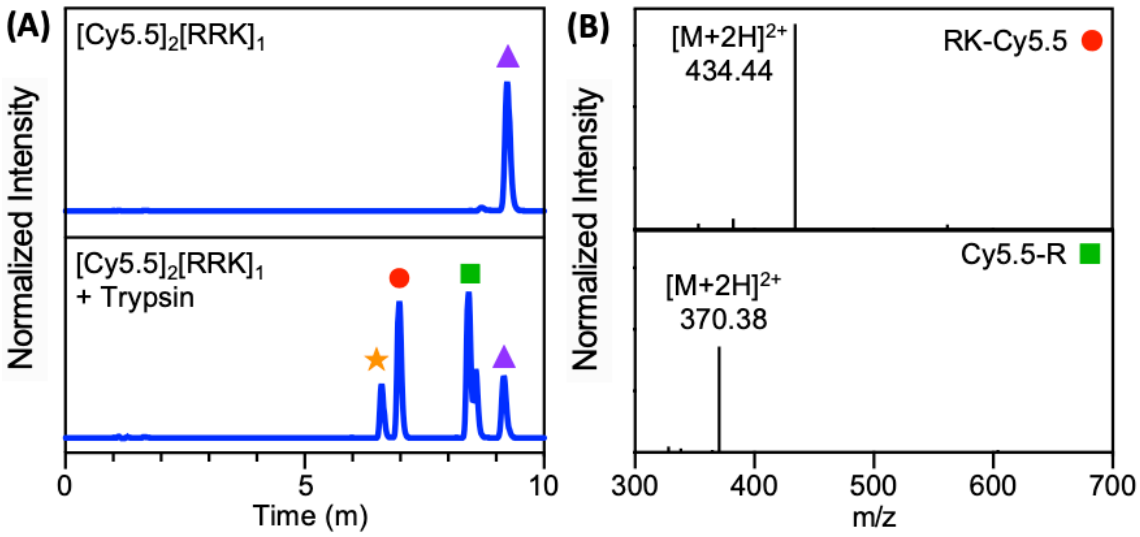

Figure 7.15. Liquid chromatograms and ESI-MS of $[Cy5.5]_2[RRK]_1$ before and after proteolysis.

(**A**) $[Cy5.5]_2[RRK]_1$ (9 μM) without (top) and with (bottom) incubation in trypsin (100 nM) for 2 h at 37 °C in NH_5CO_3 (100 mM). Uncleaved probe eluted at 9 min. After proteolysis, new peaks were observed at 6.5 min, 6.9 min, and 8.3/8.5 min (collected as a single fraction). The column was an analytical-scale Shim-pack GIS C18 (5 μm) and the detection wavelength was 680 nm. The pumps were programmed with a binary gradient from 25 – 95% B (A: H_2O (0.05% TFA), B: MeCN (0.05% TFA)) over 45 min). (**B**) The C-terminal RK-Cy5.5 fragment was detected via ESI-MS in the 6.9-min fraction (expected: 434.27, observed: 434.44) and the N-terminal Cy5.5-R fragment was detected in the 8.3/8.5 min fraction (expected: 370.22, observed: 370.38).

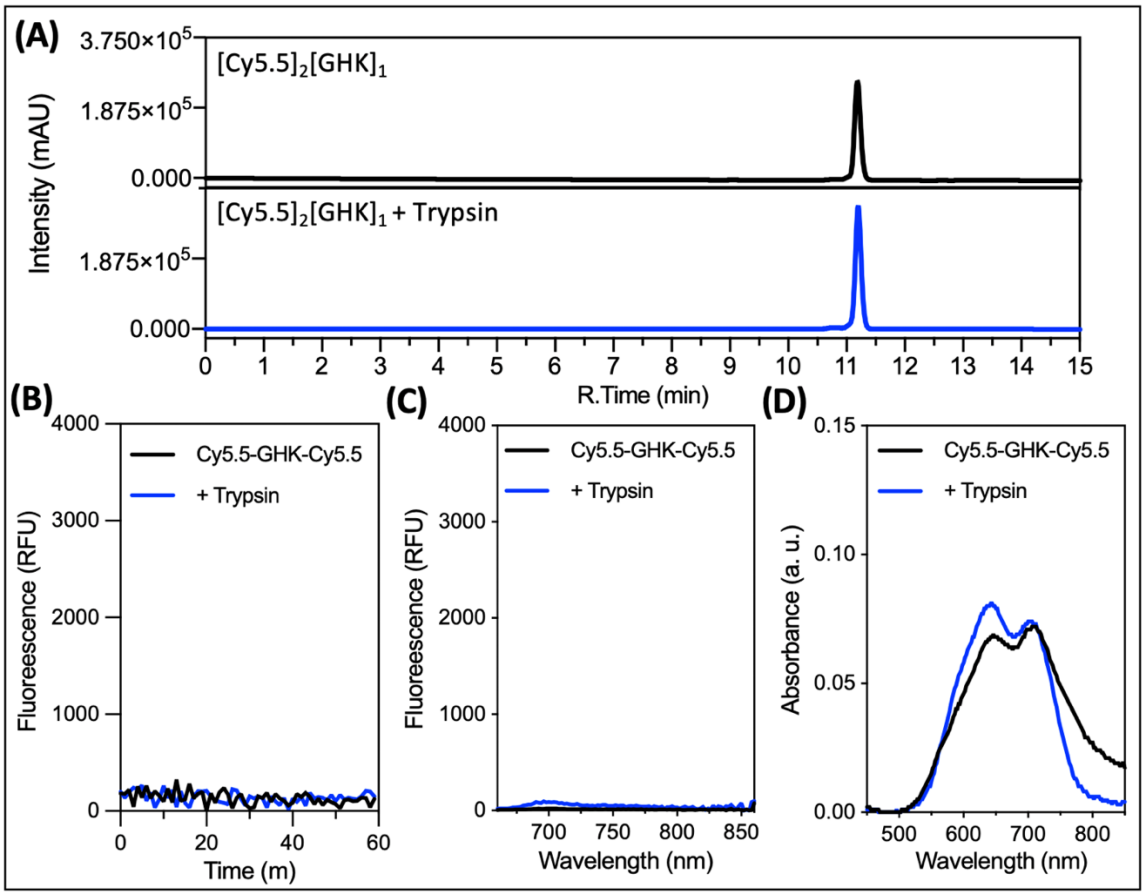

Figure 7.16. Liquid chromatograms and optical spectra of control sequence ($[Cy5.5]_2[GHK]_1$) before and after incubation with trypsin.
(**A**) $[Cy5.5]_2[GHK]_1$ (2 µM) without (top) and with (bottom) incubation in trypsin (5 µM) for 2 h at 37 °C in NH_5CO_3 (100 mM). (**B**) Kinetic fluorescence measurements of $[Cy5.5]_2[GHK]$ with and without trypsin for 1 h (ex: 600 nm, em: 700 nm). (**C**) Fluorescence spectra recorded after 1 h (ex: 600 nm, em: 660 – 850 nm). (**D**) Absorbance spectra recorded after 1 h.

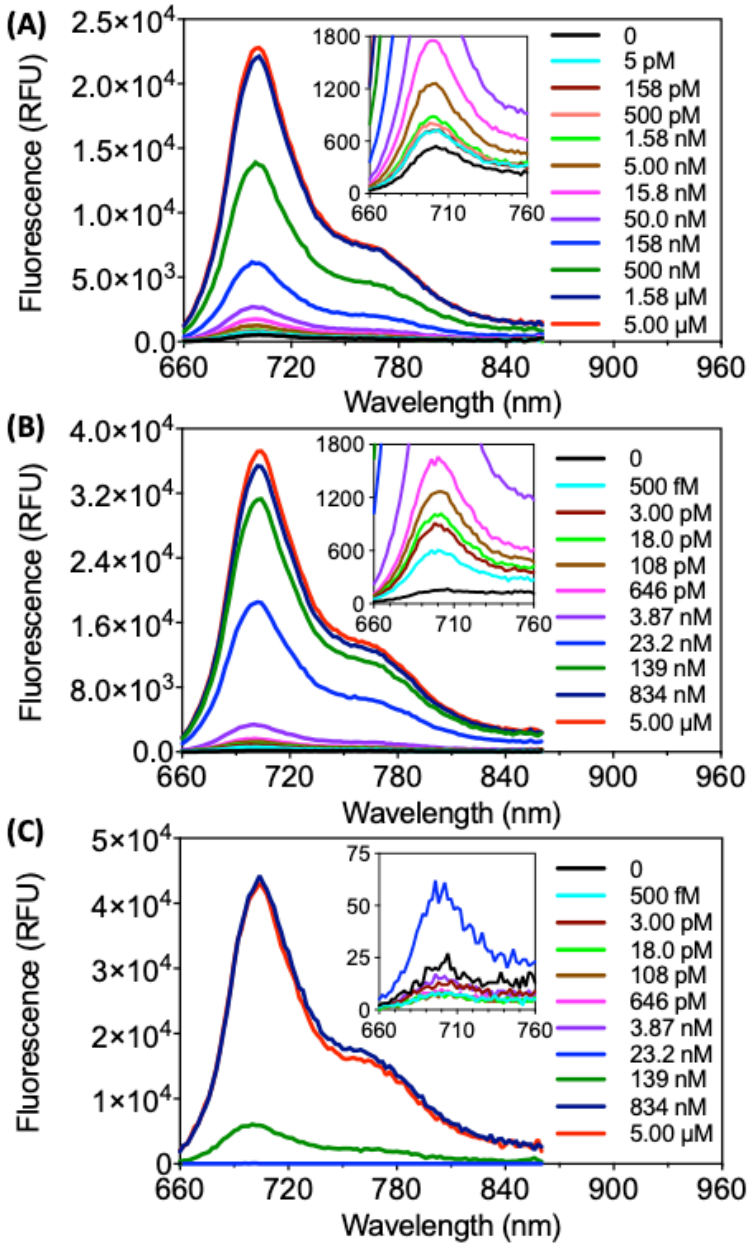

Figure 7.17. Representative fluorescence spectra for (A) $[Cy5.5]_2[RRK]_1$, (B) $[Cy5.5]_3[RRK]_2$, and (C) $[Cy5.5]_4[RRK]_3$ incubated with increasing trypsin concentrations.
Probes were maintained at 7 µM and incubated with a trypsin gradient in 10 mM NH_4HCO_3 and 1% DMSO for 1 h at 37 ° C (ex: 600 nm).

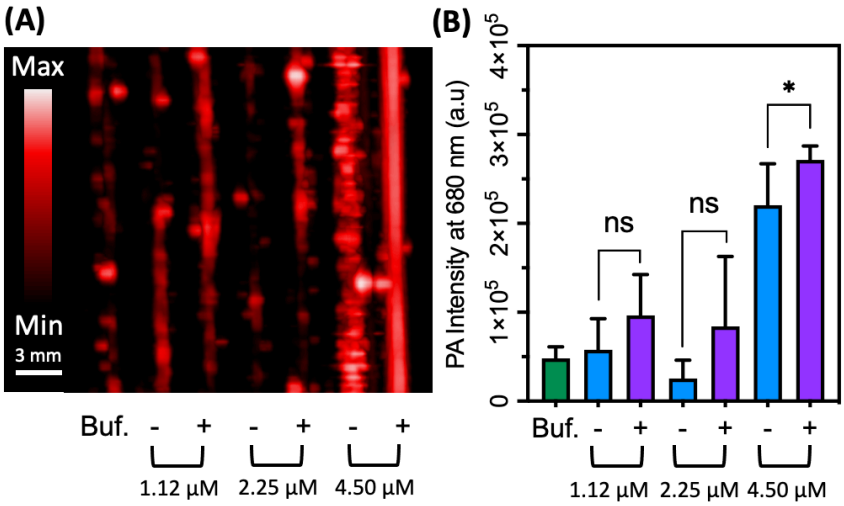

Figure 7.18. Photoacoustic imaging of $[Cy5.5]_2[RRK]_1$ cleavage at insufficient probe concentrations.

(A) Photoacoustic image of $[Cy5.5]_2[RRK]_1$ at low concentrations (1 – 4.5 µM) before (-) and after (+) incubation with trypsin. (**B**) Quantitation of (A) via integrated pixel intensity. Asterisks denote significant difference (unpaired t-test, p-value < 0.0001, n = 8 regions of interest, error bars = SD).

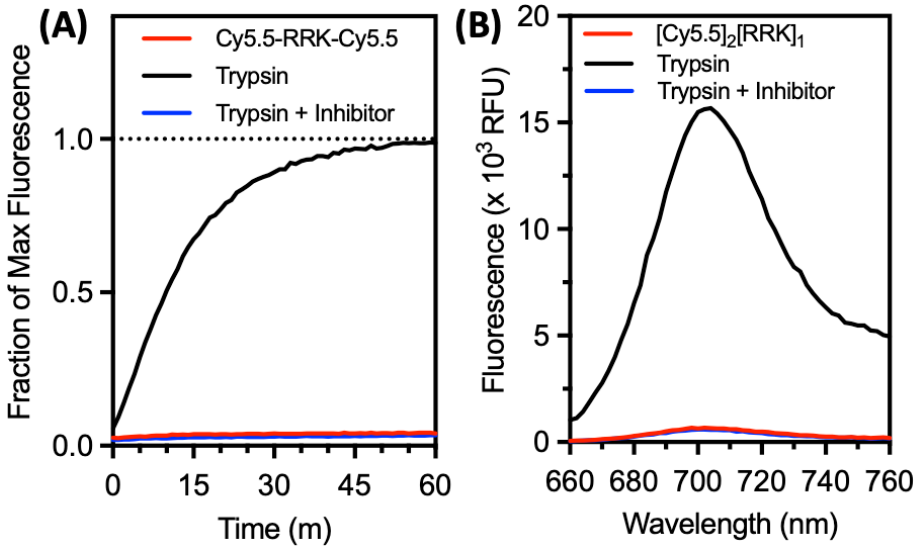

Figure 7.19. Fluorescent activation of [Cy5.5]2[RRK]1 following proteolytic cleavage by trypsin.

(A) Fluorescence over time and (**B**) spectra of $[Cy5.5]_2[RRK]_1$ (7 µM) with trypsin (5 µM) and trypsin/inhibitor (50 µM leupeptin) after 1 h incubation in 100 mM NH_5CO_3 (1% DMSO) at 37°C.

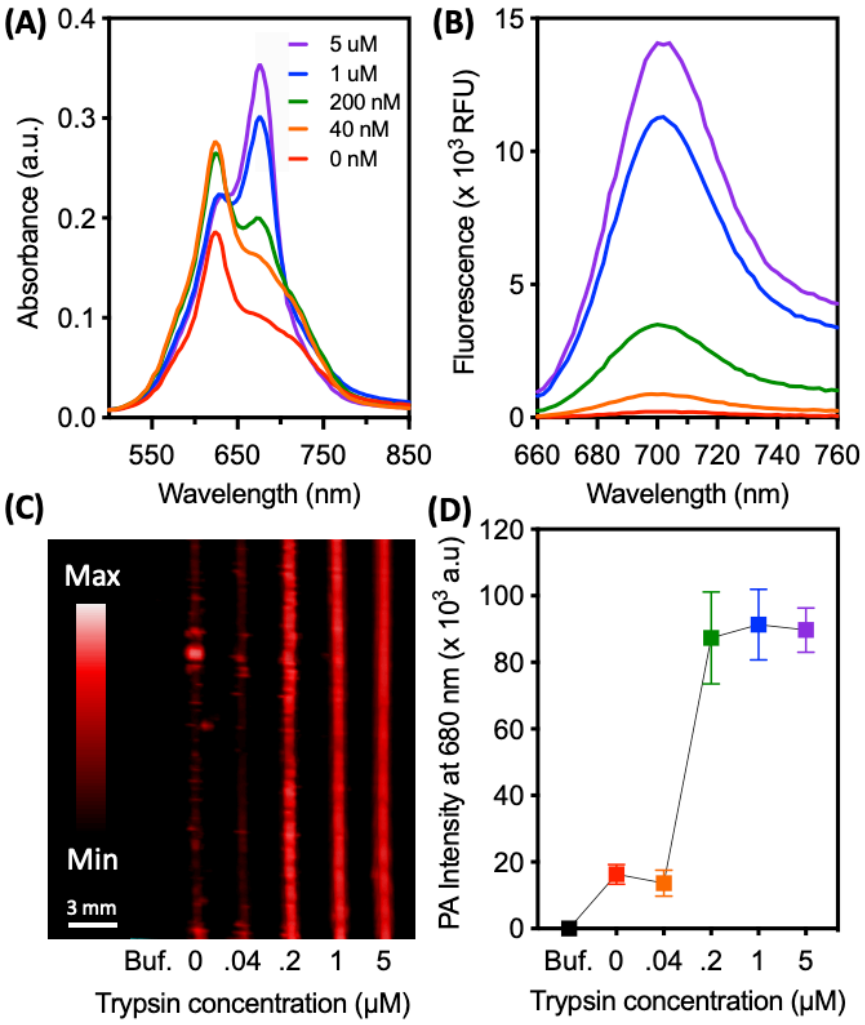

Figure 7.20. Photoacoustic sensitivity of $[Cy5.5]_2[RRK]_1$ to various trypsin concentrations. **(A)** Absorbance spectra of the dimer probe (7 μM) with 0 – 5 μM trypsin after 1 h incubation in 100 mM NH_5CO_3 (1% DMSO) at 37 ° C. As trypsin concentration increased, broadband absorption first increased, followed by an increase in the 680-nm peak and decrease in the 624-nm shoulder. (**B**) Fluorescence spectra of the samples (ex: 600 nm). (**C**) Single-wavelength photoacoustic image of the samples (ex: 680 nm). (**D**) Quantification of Panel C via integrated pixel density. Error bars = SD, n = 8 regions of interest.

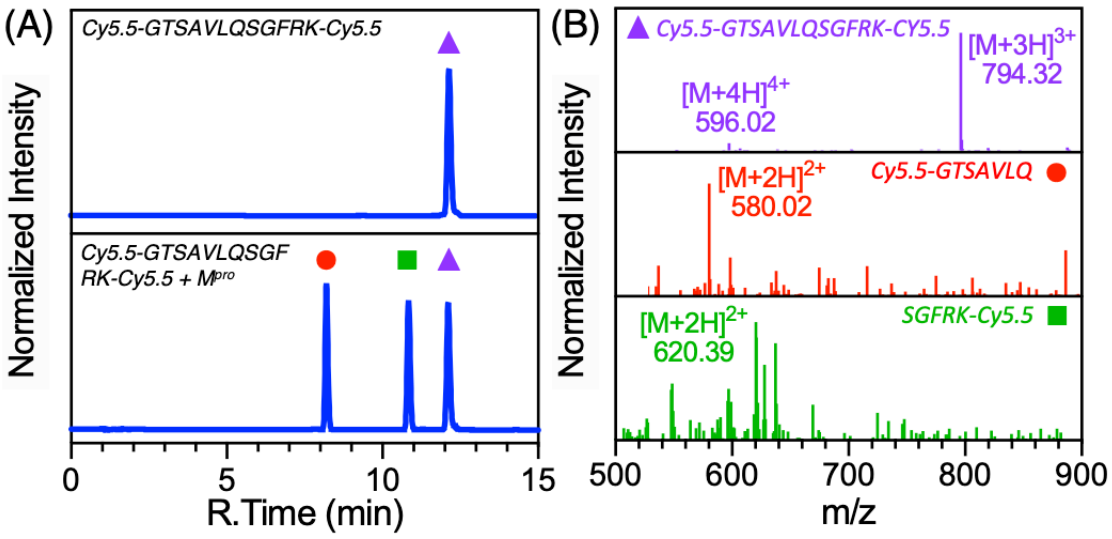

Figure 7.21. RP-HPLC and ESI-MS of M^{pro}-responsive cyanine-peptide conjugate $[Cy5.5]_2[GTSAVLQSGFRK]_1$.
(A) Top: Liquid chromatogram of pure $[Cy5.5]_2[GTSAVLQSGFRK]_1$ in buffer (18 μM, 20 mM Tris, 1 mM DTT, pH 7.4). The retention time was 12.1 min. Bottom: Liquid chromatogram of $[Cy5.5]_2[GTSAVLQSGFRK]_1$ (18 μM) incubated with M^{pro} (100 nM) for 1 h at 37 ° C (20 mM Tris, 1 mM DTT, pH 7.4). The retention times were 8.1 min, 10.7 min, and 12.1 min. Samples were eluted at 1 mL/min with a 25-min gradient from 25% to 95% B (A: water (0.05% TFA), B: acetonitrile (0.05% TFA)). **(B)** ESI-MS of the fractions in Panel A. Fraction 12.1 min (uncleaved $[Cy5.5]_2[GTSAVLQSGFRK]_1$) expected $[M+3H]^{3+}$: 794.11, detected: 794.32, expected $[M+4H]^{4+}$: 595.83, detected: 596.02. Fraction 8.1 min (N-terminal fragment Cy5.5-GTSAVLQ) expected $[M+2H]^{2+}$: 620.34, detected: 620.39. Fraction 10.7 min (C-terminal fragment SGFRK-Cy5.5) expected $[M+2H]^{2+}$: 794.11, detected: 794.41.

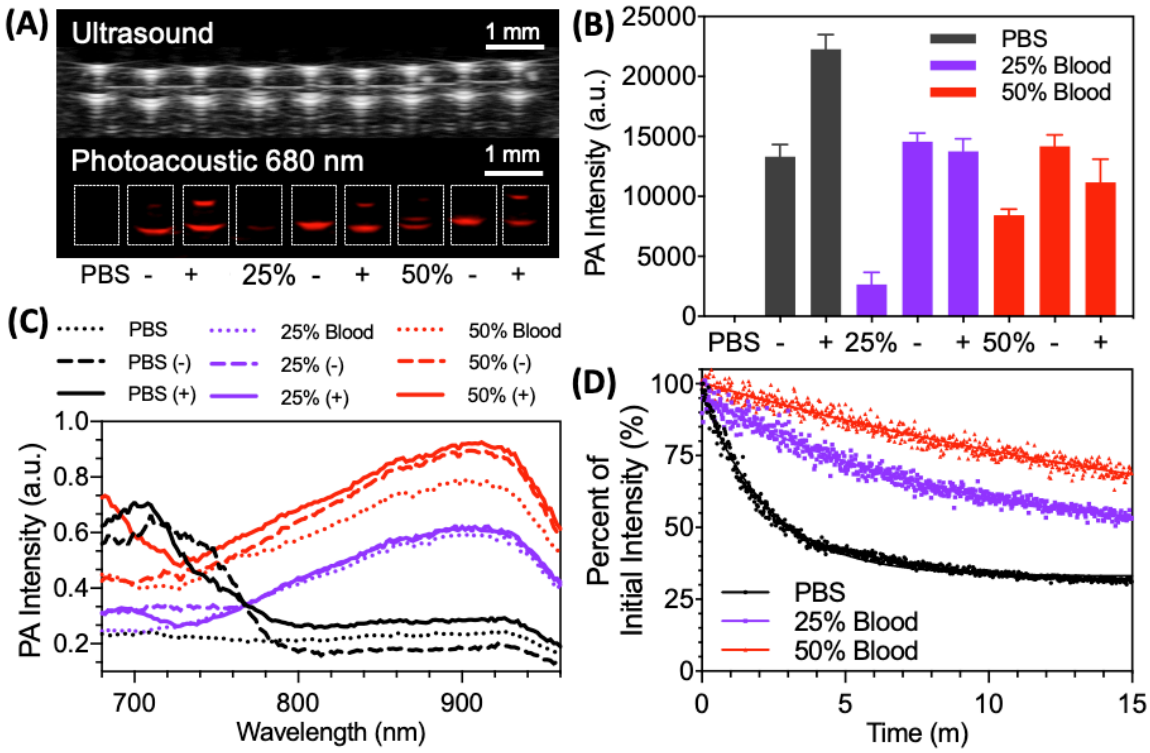

Figure 7.22. Photoacoustic signal and stability of the $[Cy5.5]_2[RRK]_1$ probe in blood.
(A) Representative photoacoustic and ultrasound B-mode image of the probe in various matrices held in polyethylene capillary tubes (left to right): PBS, probe in PBS (-), probe/trypsin in PBS (+), 25% blood, probe in 25% blood (-), probe/trypsin in 25% blood (+), 50% blood, probe in 50% blood (-), probe/trypsin in 50% blood (+). Blood was diluted with PBS (v/v), [probe] = 30 μM, [trypsin] = 1 μM. **(B)** Average intensities from the B-mode images (dashed boxes = ROIs, n = 8 images) taken at different points along the length of the samples. Samples containing probe had significantly higher intensities than matrix alone (PBS, 25%, 50% blood). The 680-nm average intensity of cleaved probe was not statistically higher than uncleaved in 25% and 50% blood likely due to the strong absorption of hemoglobin. **(C)** Photoacoustic spectra of the samples in Panel A. Both uncleaved and cleaved probe in PBS (black) are spectrally unique from hemoglobin in blood (purple, red). In each matrix, cleaved probe (solid) is spectrally unique (680-nm enhancement) from uncleaved probe (dashed). **(D)** Photostability of cleaved probe in PBS, 25% blood, and 50% blood. Each sample was continuously imaged for 15 minutes— the PA intensity at each timepoint was normalized to its initial intensity. The probe intensity was reduced by 69%, 48%, and 30% in PBS, 25% blood, and 50% blood, respectively. The higher stability in blood was due to the increased absorption of light by hemoglobin.

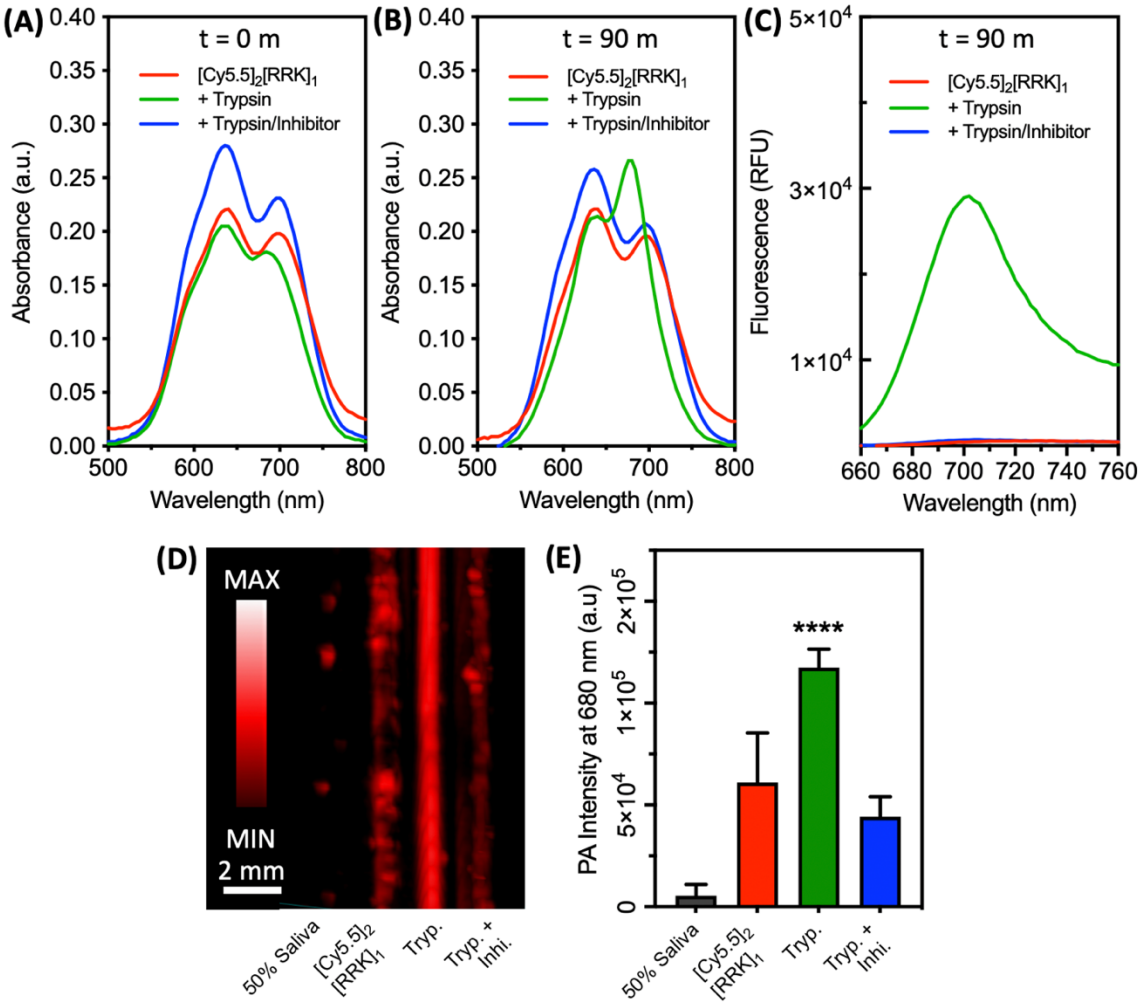

Figure 7.23. Photoacoustic imaging of [Cy5.5]2[RRK]1 cleavage by trypsin in 50% saliva. **(A)** Absorbance spectra of $[Cy5.5]_2[RRK]_1$ (7 µM) immediately after addition of trypsin (5 µM) and trypsin/inhibitor (50 µM leupeptin) in 50% pooled human saliva (v/v saliva: 100 mM NH_5CO_3). (**B**) Absorbance spectra after 90 min at 37 ° C. (**C**) Fluorescence spectra after 90 min at 37 ° C (ex: 600 nm). (**D**) Photoacoustic image of the samples at 680 nm. (**E**) Quantitation of (D) via integrated pixel density. Asterisks denote significant difference between $[Cy5.5]_2[RRK]_1$ and trypsin and trypsin with inhibitor (unpaired t-test, p-value < 0.0001, n = 8 regions of interest, error bars = SD).

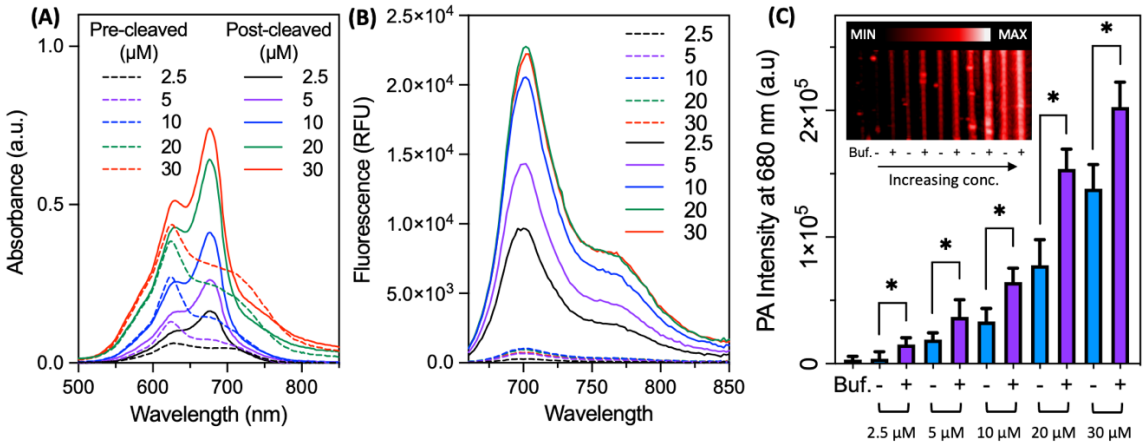

Figure 7.24. Optical and photoacoustic properties of uncleaved and cleaved $[Cy5.5]_2[RRK]_1$ at a range of probe concentrations.

(A) Absorbance spectra of $[Cy5.5]_2[RRK]_1$ at 2.5, 5, 10, 20, and 30 μM before (dashed) and after (solid) incubation with trypsin (1 h, 5 μM trypsin, 37° C, NH_4HCO_3 buffer, 1% DMSO) reveal red shifts of the peak absorption at all concentrations. **(B)** Fluorescence spectra of the same samples before (dashed) and after (solid) incubation with trypsin (ex: 600 nm) show concentration-dependent enhancement. **(C)** Photoacoustic image (inset) and quantitation of the samples excited at 680 nm. All tested concentrations showed photoacoustic enhancement of cleaved probe (purple) relative to uncleaved (blue). Asterisks denote significant difference (unpaired t test, $p < 0.05$, error bars = S.D. of eight regions of interest per sample).

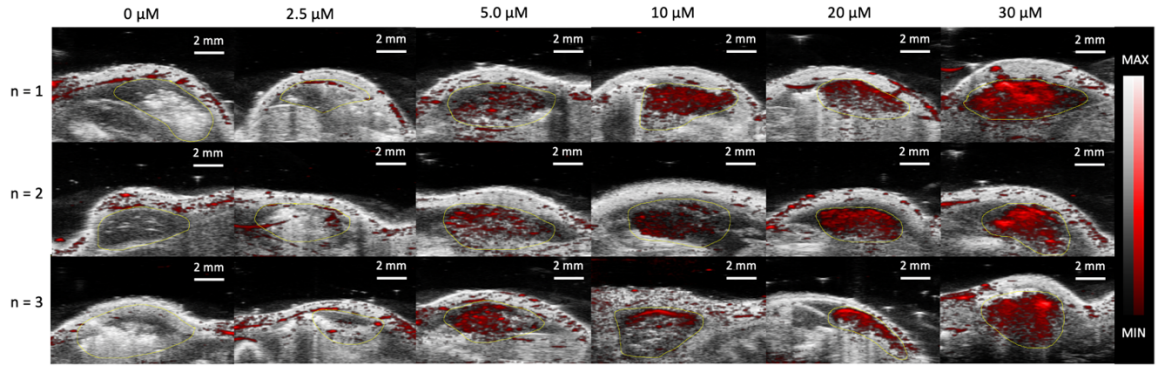

Figure 7.25. Individual photoacoustic-ultrasound images of subcutaneous injections of $[Cy5.5]_2[RRK]_1$ in nude mice.
The injection volume was the same for each concentration (100 µL of probe in 50% (v/v) Matrigel). However, normal variations in the mice and transducer coupling contributed to differences in the apparent size (and cross-sectional area) of the injection sites. ROIs were drawn in ImageJ for each injection area (yellow) based on the ultrasound image. Because the ROIs had different areas, we calculated the raw integrated density of the PA signal for each ROI and used these values for analysis in Figure 7. 7. Unlike mean pixel intensity, the raw integrated density is not skewed by pixels with zero intensity, making it appropriate for comparison of ROIs with minor differences in area.

CHAPTER 8. A PHOTOACOUSTIC-FLUORESCENT IMAGING PROBE FOR GINGIPAINS EXPRESSED BY PORPHYROMONAS GINGIVALIS

ABSTRACT: *Porphyromonas gingivalis* is a keystone pathogen in periodontal disease. We herein report a dual-modal fluorescent and photoacoustic imaging probe for the detection of gingipain proteases secreted by *P. gingivalis*. This probe harnesses the intramolecular dimerization of peptide-linked cyanine dyes to induce fluorescence and photoacoustic off-states. Upon proteolytic cleavage by Arg-specific gingipain (RgpB), five-fold photoacoustic enhancement and >100-fold fluorescence activation was measured with detection limits of 1.1 nM RgpB and 5.0E4 CFU/mL bacteria in vitro. RgpB activity was imaged in the subgingival pocket of porcine jaws with 25 nM sensitivity. The diagnostic efficacy of the probe was evaluated in gingival crevicular fluid (GCF) samples from subjects with (n = 14) and without (n = 6) periodontal disease, wherein activation was correlated to qPCR-based detection of *P. gingivalis* (Pearson's r = 0.71). The highest activity was seen in subjects with the most severe disease. Finally, photoacoustic imaging of RgpB-cleaved probe was achieved in murine brains ex vivo, demonstrating relevance and potential utility for animal models of general infection by *P. gingivalis*, motivated by the recent biological link between gingipain and Alzheimer's disease.

8.1. Introduction

Periodontitis is a chronic inflammatory disease that affects 46% of adults in the United States and generates billions of dollars per year in direct costs [525, 526]. The pathogenesis of the disease remains an active research topic; however, it is principally associated with a dysbiotic oral microbiome and the accompanying immune response [527]. Periodontitis-associated bacteria reside in the subgingival crevice, and their presence in biofilms and gingival crevicular fluid contribute to degradation of host tissue and deepening of the periodontal pocket [528]. When untreated, periodontitis causes oral pain, tooth loosening, and tooth loss. Furthermore, the long-term loading of the immune system has been linked to increased risks for cardiovascular disease [400], pre-term birth [529], cancer [401], and even dementia [402].

Periodontal health is measured via periodontal probing and clinical examination with metrics that include the pocket depth, clinical attachment level, bleeding on probing, tooth mobility, and inflammation. Together, these metrics are used to form a diagnosis. In general, this established practice is functional and affordable, but pocket depth and clinical attachment level measurements suffer from relatively high inter-examiner error due to differences in probing force/angulation while also causing patient discomfort. Moreover, these techniques largely assess the effects of disease rather than using molecular diagnostics for precision health. Therefore, new techniques to detect disease at the point-of-care—particularly with utility for imaging and identification of disease at the molecular level—remain an unmet need in the field of oral health.

Many of the periodontal pathogens that have been linked to disease are anaerobic, such as *Tannerella forsythia*, *Treponema denticola*, and *Porphyromonas gingivalis* [530].

Among this "red complex", *P. gingivalis* is the most well-characterized: Its presence in subgingival plaque has been correlated with disease progression in longitudinal human studies [531, 532]. As a function of their anaerobic metabolism, these pathogens secrete protease virulence factors that degrade extracellular proteins and modulate the host immune response[533]. *P. gingivalis*, in particular, is known to secrete proteases called gingipains that exhibit trypsin-like activity [534].

Indeed, *P. gingivalis* and gingipain proteases have attracted attention both as diagnostic and therapeutic targets. A variety of naturally derived and synthetic gingipain inhibitors have been reported in the literature while demonstrating evidence for potential treatment of periodontal disease though clinical trials have been relatively rare [535-537]. Intriguingly, evidence of gingipains has been identified in the post-mortem brains of patients with Alzheimer's disease (AD) and are the target of an ongoing AD clinical trial for a small molecule gingipain inhibitor [538]. A parallel research effort is targeting *P. gingivalis* directly with an antibody therapy [539].

From a diagnostic perspective, advances in gingipain detection have included the development of substrates and paper-based assays for *in situ* analysis [540, 541], a plasmonic nanosensor [542], and a gingipain-responsive/drug-loaded hydrogel [543]. The goal of this study was to develop an activatable probe for gingipains with utility for in vivo imaging—such work was motivated by its potential as a clinical tool for periodontal diagnosis and as a research tool for investigation of the role of gingipains in periodontitis and other diseases.

Photoacoustic imaging is particularly attractive because it augments the existing strengths of ultrasound—good tissue penetration, low cost, and real-time monitoring. It can use both exogenous and endogenous contrast based on optical absorption. Many small

molecule and nanoparticle contrast agents have been engineered for photoacoustic imaging and activatable probes for molecular imaging are particularly desirable [12]. Further, the applications of acoustic imaging and nanoscale materials have been expanding [544-546] but they have not yet been combined for oral imaging. In previous work, we introduced a dye-peptide scaffold that exploits the intramolecular coupling of cyanine dyes to generate photoacoustic and fluorescent signal upon proteolysis by trypsin. Here, we leveraged this approach to create an activatable photoacoustic and fluorescent molecular imaging agent for gingipain proteases.

8.2. Methods

8.2.1. Reagents

Peptides were purchased from GenScript Inc. (New Jersey, USA). Cy5.5-NHS was purchased from Lumiprobe, Inc. (Maryland, USA). Dimethyl sulfoxide, leupeptin, phosphate-buffered saline, tris base/HCl, dithiothreitol, triethylamine, L-cysteine, menadione, yeast extract, tryptic soy broth, and hemin were purchased from Sigma-Aldrich (Missouri, USA). Acetonitrile, trifluoroacetic acid, and sodium hydroxide were purchased from Fisher Scientific (Massachusetts, USA). Recombinant RgpB was purchased from Genovis (B0-GRX-005, Skåne, Sweden).

8.2.2. Structural Modeling Of Peptide Affinity For RgpB

To select a gingipain-cleavable peptide substrate**,** we applied a structural model of peptide-protein affinity to screen a library of pentapeptides for their affinity to the Arg-specific cysteine protease gingipain R (RgpB)[547, 548]. The RgpB protease is composed of a 435-residue, single-chain polypeptide that forms a catalytic domain and an immunoglobulin-like domain [549]. The peptide candidates were generated with three constraints: a five-residue

length, an arginine at the third residue (P_1), and a lysine at the fifth residue (C-terminus, P_2'). Peptide length was restricted to facilitate intramolecular interaction between N and C terminal dyes while reducing the likelihood of cleavage by off-target proteases. The central arginine was necessary for cleavage by RgpB, and the C-terminal lysine was chosen for its reactive free amine. To this end, a library of 8,000 pentapeptide sequences was generated using mimotopes with a combinatorial three-positional scan of the form XXRXK where X = any natural amino acid. Each sequence was screened for affinity to Arg-specific gingipain B (RgpB) using PepSite 2.0, an open-source algorithm for prediction of peptide-protein binding sites [548, 550]. Briefly, this technique predicts the relative strength and location of a peptide-protein interaction by deriving probabilities via spatial position specific scoring matrices from a library of known peptide-protein complexes. For each pentapeptide sequence, the PepSite server was queried programmatically from a Unix terminal using the published API, and the p-value representing the relative strength of the interaction with the best match on the RgpB (PDB: 1CVR) surface (i.e., the location on the protein surface with the highest affinity) was returned for each sequence. The sequences were ranked by p-value and predicted structures of the peptide-protein complexes were visualized with JMol.

8.2.3. Synthesis And Purification Of Gingipain-Cleavable Probes

The peptide-linked dimer probes were synthesized via reaction of N-hydroxysuccinimide (NHS)-activated cyanine dyes (Cy5.5) with the primary amines of the (1) N-termini and (2) C-terminal lysine residues of Ala-Pro-Arg-Ile-Lys (APRIK), Thr-Thr-Arg-Ile-Lys (TTRIK), and Glu-Glu-Arg-Glu-Lys (EEREK). For the representative reaction with APRIK, a 7-mL scintillation vial was charged with 0.9 mg peptide (1.5 μmol) in 369 μL anhydrous DMSO and 31 μL of 1% v/v triethylamine (2.25 μmol, 1.5 eqiv). Cy5.5-NHS

(3.5 µg, 4.50 µmol) was added to the solution and it was stirred at 300 rpm for 12 h at 30° C. The crude reaction mixtures were dried under vacuum centrifugation using a Vacufuge Plus (Eppendorf, Hamburg) at 60° C for 3 – 4 h. Crude reaction pellets were resuspended in binary mixtures of 25% MeCN/H_2O (v/v) and separated via RP-HPLC on a Shim-pack GIS C18 column (5 µm). The mixtures were purified with a 25% – 95% B gradient (A: H_2O (0.05% TFA), B: MeCN (0.05% TFA)) over 30 minutes. Fractions were collected and lyophilized using a FreeZone -84C freeze dryer (Labconco, Kansas City, MO). The masses of products were measured via electrospray ionization mass spectrometry (ESI-MS) in positive mode using a Micromass Quattro Ultima Triple Quadrupole mass spectrometer.

8.2.4. Anaerobic Culture

P. gingivalis and *F. nucleatum* colonies were grown on brucella blood agar plates (Anaerobe Systems) from lyophilized stocks of ATCC 33277 and ATCC 25586, respectively (KWIK-STIK, VWR). Anaerobic atmospheres were generated and maintained with commercially available anaerobic sachets with oxygen indicators (GasPak EZ Pouch System, BD). Briefly, plates were streaked with bacteria-loaded swabs and immediately placed in the gas-generating sachets. For *P. gingivalis*, light-colored colonies became visible 4-5 days of incubation at 37 °C; these colonies turned black over the following 4 days due to heme accumulation/metabolism (signature of *P. gingivalis*). *F. nucleatum* colonies were faster growing (2-4 days) and maintained a light color. Single colonies were transferred to enriched tryptic soy broth (eTSB) as described by Potempa et al [551]. To summarize, eTSB was prepared at 1-L scale by dissolving 30 g tryptic soy broth and 5 g yeast extract in 950 mL DI water followed by addition of 5 mL hemin (1 mg/mL). The pH was adjusted to 7.4 using 5 M NaOH and water was added to reach 1 L. The broth was then autoclaved follow

by aseptic addition of 5% (w/v) L-cysteine, 10 mL 1% (w/v) dithiothreitol, and 2 mL menadione (0.5 mg/mL). The solution was purged with N_2 and stored at room temperature.

8.2.5. Collection Of Gingival Crevicular Fluid From Human Subjects

The study protocol received approval from the UCSD and USC Institutional Review Boards (HS-19-00163-CR002) and was in accordance with the ethical guidelines for human subjects research established by the Helsinki Declaration of 1975. Subjects were selected from patients receiving dental treatment at the Herman Ostrow School of Dentistry. Subjects were diagnosed according to the 2017 World Workshop on the Classification of Periodontal and Peri-implant Diseases and Conditions by a board-certified periodontist faculty (K.C.J.C) via extra- and intraoral examination, periodontal probing/examination (clinical attachment level (CAL), tooth mobility, bleeding on probing, gingival biotype), and radiography. Because site-specific disease severity does not have a universal grading system, it was graded using a custom measurement scale based on the current American Academy of Periodontology classification system of periodontitis as reference. The severity classes I-III were defined as follows: Class I (≤6 mm total facial CAL), Class II (≤12 mm total facial CAL), and Class III (> 12 mm total facial CAL), where total facial CAL was calculated by summing the CAL at three facial sites for each tooth: mesiofacial, facial, and distofacial. If a diseased tooth presented site complexity, (bleeding on probing, mobility, thin biotype), then the classification was increased to a higher stage. Absorbent paper points were used to sample the gingival sulcus of each tooth site. The paper points were suspended in PBS and vortexed for 2 minutes at room temperature. An equal volume of 50% glycerol was added, and the samples were frozen at -20 °C until use.

8.2.6. Bacterial Quantitation In GCF With qPCR

To determine the number of *P. gingivalis* from each sample, genomic DNA was first isolated using DNeasy Blood and Tissue Kit (Qiagen, Valencia, CA), and quantified through NanoPhotometer (Implen, Munich, Germany). Quantitative real time PCR (qRT-PCR) using BioRad CFX Connect Real Time PCR Detection System (Hercules, CA) was done using *P. gingivalis*-specific primer pair (5'-AGGCAGCTTGCCATACTGCG-3' (forward) and 5'-ACTGTTAGCAACTACCGATGT-3' (reverse))[552]. Each PCR amplification was performed in a total volume of 25 µL containing 10 ng of gDNA, 1.25 µL of each primer (3 µM), and 12.5 µL of 2X iQ SYBR Green Supermix (BioRad, Hercules, CA). The thermocycling profile was: Cycle 1: (1X) Step 1: 95°C for 3 minutes. Cycle 2: (40X) Step 1: 95°C for 15 seconds, Step 2: 58°C for 30 seconds, Step 3: 72°C for 30 seconds. A melting analysis was performed to determine the specificity of the PCR product, and the final DNA products were denatured at 95°C for 1 minute and then incubated at 5°C below the annealing temperature for 1 minute before the temperature was increased to 95°C at a ramp rate of 0.5°C/10 seconds. Each sample was done in triplicate, and additional controls included samples without gDNA for each primer pair. The gDNA of *P. gingivalis* ATCC 33277 was used to generate the standard curve for the quantification of *P. gingivalis* cell number. Data analysis was performed based on the protocol provided by BioRad.

8.2.7. Gingipain activity measurements.

Proteolytic measurements of recombinant RgpB were performed in activity buffer (20 mM Tris buffer containing 1 mM DTT, 1 mM cysteine, pH 7.3) at 37 °C. For experiments with cultured *P. gingivalis*/*F. nucleatum* and clinical GCF samples, the supernatants or GCF were diluted by 50% (v/v) in the activity buffer prior to measurement.

Experimental detection of proteolytic cleavage via HPLC/ESI-MS was performed on an analytical Shim-pack GIS C18 column (5 μm) with a prep Spirit C18 guard column (120 A, 1 x 2.12 cm ID) and a Micromass Quattro Ultima Triple Quadrupole mass spectrometer.

8.2.8. Detection Of Gingipain In Bacterial Culture Via Immunoassay

An Rgp standard at a range of concentrations (0, 31.25, 62.5, 125, 250, 500, 1000, 2000 pg/mL in binding buffer) was applied to ELISA assay wells and treated with detection antibodies as described by the manufacturer of a commercially available ELISA kit for Rgp (MyBioSource MBS2800343, California, USA). Absorbance at 450 nm (A_{450}) was measured to quantify extent of antibody binding. Regression analysis of the data generated a linear fit of the form y = mx. Supernatants from *P. gingivalis* culture, or eTSB alone, were clarified with 10 kDa molecular weight cutoff spin filters and the solutions were applied to ELISA assay wells, treated with Rgp detection antibodies, and the A_{450} was measured.

8.2.9. Absorbance And Fluorescence Spectroscopy

Absorbance and fluorescence data were collected with a BioTek Synergy H1 plate reader. All samples were measured at 100-μL scale in 96-well plates. Generally, absorbance spectra were measured from 450 – 850 nm and fluorescence emission spectra were collected using ex: 600 nm and em: 660 – 860 nm (2-nm increments). Kinetic measurements were performed using ex: 600 nm and em: 700 nm (step: 0.5 minutes). Fluorescence area scans were collected using ex: 600 nm and em: 700 nm for 13 points in space per well.

8.2.10. In Vitro Photoacoustic Imaging

Samples for in vitro imaging were imaged with a commercially available photoacoustic-ultrasound imaging system with a 21-MHz transducer (LZ-250, Vevo LAZR, VisualSonics). Samples (20 μL) were loaded into individual 0.86 mm polyethylene tubes

and fixed in parallel within a 3D-printed holder 1 cm below the transducer in a vessel filled with water [234]. Single wavelength scans were operated at 680 nm with a repetition rate of 20 Hz (pulse width = 4-6 ns, ~45 mJ/pulse at source) [514]. To generate 3D images, the transducer was scanned with a stepper motor (step size = 0.054 mm) along the axial dimension of the tubes and B-mode frames were registered via maximum intensity projection. Photoacoustic spectra were measured from 680 nm to 900 nm (2-nm step size).

8.2.11. Ex Vivo Porcine Jaw Imaging

Resected porcine jaws (n = 3) were purchased from a local butcher (San Diego, CA). Solutions of 30 μM C2A probe (100-μL scale, 3% DMSO) were mixed with 0, 5, 10, 25, and 50 nM RgpB in activity buffer at 37°C and monitored for cleavage via absorbance and fluorescence. Solutions containing RgpB with a $\Delta OD_{680} > 0.1$ were chosen for subsequent administration to the gingival sulci of the 2nd mandibular molars of the jaws. Solutions were administered at 10-μL scale to the sulcus using syringes with 23G blunt tips. For a given jaw, the order of events was sulcus irrigation, application of ultrasound gel, imaging, and washing with faucet DI water. This process was repeated for each solution. Ultrasound gel was used for acoustic coupling and 3D photoacoustic-ultrasound images were collected using a 40-MHz transducer (LZ-550) with the Vevo LAZR system. B-mode frames were registered via maximum intensity projection.

8.2.12. Ex Vivo Murine Brain Imaging

Resected murine brains were purchased from Jackson Laboratories (Maine, USA). They were fixed in 4% paraformaldehyde for 24 hours and washed with PBS. A solution of 1% w/v agarose was heated, transferred to a petri dish, and allowed to solidify. The brains (n = 3) were placed on the agar layer and immobilized by the addition of another layer of

agar. Solutions of activity buffer, C2A (30 μM), and C2A (30 μM) + RgpB (50 nM) were prepared and incubated for 2 h: 15 μL of each were injected into the lambda points of three brains, respectively. After 5 minutes, the injections were repeated. Ultrasound gel was used for acoustic coupling and 3D photoacoustic-ultrasound images were collected using a 40-MHz transducer (LZ-550) with the Vevo LAZR system. B-mode frames were registered via maximum intensity projection.

8.3. Results And Discussion

To select a gingipain-cleavable peptide substrate, we first applied a structural model of peptide-protein affinity to screen a series of pentapeptides for their affinity to the Arg-specific cysteine protease gingipain R (RgpB, PDB: 1CVR)[547, 548]. The RgpB protease is composed of a 435-residue, single-chain polypeptide that forms a catalytic domain and an immunoglobulin-like domain [549]. The peptide candidates were generated with three constraints: a five-residue length, an arginine at the third residue (P_1), and a lysine at the fifth residue (C-terminus, P_2'). The peptide length was restricted to facilitate intramolecular interaction between N and C terminal dyes while reducing the likelihood of cleavage by off-target proteases. The central arginine was necessary for cleavage by RgpB, and the C-terminal lysine was chosen for its reactive free amine. These conditions allowed us to generate 8,000 possible sequences that were screened for affinity to RgpB using an open-source structural model (PepSite 2.0) based upon a library of known peptide-protein complexes [548]. The results were plotted as the inverse p-value to signify relative affinity (**Figure 8.1A**) where the p-value represents the statistical significance for the overall score of a given binding site defined by Petsalaki et al. [553]. Of these peptides, the top result that did not contain a cysteine (excluded to reduce effects from dithiol coupling) was APRIK (p-

value 0.0266) and was selected for probe synthesis. Additionally, the median result (TTRIK (p-value: 0.1866)) and last result (EEREK (p-value: 0.6872)) were synthesized and conjugated with dyes to serve as experimental controls for the model predictions (**Figure 8. 1B**). Visualization of the APRIK-RgpB interaction demonstrated that the peptide was predicted to bind the catalytic domain of RgpB (**Figure 8.1C**). The three candidate peptides were used to synthesize homodimer probes $[Cy5.5]_2$[APRIK], $[Cy5.5]_2$[TTRIK], and $[Cy5.5]_2$[EEREK], referred throughout as C2A, C2T, and C2E, respectively (**Figure 8.7**). RP-HPLC retention times for the conjugates decreased slightly from C2A (11.8 min) to C2T (11.7 min) to C2E (10.9 min), corresponding to the increasing hydrophilicity of the residues in each peptide (**Figure 8.8A-C**); the structures of the probes were confirmed with ESI-MS (**Figure 8.8D-F**).

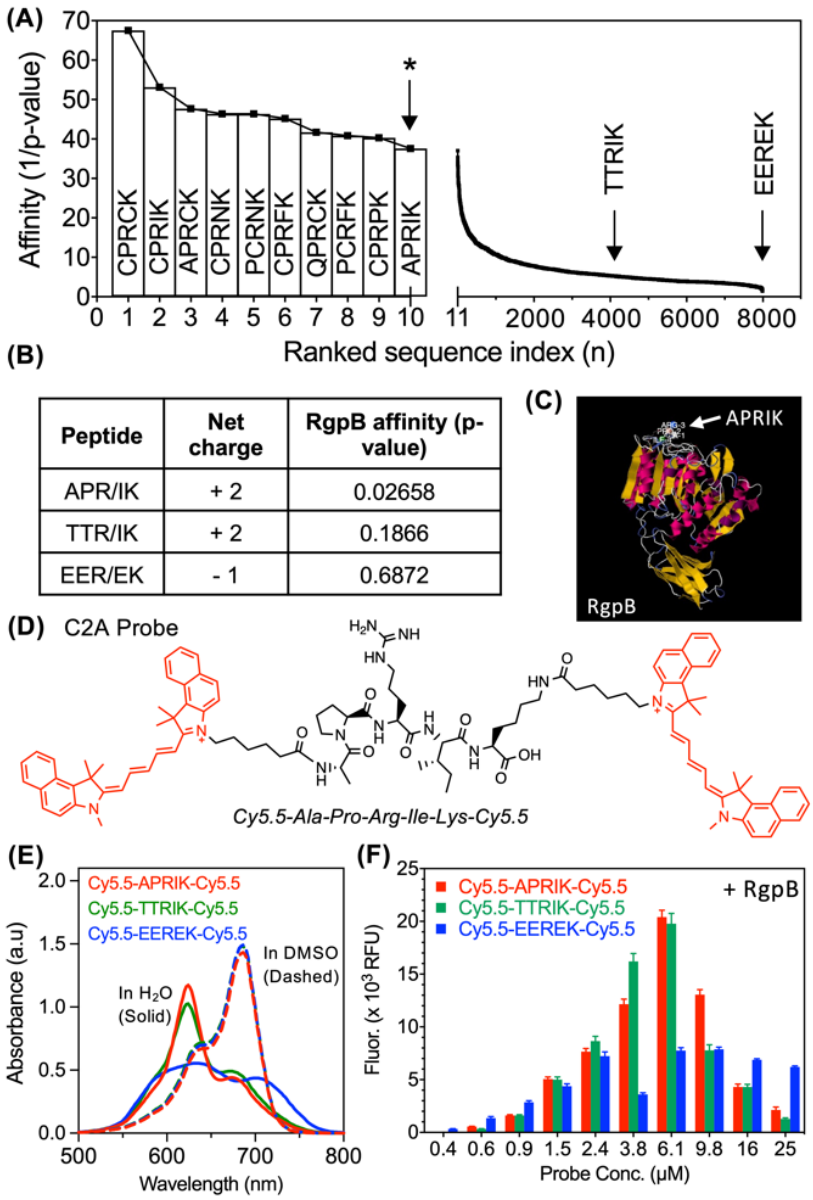

Peptide	Net charge	RgpB affinity (p-value)
APR/IK	+ 2	0.02658
TTR/IK	+ 2	0.1866
EER/EK	- 1	0.6872

Figure 8.1. Structural selection and optical validation of photoacoustic/fluorescent peptides for RgpB.

(A) Rankings of modeled peptide affinities for RgpB using an open-source structural model. All 8,000 five-residue peptides with a P1-arginine and C-terminal lysine were screened against RgpB (PDB: 1cvr). The affinities were plotted as the inverse p-values corresponding to the statistical significance of the peptide-protein interaction. APRIK was identified as the top candidate containing no cysteine residues (cysteine-containing sequences were excluded due to their potential for disulfide bridging). **(B)** APRIK, TTRIK (median affinity), and EEREK (lowest affinity) were selected for double conjugation with Cy5.5. **(C)** Structural model of top match (APRIK) with RgpB indicates preferential affinity for the catalytic domain. **(D)** Molecular structure of the dye-conjugated peptide, $[Cy5.5]_2$[APRIK]. **(E)** Absorbance spectra of the conjugates in DMSO vs. H_2O (1% DMSO) at equimolar concentrations (15 μM). **(F)** Fluorescence intensities for each conjugate after 1.5 h at a range of concentrations incubated with 25 nM RgpB.

The absorbance maxima of the conjugates in water were blue-shifted relative to their spectra in DMSO (**Figure 8.1E**)—a solvatochromic effect indicative of aromatic dye stacking[554]. This blue shift confirmed intramolecular dye coupling, i.e., DMSO promotes intramolecular separation of the dyes by neutralizing their attractive π–π interactions, thus mimicking the effect of proteolytic cleavage of the peptide linker. Indeed, the fluorescence of the intact conjugates was also self-quenched but was activated upon incubation with RgpB: We measured the fluorescence from each conjugate at a range of concentrations with constant RgpB and observed stronger fold-enhancement for C2A/C2T than C2E (**Figure 8.1F**). While C2A and C2T performed similarly in this comparison, we selected C2A for further development due to its higher predicted affinity for RgpB and higher signal to background ratio at concentrations > 6 μM. The decreased activation at higher concentrations was caused by increased self-quenching of the probes, though this is dependent upon the amount of DMSO in the mixtures. Upon incubation of C2A with RgpB, the absorbance maxima of the dyes at 680 nm were recovered with increasing concentrations of protease **(Figure 8.2A**). The fluorescence emission at 700 nm was also proportionally enhanced (**Figure 8.2B**). The fluorescence limit of detection was 1.1 nM (linearity 0 – 5 nM) (**Figure 8.2C**). Additionally, the photoacoustic intensity of the samples excited at 680 nm was proportional to their absorption (**Figure 8.2A,D**), and the photoacoustic limit of detection was 10 nM RgpB.

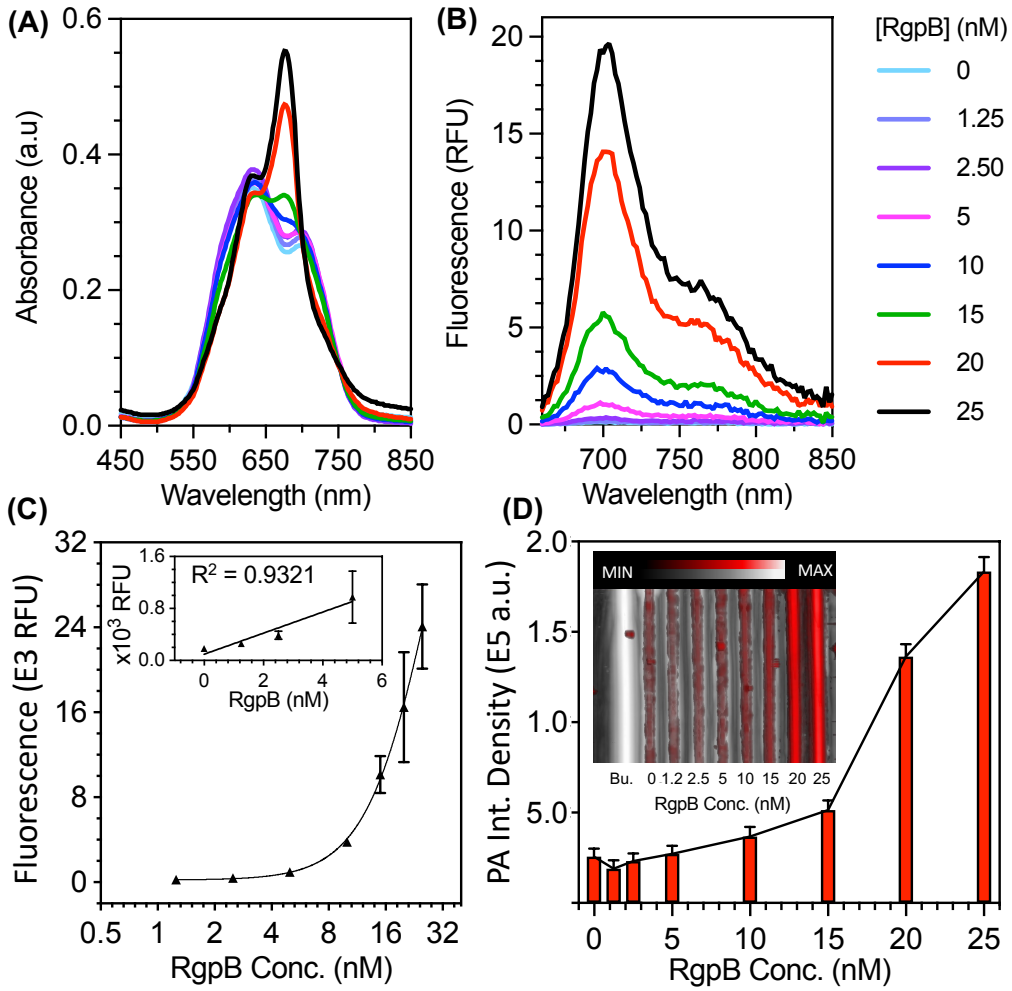

Figure 8. 2. Optical and photoacoustic limits of detection for C2A with recombinant RgpB. **(A)** Absorbance spectra of C2A incubated with 0 – 25 nM RgpB after 90 minutes. (**B**) Fluorescence spectra (ex: 600 nm, em: 700 nm) of the samples after 90 minutes. (**C**) Fluorescence limit of detection for RgpB via fluorescence area scan (ex: 625, em: 700 nm, LOD = 1.1 nM, linear range: 0 – 5 nM, $R^2 = 0.93$, n = 2, error = SEM). (**D**) Photoacoustic-ultrasound image with quantitated intensities for RgpB from 0 – 25 nM (ex: 680 nm, LOD = 15 nM, inset = raw photoacoustic ultrasound image, Bu. = buffer).

To further verify the probe's sensitivity and selectivity for gingipains associated with *P. gingivalis*, we grew and isolated bacterial supernatants from both *P. gingivalis* and another oral anaerobe, *F. nucleatum* (**Figure 8.3A**). *F. nucleatum* is a good negative control because it is also commonly identified in the gingival sulcus but is a saccharolytic and commensal bacterium known to not secrete gingipains [555]. These anaerobes were first grown

on blood agar and enumerated from liquid suspensions via optical density after development of standard curves (**Figure 8.9, Figure 8.10**). The presence of Arg-specific gingipain in the *P. gingivalis* cultures was confirmed with a commercially available enzyme-linked immunoassay (ELISA) kit (**Figure 8.11**); in addition, activity was measured by incubation with a commercially available fluorescent substrate, Boc-Phe-Ser-Arg-AMC, as previously described[556] (**Figure 8.12**). Then, upon incubation of the C2A probe with *P. gingivalis* supernatant, we directly observed cleavage of intact C2A (T_R = 21.2 min) into Cy5.5-APR (T_R = 17.2 min, $[M+2H]^{2+}$ = 412.91 m/z) and IK-Cy5.5 (T_R = 18.2 min, $[M+2H]^{2+}$ = 454.93 m/z) fragments with HPLC and ESI-MS (**Figure 8.13**), thus demonstrating the expected activity of Arg-gingipain in the bacterial supernatant and intended cleavage of C2A. Indeed, the probe activated fluorescence 135-fold over the course of 2 hours, corresponding to enhanced emission at 700 nm and absorbance at 680 nm (**Figure 8.3B, Figure 8.14**); this activation was reduced by 97% upon coincubation with leupeptin—a known gingipain inhibitor[557] (**Figure 8.3B**). The fluorescence was not activated by *F. nucleatum*. As with fluorescence, we observed an increasing trend for the photoacoustic intensities of the samples excited at 680 nm, thus demonstrating selective photoacoustic imaging of gingipains from *P. gingivalis* (**Figure 8.3C-D**). The limits of detection for the bacteria were tested via serial dilution of the supernatants in broth and determined to be 4.4E4 CFU/mL via fluorescence and 4.1E5 CFU/mL via photoacoustics (**Figure 8.3E-F, Figure 8.15**).

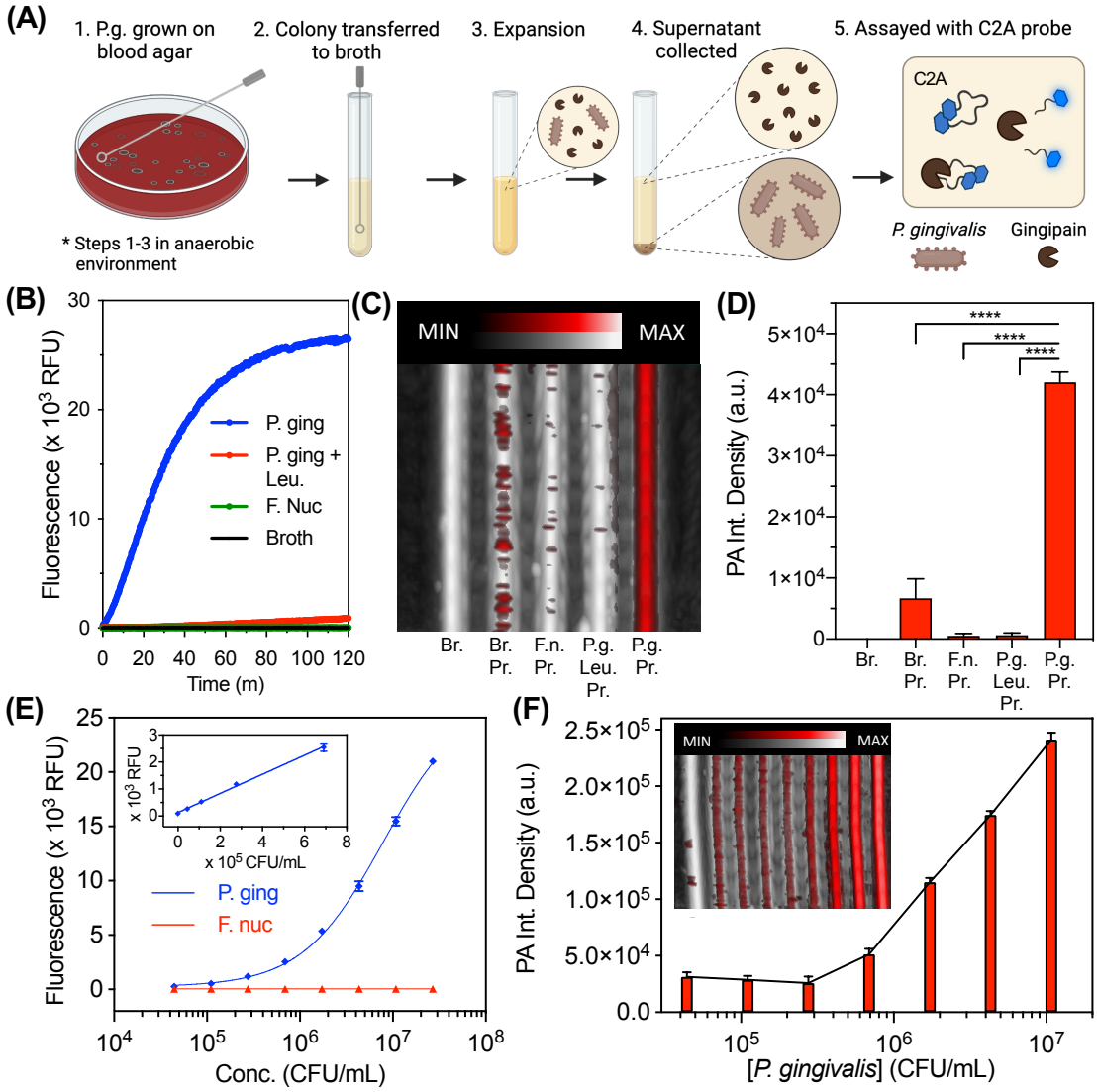

Figure 8. 3. Optical and photoacoustic properties of C2A with bacterial supernatants from cultured *P. gingivalis*.
(**A**) Schematic of workflow for bacterial growth and assay. The same steps were performed for *P. gingivalis* and *F. nucleatum*. (**B**) Kinetics of C2A (10 µM) fluorescence activation with *P. gingivalis* supernatant, *P. gingivalis* supernatant with inhibitor (50 µM leupeptin), *F. nucleatum* supernatant, and culture broth alone (tryptic soy broth). Supernatants were assayed at 37 °C after 50% (v/v) dilution in buffer (final conditions: 2.5E7 CFU/mL bacteria, 20 mM Tris, 1 mM DTT, 2% DMSO, pH 7.3) (**C**) Photoacoustic-ultrasound MIP image of the samples with 680-nm pulsed excitation. Br = Broth, Pr = Probe, F. n. = F. nucleatum, P. g. = *P. gingivalis,* Leu = Leupeptin. (**D**) Quantitation of Panel D via integrated pixel density. Error bars = SD, asterisks denote significant difference (unpaired two-tailed t-test, p-value < 0.001). (**E**) Fluorescence limit of detection for *P. gingivalis* supernatants (LOD = 4.4E4 CFU/mL, linear range: 0 – 6.9E5 CFU/mL, R^2 = 0.99). (**F**) PA image and quantitation of the same samples (ex: 680 nm) via integrated density (LOD = 4.1E5 CFU/mL, linear range: 0 - 4.3E6 CFU/mL, R^2 = 0.94).

To date, reported strategies for measurement of gingipain activity have used in vitro detection methods, including a nanobody immunoassay[540], an electrochemical biosensor[558], fluorogenic dipeptides[541], peptide-functionalized magnetic nanobeads[559], and refractometry of protein-functionalized gold nanoparticles[542]. These have reported detection limits of 7.81E6 CFU/mL bacteria, 5E5 CFU/mL bacteria, 1E5 CFU/mL bacteria, 49 CFU/mL bacteria, and 4.3 nM Kgp (CFU/mL not reported), respectively. While the C2A probe has comparable sensitivity to these in vitro sensors (fluorescence LOD: 4.4E4 CFU/mL and 1.1 nM RgpB, photoacoustic LOD: 4.1E5 CFU/mL and 15 nM RgpB), it is the first reported gingipain probe suitable for photoacoustic imaging while also achieving a dual-modal fluorescence readout, with applicability for in vivo oral photoacoustic imaging, a technique that is gaining preclinical traction [210, 358, 560]. The added value of imaging is the monitoring of disease progression or response to therapy with the spatial integration of anatomic markers of disease. Indeed, to characterize the imaging performance of the C2A probe in relevant oral anatomy, it was used to resolve the periodontal pocket/gingival sulcus of intact porcine jaws with photoacoustic-ultrasound imaging (**Figure 8.4**). Here, buffer, C2A, and C2A + RgpB (25 and 50 nM), were irrigated sequentially into the gingival sulcus of the second molar of a porcine mandible (n = 3). 3D photoacoustic-ultrasonographs of the tooth/gingiva were generated (**Figure 8.4A**, left) and anatomical markers were readily resolved in the midsagittal cross sections (**Figure 8.4A**, right), including the gingival margin (GM, pink) and alveolar bone crest (ABC, teal). The uncleaved C2A probe did not possess significantly more photoacoustic signal (red) than buffer alone (**Figure 8.4B**). However, C2A activated with 25-50 nM RgpB generated clear and increasing subgingival photoacoustic signal (**Figure 8. 4C-E,** yellow boxes), representing the subgingival distribution of RgpB-cleaved

probe. In addition, spectral imaging could distinguish the imaging signal from cleaved C2A (< 750 nm) from the relatively flat spectra from supragingival signal caused by tooth staining (**Figure 8.4F-G**). Overall, this experiment demonstrates the ability to image the spatial distribution of subgingival gingipain activity in relation to key landmarks of oral anatomy while achieving low nanomolar sensitivity.

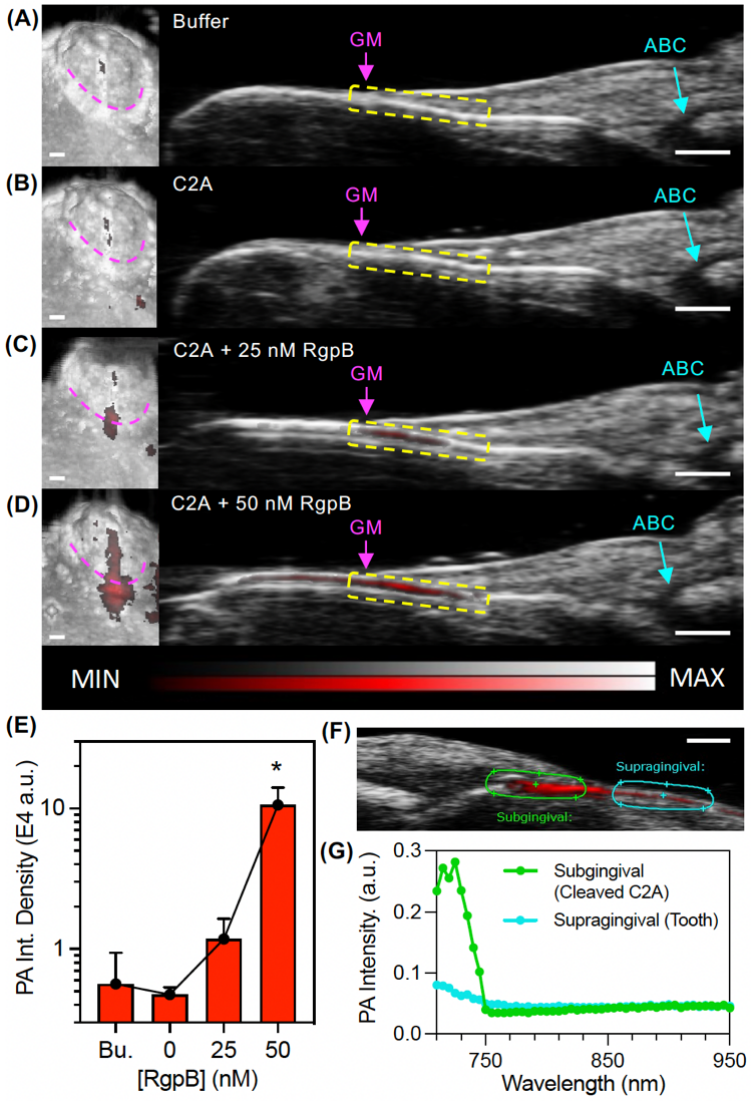

Figure 8. 4. Photoacoustic-ultrasound imaging of RgpB-activated C2A probe in the gingival sulci of porcine jaws.
(A) Left: 3D rendering of a mandibular second molar with PA signal (red) overlay on the US image (grayscale) following administration of Tris buffer at the gingival margin (pink). Right: cross-sectional image of the midsagittal plane of the tooth with the gingival margin (GM), alveolar bone crest (ABC), and gingival sulcus (yellow) labeled. **(B-D)** Images of the same site following administration of **(B)** C2A alone, **(C)** C2A + 25 nM RgpB, and **(D)** C2A + 50 nM RgpB. The sulcus was irrigated with water between imaging events. **(E)** Quantitation of the PA signal via integrated density for the maximum intensity projection of each PA image (n = 3 mandibles). **(F)** PA-US spectral image of subgingival signal corresponding to injected C2A (green ROI) and supragingival signal corresponding to background from the tooth surface (teal). **(G)** PA spectra of the regions in Panel F. Scale bars = 1 mm.

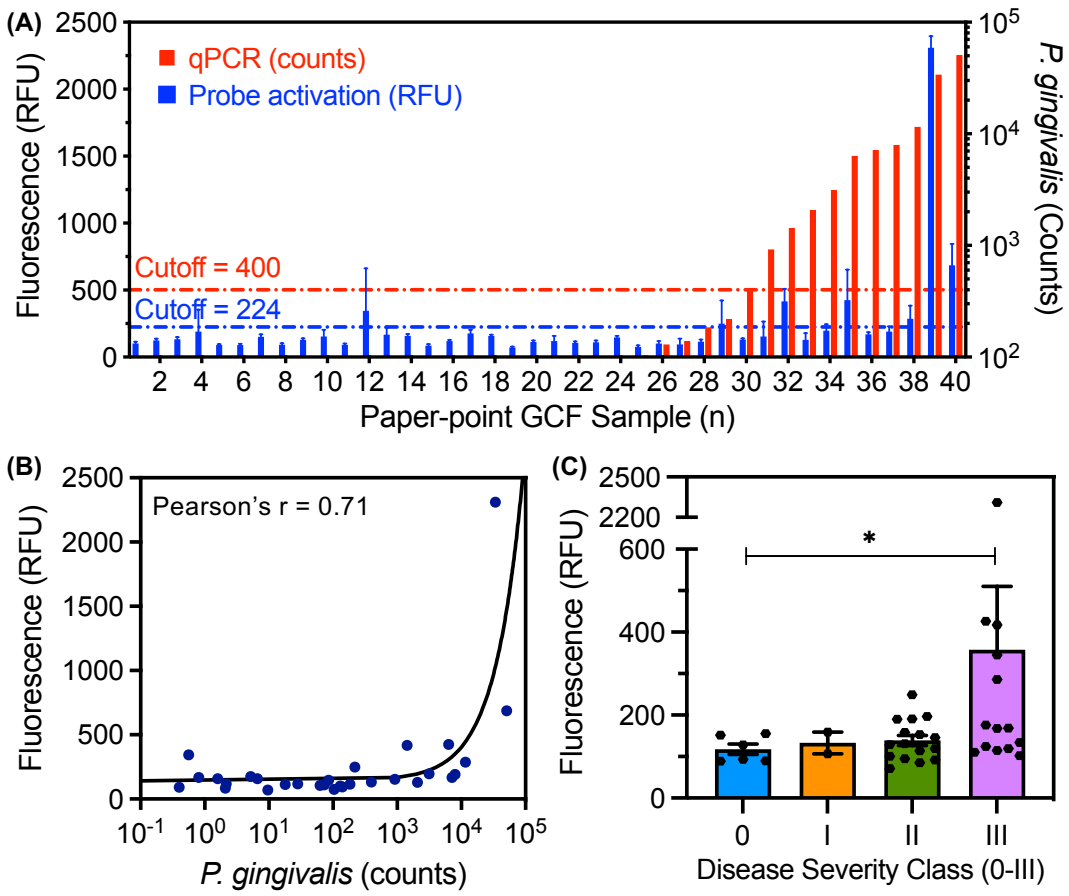

Figure 8. 5. Comparison between qPCR for P. gingivalis and fluorescence of C2A probe in GCF samples from a set of 20 subjects (n = 40 tooth sites).
(**A**) Number of *P. gingivalis* cells (red) and probe activation (blue, gingipain activity) for each GCF sample (error bars = SD of fluorescence area scans, n = 13 points per well). (**B**) Correlation between number of *P. gingivalis* cells and probe activation (Pearson's r = 0.71, two-tailed, $p < 0.0001$). (**C**) Probe activation for individual tooth sites from human subjects as a function of clinically diagnosed periodontal disease severity (Welch's one-tailed t-test, 90% confidence: p-value = 0.07 < 0.10, error bars = SEM).

In a study by Guentsch et al., ELISA was used to identify micromolar concentrations of gingipain in gingival crevicular fluid (GCF) collected with paper point sampling from patients with periodontal disease [524]. This is well above the low nanomolar detection limits of C2A for RgpB: Therefore, to evaluate the diagnostic efficacy of the C2A probe in clinically relevant samples, we collected GCF from 40 tooth sites in a set of 20 subjects, comprising both healthy patients and individuals with symptoms of periodontal disease sampled at a dental clinic. The GCF samples were assayed with both qPCR and C2A via

fluorescence to measure the number of *P. gingivalis* cells and proteolytic gingipain activity, respectively. Of these, 25% (10/40) contained *P. gingivalis* via qPCR and these were considered positives (**Figure 8.5A**). Gingipain activity via C2A fluorescence was correlated with the PCR results (Pearson's r = 0.71, **Figure 8.5B**), albeit with lower sensitivity: Fluorescence activation was observed in 5/10 of the positives and 2/30 of the negatives, corresponding to a detection rate of 50% and a false positive rate of 6.67% (**Figure 8.5A**). However, the higher sensitivity of qPCR was expected given its inherent signal amplification mechanism. Another difference is that while qPCR may reflect the amount of live and dead cells, it is not a measurement of the active gingipain activity that is evidenced to play a direct role in the pathogenic process of periodontal disease [561]. The activity data was also analyzed with respect to disease severity for each tooth site (**Figure 8.5C**). Interestingly, gingipain activity was primarily observed in the GCF from Class III sites (with the greatest total facial CAL). Though half of these sites did not exhibit gingipain activity, these results support the hypothesis that local gingipain activity may contribute to more severe periodontal damage.

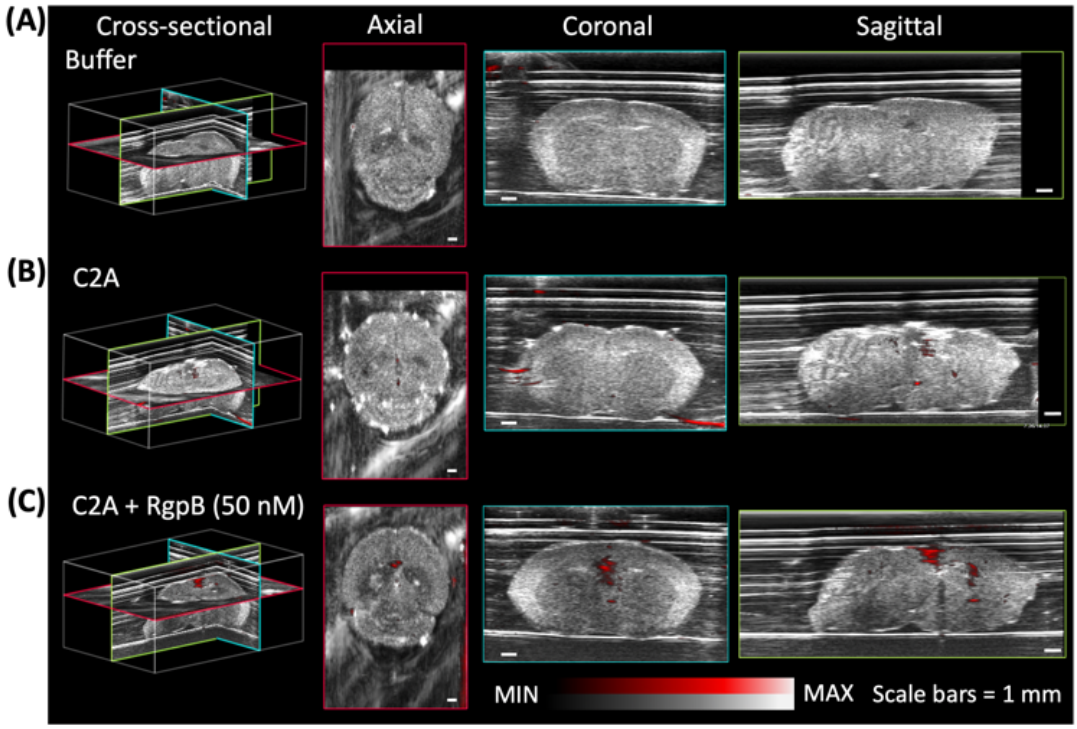

Figure 8. 6. Photoacoustic imaging of RgpB-activated C2A probe in murine brains. Photoacoustic-ultrasound images of fixed murine brains injected at the lambda point with (**A**) buffer, (**B**) C2A probe, and (**C**) C2A probe + RgpB, show enhanced intraparenchymal photoacoustic signal for RgpB-cleaved probe. Photoacoustic intensity (red) is overlaid on ultrasound intensity (grayscale). Scale bars = 1 mm.

Lastly, the potential role of *P. gingivalis* and gingipains in neurological pathologies, especially Alzheimer's disease, is of mounting research interest [538, 562-564]. Photoacoustic imaging is well-suited for real-time imaging and monitoring of murine disease models, and thus we performed proof of concept imaging of cleaved and uncleaved probe in extracted murine brains (fixed in 1% agar). The C2A probe was first incubated with RgpB at increasing probe concentrations to confirm cleavage at sufficient concentrations for imaging in animal tissue (**Figure 8.16A-B**), and the highest tested concentration (30 μM) was chosen for injection (**Figure 8.16C**). Subsequently, aliquots of buffer, C2A, and C2A + RgpB (pre-incubated and monitored for 2 h) were injected into the lambda points of respective brains

(**Figure 8.16D**)—these were then imaged in 3D with a photoacoustic-ultrasound scanner at 680 nm using sonography gel for acoustic coupling. Negligible photoacoustic signal was detected in the buffer-injected brain (**Figure 8.6A**), while minor background was observed for the uncleaved probe (**Figure 8.6B**). The strongest signal was detected from the brain injected with C2A + RgpB, visible in axial, coronal, and sagittal cross-sections of the tissue (**Figure 8.6C**). Further, spectral photoacoustic imaging of the injected brains allowed signal from C2A to be distinguished from background by its characteristic absorption/photoacoustic peak in the near infrared (**Figure 8.17**). These experiments demonstrate that the C2A probe could have value as a research tool for gingipain imaging in more complex models of infection for Alzheimer's disease pathogenesis. Future studies may integrate the probe with in vivo models of *P. gingivalis* infection, though potential limitations include issues that affect many small-molecule photoacoustic probes, including low signal to background ratio in blood at low concentrations and photoinstability associated with the dissociation of conjugated π electrons following absorption [554, 565]. Nevertheless, proof-of-concept imaging utility was demonstrated in the oral cavity and brain parenchyma using resected porcine jaws and murine brains, respectively. Lastly, in future efforts to improve sensitivity to *P. gingivalis*, a lysine residue could be included in the peptide linker for cleavage by Lys-gingipain (Kgp), in addition to D-amino acids for increased bacterial specificity [566].

8.4. Conclusions

In summary, a molecular imaging probe, C2A, was designed and synthesized to harness the intramolecular dimerization of peptide-linked cyanine dyes to induce fluorescence and photoacoustic off-states. Upon proteolytic cleavage by Arg-specific

gingipain (RgpB), 5-fold photoacoustic enhancement and >100-fold fluorescence enhancement was achieved with detection limits of 1.1 nM RgpB and 4.4E4 CFU/mL bacteria. RgpB activity was imaged in the subgingival pocket of porcine mandibles with 25 nM sensitivity. The diagnostic efficacy of the probe was evaluated in gingival crevicular fluid (GCF) samples from subjects with (n = 14) and without (n = 6) periodontal disease; activation correlated to qPCR-based detection of *P. gingivalis* (Pearson's r = 0.71), and activity was highest in subjects with the most severe disease progression. Lastly, photoacoustic imaging of RgpB-cleaved probe was demonstrated in murine brains *ex vivo*, thus demonstrating future utility for imaging studies of general infection by *P. gingivalis*.

8.5. Acknowledgements

Chapter 8, in full, has been submitted for publication of the material as it may appear in Angewandte Chemie, 2022. Moore, Colman; Tjokro, Natalia; Zhang, Brendan; Hayati, Mohammed; Cheng, Yong; Chang, Kai Chiao J.; Chen, Casey; Jokerst, J. V. The dissertation author was the primary investigator and author of this paper.

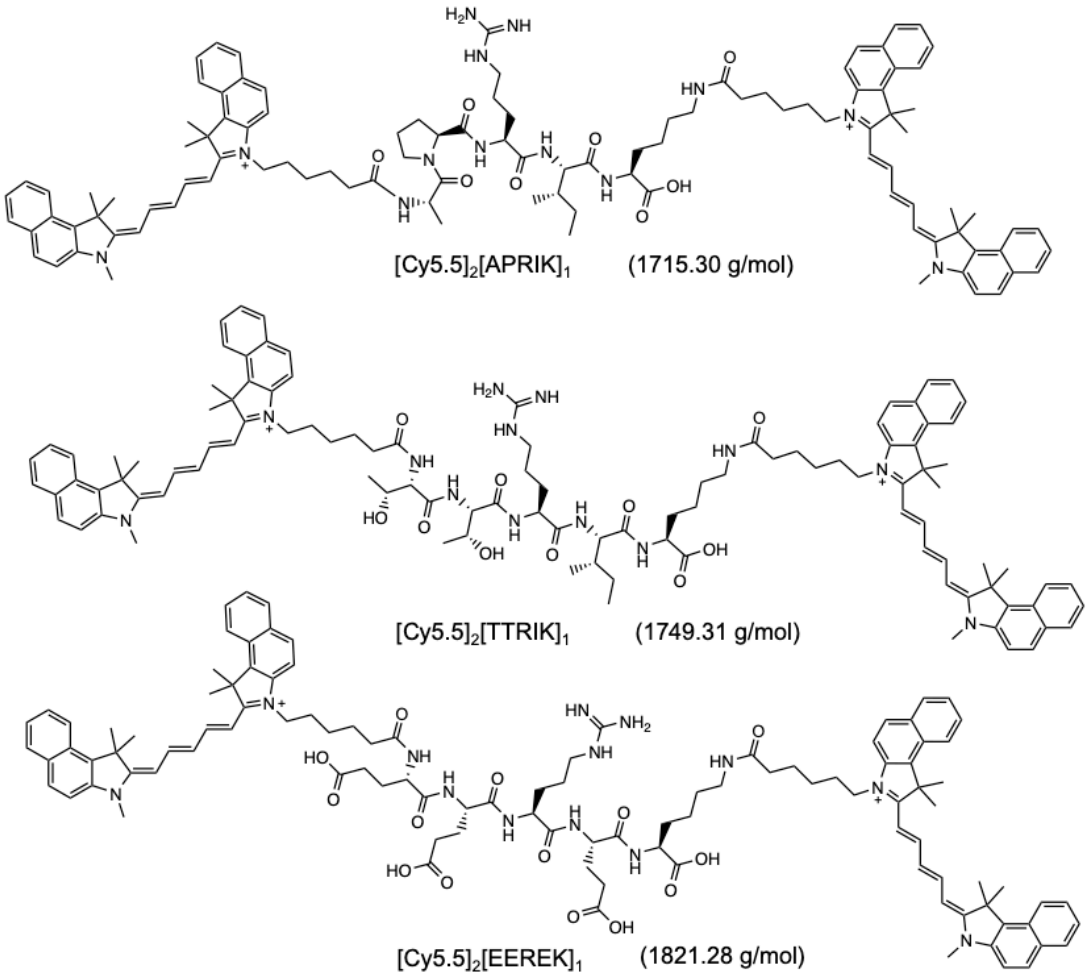

Figure 8.7. Structures of Rgp-cleavable probes.

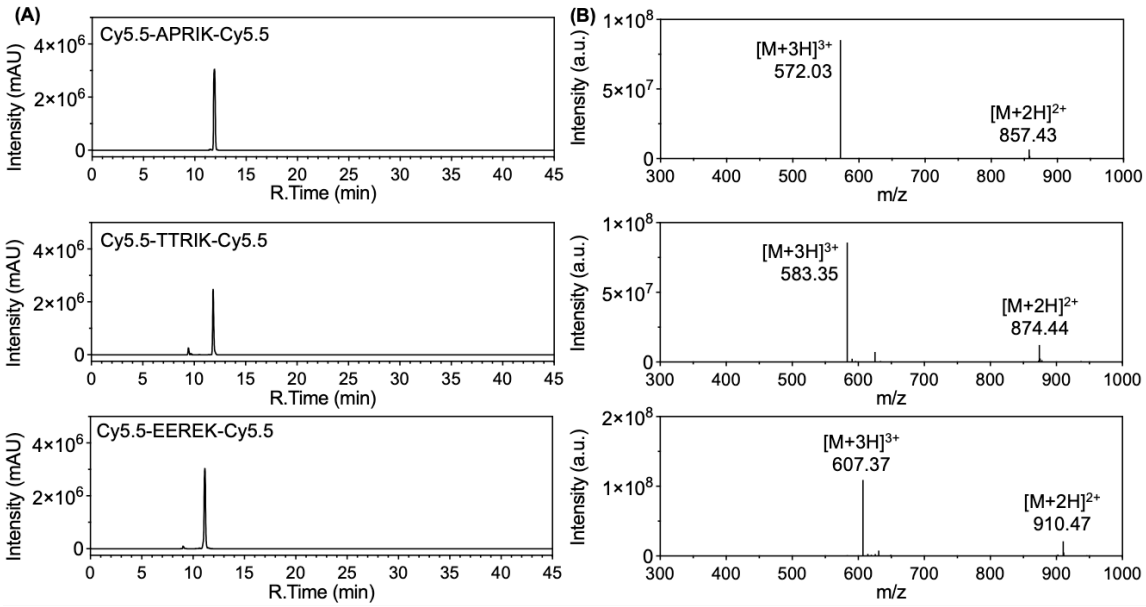

Figure 8.8. HPLC and ESI-MS of RgpB-cleavable probes.

(A) HPLC of Cy5.5-APRIK-Cy5.5 (98.4%), Cy5.5-TTRIK-Cy5.5 (89.2%), and Cy5.5-EEREK-Cy5.5 (95.4%). Samples were eluted at 1 mL/min with a 30-min gradient from 25% to 95% B (A: H_2O (0.05% TFA), B: MeCN (0.05% TFA)). (B) ESI-MS of Cy5.5-APRIK-Cy5.5 (expected $[M+3H]^{3+}$: 572.01, detected: 572.03, expected $[M+2H]^{2+}$: 857.51, detected: 857.43), Cy5.5-TTRIK-Cy5.5 (expected $[M+3H]^{3+}$: 583.35, detected: 583.35, expected $[M+2H]^{2+}$: 874.51, detected: 874.44), Cy5.5-EEREK-Cy5.5 (expected $[M+3H]^{3+}$: 607.33, detected: 607.37, expected $[M+2H]^{2+}$: 910.49, detected: 910.47).

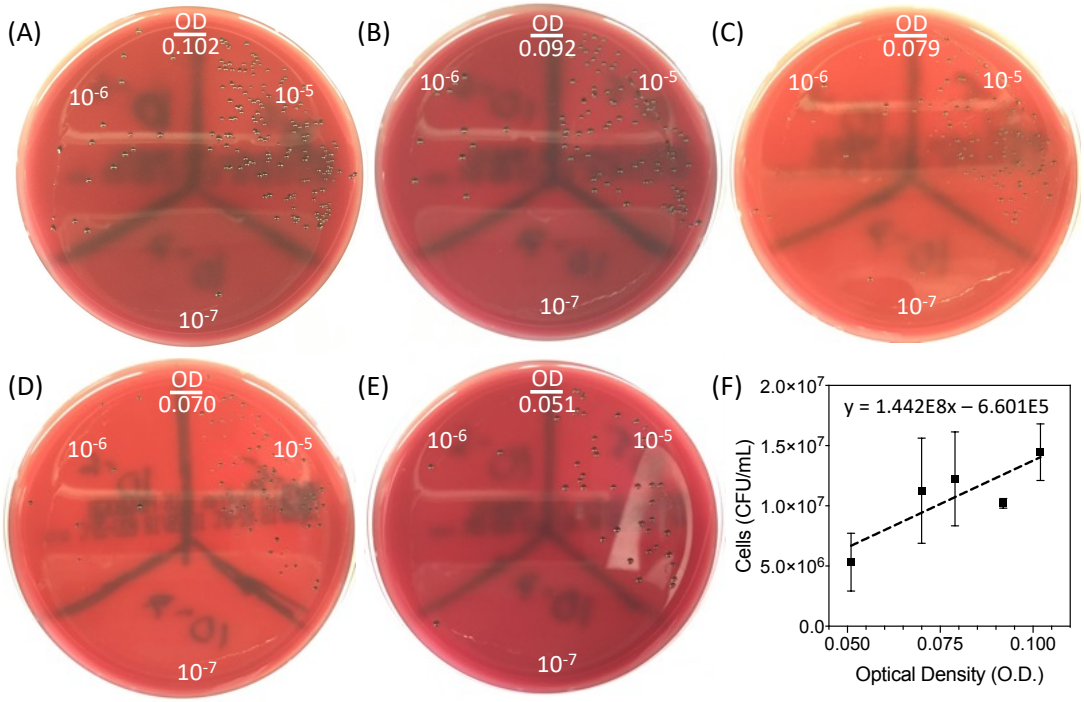

Figure 8. 9. *P. gingivalis* plates and standard curve for enumeration of colony forming units from optical density.
(A-E) *P. gingivalis* colonies (with characteristic black pigmentation) plated and grown anaerobically from liquid culture stocks between 0.051 - 0.102 OD (600 nm) and further diluted for plating by 10^{-5}, 10^{-6}, and 10^{-7}. (F) Colonies were counted and converted to CFU/mL to generate a standard curve.

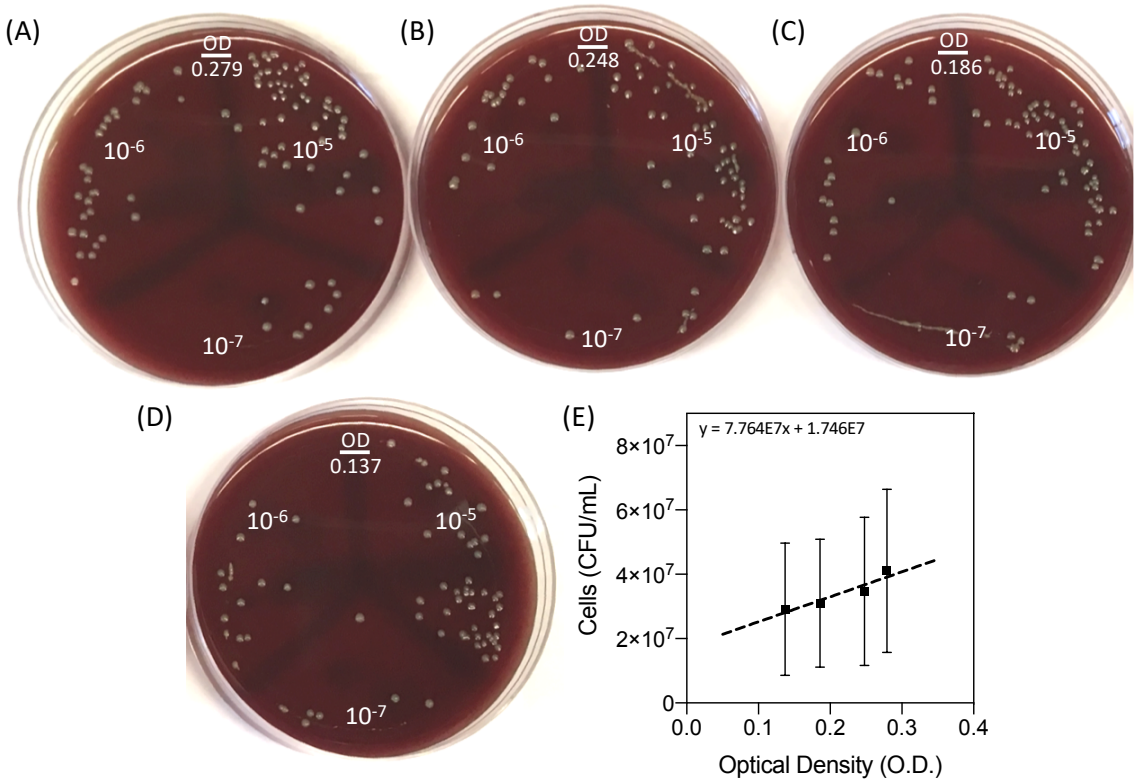

Figure 8. 10. *F. nucleatum* plates and standard curve for enumeration of colony forming units from optical density.

(A-E) *F. nucleatum* colonies plated and grown anaerobically from liquid culture stocks between 0.137 - 0.279 OD (600 nm) and further diluted for plating by 10^{-5}, 10^{-6}, and 10^{-7}. (F) Colonies were counted and converted to CFU/mL to generate a standard curve.

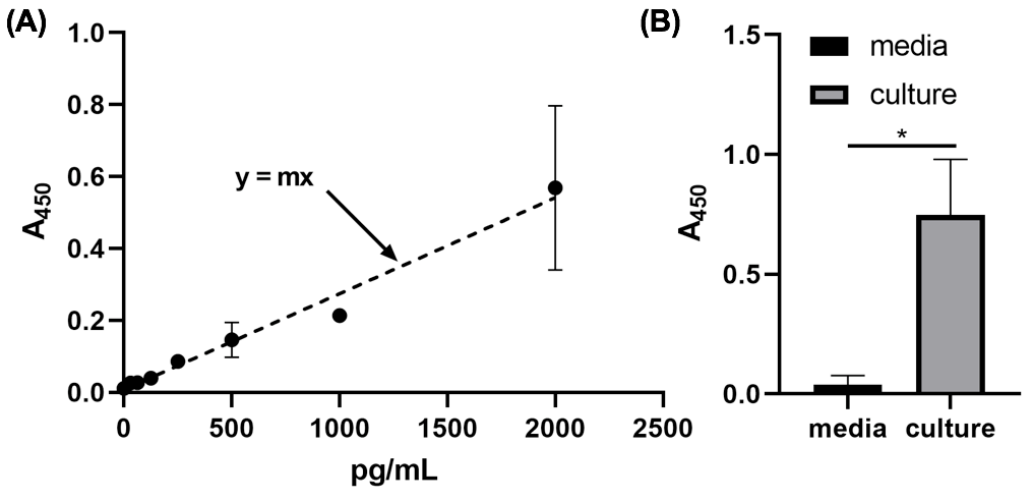

Figure 8. 11. ELISA detection of Rgp in *P. gingivalis* supernatant.
(A) Standard curve for Rgp detected via commercially available ELISA where m = 2.7 x 10^{-4} ± 0.2 x 10^{-4}. (B) P.g. culture supernatants contained significantly more Rgp than media alone. [Rgp] from supernatants = 2800 ± 600 pg/mL. Error bars represent the standard error for the mean for n = 2 experiments. Asterisks denote values from a one-tailed t-test (*$p < 0.05$).

(A)

Sample	Initial rate (RFU/min)
eTSB	123.6
P.g. + inhibitor	481.6
P.g.	25,850

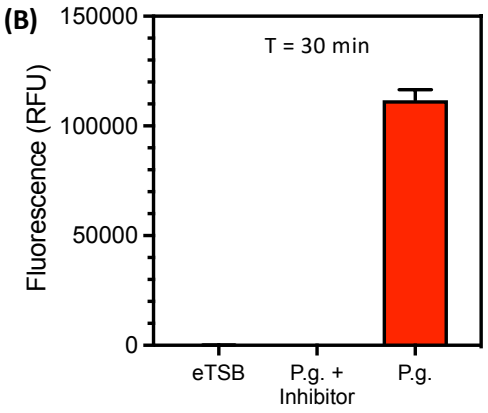

Figure 8. 12. Validation of gingipain activity in P. gingivalis supernatant with a commercial fluorescent substrate.

(A) Initial rate of activation for Boc-Phe-Ser-Arg-AMC in cell broth (eTSB: enriched tryptic soy broth), *P. gingivalis* supernatant + inhibitor (leupeptin 50 μM), and *P. gingivalis* supernatant. Each sample was diluted by 50% v/v in activity buffer (ex: 360 nm, em: 450 nm). (B) Activation after incubation for 30 minutes at 37 °C.

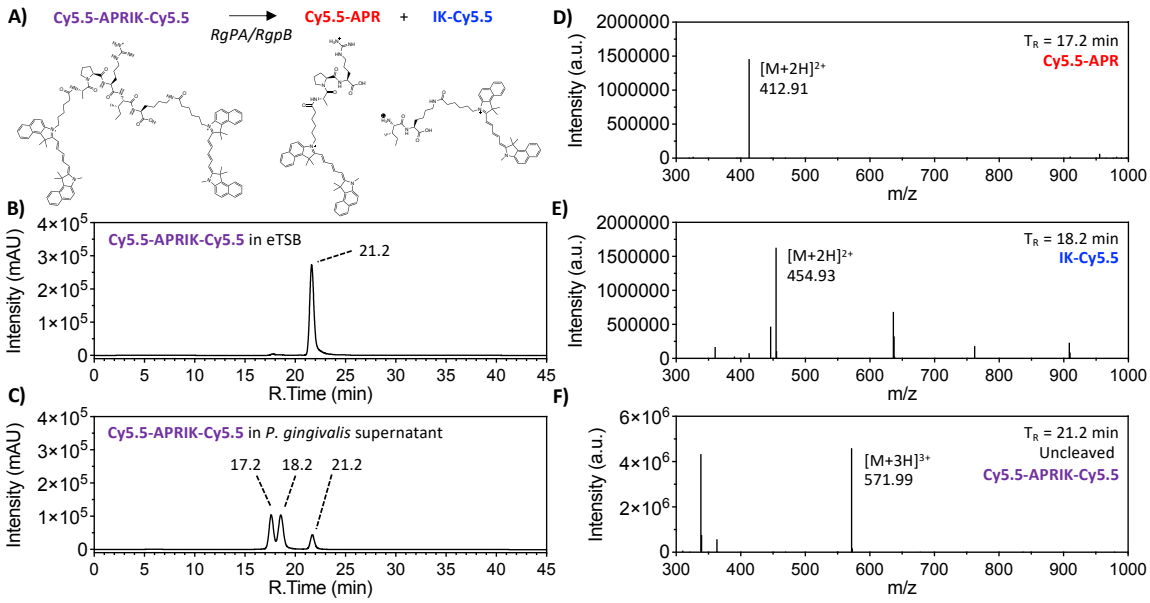

Figure 8. 13. Enzymatic cleavage of C2A by *P. gingivalis* supernatant.
(A) Schematic of proteolytic reaction and cleavage products. (B) HPLC of 10 µM C2A in 50% v/v eTSB: buffer (20 mM, 1 mM DTT, pH 7.4), 2% DMSO. The gradient was from 25-95 %B over 30 min (A: H_2O, 0.05% TFA, B: MeCN, 0.05% TFA). (C) HPLC of 10 µM C2A in 50% v/v *P. gingivalis* supernatant (2.7E7 CFU/mL): buffer. (D) ESI-MS of the 17.2-min fraction from Panel C identified as Cy5.5-APR (expected $[M+2H]^{2+}$: 412.76 m/z, detected: 412.91 m/z). (E) ESI-MS of the 18.2-min fraction identified as IK-CY5.5 (expected $[M+2H]^{2+}$: 454.26 m/z, detected: 454.93 m/z). (F) ESI-MS of the 21.2-min fraction containing uncleaved probe (expected: 572.01 m/z, detected: 571.99 m/z).

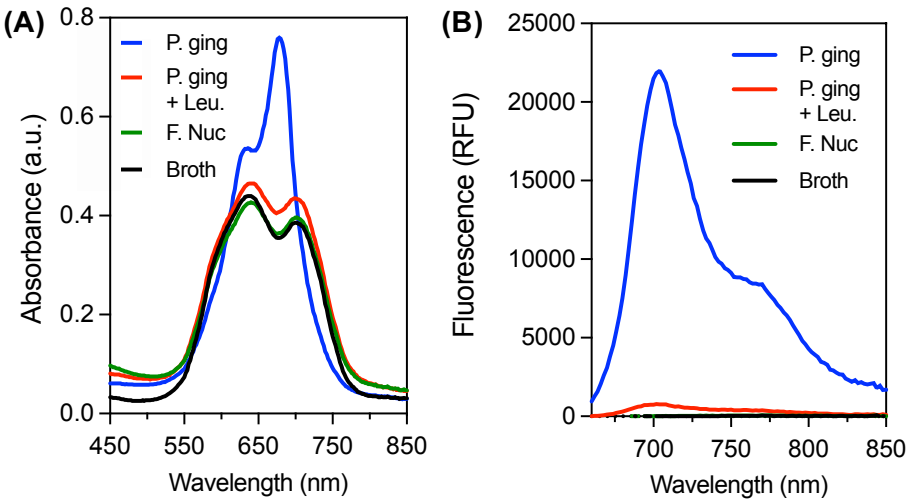

Figure 8. 14. Absorbance and fluorescence spectra for C2A incubated with supernatants from bacterial cultures.

(A) Absorbance spectra of C2A after incubation with *P. gingivalis* supernatant, *P. gingivalis* supernatant with inhibitor (50 µM leupeptin), *F. nucleatum* supernatant, and culture broth alone (eTSB). Supernatants (from 2.5E7 CFU/mL cultures)/broth were diluted by 50% v/v in activity buffer and assayed after 2 h incubation at 37°C. (B) Fluorescence emission spectra of the samples (ex: 600 nm).

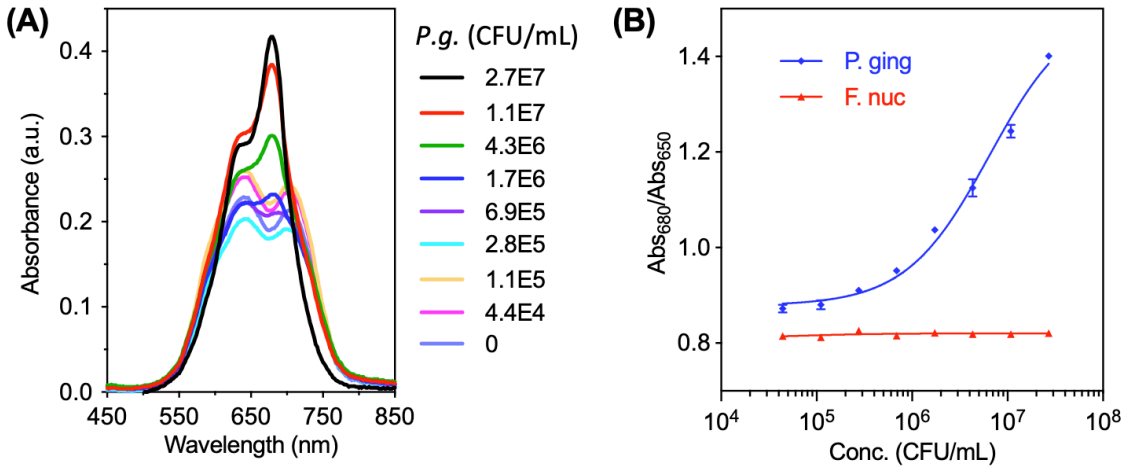

Figure 8. 15. Absorbance-based measurement of titrated P. gingivalis bacterial supernatants with C2A probe.

(A) Absorbance spectra of C2A (10 μM) incubated with a concentration gradient of *P. gingivalis* supernatants (2 h, 37 C) in 50% v/v activity buffer. (B) Limit of detection extracted from the 680/650-nm absorbance ratio for *P. gingivalis* and *F. nucleatum* (negative control).

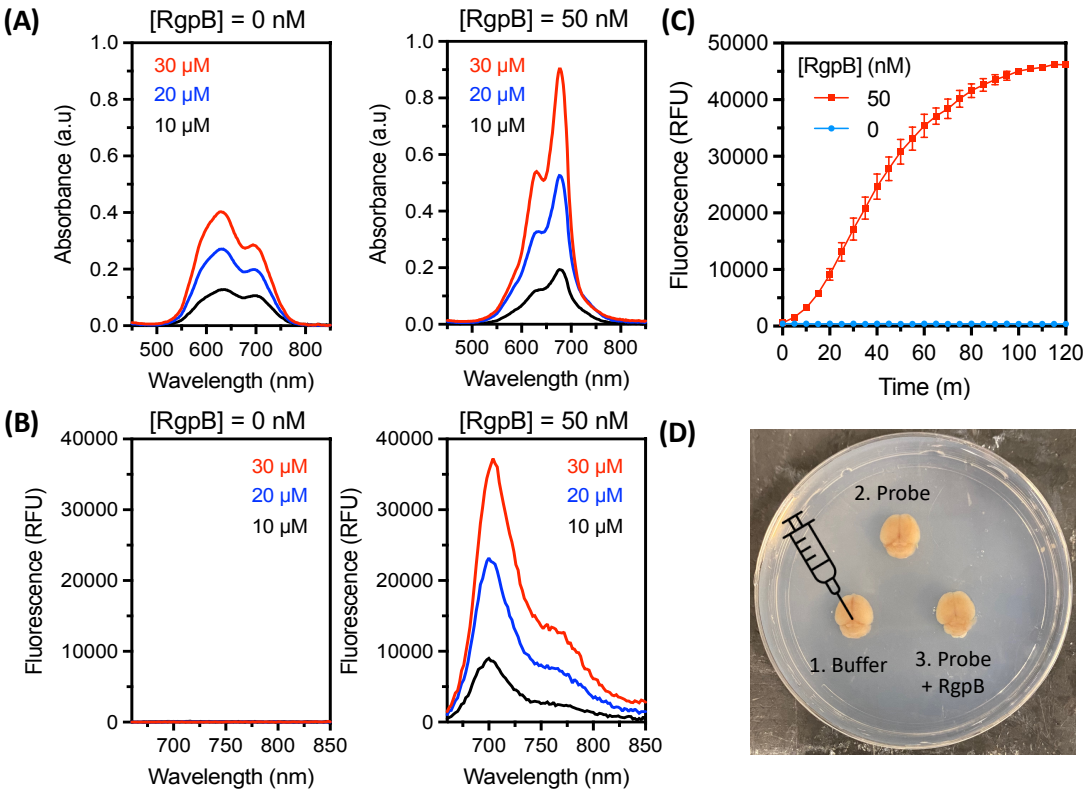

Figure 8. 16. Activation of C2A at 10 – 30 µM and phantom preparation for ex vivo murine brain imaging.

(A) Absorbance and (B) fluorescence spectra of C2A at 10, 20, and 30 µM before (left) and after (right) 2 h incubation with 50 nM RgpB. (C) Kinetics of 30-µM C2A with 50 nM RgpB used for subsequent brain injections. (D) Photograph of three murine brains embedded in a layer of 1% (w/v) agar following respective injections 15-µL injections of buffer, C2A probe (30 µM), and C2A + RgpB (50 nm).

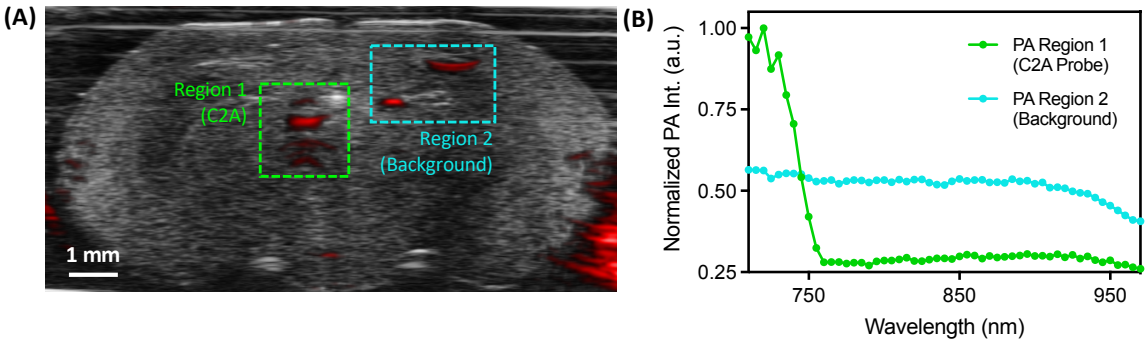

Figure 8. 17. Spectral photoacoustic imaging of C2A in a murine brain.
(A) Photoacoustic-ultrasound image of murine brain injected with C2A with two regions of interest drawn for spectral quantitation of photoacoustic signal via integrated density. (B) Normalized photoacoustic spectra for the regions of interest in Panel A: Region 1 corresponds to the injected C2A probe which can be differentiated from background signal (Region 2) by its characteristic maximum below 750 nm.

CHAPTER 9. MULTISPECTRAL NANOPARTICLE TRACKING ANALYSIS FOR REAL-TIME AND LABEL-FREE CHARACTERIZATION OF AMYLOID-β SELF-ASSEMBLY IN VITRO

ABSTRACT: The deposition of amyloid beta (Aβ) plaques and fibrils in the brain parenchyma are hallmarks of Alzheimer's disease (AD), but a mechanistic understanding of the role Aβ plays in AD has remained unclear. One important reason could be the limitations of current tools to size and count Aβ fibrils in real time. Conventional techniques from molecular biology largely use ensemble averaging; some microscopy analyses have been reported but suffer from low throughput. Nanoparticle tracking analysis is an alternative approach developed in the past decade for sizing and counting particles according to their Brownian motion; however, it is limited in sensitivity to polydisperse solutions because it uses only one laser. More recently, multispectral nanoparticle tracking analysis (MNTA) was introduced to address this limitation; it uses three visible wavelengths to quantitate heterogeneous particle distributions. Here, we used MNTA as a label-free technique to characterize the in vitro kinetics of $A\beta_{1-42}$ aggregation by measuring the size distributions of aggregates during self-assembly. Our results show that this technology can monitor the aggregation of 1E6 – 1E8 particles per mL with a temporal resolution between 15-30 minutes. We corroborated this method with the fluorescent Thioflavin-T assay and TEM, showing good agreement between the techniques (Pearson's $r = 0.821$, $P<0.0001$). We also used fluorescent gating to examine the effect of ThT on the aggregate size distribution. Finally, the biological relevance was demonstrated via fibril modulation in the presence of a polyphenolic Aβ disruptor. In summary, this approach measures Aβ assembly similar to ensemble-type measurements but with per-fibril resolution.

9.1. Introduction

Multi-spectral nanoparticle tracking analysis (MNTA) was recently introduced as a benchtop tool for quantifying particle size distributions in real time.[567] This optical technique is analogous to dynamic light scattering (DLS) and nanoparticle tracking analysis (NTA) for measuring nano-/microscale particles but offers improved capacity to track polydisperse and fluorescent suspensions. It has previously been demonstrated with various inorganic materials but investigations in the bioanalytical space have not been reported.[568, 569] Amyloid-beta (Aβ) is a notorious peptide that exhibits complex pathways of aggregation and self-assembly in physiological conditions. Self-assembling amyloid structures have long been shown to present concurrently with AD and related dementias, but it remains controversial whether they have a causative or simply correlative role. Numerous drugs have shown pre-clinical benefit (e.g. crenezumab) but failed in Phase III trials.[570-572] While this may be because Aβ is not fundamentally causative of AD, it may also be because techniques for evaluating the mechanism and rates by which Aβ self-assembles are inadequate. There is currently no single tool to quantitatively monitor its oligomerization/aggregation in real-time, in solution phase, and with per-fibril resolution of hundreds of fibrils.

Amyloidogenesis is a complex process that is still not fully elucidated—it is generally established that Aβ self-assembly follows a pathway from monomeric species (~4 kDa), to low molecular weight oligomers, to nuclei, to high molecular weight oligomers, to intermediates, to fibrils. These species vary in size and toxicity and are known to interconvert; furthermore, many different morphologies or sub-species have been reported (e.g. protofibrils, amylospheroids, amyloid-derived diffusible ligands, globulomers, etc.). The major components of Aβ plaques are $A\beta_{1\text{-}40}$ and $A\beta_{1\text{-}42}$: these refer to two isoforms of

the protein, 40 and 42 residues in length, respectively. $A\beta_{1-42}$ is typically associated with early stage nucleation and the formation of insoluble fibrils while $A\beta_{1-40}$ is more soluble and the primary form present in plasma and CSF.[573]

Many in vitro techniques have been utilized to study the formation of Aβ fibrils and transient intermediates.[574] Typically, these methods are conducted in parallel because they face various drawbacks when used alone. These can generally be divided into bulk (ensemble) and single-particle techniques. Briefly, ensemble measurements include electrophoresis/western blotting, size exclusion chromatography, light scattering (DLS, MALS), fluorescence assays (via thioflavin-T (ThT) or Congo Red), fluorescence correlation spectroscopy, dot blotting, mass spectrometry, and ELISA.[574] The most common single-particle techniques are TEM and AFM.[575] ELISA and gel electrophoresis can quantitate the bulk load of Aβ in various bodily fluids, and immunostaining can quantitate the location of Aβ fibrils in excised tissue.[576] However, these are both static techniques that inherently only study a single sample or series of samples: ELISA, gels, and immunostaining cannot monitor changes in a sample longitudinally.[577] The ThT assay can monitor the kinetics of Aβ fibril formation, but it does not provide size information.[578] TEM and Cryo-EM offer outstanding spatial resolution but are limited to viewing only a few species at a time.[579-582] Conventional light scattering techniques, such as DLS or multi-angle light scattering (MALS), suffer from the exponential dependence of scattering on particle/aggregate size, making it difficult to detect smaller species when large aggregates are present.[583-585] Total internal reflectance microscopy is another important analytical technique that has been used to monitor individual Aβ fibril aggregation in real time.[586, 587] While powerful, it is limited in throughput—it selectively monitors only those fibrils in

contact with the surfaces of quartz slides, and with a limited depth of penetration (150 nm) from the excitatory evanescent field. It also requires the use of ThT or other amyloid-binding dyes.

The working mechanism of MNTA is similar to DLS and NTA (i.e. nano-sight [588])—it measures the Brownian motion of particles via scattered light to deduce their size according to the Stokes-Einstein relation. Briefly, a multispectral light sheet illuminates a continuously changing ~2.5 nL volume, from which suspended particles scatter incident light upon a CCD (charge-coupled device) photodetector. These profiles of scattered light are tracked and recorded in order to calculate particle size via rate of diffusion. The particle number concentration can be determined by the number of scatterers and the illumination volume. The benefits of *monospectral* nanoparticle tracking analysis for Aβ characterization have previously been studied by Yang et al.[589] However, DLS and existing NTA rely upon a single wavelength light source (e.g. 633 nm), while MNTA integrates excitation from three sources (450 nm, 520 nm, 650 nm). This addresses an error source in monospectral techniques—the 6th-power dependence of Rayleigh scattering intensity (at a particular wavelength) on particle size.[590] Larger particles have non-linear dependence of scattering cross section on particle size predicted by Mie theory.[591] For both DLS and NTA, this means that in highly polydisperse solutions (such as Aβ), even negligible amounts of large aggregates can completely obscure the scattered intensity from smaller (5-50 nm) species.[584] In some applications, such as antibody production quality control, this fact is leveraged for detecting trace amounts of aggregates non-quantitatively.[592] For NTA, the masking effect of larger particles over smaller ones has been well documented: Tian et al. could not achieve simultaneous measurement of 100-nm and 1000-nm bead mixtures or 100-nm and 300-nm

bead mixtures,[593] and in mixtures of 100-nm and 200-nm beads, Krueger et al. observed a clear bias toward the larger species at all tested ratios.[594] In 2018, McElfresh et al. demonstrated that MNTA could address this limitation and accurately measured multimodal mixtures of gold and polystyrene latex particles.[567] One unresolved question was its utility for soft materials—especially those that undergo size dynamics such as aggregating proteins. Here, we evaluated MNTA as a new tool for benchtop characterization of $A\beta_{1-42}$ aggregation—a notoriously arduous and time-consuming task in the AD research community.[574, 595, 596]

9.2. Methods

9.2.1. Materials

The following reagents were acquired and used as received: Tris base (Sigma-Aldrich), ammonium hydroxide (28-30%, VWR International), sodium chloride (Sigma-Aldrich), dimethyl sulfoxide (Sigma-Aldrich), thioflavin-T (Sigma-Aldrich), $A\beta_{1-42}$ (lyophilized 0.1 mg ea, BACHEM), epigallocatechin gallate (Sigma-Aldrich), 2% uranyl acetate (Electron Microscopy Sciences), gold nanospheres (50 nm, 2 mM citrate, Nanocomposix), silver nanospheres (100 nm, 2 mM citrate, Nanocomposix), polystyrene latex spheres (460 nm: Sigma-Aldrich, 90 nm/490 nm/1000 nm: Ted Pella), Type 1 Reference Water (XZero).

9.2.2. Preparation And Storage Of $A\beta_{1-42}$.

As purchased $A\beta_{1-42}$ peptide was stored at -20 °C and aliquoted using 10% (v/v) NH_4OH. Briefly, 0.1 mg samples were resuspended in NH_4OH to a concentration of 0.5 mg/mL. The sample was then split into aliquots containing 0.025 mg each and lyophilized using a LabConco FreeZone (2.5 L). These samples were stored at -80 °C prior to use.

9.2.3. Aggregation Of $A\beta_{1-42}$ Peptide And Fluorescent Monitoring.

Aliquots were first solubilized in DMSO to a concentration of 500 μM and sonicated for 5 minutes to minimize pre-formed aggregates. The aliquots were then diluted to a concentration of 5 μM in 40 mM Tris buffer (pH 8.0) and 150 mM NaCl to initiate aggregation. Aggregation was monitored using the fluorescent molecule Thioflavin-T (ThT). This molecule is a benzothiazole dye commonly used to monitor Aβ aggregation— it binds specifically to β-sheet structures to yield enhanced fluorescence at 485 nm. For fluorescent detection, Aβ samples were incubated with 10 μM ThT in 96-well plates and monitored with a Molecular Devices SpectraMax M5 spectrophotometer. Fluorescence measurements were recorded every 5 minutes (ex: 440 nm, em: 485 nm).

9.2.4. Modulation Of $A\beta_{1-42}$ Aggregation With Epigallocatechin Gallate (EGCG).

Stock solutions of EGCG were prepared at 20 mM in DMSO. EGCG was added to fibrillous $A\beta_{1-42}$ samples (after 12 hours of aggregation as described above) for a final concentration of 50 μM EGCG. These samples were incubated for 24 hours at room temperature before characterizing with fluorescence measurements, MNTA, and TEM.

9.2.5. Transmission Electron Microscopy.

Carbon/Formvar grids (300 mesh, Ted Pella Inc.) were first exposed under a UV lamp for 1 hour to increase surface hydrophilicity. 5 μL of 5 μM Aβ (40 mM Tris, 150 mM NaCl) were drop cast on a grid and allowed to settle for 1 minute. A wedge of filter paper was applied at a right angle to the drop and used to wick away the sample. 5 μL of DI water were added to the grid and removed as before after 1 minute. 5 μL of uranyl acetate (2%) were then applied and allowed to stain for 30 s before removal as before. Imaging was

performed with a JEOL 1200 EX II TEM at 80 kV and micrographs were captured with a 2K X2 KGatan CCD camera.

9.2.6. MNTA Measurements.

MNTA measurements were conducted using a commercially available ViewSizer 3000 from Horiba Scientific (Irvine, CA) at 27° C. Details of this system have been described previously but are briefly summarized below.[567] For all Aβ measurements, the instrument settings were as follows: 15 ms exposure, 24 dB gain, 70 mW blue laser power, 12 mW green laser power, and 8 mW red laser power. Incident light from these sources is scattered by the sample and photons are sorted by wavelength with a Bayer filter and detected with a CCD photodetector. In this way, each channel of light is recorded by distinct pixels of the CCD. Each of these channels is then separated to form grayscale images comprised of the scattered light profiles (i.e. spots/blobs) from the particles in the excitation field of view (162 μm x 288 μm x 50 μm). Automated noise analysis is performed to determine the optimal wavelength for representing each particle (ensuring optimal scattering for a given particle size), and a final 8-bit composite video is generated for tracking analysis.[567] The system also performs user-definable image thresholding to reduce background noise from the camera. By default, a Gaussian blur filter (to reduce speckling) and 10% noise threshold (expressed as a percentage value of the total number of pixels) are applied such that all pixels below this threshold are set to zero (0-255 range). For measurements with fluorescent gating, the green and red lasers were deactivated, and a 450-nm long-pass filter was inserted between the sample cuvette and detector.

Samples were prepared as described above and used to fill a quartz cuvette cell with a minimum of 0.4 mL. For each sample or time point, 15 videos were recorded at a framerate

of 30 fps for 10 seconds (300 frames per video). Between each video, samples were stirred at a speed of ~30 rpm for 5 s with a 5 mm PTFE stir bar to push a new volume of sample into the illuminated region. After stirring, the sample was allowed to equilibrate for 10 s to minimize directional flow. Particle detection was initiated according to a user-definable intensity threshold. Here, we used a dynamic detection threshold of 2 standard deviations above the median (e.g. if the median pixel intensity of a frame was 70, and the standard deviation of pixel intensities was 5.1, then particles with intensities (calculated for a 20-pixel feature diameter) less than 70 + 2*5.1, or 80, were not counted). This dynamic threshold is more robust for polydisperse samples than a constant minimum intensity as it accounts for the total frame intensity.[597] For each video, time-resolved particle coordinates were acquired by determination of radial symmetry centers.[598]

Mathematically, the calculated diffusion coefficient (and hydrodynamic diameter) is extracted from the optimized least-squares fit (OLSF) of the MSD curve for a given particle track. However, it has been established that the finite length of a single-particle trajectory highly influences the MSD fit:[599] For large time lags, the increased variance and correlated values of the MSD can significantly contribute to error; for short time lags, the MSD variance is heavily affected by dynamic localization error and motion blur.[600, 601] To address these issues, MNTA applies Cramér-Rao statistics to optimize the least-squares fit of the MSD on a track by track basis: The system ignores the track or calculates the hydrodynamic diameter according to the relative uncertainty on D (mathematically expressed in detail by Michalet et al.).[602] Specifically, a maximum threshold value of 0.4 for the relative uncertainty was used. Further tracking parameters were as follows: The maximum jump distance was 20 pixels, the minimum number of frames for tracking analysis was 5, and the maximum

number of frames a particle could be lost before ending a track was 2. These are factory-set but adjustable values for the system. The extraction of particle size is as follows: First, the mean-squared displacement (MSD) is calculated from the time-resolved coordinates of each particle, x_i and y_i over N frames according to Equation (1).

$$\textbf{(1)}\ MSD(n) = \frac{1}{N-n}\sum_{i=1}^{N-n}(x_{i+n} - x_i)^2 + (y_{i+n} - y_i)^2$$

From the MSD for a given particle, the diffusion coefficient D is determined using the time delay between frames $\boldsymbol{\Delta t}$ and an optimized least-squares fit of the MSD as a function of n (Equation (2))[567].

$$\textbf{(2)}\ MSD\ (n) = (4\Delta tD)n$$

The hydrodynamic diameter d_H is then calculated according to the Stokes-Einstein Equation (3). Here, k_B is the Boltzmann constant, T is temperature, and η is the solvent viscosity.

$$\textbf{(3)}\ d_H = \frac{k_B T}{3\pi\eta D}$$

9.3. Results And Discussion

9.3.1. Application Of MNTA To Concentration And Size Measurements Of Inorganic Nanoparticles.

Inorganic nanoparticles and solution phase aggregates of $A\beta_{1\text{-}42}$ were quantified using MNTA with a commercially available system from Horiba Scientific illustrated and described in **Figure 9.1.** The raw data generated by the instrument comprises a series of videos (~10 s each) that display the scattered light profiles from particles in solution. The number of videos is defined by the user and is a tradeoff between total acquisition time and total particle counts—we used 15 videos per Aβ sample and did not observe a significant effect of video number on concentration measurements (**Figure 9.7**). Each frame of a video

represents a snapshot of the particle positions in a 2.5-nL rectangular volume, i.e. the volume illuminated by the focused light sheet, at a particular time. The positions of the particles are recorded via tracking of radial centers and used to calculate the size of the particles according to their degree of Brownian motion.[598, 602, 603]

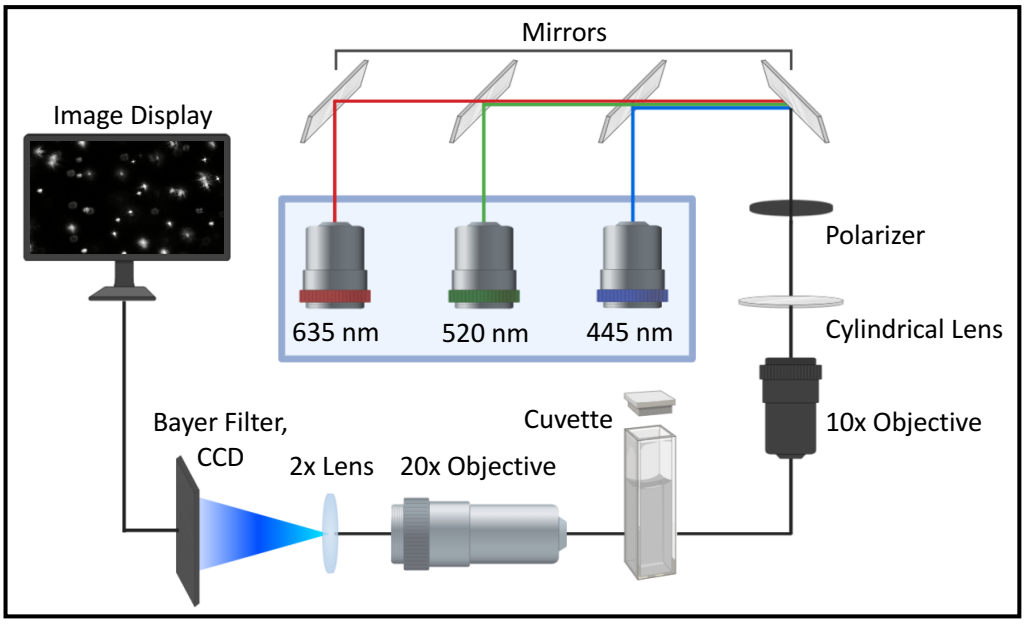

Figure 9.1. Schematic of MNTA instrumentation.
The instrument consists of three individual light sources (635 nm, 520 nm, and 445 nm) with adjustable power levels, dichroic mirrors to form a single sheet of light, a polarizer, a cylindrical lens, a 10X objective lens, a sample cuvette, a 20X objective lens, a 2X lens, a Bayer filter, and a CCD detector for image capture.

We first assessed the measurable concentration range of the MNTA system by diluting gold, silver, and polystyrene latex (PSL) spheres across four orders of magnitude (**Figure 9.2**). We assigned the absolute (calculated) concentrations by diluting from the stock values provided by the suppliers. As these are most commonly determined via mass concentrations of starting material, they are inherently estimates that rely on the perfect uniformity of the particles. Though deviations in the measured concentrations existed on a per-sample basis, we did not observe significant variation in the measurable range across

these particle types/sizes, observing a linear trend between 10^6-10^8 particles/mL (**Figure 9.2A**). Particle size distributions for the gold, silver, and PSL particles are shown in **Figure 9.2B-D** to confirm accuracy of the size measurements.

To understand how MNTA compares to single-wavelength NTA, we investigated particles and mixtures with sizes relevant to Aβ species, particularly from < 100 nm to 1000 nm. Rather than comparison to a commercial single-wavelength system (e.g. NanoSight), we selectively activated/deactivated the component lasers of the MNTA system. This allowed isolation of the effect of wavelength on results, as all other hardware and processing elements were constant. Acquisition settings for the PSL solutions are detailed in **Table 9.1**. In **Figure 9.8**, we used MNTA to measure monomodal solutions of nominal 90-nm (**row A**), 490-nm (**row B**), and 1,000-nm PSL particles (**row C**) (TEM-standard grade). For each row, panels **i-iv** show the raw particle counts for multispectral (**i**), blue (**ii**), green (**iii**), and red (**iv**) excitation. The shaded regions indicate the median 80% of particle counts (where D10 and D90 are the left and right boundaries, respectively). From these plots, we observe that each of the three particle sizes has an ideal excitation wavelength, as revealed by the spread of the D10-D90 range. For 90-nm particles, the blue wavelength reduces this spread by 34% relative to green and 48% relative to green. For 490-nm particles, the green wavelength is best (23% narrower relative to blue and 14% relative to red), and for 1000-nm particles, the red wavelength is best (41% narrower relative to blue and 28% relative to green). In the case of 90-nm PSL, we also observe a decrease in the total number of particle counts as the excitation wavelength shifts from blue to green to red. This wavelength-dependent scattering is expected from Mie theory. The consequence is that no single wavelength is ideal for all particle sizes that span the nano size regime.

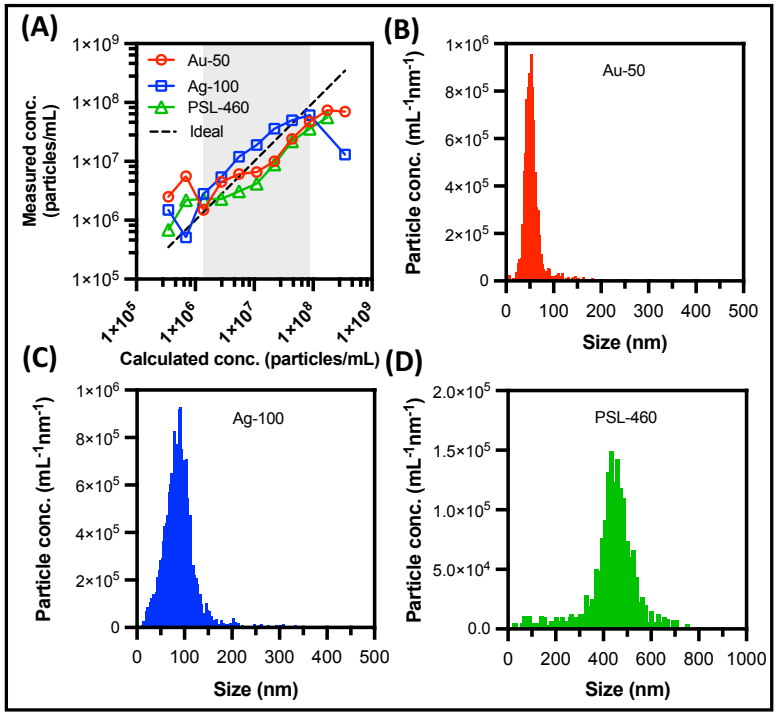

Figure 9.2. Measurement of inorganic particle concentrations and size distributions using MNTA.
(**A**) Commercial gold nanospheres (2 mM citrate, nominal d = 50 nm), silver nanospheres (2 mM citrate, nominal d = 100 nm), and polystyrene latex spheres (aqueous, nominal d = 460 nm) were diluted in water (XZero Type 1 reference water) across four orders of magnitude from their stock concentration (x-axis) provided by the manufacturer. The concentrations measured with MNTA for each dilution were plotted on the y-axis. The dashed line represents an ideal linear relationship for comparison. The shaded region shows the concentrations for which linearity was observed, between 1E6-1E8 particles/mL (Au-50: $R^2 = 0.9852$, Ag-100: $R^2 = 0.9926$, PSL-460: $R^2 = 0.9740$). (**B-D**) The size distributions of the particles in (**A**) are shown for (**B**) Au-50 (**C**) Ag-100 and (**D**) PSL-460 and are presented at calculated concentrations of 4.4E7 particles/mL, 4.4E7 particles/mL, and 8.7E7 particles/mL, respectively. The recorded sizes were as follows: Au-50 (modal: 50 nm, avg: 59 nm), Ag-100 (modal: 91 nm, avg: 93 nm), PSL-460 (modal: 437 nm, avg: 457 nm).

To investigate this further, we prepared trimodal mixtures of these PSL particles across a full order of magnitude of concentrations (**Figure 9.9**). We measured mixtures with relative concentration ratios of 10: 5: 1 (**row A**), 1: 1: 1 (**row B**), and 1: 5: 10 (**row C**) (PSL-90: PSL-490: PSL-1000). Panels **i-iv** show the particle counts for multispectral (**i**), blue (**ii**), green (**iii**), and red (**iv**) excitation. The histograms are presented with dashed lines to show the nominal diameters for each particle type. In addition, the shaded regions approximate

the width of the distribution for each particle type: They were calculated by taking one standard deviation above and below the modal size for each type. The standard deviations of the monomodal particle distributions in **Figure 9.8** were used for this purpose. The particle counts in each region were summed to calculate relative concentration ratios. Collectively, the quality of the measurements can be determined by observing the distance of the modal size (highest bin) from the nominal size (dashed line) and by measuring the particle count ratio between the three shaded regions. Panel (**v)** for each row compares the measured particle ratios versus their theoretical ratio (gray).

It is obvious that the green and red lasers are insufficient for detection of small particles (e.g. 90-nm) when larger species (490-nm and 1000-nm) are present at comparable concentrations (**Figure 9.9Aiii, 9.9Aiv, 9.9Biii, 9.9Biv**). Green and red only count 9% and 1%, respectively, of the PSL-90 particles detected with multispectral (RGB) excitation for the 10:5:1 mixture (**Figure 9.9Ai-v**). When comparing RGB excitation to blue-only for the 10:5:1 mixture, we see that RGB is closer to the ideal ratio than blue-only (**Figure 9.9Av**). However, blue is superior over green and red if only a single wavelength is available. For the 1:1:1 mixture (**Figure 9.9Bi-v**), PSL-90 and PSL-490 are well accounted for by RGB but PSL-1000 is undercounted (**Figure 9.9Bv**). Blue also undersizes the PSL-90 in this mixture (**Figure 9.9Bii**). Each configuration had difficulty with the 1:5:10 mixture (**Figure 9.9Ci-v**). This is a particularly challenging case due to the high number of intensely scattering large particles, preventing good resolution of the 90-nm population even for the RGB configuration. We conclude that RGB excitation is well-suited for polydisperse mixtures over single-wavelength excitation especially for mixtures that are either skewed toward smaller particles in number or evenly distributed.

In NTA, one important parameter is the max jump distance (MJD). During analysis of recorded videos, the processing algorithm compares the positions of particles in one frame to the subsequent frame to construct tracks of finite length. The MJD is a threshold distance— if a particle is found in a successive frame within the MJD from a particle in the previous frame, then a track segment is formed. The track continues to grow until no particle is found within the MJD of a successive frame, or until multiple particles are found within the MJD, thereby terminating the track. Ideally, the MJD should be set unique to each population size. This is obviously quite difficult during dynamic experiments such as amyloid aggregation where the samples are not only polydisperse but also changing dynamically. In lieu of this, the MJD should at least be set such that it does not exclude small particles that diffuse at a higher rate than larger particles. We performed MNTA measurements on three small nanoparticle standards (50-nm, 90-nm, and 100-nm) across a range of MJDs and plotted the particle counts with respect to the MJD (**Figure 9.10**). From this data, we observed that a MJD of 20 pixels was sufficient for measuring 97 ± 2% of particles present in the 50 – 100 nm size range, a reasonable lower range of confidence. Therefore, we used a MJD of 20 for Aβ measurements.

9.3.2. Real-Time Monitoring Of $A\beta_{1-42}$ Aggregates.

Solid $A\beta_{1-42}$ peptide was pretreated and individually aliquoted using 10% NH_4OH followed by lyophilization to minimize initial aggregation[604]. To illustrate the raw data from $A\beta_{1-42}$ as visualized by MNTA, **Figure 9.11** first compares the initial video frame of recorded data from aggregation buffer before (**Figure 9.11A**) and after (**Figure 9.11B**) the addition of $A\beta_{1-42}$ (**Figure 9.12** for distributions). It then shows the conversion to 8-bit data (**Figure 9.11C**) that is used for particle tracking (**Figure 9.11D-G**). Using MNTA, we found that

upon resolubilization in buffer (40 mM Tris, 150 mM NaCl, pH 8.0), these $A\beta_{1\text{-}42}$ aliquots already contained some intermediates with an average size of 160 ± 10 nm (± standard deviation of n=4 replicate means). This is indicative of the high instability of the $A\beta_{1\text{-}42}$ peptide and reflects prior reports.[605, 606] For a given sample, we routinely observed increases in the average size and standard deviation (i.e. polydispersity) of the aggregate distribution over the course of measurement (12 h, 30 min intervals).

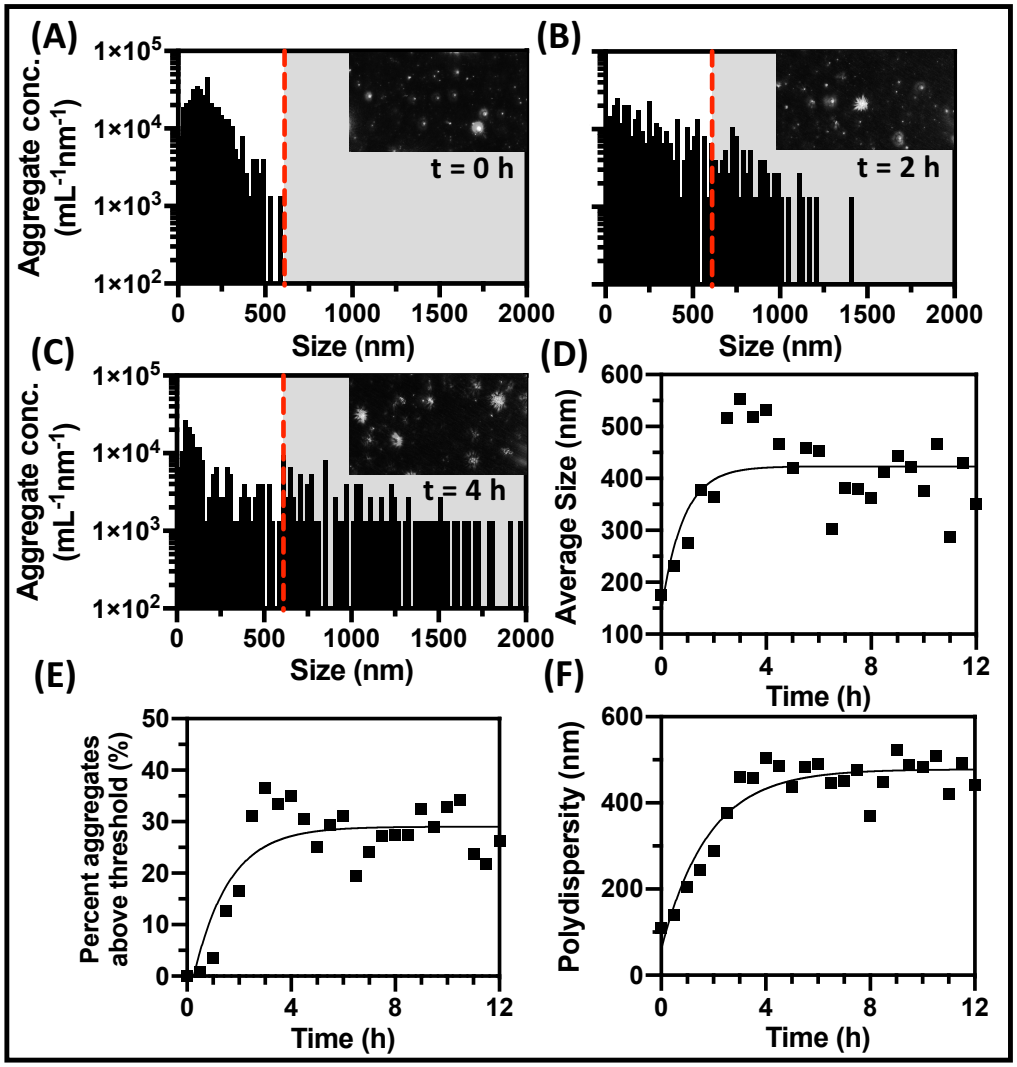

Figure 9.3. Particle size distributions and growth trends from a single aggregation experiment using MNTA.
(**A-D**) $A\beta_{1\text{-}42}$ was incubated in Tris (40 mM, 150 mM NaCl, pH 8.0) and measured every hour. Particle size distributions recorded at (**A**) 0, (**B**) 1, and (**C**) 4 hours. The red plane indicates the size of the largest aggregate detected at t = 0 h. Pre-grayscale video frames taken from the first frame of each raw video file are presented in the insets, showing the scattered light from individual aggregates at each time point. (**D**) The average size of aggregates in solution plotted against time for a representative aggregation experiment indicate fibril growth. (**E**) The total percentage of measured aggregates above the t = 0 state (red line) can also be plotted over time as an alternative metric of growth. (**F**) The standard deviation of the particle size distribution (i.e. the polydispersity) shows the spreading of the distribution over 4 h followed by an equilibrium state matching the size trend. Kinetic data in **D-F** are presented with a least-squares one-phase association fit.

The viscosity of the sample changes as a function of protein concentration, and the viscosity is a key parameter in the Stokes-Einstein relationship.[607] In order to account for the

different viscosity of the protein solutions relative to water,[608, 609] we adapted a simple protocol that has been previously demonstrated using DLS.[610] We validated the extension of this technique to MNTA by comparing viscosity measurements of aqueous glycerol solutions to their known theoretical values (**Figure 9.13**). We observed a linear correlation (R^2 = 0.9544) between theoretical viscosities of glycerol-water mixtures and MNTA-measured viscosities. We used the same protocol for measuring the viscosity of aqueous Aβ. This first entailed measuring the size distribution of a stock sample of polystyrene latex spheres (nominal diameter 90 nm) at a high concentration in water. The particles were then measured at the same concentration in 5 μM Aβ. This resulted in average measured diameters of 84 nm (d_1) in water and 161 nm (d_2) in 5 μM Aβ (**Figure 9.14**). Therefore, the viscosity of the Aβ solution was calculated according to $\eta = (d_2/d_1)*\eta_{H2O,27C}$ = (161 nm/84 nm)*0.85 cP = 1.63 cP. This value was used for processing all Aβ aggregation experiments.

Representative data generated from a single sample monitored with MNTA is shown in **Figure 9.3**. To aid in distinguishing changes in the size distribution, we defined a minimum size threshold for aggregation as the largest particle detected by the t = 0 h MNTA measurement (**Figure 9.3A**, red dashed line). Therefore, each sample served as its own control and baseline for aggregation. Particle size distributions were collected every half hour but are visualized at 3 time points of growth (t = 0, 2, 4 h) to demonstrate the widening of the size distribution and the number increase in larger aggregates (particles >690 nm for this sample) during the growth phase. The aggregate counts have units of mL^{-1} nm^{-1} because they are grouped as a histogram of bins with 20-nm widths— each bar corresponds to the concentration of aggregates in that particular bin.

The average sizes (± standard deviations of the size distributions) measured for panels **A-C** were 180 ± 110 nm (0 h), 360 nm ± 290 (2 h), and 530 nm ± 500 nm (4 h). Here, the standard deviations provide the simplest metric for quantifying the spread of the size distributions. We use them as convenient surrogate values for the polydispersity of the solutions, and for observing kinetic changes in the polydispersity. Since the size distributions are not normal, Chebyshev's theorem can be a useful rule of thumb: at least 75% of the measured aggregates lie within two standard deviations of the mean (this is overly conservative as sizes cannot be ≤ 0). While D10, D50, and D90 values offer a more rigorous description of particle size distributions, standard deviations were suitable for our kinetic analysis.

In addition to Brownian motion-based sizing, the real-time display of scattered light from samples provides a qualitative confirmation of aggregation via increased scattering intensity on a per-particle basis, shown as still-frames from the raw videos in the upper-right of **Figure 9.3A-C**. **Figure 9.3D** shows the trend in average $A\beta_{1\text{-}42}$ aggregate size for the same sample every 30 min, which indicated that the majority of growth occurred during the first 4 h and reached an equilibrium after this point. The extent of aggregation could also be visualized and quantified according to the percentage of total aggregates larger than the maximum size measured in the initial state (**Figure 9.3E**). **Figure 9.3E** shows that this value plateaued after reaching a value of ~29% over 4 h incubation. Third, the polydispersity of the size distribution, as represented by its standard deviation (**Figure 9.3F**), followed the same trend.

9.3.3. Comparison Of MNTA To ThT Assay And TEM.

In order to validate the kinetic trends of native $A\beta_{1-42}$ acquired with MNTA and assess reproducibility, we measured aggregate size distributions across four replicates in parallel with the fluorescence ThT assay (ex: 440 nm, em: 485 nm): The average size trend measured by MNTA was positively correlated with ThT fluorescence when the techniques were conducted simultaneously (Pearson's $r = 0.821$, $P < 0.0001$; **Figure 9.4A**). Size distributions from the individual replicates are presented in **Figure 9.15**. The relative standard deviation in measurement over this time course ranged from 7% to 44% for MNTA and 6% to 48% for ThT fluorescence. On average, we measured 100% growth in average size and a 320% increase in raw ThT fluorescence over the first 4 h of incubation. These values did not significantly change by the 12 h time points. We observed that average size fluctuations between 300-400 nm were not matched by differences in ThT fluorescence on a per-time-point basis (**Figure 9.4A**). This could suggest dynamic coalescence/decoupling without changes in total beta-sheet content, but we also cannot rule out sampling bias in the MNTA technique relative to the ensemble average of whole sample fluorescence. On average, the polydispersity increased with the same trend as the average size (**Figure 9.4B**). We also observed a linear decrease of 40% (non-zero slope, $P < 0.0001$) in total aggregate concentration from 5.4E6 mL^{-1} to 3.2E6 mL^{-1}) over the 12 hours measured (**Figure 9.4C**). This could be due to the gradual integration of smaller species into larger aggregates resulting in a lower total aggregate concentration. Over the course of the measurement period, it is also likely that the largest fibrils sediment below the illuminated volume and are not resampled. Regardless, even if sampled, we note that the processing used for

nanoparticle tracking analysis cannot be used to measure multiple-micron sized particles (e.g. > 2 μm), as their MSD vs. Δt will not obey a linear fit.

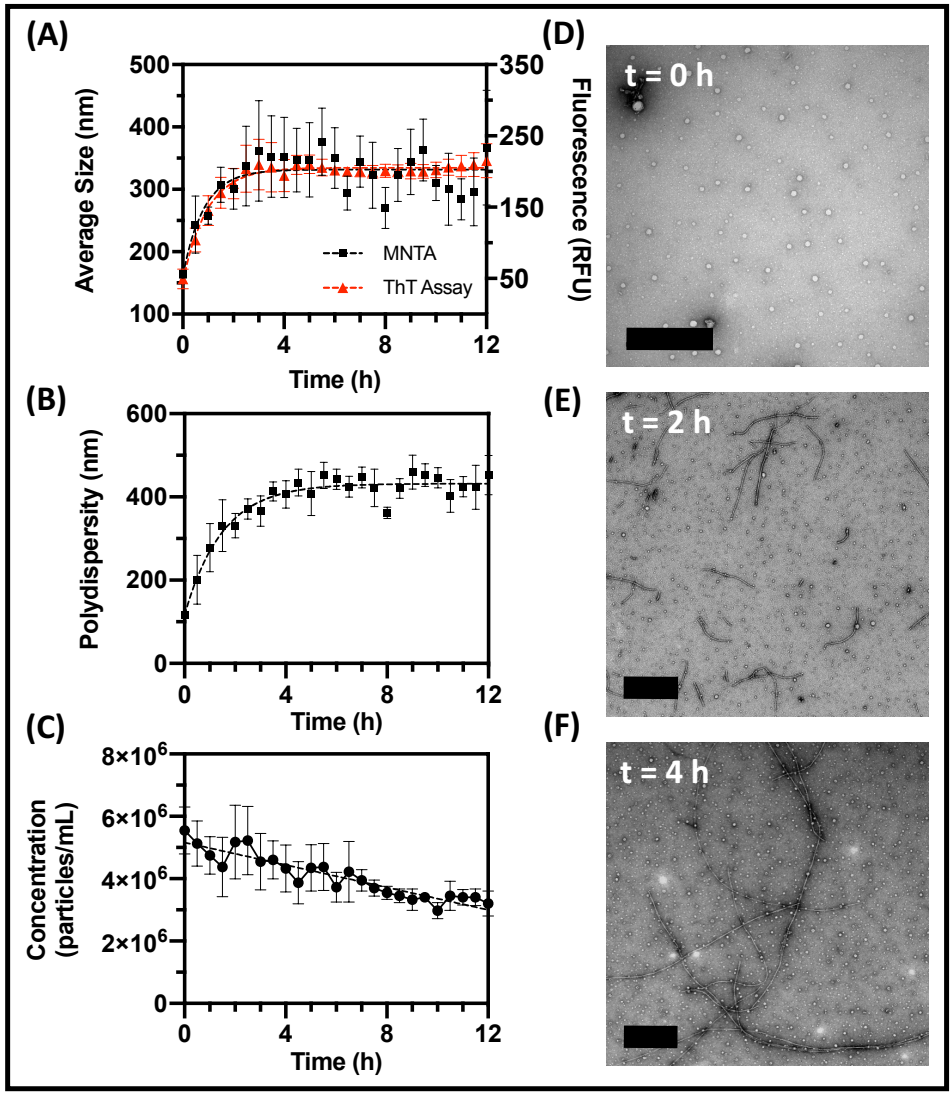

Figure 9.4. Averaged kinetic trends of Aβ1-42 aggregation using MNTA in tandem with the fluorescence ThT assay and TEM.
(A) The kinetics of aggregation are plotted via average size using MNTA and fluorescence using the ThT assay. MNTA size kinetics are correlated to the gold standard ThT fluorescence assay (Pearson's r = 0.821, P < 0.0001). Error bars = SEM, n = 4 replicates. (**B**) The average polydispersity of the size distributions measured hourly indicates widening of the size distributions until a plateau at 4-5 h. Error bars = SEM, n = 4. (**C**) The concentration of aggregates (0-2 μm range) measured via MNTA decreases over time. R^2 = 0.851, error bars = SEM, n = 4. (**D-F**) TEM images at T = 0, 2, and 4 h reveal formation of mature fibrils. Scale bars = 500 nm.

To further validate the accuracy of monitoring aggregation with MNTA, we imaged the $A\beta_{1-42}$ at various time points using TEM. Representative images are shown at t = 0 h, t = 2 h, and t = 4 h (**Figure 9.4D-F**). We observed spherical intermediates and potentially oligomeric species at t = 0 h that grew into large micron-scale fibrils after 4 hours. The sizes were not quantitatively estimated from TEM images due to the significant heterogeneity of $A\beta_{1-42}$ fibrils and difficulty in distinguishing individual species; however, fibrillary growth was observed similar to prior work.[611] TEM showed no further growth beyond 4 hours, which is consistent with the plateau in size and fluorescence observed at 4 hours with MNTA and the ThT assay, respectively.

9.3.4. MNTA Measurements Of $A\beta_{1-42}$ Fibrillation With Fluorescent Gating

ThT binds specifically to the β-sheet regions that form during Aβ aggregation, and the ThT assay is a workhorse in Alzheimer's disease research. ThT has no fluorescence signal when unbound but produces fluorescence when bound to Aβ (excitation at ~485 nm; **Figure 9.5A**). Thus, we evaluated the use of MNTA with and without the addition of ThT. MNTA can be performed using light scattering as described, but light emitted by fluorescent samples can also be isolated and used for tracking by placing an optical filter between the sample and detector. We used MNTA with and without fluorescent gating to distinguish two types of signal: (1) scattered excitation light and (2) fluorescence from ThT bound to Aβ. **Figure 9.5B** shows an $A\beta_{1-42}$ solution that does not contain ThT monitored for 4 h. The same solution was measured in parallel with fluorescent gating (**Figure 9.5D**), which entailed deactivation of the red and green lasers while maintaining the blue (445 nm) and inserting a 450 nm long-pass filter between the sample and detector. The blue excitation was chosen to most closely match the absorbance maximum of ThT (440 nm). Here, the total number of

raw particle counts detected over the course of measurement was 20 times lower (97 vs. 2,186) than without fluorescent gating. This is because no fluorescent light was produced by the $A\beta_{1\text{-}42}$, and the scattered excitation light was removed by the filter. In contrast, when the same sample was incubated with 10 μM ThT, the aggregates were obvious both with (**Figure 9.5E**) and without fluorescent gating (**Figure 9.5C**). For samples that contained ThT (**Figure 9.5C, E**), we observed a larger average size with fluorescent gating than without after 4 h (470 ± 160 nm vs. 360 ± 180 nm)—this was supported by the lower number of smaller aggregates detected in the fluorescence-gated sample. The modal size of the fluorescence-gated sample was 440 nm while the non-gated sample was 30 nm after 4 h. This difference supports the hypothesis that after fluorescent gating, detection was selective towards aggregates with more bound ThT, i.e. larger species with higher β-sheet content.

Perhaps more notably, we observed a significantly different shape of the size distribution between $A\beta_{1\text{-}42}$ incubated with (**Figure 9.5C**) and without (**Figure 9.5B**) ThT. Although the average sizes of these two samples were comparable, (360 nm vs. 410 nm), the standard deviation of these distributions were 180 nm and 480 nm, respectively. To further examine this effect, we allowed $A\beta_{1\text{-}42}$ to aggregate and added ThT after 4 h had elapsed (**Figure 9.16**). We did not observe the same shift in the distribution as when it was present throughout the measurement though an increased number of particles were detected in the 500-1,500 nm range. This could be due to the addition of ThT fluorescence to the scattered light already produced by each aggregate effectively increasing the sensitivity to fibrils with bound ThT. These observations collectively suggest that ThT could play an interfering role, though minor, in the formation or stability of certain Aβ species—an idea that has been suggested previously in the literature.[578, 612] A full investigation of the ThT- Aβ interaction is

beyond the scope of this work, but our data indicate the potential utility of MNTA for mechanistic studies of aggregation-sensitive dyes. Importantly, as a tool for monitoring the raw aggregation state of peptides/proteins, MNTA does not require the use of exogenous dyes, and we consider this label-free sensing a notable advantage of the technique.

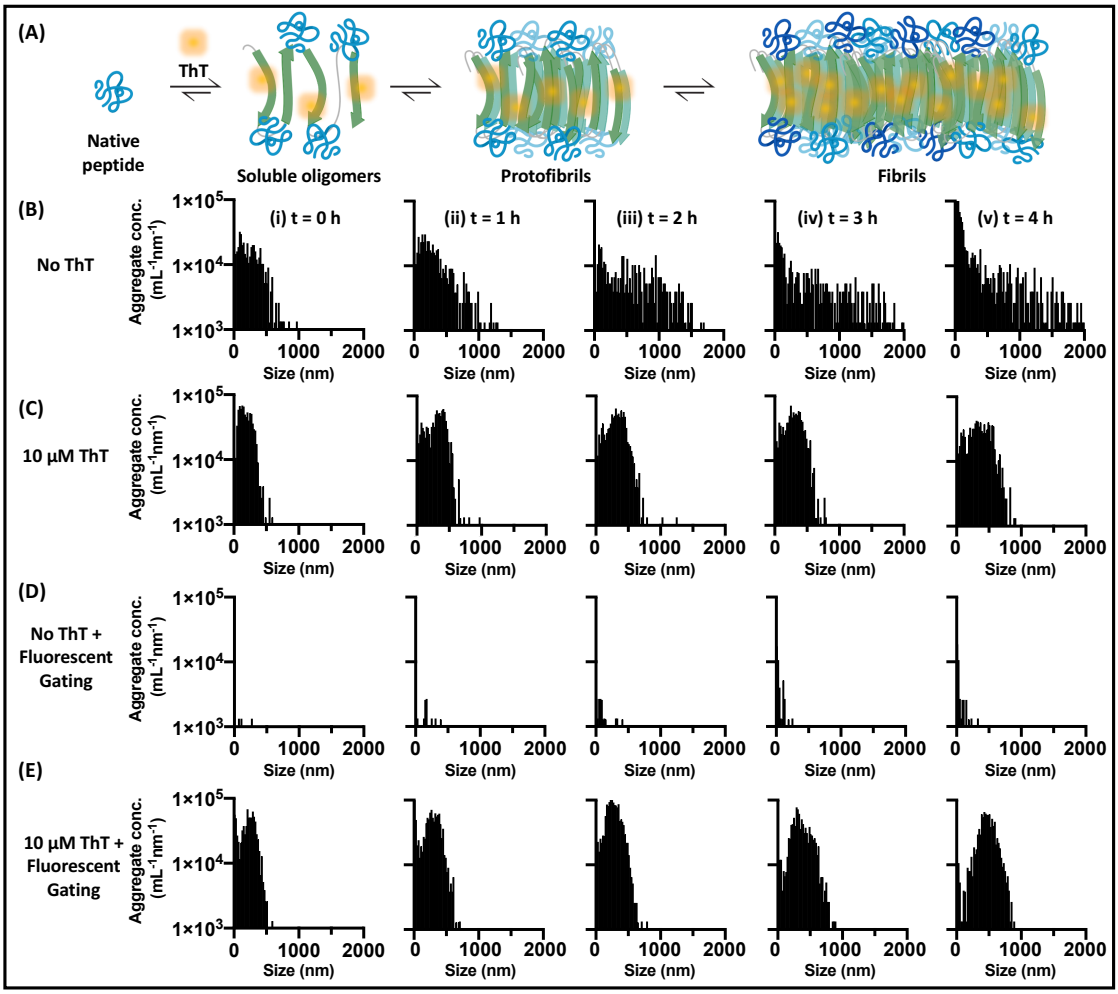

Figure 9.5. MNTA with and without fluorescence gating and the effects of ThT on Aβ1-42 size distributions.
(**A**) Schematic of the ThT-Aβ interaction. ThT selectively binds beta-sheet motifs that form during oligomerization and fibrillation. This decreases the non-radiative rate of decay of the fluorophore and activates its fluorescence. (**B**) Size distributions measured without ThT using NTA mode (all three lasers, no filter) from t = 0 – 4 h. (**C**) Aβ size distributions measured with 10 µM ThT using NTA mode from t = 0 – 4 h. (**D**) Aβ size distributions measured without ThT using fluorescent gating (only 445 nm laser activated with a 450 nm long-pass filter for removal of non-fluorescent/scattered light) from t = 0 – 4 h. (**E**) Aβ size distributions measured with 10 µM ThT using fluorescent gating from t = 0 – 4 h.

9.3.5. MNTA For Monitoring Potential Inhibitors Of $A\beta_{1-42}$ Fibrillation

To evaluate the ability to measure small-molecule-based alterations in $A\beta_{1-42}$ fibrillation with MNTA, we incubated samples with a naturally produced polyphenol with previously reported activity against Aβ aggregation for 24 hours: epigallocatechin gallate (EGCG).[613-615] **Figure 9.6A-B** shows a typical size distribution after 12 h followed by its shift toward the initial state after 24 h EGCG incubation (**Figure 9.6C**). In this sample, no aggregates were observed above the t = 0 h threshold following EGCG incubation. By averaging three replicates, the total concentration of aggregates transitioned from 2.8E6 mL^{-1} (t = 0 h) to 6.3E5 mL^{-1} (t = 12 h) to 2.2E6 mL^{-1} (t = 12 h + 24 h EGCG). We conducted these experiments in parallel with the ThT assay (**Figure 9.6D**) and observed a correlation between the average sizes measured with MNTA and ThT fluorescence. This suggested that the fluorescence reduction related to the reduction in aggregate size, and reinforced the notion that MNTA could monitor $A\beta_{1-42}$ disruption without an exogenous dye. Finally, we used TEM as secondary confirmation of $A\beta_{1-42}$ remodeling via EGCG: **Figure 9.6E** shows a TEM image of mature $A\beta_{1-42}$ fibrils (12-h growth) after they have been incubated with EGCG for 24 h. These aggregates resemble the intermediate species observed during the growth stages of fibrillation rather than the extensive and filamentous network of mature fibrils associated with complete aggregation.

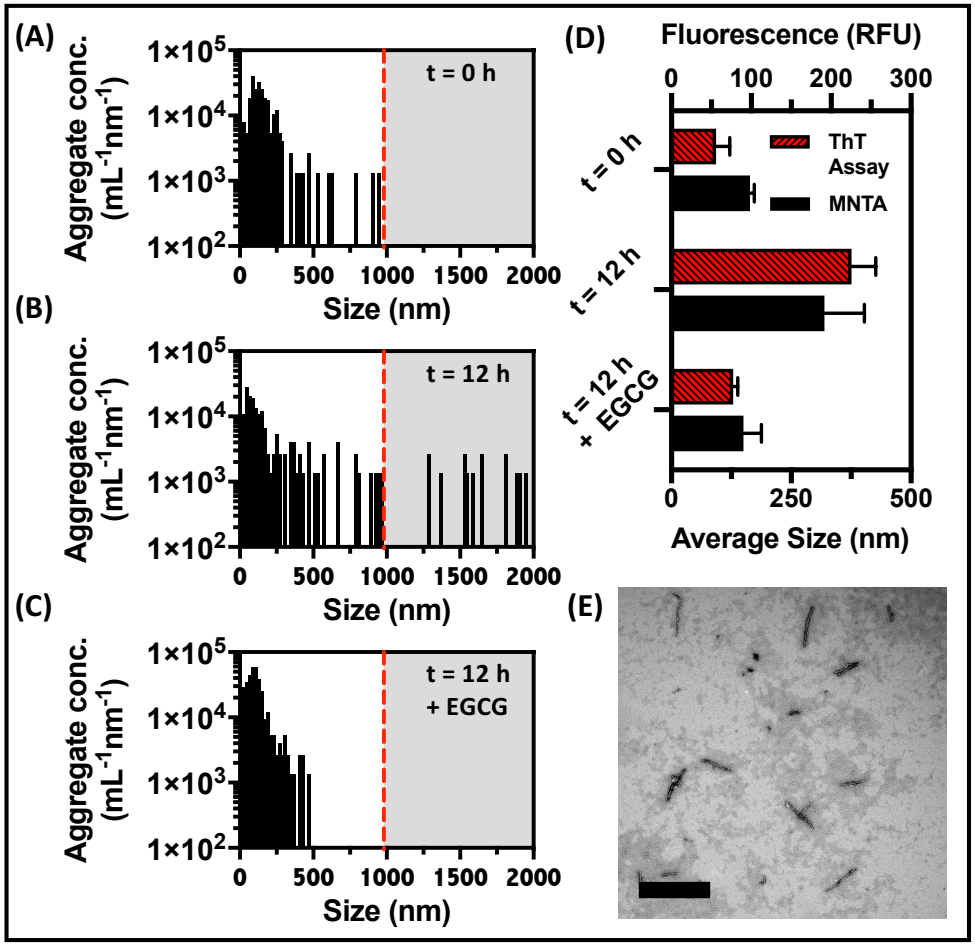

Figure 9.6. Modulation of Aβ1-42 fibrils using a previously reported disruptor of aggregation can be monitored with MNTA.
(**A-C**). Particle size distributions recorded at (**A**) 0 h and (**B**) 12 h for 5 μM $A\beta_{1-42}$, followed by (**C**) 24 h incubation in EGCG at 37° C. The red line indicates the size of the largest aggregate detected at t = 0 h. (**D**) The fluorescence measured via ThT assay and average size measured via MNTA are shown before (t = 0 h: 160 ± 8.7 nm, 56.0 ± 23.9 RFU) and after aggregation (t = 12 h: 320 ± 83 nm, 226 ± 42.8 RFU) followed by 24 h EGCG incubation (t = 12 h + EGCG: 150 ± 38 nm, 77.5 ± 7.89 RFU). Error bars = SEM, n = 3. (**E**) TEM of the $A\beta_{1-42}$ aggregates after EGCG incubation reveal intermediate-sized species. Scale bars = 500 nm.

9.3.6. Practical Considerations And Limitations

The emphasis of this first work on MNTA for Aβ aggregation is its utility for label-free kinetic monitoring and aggregate counting in solution phase with potential for size-based analysis. Hydrodynamic diameters were calculated according to the Stokes-Einstein relation. Therefore, average sizes reported represent spheres of equal diffusion coefficients.

For this reason, high-resolution imaging techniques such as TEM and AFM remain the most accurate choices for morphological characterization of aggregates and fibrils. Nevertheless, more sophisticated hydrodynamic models could be implemented in future work that account for dynamic viscosities and rod/fibrillous particle dimensions.[616]

The lower size limit of detection for a particle is governed both by its scattering cross-section and the sensitivity of the optics (e.g. camera gain, exposure time, and laser power). In this work, we used laser power settings optimized for polydisperse solutions (where power increases from red, to green, to blue to compensate for differential scattering) and factory-default camera settings for all Aβ experiments. 2% of all Aβ aggregates we detected were in the 0-10 nm binwidth. The manufacturer quotes a lower limit of 10 nm, which is roughly the same as commercial NanoSight. The upper size limit of measurement occurs near the point at which sedimentation begins to dominate over diffusion. This is both material specific (density) and governed by the resolution of the camera, as even sinking particles experience Brownian motion that is detectable with high enough resolution. In ambient aqueous conditions, the root-mean-square-displacement (L) for a 1,500-nm particle in the MNTA system is one pixel. This is the distance the particle can be predicted to travel between frames. For a 2,000-nm particle, L = 0.9 pixels. Therefore, error will begin to be introduced into the MSD fitting for particles above 1,500 nm, and the upper limit of accuracy lies in this range. Since the presence of larger aggregates was still of interest to us, we set the upper bound for analysis at 2,000 nm (note: NTA also conventionally uses 2,000 nm as an upper limit for analysis).[617]For concentration measurements, we found that MNTA provided reasonable values within 2 orders of magnitude (~1E6-1E8 particles/mL for Au/Ag/PSL nanospheres). The upper concentration limit is constrained by overlapping scattering profiles

that cannot be distinguished by particle-tracking algorithms; the lower limit is due to the distance between suspended particles exceeding the illuminated field-of-view. In the future, implementation of a recently developed modified displacement probability model could improve the upper concentration limit.[618]

To mitigate against potential selection bias from the small sampled volume (2.5 nL * *n* videos), a higher number of videos can be recorded. The same strategy can be applied for lowering the concentration limit of detection, which is on the order of 1E6 particles/mL for inorganic nanoparticles. However, this should be weighed against the increased measurement time and frequency of sample stirring, which can interfere with unstable samples such as aggregating proteins. Despite these considerations, our data suggests that MNTA is a promising benchtop tool for studying the aggregation states of the Aβ peptide, especially when compared to monospectral light scattering techniques that are limited in their resolving power of polydisperse solutions.

9.4. Conclusions

This work reports the first application of multispectral nanoparticle tracking analysis to the characterization of Aβ aggregation. We determined that it could monitor the dynamics of $A\beta_{1-42}$ aggregate size distributions longitudinally and label-free via kinetic correlation with the ubiquitous ThT assay. In addition, fluorescently tagged aggregates could be selectively measured by utilizing an appropriate excitation laser and filter. Simultaneous measurement via ThT fluorescence and TEM also suggest that MNTA is suitable for assessing potential disruptors of $A\beta_{1-42}$ fibrillation. The benchtop measurement takes between 15-30 minutes for analysis and processing, while achieving real-time analysis of hundreds of fibrils per imaging event.

9.5. Acknowledgements

Chapter 9, in full, is a reprint of the material as it appears in Analytical Chemistry, vol. 144, 78-89, 2019. Moore, Colman; Wing, Ryan; Pham, Timothy; Jokerst, Jesse V. The dissertation author was the primary investigator and author of this paper.

Particle Type	Laser	Gain (mW)	Exposure (ms)	Particle Ratio (90: 490: 1000)	Laser	Gain (mW)	Exposure (ms)
PSL-90	R	40	15	10:5:1	R	24	15
PSL-90	G	40	15	10:5:1	G	24	15
PSL-90	B	40	15	10:5:1	B	24	15
PSL-90	RGB	40	15	10:5:1	RGB	24	15
PSL-490	R	11	15	1:1:1	R	24	31
PSL-490	G	11	15	1:1:1	G	24	31
PSL-490	B	11	15	1:1:1	B	24	31
PSL-490	RGB	4	15	1:1:1	RGB	24	31
PSL-1000	R	15	15	1:5:10	R	6	32
PSL-1000	G	15	15	1:5:10	G	6	32
PSL-1000	B	15	15	1:5:10	B	0	32
PSL-1000	RGB	5	15	1:5:10	RGB	0	32

Table 9.1. Acquisition settings for PSL particle measurements.
Blue (445 nm), green (520 nm), and red (635 nm) wavelengths were used for all samples. Gain and exposure settings were adjusted on a per-sample basis to maximize the number of focused particles on the screen while minimizing noise from highly scattering particles. These settings were matched between samples of the same composition when possible. The theoretical concentrations (diluted from the stock values provided by the supplier) for the PSL mixtures were as follows: 10:5:1 (90-nm: 490-nm: 1000-nm) = 6.7E7 mL^{-1}, 3.3E7 mL^{-1}, 6.7E6 mL^{-1}. 1:1:1 = 1.25E7 mL^{-1}, 1.25E7 mL^{-1}, 1.25E7 mL^{-1}. 1:5:10 = 5.0E6 mL^{-1}, 2.5E7 mL^{-1}, 5.0E7 mL^{-1}.

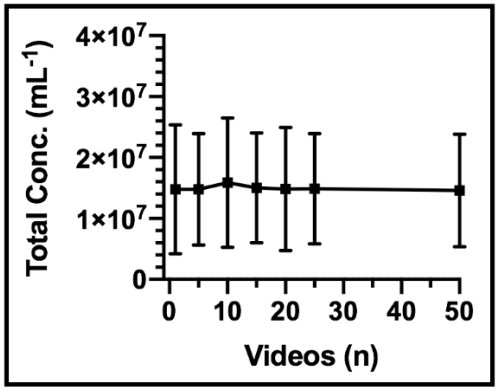

Figure 9.7. Effect of video number on total measured aggregate concentration.
Total concentration was measured with MNTA for 5 μM $A\beta_{1\text{-}42}$ after solubilizing in 40 mM Tris for increasing numbers of recorded videos (n = 3, error bars = SEM).

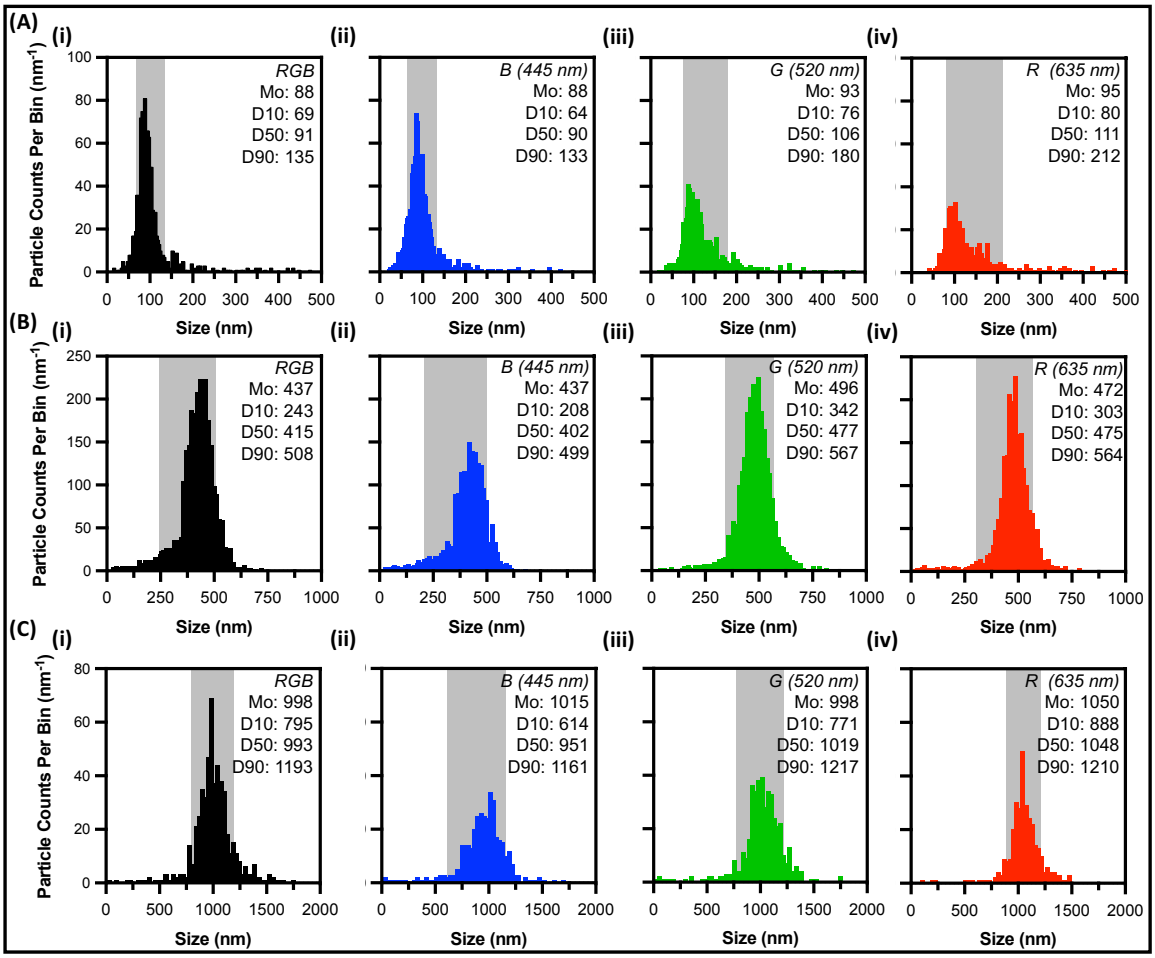

Figure 9.8. Multispectral versus monospectral excitation for NTA of monomodal PSL spheres (nominal diameters: 90 nm, 490 nm, and 1,000 nm).
Size distributions of nominal (**A**) 90-nm PSL spheres, (**B**) 490-nm PSL spheres, and (**C**) 1,000-nm PSL spheres measured with (**i**) three lasers: red (635 nm, 8 mW), green (520 nm, 12 mW), and blue (445 nm, 70 mW), (**ii**) blue only (445 nm, 70 mW), (**iii**) green only (520 nm, 12 mW), and (**iv**) red only (635 nm, 8 mW). The modal particle size (Mo) is shown for each distribution. D10, D50, and D90 values refer to the size that 10%, 50%, and 90% of measured particles fall below. Shaded regions indicate the D10 (left edge) and D90 (right edge) values. These plots demonstrate the dependence of both the width of the size distribution and the number of particle counts on wavelength choice.

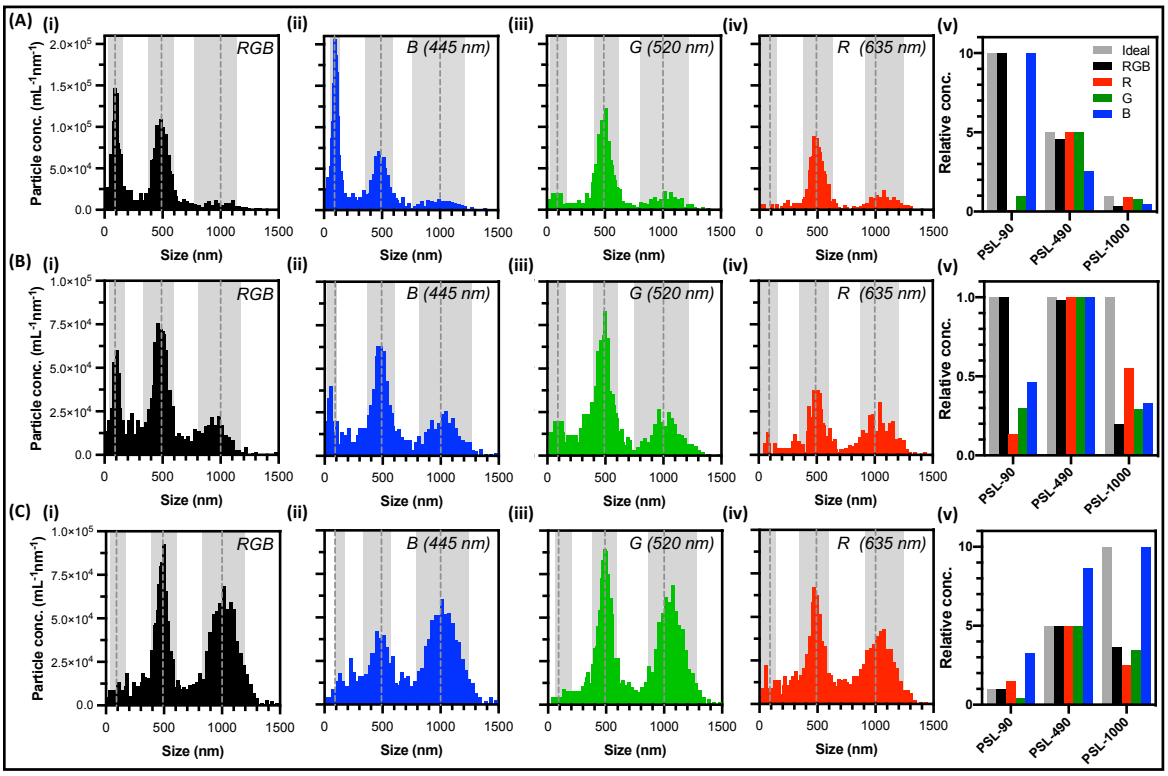

Figure 9.9. Multispectral versus monospectral excitation for NTA of trimodal mixtures of PSL spheres (nominal diameters: 90 nm, 490 nm, and 1,000 nm).

Size distributions of PSL mixtures with relative concentration ratios of (**A**) 10: 5: 1 (90-nm: 490-nm: 1000-nm), (**B**) 1: 1: 1, and (**C**) 1: 5: 10 measured with (**i**) three lasers: red (635 nm, 8 mW), green (520 nm, 12 mW), and blue (445 nm, 70 mW), (**ii**) blue only (445 nm, 70 mW), (**iii**) green only (520 nm, 12 mW), and (**iv**) red only (635 nm, 8 mW). The dashed line in each panel corresponds to the nominal diameter of the particle subpopulation. The shaded regions approximate the particle counts attributable to a given particle subpopulation. These boundaries were applied by taking the modal size of the subpopulation and adding/subtracting one standard deviation of the size distribution as measured for its respective monomodal sample (**Figure 8. S2**). The particle counts in each shaded region were summed and normalized for comparison to the ideal ratio in panel (**v**) of each row.

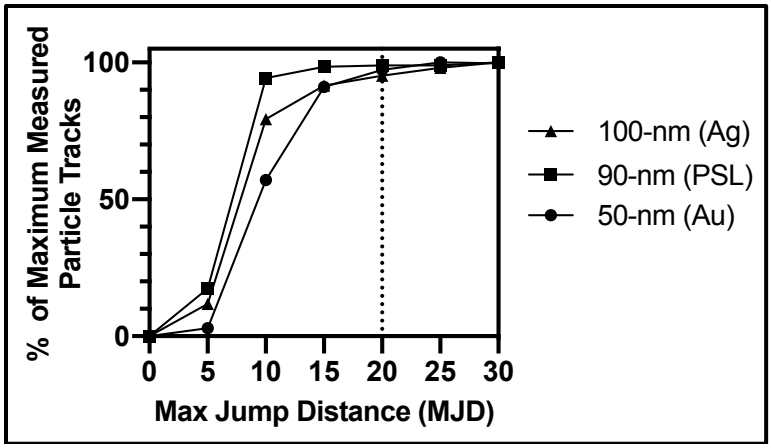

Figure 9.10. Detection of small nanoparticles as a function of max jump distance (MJD). Commercially available nanoparticle standards with average diameters of 50 nm (Au), 90 nm (PSL), and 100 nm (Ag) were used to determine a reasonable value for the MJD for routine analysis of polydisperse Aβ solutions containing small (<100 nm) aggregates. The size distribution of each particle type was measured for a range of MJDs from 0-30 pixels (camera calibration constant = 190 nm/pix). The number of particle counts for each distribution (at each MJD) was recorded and each value was normalized to the count for a MJD of 30 pixels, where a plateau in the measured counts was observed. The dotted line at MJD = 20 corresponds to the value used for Aβ experiments in this work. This data indicates that an MJD of 20 was sufficient for detecting 97 ± 2% of diffusing particles/aggregates in the 50 – 100 nm size range for a given sample.

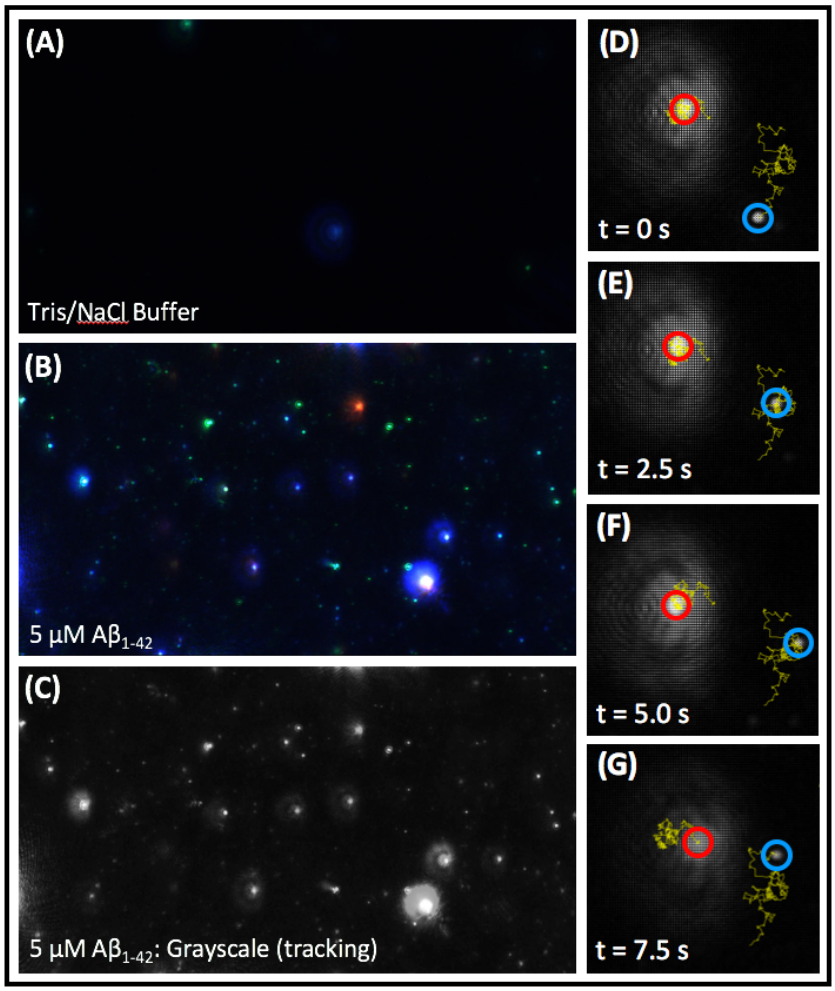

Figure 9.11. Principle of MNTA for Aβ sizing via Brownian dynamics.
(**A**) Color video-frame from MNTA showing the minimal scattering from background particles in aggregation buffer (40 mM Tris, pH 8.0, 150 mM NaCl). (**B**) Color video-frame showing the multispectral scattering of aggregates in solution after addition of 5 μM Aβ. The variety of scattering intensities from the red (635 nm), green (520 nm), and blue (445 nm) lasers is due to the polydispersity of the Aβ aggregates and the wavelength to particle size scattering dependence. (**C**) The same video-frame as (**B**) after conversion to 8-bit grayscale—these grayscale videos are used for tracking analysis. (**D-G**) A magnification of (**C**) is presented to illustrate the different track lengths of two diffusing particles over time: (**D**) t = 0 s, (**E**) t = 2.5 s, (**F**) t = 5.0 s, and (**G**) t = 7.5 s. A larger particle—indicated by the red circle and higher scattering intensity—diffuses more slowly than a smaller particle (blue circle). Their path lengths are traced in yellow and illustrate their size-dependent diffusivities.

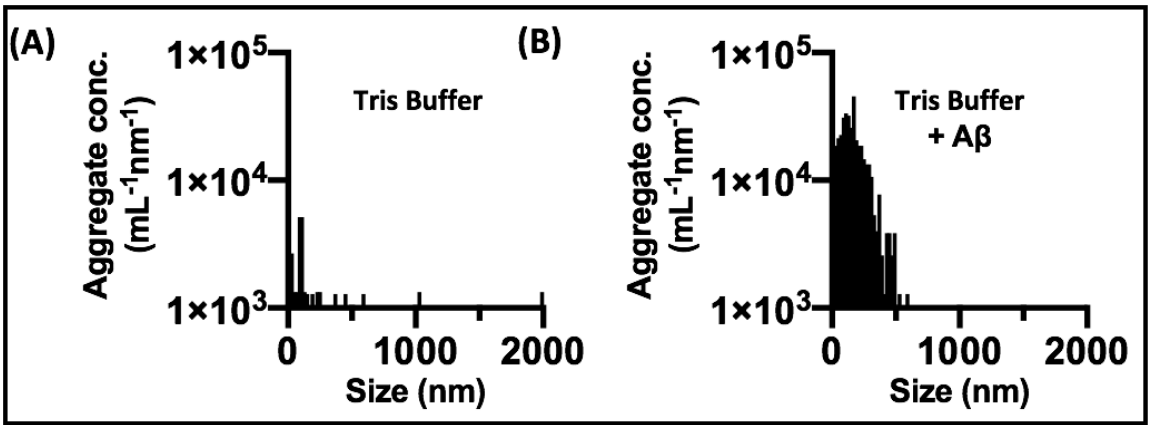

Figure 9.12. Comparison of the measured size distribution for buffer (Tris 40 mM, NaCl 150 mM) before and after addition of Aβ1-42.

(A) Size distribution for aggregation buffer measured with MNTA**.** The total concentration detected for buffer was 1.6E6 particles/mL, where only 30% of counts were in the 20-2,000 nm range (5.9E5 particles/mL). In contrast, 98±2% of counts from Aβ samples (n=5) were in the 20-2,000 nm range. **(B)** Representative size distribution for 5 μM $A\beta_{1\text{-}42}$ at t = 0 h. The average concentration was 5.4E6 particles/mL between 20-2,000 nm, 9-fold higher than in buffer.

(A)

% Glycerol	Theoretical Visc. (cP)
0	0.85343
5%	0.99155
10%	1.1616
15%	1.3734
20%	1.6403
25%	1.9813
30%	2.4235

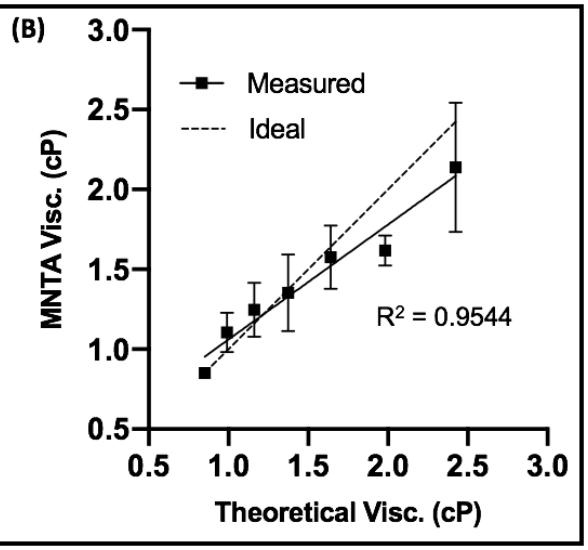

Figure 9.13. Evaluation of viscosity measurements using MNTA.
(**A**) The true viscosities of water-glycerol mixtures are theoretically known (adapted from Volk and Kähler)[1] and are presented for reference. (**B**) Monomodal PSL particles (nominal 90-nm diameter) were diluted to a concentration of 2.5E8 mL^{-1} in glycerol-water mixtures ranging from 0-30% glycerol. The ratio of the average size measured in water to the size measured in each glycerol-water mixture was used to calculate viscosity. The theoretical viscosities were plotted with respect to the MNTA measured values (solid line). Error bars represent standard deviation of three replicates. The dashed line represents an ideal 1: 1 correlation. Average viscosities measured via MNTA were directly correlated with theoretical viscosities for glycerol-water mixtures (R^2 = 0.9544). The slope of the measured vs. theoretical viscosity curve deviated from ideality by 32% (slope of 0.72 vs. 1.00).

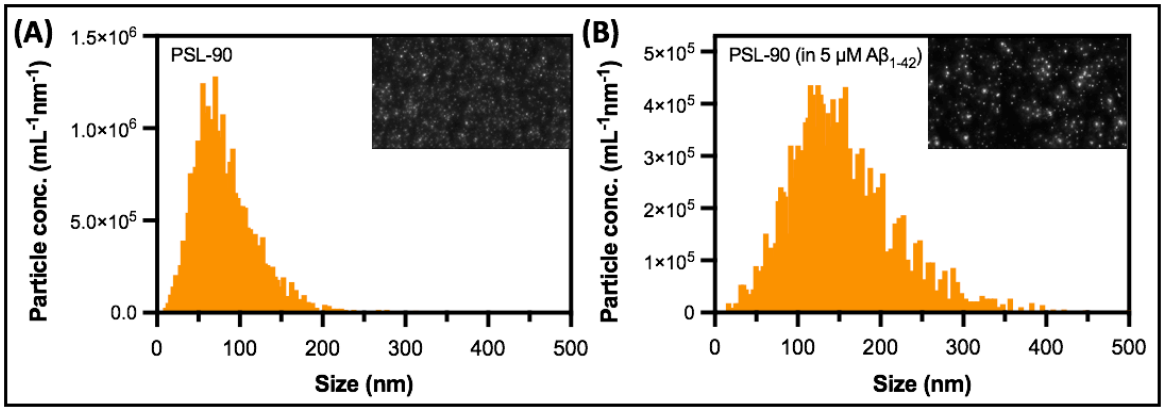

Figure 9.14. Determination of viscosity of Aβ1-42 solution using MNTA.
(A) Particle size distribution of PSL particles (nominal d = 90 nm) measured in water. The average size was 84 nm. A high PSL concentration (8.6E7 particles/mL measured) was used to mitigate the potential influence of Aβ aggregates on the distribution. The PSL concentration was 16-fold higher than the average particle concentration of 5 μM $A\beta_{1\text{-}42}$ in aggregation buffer (5.5E6 particles/mL). **(B)** Size distribution of the same PSL particles diluted in 5 μM $A\beta_{1\text{-}42}$ rather than water alone. The average size was 161 nm, indicating a solution of higher viscosity ($\eta = (d_2/d_1)*\eta_{H2O,27C}$ = (161 nm/84 nm)*0.85 cP = 1.63 cP) according to the Stokes-Einstein equation.

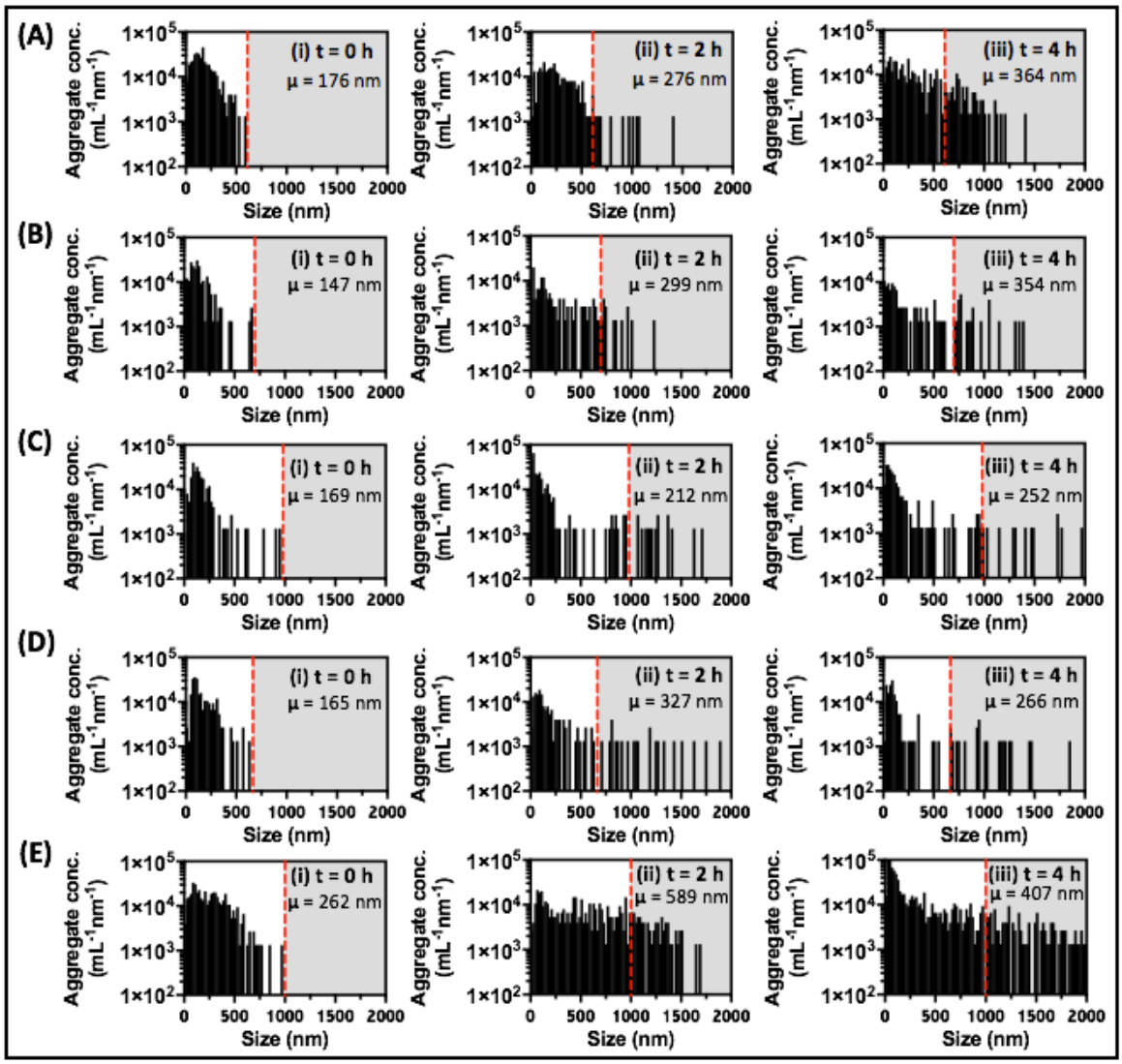

Figure 9.15. Individual replicates for all aggregation experiments showing size distributions at three time points.

(A-E) Aggregate size distributions during the growth period corresponding to the **(A)** first, **(B)** second, **(C)** third, **(D)** fourth, and **(E)** fifth replicate experiments of monitoring $A\beta_{1\text{-}42}$ (5 μM) aggregation at t = 0, 2, and 4 h. Note: the fifth replicate was not included in Figure 8. 5 averaging because measurements were not recorded for the full 12 h.

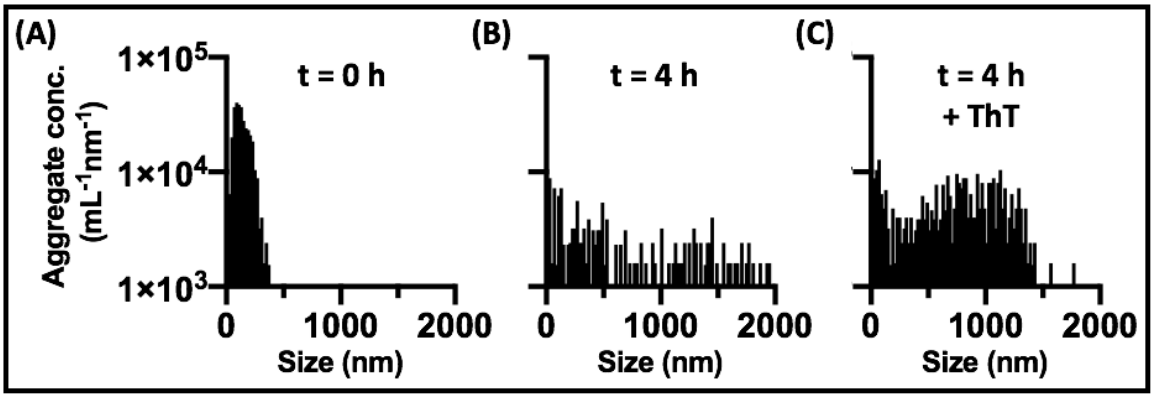

Figure 9.16. Effect of ThT addition on the measured size distribution of Aβ1-42 after aggregation has already proceeded.

(A) $A\beta_{1\text{-}42}$ (5 μM) size distribution after solubilizing in buffer (Tris 40 mM, NaCl 150 mM). The average size was 146 nm and the standard deviation was 43 nm. **(B)** The same sample measured after 4 h. The average size was 717 nm and the standard deviation was 572 nm. (C) ThT (10 μM) was added immediately after the t = 4 h measurement in panel B. The average size was 733 nm and the standard deviation was 410 nm. This did not have the same modulatory effect observed as when ThT was present from t = 0 h (Figure 8. 6C); however, an increased sensitivity to 500-1500 nm aggregates was observed.

REFERENCES

1. Ntziachristos, V.; Razansky, D., Molecular Imaging by Means of Multispectral Optoacoustic Tomography (MSOT). *Chemical Reviews* **2010,** *110* (5), 2783-2794.

2. Kim, C.; Favazza, C.; Wang, L. V., In vivo photoacoustic tomography of chemicals: high-resolution functional and molecular optical imaging at new depths. *Chemical reviews* **2010,** *110* (5), 2756-2782.

3. Wang, L. V.; Hu, S., Photoacoustic Tomography: In Vivo Imaging from Organelles to Organs. *Science (New York, N.y.)* **2012,** *335* (6075), 1458-1462.

4. Xia, J.; Yao, J.; Wang, L. V., Photoacoustic tomography: principles and advances. *Electromagnetic waves (Cambridge, Mass.)* **2014,** *147*, 1-22.

5. Wang, L. V.; Yao, J., A practical guide to photoacoustic tomography in the life sciences. *Nat Meth* **2016,** *13* (8), 627-638.

6. Beard, P., Biomedical photoacoustic imaging. *Interface Focus* **2011,** *1* (4), 602-631.

7. Luke, G. P.; Yeager, D.; Emelianov, S. Y., Biomedical applications of photoacoustic imaging with exogenous contrast agents. *Annals of biomedical engineering* **2012,** *40* (2), 422-437.

8. Weber, J.; Beard, P. C.; Bohndiek, S. E., Contrast agents for molecular photoacoustic imaging. *Nat Meth* **2016,** *13* (8), 639-650.

9. Nie, L.; Chen, X., Structural and functional photoacoustic molecular tomography aided by emerging contrast agents. *Chemical Society Reviews* **2014,** *43* (20), 7132-7170.

10. Fu, Q.; Zhu, R.; Song, J.; Yang, H.; Chen, X., Photoacoustic Imaging: Contrast Agents and Their Biomedical Applications. *Advanced Materials* **2018,** *0* (0), 1805875.

11. Huang, X.; Song, J.; Yung, B. C.; Huang, X.; Xiong, Y.; Chen, X., Ratiometric optical nanoprobes enable accurate molecular detection and imaging. *Chemical Society Reviews* **2018,** *47* (8), 2873-2920.

12. Miao, Q.; Pu, K., Emerging Designs of Activatable Photoacoustic Probes for Molecular Imaging. *Bioconjugate Chemistry* **2016,** *27* (12), 2808-2823.

13. Li, W.; Chen, X., Gold nanoparticles for photoacoustic imaging. *Nanomedicine* **2015,** *10* (2), 299-320.

14. Manohar, S.; Ungureanu, C.; Van Leeuwen, T. G., Gold nanorods as molecular contrast agents in photoacoustic imaging: the promises and the caveats. *Contrast Media & Molecular Imaging* **2011,** *6* (5), 389-400.

15. Cho, E. C.; Glaus, C.; Chen, J.; Welch, M. J.; Xia, Y., Inorganic nanoparticle-based contrast agents for molecular imaging. *Trends in molecular medicine* **2010,** *16* (12), 561-573.

16. Lin, L.-S.; Song, J.; Yang, H.-H.; Chen, X., Yolk–Shell Nanostructures: Design, Synthesis, and Biomedical Applications. *Advanced Materials* **2018,** *30* (6), 1704639.

17. Liu, Y.; Bhattarai, P.; Dai, Z.; Chen, X., Photothermal therapy and photoacoustic imaging via nanotheranostics in fighting cancer. *Chemical Society Reviews* **2019**.

18. Huang, K.; Zhang, Y.; Lin, J.; Huang, P., Nanomaterials for photoacoustic imaging in the second near-infrared window. *Biomaterials science* **2018**.

19. Jiang, Y.; Pu, K., Molecular Fluorescence and Photoacoustic Imaging in the Second Near-Infrared Optical Window Using Organic Contrast Agents. *Advanced Biosystems* **2018,** *2* (5), 1700262.

20. Jiang, Y.; Pu, K., Advanced photoacoustic imaging applications of near-infrared absorbing organic nanoparticles. *Small* **2017,** *13* (30), 1700710.

21. Li, K.; Liu, B., Polymer-encapsulated organic nanoparticles for fluorescence and photoacoustic imaging. *Chemical Society Reviews* **2014,** *43* (18), 6570-6597.

22. Li, J.; Pu, K., Development of organic semiconducting materials for deep-tissue optical imaging, phototherapy and photoactivation. *Chemical Society Reviews* **2019,** *48* (1), 38-71.

23. Jiang, Y.; Pu, K., Multimodal Biophotonics of Semiconducting Polymer Nanoparticles. *Accounts of Chemical Research* **2018,** *51* (8), 1840-1849.

24. Hu, S.; Wang, L. V., Neurovascular photoacoustic tomography. *Frontiers in neuroenergetics* **2010,** *2*, 10.

25. Wang, D.; Wu, Y.; Xia, J., Review on photoacoustic imaging of the brain using nanoprobes. *Neurophotonics* **2016,** *3* (1), 010901.

26. Hu, S.; Wang, L. V., Photoacoustic imaging and characterization of the microvasculature. *Journal of biomedical optics* **2010,** *15* (1), 011101.

27. Mallidi, S.; Luke, G. P.; Emelianov, S., Photoacoustic imaging in cancer detection, diagnosis, and treatment guidance. *Trends in biotechnology* **2011,** *29* (5), 213-221.

28. Xia, J.; Kim, C.; Lovell, J. F., Opportunities for Photoacoustic-Guided Drug Delivery. *Curr Drug Targets* **2015,** *16* (6), 571-81.

29. Bell, A. G., The photophone. *Journal of the Franklin Institute* **1880,** *110* (4), 237-248.

30. Bell, A. G., The Production of Sound by Radiant Energy. *Science* **1881,** *2* (48), 242-253.

31. Rosencwaig, A.; Gersho, A., Theory of the photoacoustic effect with solids. *Journal of Applied Physics* **1976,** *47* (1), 64-69.

32. Bowen, T., Radiation-induced thermoacoustic imaging. Google Patents: 1983.

33. Kruger, R. A., Photoacoustic ultrasound. *Medical Physics* **1994,** *21* (1), 127-131.

34. Kruger, R. A.; Liu, P.; Fang, Y. R.; Appledorn, C. R., Photoacoustic ultrasound (PAUS)—Reconstruction tomography. *Medical Physics* **1995,** *22* (10), 1605-1609.

35. Hoelen, C.; De Mul, F.; Pongers, R.; Dekker, A., Three-dimensional photoacoustic imaging of blood vessels in tissue. *Optics letters* **1998,** *23* (8), 648-650.

36. Wang, L. V.; Zhao, X.; Sun, H.; Ku, G., Microwave-induced acoustic imaging of biological tissues. *Review of scientific instruments* **1999,** *70* (9), 3744-3748.

37. Zackrisson, S.; van de Ven, S.; Gambhir, S., Light in and sound out: emerging translational strategies for photoacoustic imaging. *Cancer research* **2014,** *74* (4), 979-1004.

38. Sordillo, L. A.; Pu, Y.; Pratavieira, S.; Budansky, Y.; Alfano, R. R., Deep optical imaging of tissue using the second and third near-infrared spectral windows. *Journal of Biomedical Optics* **2014,** *19* (5), 056004-056004.

39. Frangioni, J. V., In vivo near-infrared fluorescence imaging. *Current opinion in chemical biology* **2003,** *7* (5), 626-634.

40. Cox, B.; Laufer, J. G.; Arridge, S. R.; Beard, P. C., Quantitative spectroscopic photoacoustic imaging: a review. *Journal of Biomedical Optics* **2012,** *17* (6), 0612021-06120222.

41. Maslov, K.; Wang, L. V., Photoacoustic imaging of biological tissue with intensity-modulated continuous-wave laser. *Journal of biomedical optics* **2008,** *13* (2), 024006-024006-5.

42. Wang, X.; Pang, Y.; Ku, G.; Xie, X.; Stoica, G.; Wang, L. V., Noninvasive laser-induced photoacoustic tomography for structural and functional in vivo imaging of the brain. *Nature biotechnology* **2003,** *21* (7), 803-806.

43. Lashkari, B.; Mandelis, A., Comparison between pulsed laser and frequency-domain photoacoustic modalities: signal-to-noise ratio, contrast, resolution, and maximum depth detectivity. *Review of Scientific Instruments* **2011,** *82* (9), 094903.

44. Xu, M.; Wang, L. V., Photoacoustic imaging in biomedicine. *Review of scientific instruments* **2006,** *77* (4), 041101.

45. Pramanik, M.; Wang, L. V., Thermoacoustic and photoacoustic sensing of temperature. *Journal of biomedical optics* **2009,** *14* (5), 054024-054024-7.

46. Wang, L. V., Multiscale photoacoustic microscopy and computed tomography. *Nature photonics* **2009,** *3* (9), 503-509.

47. Zhang, C.; Wang, Y., Comparison of Various Imaging Modes for Photoacoustic Tomography. Springer Berlin Heidelberg: 2009; pp 121-124.

48. Hu, S.; Maslov, K.; Wang, L. V., Second-generation optical-resolution photoacoustic microscopy with improved sensitivity and speed. *Optics Letters* **2011,** *36* (7), 1134.

49. Zhang, C.; Maslov, K. I.; Hu, S.; Wang, L. V.; Chen, R.; Zhou, Q.; Shung, K. K. In *Reflection-mode submicron-resolution in vivo photoacoustic microscopy*, SPIE: 2012; p 4.

50. Ansari, R.; Zhang, E. Z.; Desjardins, A. E.; Beard, P. C., All-optical forward-viewing photoacoustic probe for high-resolution 3D endoscopy. *Light: Science & Applications* **2018,** *7* (1), 75.

51. Zhang, H. F.; Maslov, K.; Stoica, G.; Wang, L. V., Functional photoacoustic microscopy for high-resolution and noninvasive in vivo imaging. *Nature Biotechnology* **2006,** *24*, 848.

52. Lan, B.; Liu, W.; Wang, Y.-c.; Shi, J.; Li, Y.; Xu, S.; Sheng, H.; Zhou, Q.; Zou, J.; Hoffmann, U.; Yang, W.; Yao, J., High-speed widefield photoacoustic microscopy of small-animal hemodynamics. *Biomed. Opt. Express* **2018,** *9* (10), 4689-4701.

53. Lan, B.; Liu, W.; Yao, J. In *High-speed wide-field photoacoustic microscopy*, Clinical and Translational Biophotonics, Optical Society of America: 2018; p JTu3A. 68.

54. Favazza, C. P.; Jassim, O.; Cornelius, L. A.; Wang, L. V., In vivo photoacoustic microscopy of human cutaneous microvasculature and a nevus. *Journal of Biomedical Optics* **2011,** *16* (1), 016015.

55. Park, K.; Kim, J. Y.; Lee, C.; Jeon, S.; Lim, G.; Kim, C., Handheld Photoacoustic Microscopy Probe. *Scientific Reports* **2017,** *7* (1), 13359.

56. Xu, M.; Wang, L. V., Universal back-projection algorithm for photoacoustic computed tomography. *Physical Review E* **2005,** *71* (1), 016706.

57. Schellenberg, M. W.; Hunt, H. K., Hand-held optoacoustic imaging: A review. *Photoacoustics* **2018,** *11*, 14-27.

58. Yang, J.-M.; Maslov, K.; Yang, H.-C.; Zhou, Q.; Shung, K. K.; Wang, L. V., Photoacoustic endoscopy. *Optics letters* **2009,** *34* (10), 1591-1593.

59. Yang, J.-M.; Favazza, C.; Chen, R.; Yao, J.; Cai, X.; Maslov, K.; Zhou, Q.; Shung, K. K.; Wang, L. V., Simultaneous functional photoacoustic and ultrasonic endoscopy of internal organs in vivo. *Nature medicine* **2012,** *18* (8), 1297-1302.

60. Nikoozadeh, A.; Choe, J. W.; Kothapalli, S.-R.; Moini, A.; Sanjani, S. S.; Kamaya, A.; Oralkan, Ö.; Gambhir, S. S.; Khuri-Yakub, P. T. In *Photoacoustic imaging using a 9F microLinear CMUT ICE catheter*, Ultrasonics Symposium (IUS), 2012 IEEE International, IEEE: 2012; pp 24-27.

61. Zhang, H. F.; Maslov, K.; Wang, L. V., In vivo imaging of subcutaneous structures using functional photoacoustic microscopy. *Nature protocols* **2007,** *2* (4), 797-804.

62. Yao, J.; Wang, L.; Yang, J.-M.; Maslov, K. I.; Wong, T. T. W.; Li, L.; Huang, C.-H.; Zou, J.; Wang, L. V., High-speed label-free functional photoacoustic microscopy of mouse brain in action. *Nat Meth* **2015,** *12* (5), 407-410.

63. Wang, L. V.; Wu, H.-i., *Biomedical optics: principles and imaging*. John Wiley & Sons: 2012.

64. Zhang, H. F.; Maslov, K.; Sivaramakrishnan, M.; Stoica, G.; Wang, L. V., Imaging of hemoglobin oxygen saturation variations in single vessels in vivo using photoacoustic microscopy. *Applied physics letters* **2007,** *90* (5), 053901.

65. Oh, J.-T.; Li, M.-L.; Zhang, H. F.; Maslov, K.; Stoica, G.; Wang, L. V., Three-dimensional imaging of skin melanoma in vivo by dual-wavelength photoacoustic microscopy. *Journal of biomedical optics* **2006,** *11* (3), 034032-034032-4.

66. Allen, T. J.; Hall, A.; Dhillon, A. P.; Owen, J. S.; Beard, P. C., Spectroscopic photoacoustic imaging of lipid-rich plaques in the human aorta in the 740 to 1400 nm wavelength range. *Journal of biomedical optics* **2012,** *17* (6), 0612091-06120910.

67. Lemaster, J. E.; Jokerst, J. V., What is new in nanoparticle-based photoacoustic imaging? *Wiley Interdisciplinary Reviews: Nanomedicine and Nanobiotechnology* **2017,** *9* (1).

68. Thakor, A. S.; Jokerst, J. V.; Ghanouni, P.; Campbell, J. L.; Mittra, E.; Gambhir, S. S., Clinically approved nanoparticle imaging agents. *Journal of Nuclear Medicine* **2016,** *57* (12), 1833-1837.

69. Albanese, A.; Tang, P. S.; Chan, W. C. W., The Effect of Nanoparticle Size, Shape, and Surface Chemistry on Biological Systems. *Annual Review of Biomedical Engineering* **2012,** *14* (1), 1-16.

70. Sun, T.; Zhang, Y. S.; Pang, B.; Hyun, D. C.; Yang, M.; Xia, Y., Engineered Nanoparticles for Drug Delivery in Cancer Therapy. *Angewandte Chemie International Edition* **2014,** *53* (46), 12320-12364.

71. Jain, P. K.; Lee, K. S.; El-Sayed, I. H.; El-Sayed, M. A., Calculated Absorption and Scattering Properties of Gold Nanoparticles of Different Size, Shape, and Composition: Applications in Biological Imaging and Biomedicine. *The Journal of Physical Chemistry B* **2006,** *110* (14), 7238-7248.

72. Feis, A.; Gellini, C.; Salvi, P. R.; Becucci, M., Photoacoustic excitation profiles of gold nanoparticles. *Photoacoustics* **2014,** *2* (1), 47-53.

73. Zhou, Y.; Wang, D.; Zhang, Y.; Chitgupi, U.; Geng, J.; Wang, Y.; Zhang, Y.; Cook, T. R.; Xia, J.; Lovell, J. F., A Phosphorus Phthalocyanine Formulation with Intense Absorbance at 1000 nm for Deep Optical Imaging. *Theranostics* **2016,** *6* (5), 688-697.

74. Salehi, H. S.; Kumavor, P. D.; Li, H.; Alqasemi, U.; Wang, T.; Xu, C.; Zhu, Q., Design of optimal light delivery system for co-registered transvaginal ultrasound and photoacoustic imaging of ovarian tissue. *Photoacoustics* **2015,** *3* (3), 114-122.

75. El-Gohary, S. H.; Metwally, M. K.; Eom, S.; Jeon, S. H.; Byun, K. M.; Kim, T.-S., Design study on photoacoustic probe to detect prostate cancer using 3D Monte Carlo simulation and finite element method. *Biomedical Engineering Letters* **2014,** *4* (3), 250-257.

76. Bell, M. A. L.; Kuo, N. P.; Song, D. Y.; Kang, J. U.; Boctor, E. M., In vivo visualization of prostate brachytherapy seeds with photoacoustic imaging. *Journal of biomedical optics* **2014,** *19* (12), 126011-126011.

77. Yang, J.-M.; Favazza, C. P.; Yao, J.; Chen, R.; Zhou, Q.; Shung, K. K.; Wang, L. V. In *Three-dimensional photoacoustic and ultrasonic endoscopic imaging of two rabbit esophagi*, SPIE BiOS, International Society for Optics and Photonics: 2015; pp 932334-932334-8.

78. Smith, A. M.; Mancini, M. C.; Nie, S., Bioimaging: second window for in vivo imaging. *Nature nanotechnology* **2009,** *4* (11), 710-711.

79. Jiang, Y.; Upputuri, P. K.; Xie, C.; Lyu, Y.; Zhang, L.; Xiong, Q.; Pramanik, M.; Pu, K., Broadband Absorbing Semiconducting Polymer Nanoparticles for Photoacoustic Imaging in Second Near-Infrared Window. *Nano Letters* **2017,** *17* (8), 4964-4969.

80. Welsher, K.; Liu, Z.; Sherlock, S. P.; Robinson, J. T.; Chen, Z.; Daranciang, D.; Dai, H., A route to brightly fluorescent carbon nanotubes for near-infrared imaging in mice. *Nature nanotechnology* **2009,** *4* (11), 773-780.

81. Park, J. E.; Kim, M.; Hwang, J. H.; Nam, J. M., Golden Opportunities: Plasmonic Gold Nanostructures for Biomedical Applications based on the Second Near-Infrared Window. *Small Methods* **2017,** *1* (3), 1600032.

82. Ku, G.; Zhou, M.; Song, S.; Huang, Q.; Hazle, J.; Li, C., Copper sulfide nanoparticles as a new class of photoacoustic contrast agent for deep tissue imaging at 1064 nm. *Acs Nano* **2012,** *6* (8), 7489-7496.

83. Homan, K. A.; Souza, M.; Truby, R.; Luke, G. P.; Green, C.; Vreeland, E.; Emelianov, S., Silver Nanoplate Contrast Agents for in Vivo Molecular Photoacoustic Imaging. *ACS Nano* **2012,** *6* (1), 641-650.

84. Steeg, P. S.; Theodorescu, D., Metastasis: a therapeutic target for cancer. *Nature clinical practice. Oncology* **2008,** *5* (4), 206-219.

85. Grootendorst, D.; Jose, J.; Wouters, M.; van Boven, H.; Van der Hage, J.; Van Leeuwen, T.; Steenbergen, W.; Manohar, S.; Ruers, T., First experiences of photoacoustic imaging for detection of melanoma metastases in resected human lymph nodes. *Lasers in surgery and medicine* **2012,** *44* (7), 541-549.

86. Langhout, G. C.; Grootendorst, D. J.; Nieweg, O. E.; Wouters, M. W. J. M.; Hage, J. A. v. d.; Jose, J.; Boven, H. v.; Steenbergen, W.; Manohar, S.; Ruers, T. J. M., Detection of melanoma metastases in resected human lymph nodes by noninvasive multispectral photoacoustic imaging. *Journal of Biomedical Imaging* **2014,** *2014*, 5.

87. Luke, G. P.; Emelianov, S. Y., Label-free Detection of Lymph Node Metastases with US-guided Functional Photoacoustic Imaging. *Radiology* **2015,** *277* (2), 435-442.

88. Wang, Y.; Hu, S.; Maslov, K.; Zhang, Y.; Xia, Y.; Wang, L. V., In vivo integrated photoacoustic and confocal microscopy of hemoglobin oxygen saturation and oxygen partial pressure. *Optics letters* **2011,** *36* (7), 1029-1031.

89. Ning, B.; Kennedy, M. J.; Dixon, A. J.; Sun, N.; Cao, R.; Soetikno, B. T.; Chen, R.; Zhou, Q.; Shung, K. K.; Hossack, J. A., Simultaneous photoacoustic microscopy of microvascular anatomy, oxygen saturation, and blood flow. *Optics letters* **2015,** *40* (6), 910-913.

90. Xi, L.; Grobmyer, S. R.; Wu, L.; Chen, R.; Zhou, G.; Gutwein, L. G.; Sun, J.; Liao, W.; Zhou, Q.; Xie, H., Evaluation of breast tumor margins in vivo with intraoperative photoacoustic imaging. *Optics express* **2012,** *20* (8), 8726-8731.

91. Neuschmelting, V.; Burton, N. C.; Lockau, H.; Urich, A.; Harmsen, S.; Ntziachristos, V.; Kircher, M. F., Performance of a Multispectral Optoacoustic Tomography (MSOT) System equipped with 2D vs. 3D Handheld Probes for Potential Clinical Translation. *Photoacoustics* **2016,** *4* (1), 1-10.

92. Neuschmelting, V.; Lockau, H.; Ntziachristos, V.; Grimm, J.; Kircher, M. F., Lymph Node Micrometastases and In-Transit Metastases from Melanoma: In Vivo Detection with Multispectral Optoacoustic Imaging in a Mouse Model. *Radiology* **2016,** *280* (1), 137-150.

93. Horiguchi, A.; Tsujita, K.; Irisawa, K.; Kasamatsu, T.; Hirota, K.; Kawaguchi, M.; Shinchi, M.; Ito, K.; Asano, T.; Shinmoto, H.; Tsuda, H.; Ishihara, M., A pilot study of photoacoustic imaging system for improved real-time visualization of neurovascular bundle during radical prostatectomy. *The Prostate* **2016,** *76* (3), 307-315.

94. Moradi, H.; Tang, S.; Salcudean, S. E., Toward Intra-Operative Prostate Photoacoustic Imaging: Configuration Evaluation and Implementation Using the da Vinci Research Kit. *IEEE Transactions on Medical Imaging* **2019,** *38* (1), 57-68.

95. Gandhi, N.; Allard, M.; Kim, S.; Kazanzides, P.; Lediju Bell, M. A., Photoacoustic-based approach to surgical guidance performed with and without a da Vinci robot. *Journal of Biomedical Optics* **2017,** *22* (12), 121606.

96. Eddins, B.; Bell, M. A. L., Design of a multifiber light delivery system for photoacoustic-guided surgery. *Journal of biomedical optics* **2017,** *22* (4), 041011.

97. Wang, B.; Karpiouk, A.; Yeager, D.; Amirian, J.; Litovsky, S.; Smalling, R.; Emelianov, S., Intravascular photoacoustic imaging of lipid in atherosclerotic plaques in the presence of luminal blood. *Optics letters* **2012,** *37* (7), 1244-1246.

98. Wang, B.; Su, J. L.; Karpiouk, A. B.; Sokolov, K. V.; Smalling, R. W.; Emelianov, S. Y., Intravascular photoacoustic imaging. *IEEE Journal of selected topics in Quantum Electronics* **2010,** *16* (3), 588-599.

99. Jansen, K.; Van Der Steen, A. F.; van Beusekom, H. M.; Oosterhuis, J. W.; van Soest, G., Intravascular photoacoustic imaging of human coronary atherosclerosis. *Optics letters* **2011,** *36* (5), 597-599.

100. Wu, M.; Springeling, G.; Lovrak, M.; Mastik, F.; Iskander-Rizk, S.; Wang, T.; Van Beusekom, H. M.; Van Der Steen, A.; Van Soest, G., Real-time volumetric lipid imaging in vivo by intravascular photoacoustics at 20 frames per second. *Biomed. Opt. Express* **2017,** *8* (2), 943-953.

101. Yang, J.-M.; Li, C.; Chen, R.; Zhou, Q.; Shung, K. K.; Wang, L. V., Catheter-based photoacoustic endoscope. *Journal of biomedical optics* **2014,** *19* (6), 066001.

102. Iwashita, T.; Nakai, Y.; Lee, J. G.; Park, D. H.; Muthusamy, V. R.; Chang, K. J., Newly-developed, forward-viewing echoendoscope: A comparative pilot study to the standard echoendoscope in the imaging of abdominal organs and feasibility of endoscopic ultrasound-guided interventions. *Journal of Gastroenterology and Hepatology* **2012,** *27* (2), 362-367.

103. Dong, B.; Chen, S.; Zhang, Z.; Sun, C.; Zhang, H. F., Photoacoustic probe using a microring resonator ultrasonic sensor for endoscopic applications. *Optics letters* **2014,** *39* (15), 4372-4375.

104. Jokerst, J. V.; Cole, A. J.; Van de Sompel, D.; Gambhir, S. S., Gold nanorods for ovarian cancer detection with photoacoustic imaging and resection guidance via Raman imaging in living mice. *ACS nano* **2012,** *6* (11), 10366-10377.

105. Kircher, M. F.; de la Zerda, A.; Jokerst, J. V.; Zavaleta, C. L.; Kempen, P. J.; Mittra, E.; Pitter, K.; Huang, R.; Campos, C.; Habte, F.; Sinclair, R.; Brennan, C. W.; Mellinghoff, I. K.; Holland, E. C.; Gambhir, S. S., A Brain Tumor Molecular Imaging Strategy Using A New Triple-Modality MRI-Photoacoustic-Raman Nanoparticle. *Nature medicine* **2012,** *18* (5), 829-834.

106. Guan, T.; Shang, W.; Li, H.; Yang, X.; Fang, C.; Tian, J.; Wang, K., From Detection to Resection: Photoacoustic Tomography and Surgery Guidance with Indocyanine Green Loaded Gold Nanorod@liposome Core–Shell Nanoparticles in Liver Cancer. *Bioconjugate Chemistry* **2017,** *28* (4), 1221-1228.

107. Wilson, K. E.; Bachawal, S. V.; Abou-Elkacem, L.; Jensen, K.; Machtaler, S.; Tian, L.; Willmann, J. K., Spectroscopic Photoacoustic Molecular Imaging of Breast Cancer using a B7-H3-targeted ICG Contrast Agent. *Theranostics* **2017,** *7* (6), 1463-1476.

108. Grootendorst, D. J.; Jose, J.; Fratila, R. M.; Visscher, M.; Velders, A. H.; Ten Haken, B.; Van Leeuwen, T. G.; Steenbergen, W.; Manohar, S.; Ruers, T. J., Evaluation of superparamagnetic iron oxide nanoparticles (Endorem®) as a photoacoustic contrast agent for intra-operative nodal staging. *Contrast media & molecular imaging* **2013,** *8* (1), 83-91.

109. Ray, A.; Wang, X.; Lee, Y.-E. K.; Hah, H. J.; Kim, G.; Chen, T.; Orringer, D. A.; Sagher, O.; Liu, X.; Kopelman, R., Targeted blue nanoparticles as photoacoustic contrast agent for brain tumor delineation. *Nano research* **2011,** *4* (11), 1163-1173.

110. Maeda, A.; Bu, J.; Chen, J.; Zheng, G.; DaCosta, R. S., Dual in vivo Photoacoustic and Fluorescence Imaging of HER2 Expression in Breast Tumors for Diagnosis, Margin Assessment, and Surgical Guidance. *Molecular Imaging* **2015,** *14* (1), 7290.2014.00043.

111. Harisinghani, M. G.; Barentsz, J.; Hahn, P. F.; Deserno, W. M.; Tabatabaei, S.; van de Kaa, C. H.; de la Rosette, J.; Weissleder, R., Noninvasive Detection of Clinically Occult Lymph-Node Metastases in Prostate Cancer. *New England Journal of Medicine* **2003,** *348* (25), 2491-2499.

112. Xi, L.; Zhou, G.; Gao, N.; Yang, L.; Gonzalo, D. A.; Hughes, S. J.; Jiang, H., Photoacoustic and Fluorescence Image-Guided Surgery Using a Multifunctional Targeted Nanoprobe. *Annals of surgical oncology* **2014,** *21* (5), 1602-1609.

113. Shakiba, M.; Ng, K. K.; Huynh, E.; Chan, H.; Charron, D. M.; Chen, J.; Muhanna, N.; Foster, F. S.; Wilson, B. C.; Zheng, G., Stable J-aggregation enabled dual photoacoustic and fluorescence nanoparticles for intraoperative cancer imaging. *Nanoscale* **2016,** *8* (25), 12618-12625.

114. Mallidi, S.; Larson, T.; Tam, J.; Joshi, P. P.; Karpiouk, A.; Sokolov, K.; Emelianov, S., Multiwavelength photoacoustic imaging and plasmon resonance coupling of gold nanoparticles for selective detection of cancer. *Nano letters* **2009,** *9* (8), 2825-2831.

115. Sethuraman, S.; Amirian, J. H.; Litovsky, S. H.; Smalling, R. W.; Emelianov, S. Y., Spectroscopic intravascular photoacoustic imaging to differentiate atherosclerotic plaques. *Optics express* **2008,** *16* (5), 3362-3367.

116. Afshar-Oromieh, A.; Malcher, A.; Eder, M.; Eisenhut, M.; Linhart, H.; Hadaschik, B.; Holland-Letz, T.; Giesel, F.; Kratochwil, C.; Haufe, S., PET imaging with a [68 Ga] gallium-labelled PSMA ligand for the diagnosis of prostate cancer: biodistribution in humans and first evaluation of tumour lesions. *European journal of nuclear medicine and molecular imaging* **2013,** *40* (4), 486-495.

117. Yang, K.; Wan, J.; Zhang, S.; Zhang, Y.; Lee, S.-T.; Liu, Z., In vivo pharmacokinetics, long-term biodistribution, and toxicology of PEGylated graphene in mice. *ACS nano* **2010,** *5* (1), 516-522.

118. Li, L.; Zhu, L.; Ma, C.; Lin, L.; Yao, J.; Wang, L.; Maslov, K.; Zhang, R.; Chen, W.; Shi, J.; Wang, L. V., Single-impulse panoramic photoacoustic computed tomography of small-animal whole-body dynamics at high spatiotemporal resolution. *Nature Biomedical Engineering* **2017,** *1*, 0071.

119. Lyu, Y.; Fang, Y.; Miao, Q.; Zhen, X.; Ding, D.; Pu, K., Intraparticle Molecular Orbital Engineering of Semiconducting Polymer Nanoparticles as Amplified Theranostics for in Vivo Photoacoustic Imaging and Photothermal Therapy. *ACS Nano* **2016,** *10* (4), 4472-4481.

120. Zhang, Y.; Jeon, M.; Rich, L. J.; Hong, H.; Geng, J.; Zhang, Y.; Shi, S.; Barnhart, T. E.; Alexandridis, P.; Huizinga, J. D., Non-invasive multimodal functional imaging of the intestine with frozen micellar naphthalocyanines. *Nature nanotechnology* **2014,** *9* (8), 631-638.

121. Liu, T.; Wang, C.; Cui, W.; Gong, H.; Liang, C.; Shi, X.; Li, Z.; Sun, B.; Liu, Z., Combined photothermal and photodynamic therapy delivered by PEGylated MoS2 nanosheets. *Nanoscale* **2014,** *6* (19), 11219-11225.

122. Tian, G.; Zhang, X.; Zheng, X.; Yin, W.; Ruan, L.; Liu, X.; Zhou, L.; Yan, L.; Li, S.; Gu, Z.; Zhao, Y., Multifunctional RbxWO3 Nanorods for Simultaneous Combined Chemo-photothermal Therapy and Photoacoustic/CT Imaging. *Small* **2014,** *10* (20), 4160-4170.

123. Moon, G. D.; Choi, S.-W.; Cai, X.; Li, W.; Cho, E. C.; Jeong, U.; Wang, L. V.; Xia, Y., A New Theranostic System Based on Gold Nanocages and Phase-Change Materials with Unique Features for Photoacoustic Imaging and Controlled Release. *Journal of the American Chemical Society* **2011,** *133* (13), 4762-4765.

124. Manivasagan, P.; Bharathiraja, S.; Bui, N. Q.; Jang, B.; Oh, Y.-O.; Lim, I. G.; Oh, J., Doxorubicin-loaded fucoidan capped gold nanoparticles for drug delivery and photoacoustic imaging. *International journal of biological macromolecules* **2016,** *91*, 578-588.

125. Zhong, J.; Yang, S.; Wen, L.; Xing, D., Imaging-guided photoacoustic drug release and synergistic chemo-photoacoustic therapy with paclitaxel-containing nanoparticles. *Journal of Controlled Release* **2016,** *226*, 77-87.

126. Ho, I.-T.; Sessler, J. L.; Gambhir, S. S.; Jokerst, J. V., Parts per billion detection of uranium with a porphyrinoid-containing nanoparticle and in vivo photoacoustic imaging. *Analyst* **2015,** *140* (11), 3731-3737.

127. Cash, K. J.; Li, C.; Xia, J.; Wang, L. V.; Clark, H. A., Optical Drug Monitoring: Photoacoustic Imaging of Nanosensors to Monitor Therapeutic Lithium in Vivo. *ACS Nano* **2015,** *9* (2), 1692-1698.

128. Jeevarathinam, A. S.; Pai, N.; Huang, K.; Hariri, A.; Wang, J.; Bai, Y.; Wang, L.; Hancock, T.; Keys, S.; Penny, W.; Jokerst, J. V., A cellulose-based photoacoustic sensor to measure heparin concentration and activity in human blood samples. *Biosensors and Bioelectronics* **2019,** *126*, 831-837.

129. Wilson, K.; Homan, K.; Emelianov, S., Biomedical photoacoustics beyond thermal expansion using triggered nanodroplet vaporization for contrast-enhanced imaging. *Nature Communications* **2012,** *3*, 618.

130. Lovell, J. F.; Jin, C. S.; Huynh, E.; Jin, H.; Kim, C.; Rubinstein, J. L.; Chan, W. C. W.; Cao, W.; Wang, L. V.; Zheng, G., Porphysome nanovesicles generated by porphyrin bilayers for use as multimodal biophotonic contrast agents. *Nat Mater* **2011,** *10* (4), 324-332.

131. Huynh, E.; Jin, C. S.; Wilson, B. C.; Zheng, G., Aggregate Enhanced Trimodal Porphyrin Shell Microbubbles for Ultrasound, Photoacoustic, and Fluorescence Imaging. *Bioconjugate Chemistry* **2014,** *25* (4), 796-801.

132. Roberts, S.; Seeger, M.; Jiang, Y.; Mishra, A.; Sigmund, F.; Stelzl, A.; Lauri, A.; Symvoulidis, P.; Rolbieski, H.; Preller, M.; Deán-Ben, X. L.; Razansky, D.; Orschmann, T.; Desbordes, S. C.; Vetschera, P.; Bach, T.; Ntziachristos, V.; Westmeyer, G. G., Calcium Sensor for Photoacoustic Imaging. *Journal of the American Chemical Society* **2017**.

133. Wang, J.; Chen, F.; Arconada-Alvarez, S. J.; Hartanto, J.; Yap, L.-P.; Park, R.; Wang, F.; Vorobyova, I.; Dagliyan, G.; Conti, P. S., A Nanoscale Tool for Photoacoustic-based Measurements

of Clotting Time and Therapeutic Drug Monitoring of Heparin. *Nano Letters* **2016,** *16* (10), 6265-6271.

134. Wang, J.; Jeevarathinam, A. S.; Humphries, K.; Jhunjhunwala, A.; Chen, F.; Hariri, A.; Miller III, B. R.; Jokerst, J. V., A Mechanistic Investigation of Methylene Blue and Heparin Interactions and Their Photoacoustic Enhancement. *Bioconjugate chemistry* **2018**.

135. Raschke, R. A.; Reilly, B. M.; Guidry, J. R.; Fontana, J. R.; Srinivas, S., The weight-based heparin dosing nomogram compared with a standard care nomogram: a randomized controlled trial. *Annals of Internal Medicine* **1993,** *119* (9), 874-881.

136. Jeon, M.; Song, W.; Huynh, E.; Kim, J.; Kim, J.; Helfield, B. L.; Leung, B. Y.; Geortz, D. E.; Zheng, G.; Oh, J., Methylene blue microbubbles as a model dual-modality contrast agent for ultrasound and activatable photoacoustic imaging. *Journal of biomedical optics* **2014,** *19* (1), 016005.

137. Ashkenazi, S., Photoacoustic lifetime imaging of dissolved oxygen using methylene blue. *Journal of Biomedical Optics* **2010,** *15* (4), 040501.

138. Song, K. H.; Stein, E. W.; Margenthaler, J. A.; Wang, L. V., Noninvasive photoacoustic identification of sentinel lymph nodes containing methylene blue in vivo in a rat model. *Journal of biomedical optics* **2008,** *13* (5), 054033.

139. Morgounova, E.; Shao, Q.; Hackel, B. J.; Thomas, D. D.; Ashkenazi, S., Photoacoustic lifetime contrast between methylene blue monomers and self-quenched dimers as a model for dual-labeled activatable probes. *Journal of biomedical optics* **2013,** *18* (5), 056004.

140. Wang, J.; Lin, C.-y.; Moore, C.; Jhunjhunwala, A.; Jokerst, J. V., Switchable Photoacoustic Intensity of Methylene Blue via Sodium Dodecyl Sulfate Micellization. *Langmuir* **2017**.

141. Taruttis, A.; Morscher, S.; Burton, N. C.; Razansky, D.; Ntziachristos, V., Fast Multispectral Optoacoustic Tomography (MSOT) for Dynamic Imaging of Pharmacokinetics and Biodistribution in Multiple Organs. *PLOS ONE* **2012,** *7* (1), e30491.

142. Razansky, D.; Distel, M.; Vinegoni, C.; Ma, R.; Perrimon, N.; Köster, R. W.; Ntziachristos, V., Multispectral opto-acoustic tomography of deep-seated fluorescent proteins in vivo. *nature photonics* **2009,** *3* (7), 412.

143. Hannah, A.; Luke, G.; Wilson, K.; Homan, K.; Emelianov, S., Indocyanine Green-Loaded Photoacoustic Nanodroplets: Dual Contrast Nanoconstructs for Enhanced Photoacoustic and Ultrasound Imaging. *ACS Nano* **2014,** *8* (1), 250-259.

144. Hong, G.; Antaris, A. L.; Dai, H., Near-infrared fluorophores for biomedical imaging. *Nature Biomedical Engineering* **2017,** *1* (1), 0010.

145. Pappone, C.; Rosanio, S.; Oreto, G.; Tocchi, M.; Gugliotta, F.; Vicedomini, G.; Salvati, A.; Dicandia, C.; Mazzone, P.; Santinelli, V., Circumferential radiofrequency ablation of pulmonary vein ostia. *Circulation* **2000,** *102* (21), 2619-2628.

146. Pacella, C. M.; Bizzarri, G.; Spiezia, S.; Bianchini, A.; Guglielmi, R.; Crescenzi, A.; Pacella, S.; Toscano, V.; Papini, E., Thyroid tissue: US-guided percutaneous laser thermal ablation. *Radiology* **2004,** *232* (1), 272-280.

147. Young, J. K.; Figueroa, E. R.; Drezek, R. A., Tunable nanostructures as photothermal theranostic agents. *Annals of biomedical engineering* **2012,** *40* (2), 438-459.

148. Huang, X.; El-Sayed, I. H.; Qian, W.; El-Sayed, M. A., Cancer cell imaging and photothermal therapy in the near-infrared region by using gold nanorods. *Journal of the American Chemical Society* **2006,** *128* (6), 2115-2120.

149. Shashkov, E. V.; Everts, M.; Galanzha, E. I.; Zharov, V. P., Quantum dots as multimodal photoacoustic and photothermal contrast agents. *Nano letters* **2008,** *8* (11), 3953-3958.

150. Yang, K.; Zhang, S.; Zhang, G.; Sun, X.; Lee, S.-T.; Liu, Z., Graphene in mice: ultrahigh in vivo tumor uptake and efficient photothermal therapy. *Nano letters* **2010,** *10* (9), 3318-3323.

151. Ke, H.; Wang, J.; Dai, Z.; Jin, Y.; Qu, E.; Xing, Z.; Guo, C.; Yue, X.; Liu, J., Gold-Nanoshelled Microcapsules: A Theranostic Agent for Ultrasound Contrast Imaging and Photothermal Therapy. *Angewandte Chemie* **2011,** *123* (13), 3073-3077.

152. Huang, P.; Lin, J.; Li, W.; Rong, P.; Wang, Z.; Wang, S.; Wang, X.; Sun, X.; Aronova, M.; Niu, G., Biodegradable gold nanovesicles with an ultrastrong plasmonic coupling effect for photoacoustic imaging and photothermal therapy. *Angewandte Chemie* **2013,** *125* (52), 14208-14214.

153. Lin, L.-S.; Cong, Z.-X.; Cao, J.-B.; Ke, K.-M.; Peng, Q.-L.; Gao, J.; Yang, H.-H.; Liu, G.; Chen, X., Multifunctional Fe3O4@Polydopamine Core–Shell Nanocomposites for Intracellular mRNA Detection and Imaging-Guided Photothermal Therapy. *ACS Nano* **2014,** *8* (4), 3876-3883.

154. Lovell, J. F.; Jin, C. S.; Huynh, E.; MacDonald, T. D.; Cao, W.; Zheng, G., Enzymatic Regioselection for the Synthesis and Biodegradation of Porphysome Nanovesicles. *Angewandte Chemie International Edition* **2012,** *51* (10), 2429-2433.

155. Cheng, L.; Liu, J.; Gu, X.; Gong, H.; Shi, X.; Liu, T.; Wang, C.; Wang, X.; Liu, G.; Xing, H., PEGylated WS2 Nanosheets as a Multifunctional Theranostic Agent for in vivo Dual-Modal CT/Photoacoustic Imaging Guided Photothermal Therapy. *Advanced Materials* **2014,** *26* (12), 1886-1893.

156. Chen, Y.-S.; Yoon, S. J.; Frey, W.; Dockery, M.; Emelianov, S., Dynamic contrast-enhanced photoacoustic imaging using photothermal stimuli-responsive composite nanomodulators. *Nature communications* **2017,** *8*, 15782.

157. Lightdale, C. J.; Heier, S. K.; Marcon, N. E.; McCaughan, J. S.; Gerdes, H.; Overholt, B. F.; Sivak, M. V.; Stiegmann, G. V.; Nava, H. R., Photodynamic therapy with porfimer sodium versus thermal ablation therapy with Nd: YAG laser for palliation of esophageal cancer: a multicenter randomized trial. *Gastrointestinal endoscopy* **1995,** *42* (6), 507-512.

158. Hongcharu, W.; Taylor, C. R.; Aghassi, D.; Suthamjariya, K.; Anderson, R. R.; Chang, Y., Topical ALA-photodynamic therapy for the treatment of acne vulgaris. *Journal of Investigative Dermatology* **2000,** *115* (2), 183-192.

159. Kharkwal, G. B.; Sharma, S. K.; Huang, Y. Y.; Dai, T.; Hamblin, M. R., Photodynamic therapy for infections: clinical applications. *Lasers in surgery and medicine* **2011,** *43* (7), 755-767.

160. Bressler, N., Photodynamic therapy of subfoveal choroidal neovascularization in age-related macular degeneration with verteporfin: two-year results of 2 randomized clinical trials-tap report 2. *Archives of ophthalmology (Chicago, Ill.: 1960)* **2001,** *119* (2), 198-207.

161. Agostinis, P.; Berg, K.; Cengel, K. A.; Foster, T. H.; Girotti, A. W.; Gollnick, S. O.; Hahn, S. M.; Hamblin, M. R.; Juzeniene, A.; Kessel, D., Photodynamic therapy of cancer: an update. *CA: a cancer journal for clinicians* **2011,** *61* (4), 250-281.

162. Ho, C. J. H.; Balasundaram, G.; Driessen, W.; McLaren, R.; Wong, C. L.; Dinish, U.; Attia, A. B. E.; Ntziachristos, V.; Olivo, M., Multifunctional photosensitizer-based contrast agents for photoacoustic imaging. *Scientific reports* **2014,** *4*.

163. Idris, N. M.; Gnanasammandhan, M. K.; Zhang, J.; Ho, P. C.; Mahendran, R.; Zhang, Y., In vivo photodynamic therapy using upconversion nanoparticles as remote-controlled nanotransducers. *Nature medicine* **2012,** *18* (10), 1580-1585.

164. Shao, P.; Chapman, D. W.; Moore, R. B.; Zemp, R. J. In *Monitoring photodynamic therapy with photoacoustic microscopy*, SPIE: 2015; p 6.

165. Srivatsan, A.; Jenkins, S. V.; Jeon, M.; Wu, Z.; Kim, C.; Chen, J.; Pandey, R. K., Gold nanocage-photosensitizer conjugates for dual-modal image-guided enhanced photodynamic therapy. *Theranostics* **2014,** *4* (2), 163.

166. Lin, J.; Wang, S.; Huang, P.; Wang, Z.; Chen, S.; Niu, G.; Li, W.; He, J.; Cui, D.; Lu, G., Photosensitizer-loaded gold vesicles with strong plasmonic coupling effect for imaging-guided photothermal/photodynamic therapy. *ACS nano* **2013,** *7* (6), 5320-5329.

167. Guo, W.; Qiu, Z.; Guo, C.; Ding, D.; Li, T.; Wang, F.; Sun, J.; Zheng, N.; Liu, S., Multifunctional Theranostic Agent of Cu2(OH)PO4 Quantum Dots for Photoacoustic Image-Guided Photothermal/Photodynamic Combination Cancer Therapy. *ACS Applied Materials & Interfaces* **2017,** *9* (11), 9348-9358.

168. Clift, M. J. D.; Stone, V., Quantum dots: an insight and perspective of their biological interaction and how this relates to their relevance for clinical use. *Theranostics* **2012,** *2* (7), 668-680.

169. Laufer, J.; Johnson, P.; Zhang, E.; Treeby, B.; Cox, B.; Pedley, B.; Beard, P., In vivo preclinical photoacoustic imaging of tumor vasculature development and therapy. *Journal of biomedical optics* **2012,** *17* (5), 0560161-0560168.

170. Bohndiek, S. E.; Sasportas, L. S.; Machtaler, S.; Jokerst, J. V.; Hori, S.; Gambhir, S. S., Photoacoustic Tomography Detects Early Vessel Regression and Normalization During Ovarian Tumor Response to the Antiangiogenic Therapy Trebananib. *J Nucl Med* **2015,** *56* (12), 1942-7.

171. Zhang, J.; Zhen, X.; Upputuri, P. K.; Pramanik, M.; Chen, P.; Pu, K., Activatable Photoacoustic Nanoprobes for In Vivo Ratiometric Imaging of Peroxynitrite. *Advanced Materials* **2017,** *29* (6), 1604764.

172. Kim, T.; Zhang, Q.; Li, J.; Zhang, L.; Jokerst, J. V., A Gold/Silver Hybrid Nanoparticle for Treatment and Photoacoustic Imaging of Bacterial Infection. *ACS Nano* **2018,** *12* (6), 5615-5625.

173. Ng, K. K.; Shakiba, M.; Huynh, E.; Weersink, R. A.; Roxin, Á.; Wilson, B. C.; Zheng, G., Stimuli-Responsive Photoacoustic Nanoswitch for in Vivo Sensing Applications. *ACS Nano* **2014,** *8* (8), 8363-8373.

174. Dragulescu-Andrasi, A.; Kothapalli, S.-R.; Tikhomirov, G. A.; Rao, J.; Gambhir, S. S., Activatable Oligomerizable Imaging Agents for Photoacoustic Imaging of Furin-Like Activity in Living Subjects. *Journal of the American Chemical Society* **2013,** *135* (30), 11015-11022.

175. Luis Dean-Ben, X.; Razansky, D., Adding fifth dimension to optoacoustic imaging: volumetric time-resolved spectrally enriched tomography. *Light Sci Appl* **2014,** *3*, e137.

176. Halliwell, B., Reactive oxygen species in living systems: source, biochemistry, and role in human disease. *The American journal of medicine* **1991,** *91* (3), S14-S22.

177. Alfadda, A. A.; Sallam, R. M., Reactive Oxygen Species in Health and Disease. *Journal of Biomedicine and Biotechnology* **2012,** *2012*, 14.

178. Brieger, K.; Schiavone, S.; Miller Jr, F. J.; Krause, K.-H., Reactive oxygen species: from health to disease. *Swiss medical weekly* **2012,** *142*, w13659.

179. Görlach, A.; Dimova, E. Y.; Petry, A.; Martínez-Ruiz, A.; Hernansanz-Agustín, P.; Rolo, A. P.; Palmeira, C. M.; Kietzmann, T., Reactive oxygen species, nutrition, hypoxia and diseases: Problems solved? *Redox Biology* **2015,** *6*, 372-385.

180. Pu, K.; Shuhendler, A. J.; Jokerst, J. V.; Mei, J.; Gambhir, S. S.; Bao, Z.; Rao, J., Semiconducting polymer nanoparticles as photoacoustic molecular imaging probes in living mice. *Nat Nano* **2014,** *9* (3), 233-239.

181. Pacher, P.; Beckman, J. S.; Liaudet, L., Nitric oxide and peroxynitrite in health and disease. *Physiological reviews* **2007,** *87* (1), 315-424.

182. Yoon, Y.; Lee, P. J.; Kurilova, S.; Cho, W., In situ quantitative imaging of cellular lipids using molecular sensors. *Nat Chem* **2011,** *3* (11), 868-874.

183. Kullo, I. J.; Trejo-Gutierrez, J. F.; Lopez-Jimenez, F.; Thomas, R. J.; Allison, T. G.; Mulvagh, S. L.; Arruda-Olson, A. M.; Hayes, S. N.; Pollak, A. W.; Kopecky, S. L.; Hurst, R. T., A Perspective on the New American College of Cardiology/American Heart Association Guidelines for Cardiovascular Risk Assessment. *Mayo Clinic Proceedings 89* (9), 1244-1256.

184. Beard, P. C.; Mills, T., Characterization of post mortem arterial tissue using time-resolved photoacoustic spectroscopy at 436, 461 and 532 nm. *Physics in medicine and biology* **1997,** *42* (1), 177.

185. Allen, T. J.; Beard, P. C. In *Photoacoustic characterisation of vascular tissue at NIR wavelengths*, 2009; pp 71770A-71770A-9.

186. Abran, M.; Cloutier, G.; Cardinal, M.-H. R.; Chayer, B.; Tardif, J.-C.; Lesage, F., Development of a photoacoustic, ultrasound and fluorescence imaging catheter for the study of atherosclerotic plaque. *IEEE transactions on biomedical circuits and systems* **2014,** *8* (5), 696-703.

187. Sangha, G. S.; Phillips, E. H.; Goergen, C. J., In vivo photoacoustic lipid imaging in mice using the second near-infrared window. *Biomed. Opt. Express* **2017,** *8* (2), 736-742.

188. Wilson, R. H.; Nadeau, K. P.; Jaworski, F. B.; Tromberg, B. J.; Durkin, A. J., Review of short-wave infrared spectroscopy and imaging methods for biological tissue characterization. *Journal of Biomedical Optics* **2015,** *20* (3), 030901.

189. Wang, P.; Ma, T.; Slipchenko, M. N.; Liang, S.; Hui, J.; Shung, K. K.; Roy, S.; Sturek, M.; Zhou, Q.; Chen, Z., High-speed intravascular photoacoustic imaging of lipid-laden atherosclerotic plaque enabled by a 2-kHz barium nitrite raman laser. *Scientific reports* **2014,** *4*, 6889.

190. Chen, Y. S.; Frey, W.; Walker, C.; Aglyamov, S.; Emelianov, S., Sensitivity enhanced nanothermal sensors for photoacoustic temperature mapping. *Journal of biophotonics* **2013,** *6* (6-7), 534-542.

191. Larina, I. V.; Larin, K. V.; Esenaliev, R. O., Real-time optoacoustic monitoring of temperature in tissues. *Journal of Physics D: Applied Physics* **2005,** *38* (15), 2633.

192. Ke, H.; Tai, S.; Wang, L. V., Photoacoustic thermography of tissue. *Journal of biomedical optics* **2014,** *19* (2), 026003.

193. Wang, S.-H.; Wei, C.-W.; Jee, S.-H.; Li, P.-C. In *Photoacoustic temperature measurements for monitoring of thermal therapy*, Photons Plus Ultrasound: Imaging and Sensing 2009, International Society for Optics and Photonics: 2009; p 71771S.

194. Zhou, Y.; Tang, E.; Luo, J.; Yao, J. In *Deep-tissue temperature mapping by multi-illumination photoacoustic tomography aided by a diffusion optical model: a numerical study*, SPIE: 2018; p 10.

195. Liu, W.; Lan, B.; Hu, L.; Chen, R.; Zhou, Q.; Yao, J. In *Photoacoustic thermal flowmetry with a single light source*, SPIE: 2017; p 6.

196. Gillies, R.; Raghunand, N.; Garcia-Martin, M.; Gatenby, R., *pH imaging: A review of pH measurement methods and applications in cancers*. 2004; Vol. 23, p 57-64.

197. Han, J.; Burgess, K., Fluorescent Indicators for Intracellular pH. *Chemical Reviews* **2010,** *110* (5), 2709-2728.

198. Miao, Q.; Lyu, Y.; Ding, D.; Pu, K., Semiconducting Oligomer Nanoparticles as an Activatable Photoacoustic Probe with Amplified Brightness for In Vivo Imaging of pH. *Advanced Materials* **2016,** *28* (19), 3662-3668.

199. Huang, P.; Gao, Y.; Lin, J.; Hu, H.; Liao, H.-S.; Yan, X.; Tang, Y.; Jin, A.; Song, J.; Niu, G.; Zhang, G.; Horkay, F.; Chen, X., Tumor-Specific Formation of Enzyme-Instructed Supramolecular Self-Assemblies as Cancer Theranostics. *ACS Nano* **2015,** *9* (10), 9517-9527.

200. Mu, J.; Lin, J.; Huang, P.; Chen, X., Development of endogenous enzyme-responsive nanomaterials for theranostics. *Chemical Society Reviews* **2018**.

201. Xu, Y.; Wang, L. V., Effects of acoustic heterogeneity in breast thermoacoustic tomography. *IEEE transactions on ultrasonics, ferroelectrics, and frequency control* **2003,** *50* (9), 1134-1146.

202. Hariri, A.; Fatima, A.; Mohammadian, N.; Mahmoodkalayeh, S.; Ansari, M. A.; Bely, N.; Avanaki, M. R., Development of low-cost photoacoustic imaging systems using very low-energy pulsed laser diodes. *Journal of biomedical optics* **2017,** *22* (7), 075001.

203. Hariri, A.; Lemaster, J.; Wang, J.; Jeevarathinam, A. S.; Chao, D. L.; Jokerst, J. V., The characterization of an economic and portable LED-based photoacoustic imaging system to facilitate molecular imaging. *Photoacoustics* **2018,** *9*, 10-20.

204. Zhu, Y.; Xu, G.; Yuan, J.; Jo, J.; Gandikota, G.; Demirci, H.; Agano, T.; Sato, N.; Shigeta, Y.; Wang, X., Light emitting diodes based photoacoustic imaging and potential clinical applications. *Scientific reports* **2018,** *8* (1), 9885.

205. Antaris, A. L.; Chen, H.; Diao, S.; Ma, Z.; Zhang, Z.; Zhu, S.; Wang, J.; Lozano, A. X.; Fan, Q.; Chew, L., A high quantum yield molecule-protein complex fluorophore for near-infrared II imaging. *Nature communications* **2017,** *8*, 15269.

206. Zhu, S.; Yang, Q.; Antaris, A. L.; Yue, J.; Ma, Z.; Wang, H.; Huang, W.; Wan, H.; Wang, J.; Diao, S., Molecular imaging of biological systems with a clickable dye in the broad 800-to 1,700-nm near-infrared window. *Proceedings of the National Academy of Sciences* **2017,** *114* (5), 962-967.

207. Finlay, M. C.; Mosse, C. A.; Colchester, R. J.; Noimark, S.; Zhang, E. Z.; Ourselin, S.; Beard, P. C.; Schilling, R. J.; Parkin, I. P.; Papakonstantinou, I.; Desjardins, A. E., Through-needle all-optical ultrasound imaging in vivo: a preclinical swine study. *Light: Science &Amp; Applications* **2017,** *6*, e17103.

208. Xi, L.; Jiang, H., Integrated photoacoustic and diffuse optical tomography system for imaging of human finger joints in vivo. *Journal of Biophotonics* **2016,** *9* (3), 213-217.

209. Lin, C. Y.; Chen, F.; Hariri, A.; Chen, C. J.; Wilder-Smith, P.; Takesh, T.; Jokerst, J. V., Photoacoustic Imaging for Noninvasive Periodontal Probing Depth Measurements. *Journal of Dental Research* **2017**, 0022034517729820.

210. Moore, C.; Bai, Y.; Hariri, A.; Sanchez, J. B.; Lin, C.-Y.; Koka, S.; Sedghizadeh, P.; Chen, C.; Jokerst, J. V., Photoacoustic imaging for monitoring periodontal health: A first human study. *Photoacoustics* **2018,** *12*, 67-74.

211. Aliroteh, M.; Scott, G.; Arbabian, A., Frequency-modulated magneto-acoustic detection and imaging. *Electronics letters* **2014,** *50* (11), 790-792.

212. Mehrmohammadi, M.; Oh, J.; Aglyamov, S. R.; Karpiouk, A. B.; Emelianov, S. Y. In *Pulsed magneto-acoustic imaging*, Engineering in Medicine and Biology Society, 2009. EMBC 2009. Annual International Conference of the IEEE, IEEE: 2009; pp 4771-4774.

213. Webb, A.; Kagadis, G. C., Introduction to biomedical imaging. *Medical Physics* **2003,** *30* (8), 2267-2267.

214. Massoud, T. F.; Gambhir, S. S., Molecular imaging in living subjects: seeing fundamental biological processes in a new light. *Genes & development* **2003,** *17* (5), 545-580.

215. Shen, B.; Jeon, J.; Palner, M.; Ye, D.; Shuhendler, A.; Chin, F. T.; Rao, J., Positron emission tomography imaging of drug-induced tumor apoptosis with a caspase-triggered nanoaggregation probe. *Angewandte Chemie International Edition* **2013,** *52* (40), 10511-10514.

216. Mulder, W. J.; Strijkers, G. J.; van Tilborg, G. A.; Griffioen, A. W.; Nicolay, K., Lipid-based nanoparticles for contrast-enhanced MRI and molecular imaging. *NMR in Biomedicine: An International Journal Devoted to the Development and Application of Magnetic Resonance In vivo* **2006,** *19* (1), 142-164.

217. Na, H. B.; Song, I. C.; Hyeon, T., Inorganic nanoparticles for MRI contrast agents. *Advanced materials* **2009,** *21* (21), 2133-2148.

218. Liang, G.; Ronald, J.; Chen, Y.; Ye, D.; Pandit, P.; Ma, M. L.; Rutt, B.; Rao, J., Controlled Self-Assembling of Gadolinium Nanoparticles as Smart Molecular Magnetic Resonance Imaging Contrast Agents. *Angewandte Chemie International Edition* **2011,** *50* (28), 6283-6286.

219. Park, J. Y.; Baek, M. J.; Choi, E. S.; Woo, S.; Kim, J. H.; Kim, T. J.; Jung, J. C.; Chae, K. S.; Chang, Y.; Lee, G. H., Paramagnetic ultrasmall gadolinium oxide nanoparticles as advanced T 1 MRI contrast agent: account for large longitudinal relaxivity, optimal particle diameter, and in vivo T 1 MR images. *ACS nano* **2009,** *3* (11), 3663-3669.

220. Kim, T.; Momin, E.; Choi, J.; Yuan, K.; Zaidi, H.; Kim, J.; Park, M.; Lee, N.; McMahon, M. T.; Quinones-Hinojosa, A., Mesoporous silica-coated hollow manganese oxide nanoparticles as positive T 1 contrast agents for labeling and MRI tracking of adipose-derived mesenchymal stem cells. *Journal of the American Chemical Society* **2011,** *133* (9), 2955-2961.

221. Qiao, R.; Yang, C.; Gao, M., Superparamagnetic iron oxide nanoparticles: from preparations to in vivo MRI applications. *Journal of Materials Chemistry* **2009,** *19* (35), 6274-6293.

222. Reske, S. N.; Kotzerke, J., FDG-PET for clinical use. *European journal of nuclear medicine* **2001,** *28* (11), 1707-1723.

223. Ametamey, S. M.; Honer, M.; Schubiger, P. A., Molecular imaging with PET. *Chemical reviews* **2008,** *108* (5), 1501-1516.

224. Khalil, M. M.; Tremoleda, J. L.; Bayomy, T. B.; Gsell, W., Molecular SPECT imaging: an overview. *International journal of molecular imaging* **2011,** *2011*.

225. Ronald, J. A.; Kim, B.-S.; Gowrishankar, G.; Namavari, M.; Alam, I. S.; D'Souza, A.; Nishikii, H.; Chuang, H.-Y.; Ilovich, O.; Lin, C.-F., A PET imaging strategy to visualize activated T cells in acute graft-versus-host disease elicited by allogenic hematopoietic cell transplant. *Cancer research* **2017,** *77* (11), 2893-2902.

226. Kiessling, F.; Fokong, S.; Koczera, P.; Lederle, W.; Lammers, T., Ultrasound microbubbles for molecular diagnosis, therapy, and theranostics. *Journal of nuclear medicine* **2012,** *53* (3), 345-348.

227. Deckers, R.; Moonen, C. T., Ultrasound triggered, image guided, local drug delivery. *Journal of Controlled Release* **2010,** *148* (1), 25-33.

228. Luker, G. D.; Luker, K. E., Optical imaging: current applications and future directions. *Journal of Nuclear Medicine* **2008,** *49* (1), 1-4.

229. Sorensen, A. G., Magnetic resonance as a cancer imaging biomarker. *Journal of clinical oncology* **2006,** *24* (20), 3274-3281.

230. Mitragotri, S., Healing sound: the use of ultrasound in drug delivery and other therapeutic applications. *Nature reviews Drug discovery* **2005,** *4* (3), 255.

231. Moore, C.; Jokerst, J. V., Strategies for Image-Guided Therapy, Surgery, and Drug Delivery Using Photoacoustic Imaging. *THERANOSTICS* **2019,** *9* (6), 1550-1571.

232. Bell, A. G., The Production of Sound by Radiant Energy. *Science* **1881,** *os-2* (49), 242-253.

233. Zhou, Y.; Xing, W.; Maslov, K. I.; Cornelius, L. A.; Wang, L. V., Handheld photoacoustic microscopy to detect melanoma depth in vivo. *Optics letters* **2014,** *39* (16), 4731-4734.

234. Arconada-Alvarez, S. J.; Lemaster, J. E.; Wang, J.; Jokerst, J. V., The development and characterization of a novel yet simple 3D printed tool to facilitate phantom imaging of photoacoustic contrast agents. *Photoacoustics* **2017,** *5*, 17-24.

235. Jokerst, J. V.; Van de Sompel, D.; Bohndiek, S. E.; Gambhir, S. S., Cellulose nanoparticles are a biodegradable photoacoustic contrast agent for use in living mice. *Photoacoustics* **2014,** *2* (3), 119-127.

236. Hirsch, L. R.; Stafford, R. J.; Bankson, J.; Sershen, S. R.; Rivera, B.; Price, R.; Hazle, J. D.; Halas, N. J.; West, J. L., Nanoshell-mediated near-infrared thermal therapy of tumors under magnetic resonance guidance. *Proceedings of the National Academy of Sciences* **2003,** *100* (23), 13549-13554.

237. Riley, R. S.; Day, E. S., Gold nanoparticle-mediated photothermal therapy: applications and opportunities for multimodal cancer treatment. *Wiley Interdisciplinary Reviews: Nanomedicine and Nanobiotechnology* **2017,** *9* (4), e1449.

238. Huang, P.; Lin, J.; Li, W.; Rong, P.; Wang, Z.; Wang, S.; Wang, X.; Sun, X.; Aronova, M.; Niu, G., Biodegradable gold nanovesicles with an ultrastrong plasmonic coupling effect for photoacoustic imaging and photothermal therapy. *Angewandte Chemie International Edition* **2013,** *52* (52), 13958-13964.

239. Sheng, Z.; Song, L.; Zheng, J.; Hu, D.; He, M.; Zheng, M.; Gao, G.; Gong, P.; Zhang, P.; Ma, Y., Protein-assisted fabrication of nano-reduced graphene oxide for combined in vivo photoacoustic imaging and photothermal therapy. *Biomaterials* **2013,** *34* (21), 5236-5243.

240. Lovell, J. F.; Jin, C. S.; Huynh, E.; Jin, H.; Kim, C.; Rubinstein, J. L.; Chan, W. C.; Cao, W.; Wang, L. V.; Zheng, G., Porphysome nanovesicles generated by porphyrin bilayers for use as multimodal biophotonic contrast agents. *Nature materials* **2011,** *10* (4), 324.

241. Lin, L.-S.; Cong, Z.-X.; Cao, J.-B.; Ke, K.-M.; Peng, Q.-L.; Gao, J.; Yang, H.-H.; Liu, G.; Chen, X., Multifunctional Fe3O4@ polydopamine core–shell nanocomposites for intracellular mRNA detection and imaging-guided photothermal therapy. *ACS nano* **2014,** *8* (4), 3876-3883.

242. Gong, F.; Cheng, L.; Yang, N.; Jin, Q.; Tian, L.; Wang, M.; Li, Y.; Liu, Z., Bimetallic Oxide MnMoOX Nanorods for in Vivo Photoacoustic Imaging of GSH and Tumor-Specific Photothermal Therapy. *Nano Letters* **2018,** *18* (9), 6037-6044.

243. Lyu, Y.; Zeng, J.; Jiang, Y.; Zhen, X.; Wang, T.; Qiu, S.; Lou, X.; Gao, M.; Pu, K., Enhancing Both Biodegradability and Efficacy of Semiconducting Polymer Nanoparticles for Photoacoustic Imaging and Photothermal Therapy. *ACS Nano* **2018,** *12* (2), 1801-1810.

244. Shen, Y.; Shuhendler, A. J.; Ye, D.; Xu, J.-J.; Chen, H.-Y., Two-photon excitation nanoparticles for photodynamic therapy. *Chemical Society Reviews* **2016,** *45* (24), 6725-6741.

245. Ho, C. J. H.; Balasundaram, G.; Driessen, W.; McLaren, R.; Wong, C. L.; Dinish, U. S.; Attia, A. B. E.; Ntziachristos, V.; Olivo, M., Multifunctional Photosensitizer-Based Contrast Agents for Photoacoustic Imaging. *Scientific Reports* **2014,** *4*, 5342.

246. Idris, N. M.; Gnanasammandhan, M. K.; Zhang, J.; Ho, P. C.; Mahendran, R.; Zhang, Y., In vivo photodynamic therapy using upconversion nanoparticles as remote-controlled nanotransducers. *Nature medicine* **2012,** *18* (10), 1580.

247. Shao, P.; Chapman, D. W.; Moore, R. B.; Zemp, R. J., Monitoring photodynamic therapy with photoacoustic microscopy. *Journal of Biomedical Optics* **2015,** *20* (10), 106012.

248. Guo, W.; Qiu, Z.; Guo, C.; Ding, D.; Li, T.; Wang, F.; Sun, J.; Zheng, N.; Liu, S., Multifunctional theranostic agent of Cu2 (OH) PO4 quantum dots for photoacoustic image-guided photothermal/photodynamic combination cancer therapy. *ACS applied materials & interfaces* **2017,** *9* (11), 9348-9358.

249. Hu, J.; Tang, Y. a.; Elmenoufy, A. H.; Xu, H.; Cheng, Z.; Yang, X., Nanocomposite-Based Photodynamic Therapy Strategies for Deep Tumor Treatment. *Small* **2015,** *11* (44), 5860-5887.

250. Gupta, N.; Price, P.; Aboagye, E., PET for in vivo pharmacokinetic and pharmacodynamic measurements. *European Journal of Cancer* **2002,** *38* (16), 2094-2107.

251. Zhong, J.; Yang, S.; Zheng, X.; Zhou, T.; Xing, D., In vivo photoacoustic therapy with cancer-targeted indocyanine green-containing nanoparticles. *Nanomedicine* **2013,** *8* (6), 903-919.

252. Manivasagan, P.; Bharathiraja, S.; Bui, N. Q.; Lim, I. G.; Oh, J., Paclitaxel-loaded chitosan oligosaccharide-stabilized gold nanoparticles as novel agents for drug delivery and photoacoustic imaging of cancer cells. *International Journal of Pharmaceutics* **2016,** *511* (1), 367-379.

253. Tian, G.; Zhang, X.; Zheng, X.; Yin, W.; Ruan, L.; Liu, X.; Zhou, L.; Yan, L.; Li, S.; Gu, Z., Multifunctional RbxWO3 Nanorods for Simultaneous Combined Chemo-photothermal Therapy and Photoacoustic/CT Imaging. *Small* **2014,** *10* (20), 4160-4170.

254. Bao, T.; Yin, W.; Zheng, X.; Zhang, X.; Yu, J.; Dong, X.; Yong, Y.; Gao, F.; Yan, L.; Gu, Z., One-pot synthesis of PEGylated plasmonic MoO3–x hollow nanospheres for photoacoustic imaging guided chemo-photothermal combinational therapy of cancer. *Biomaterials* **2016,** *76*, 11-24.

255. Song, X. R.; Wang, X.; Yu, S. X.; Cao, J.; Li, S. H.; Li, J.; Liu, G.; Yang, H. H.; Chen, X., Co9Se8 Nanoplates as a New Theranostic Platform for Photoacoustic/Magnetic Resonance Dual-Modal-Imaging-Guided Chemo-Photothermal Combination Therapy. *Advanced Materials* **2015,** *27* (21), 3285-3291.

256. Liu, J.; Wang, C.; Wang, X.; Wang, X.; Cheng, L.; Li, Y.; Liu, Z., Mesoporous silica coated single-walled carbon nanotubes as a multifunctional light-responsive platform for cancer combination therapy. *Advanced Functional Materials* **2015,** *25* (3), 384-392.

257. Song, J.; Yang, X.; Jacobson, O.; Lin, L.; Huang, P.; Niu, G.; Ma, Q.; Chen, X., Sequential drug release and enhanced photothermal and photoacoustic effect of hybrid reduced graphene oxide-loaded ultrasmall gold nanorod vesicles for cancer therapy. *ACS nano* **2015,** *9* (9), 9199-9209.

258. Duan, S.; Yang, Y.; Zhang, C.; Zhao, N.; Xu, F.-J., NIR-Responsive Polycationic Gatekeeper-Cloaked Hetero-Nanoparticles for Multimodal Imaging-Guided Triple-Combination Therapy of Cancer. *Small* **2017,** *13* (9), 1603133.

259. Coldur, F.; Andac, M., All-solid-state polyvinyl chloride membrane lithium-selective electrode with improved selectivity and its application in serum lithium assay. *Sensor Letters* **2011,** *9* (5), 1738-1744.

260. Belmaker, R., Bipolar disorder. *New England Journal of Medicine* **2004,** *351* (5), 476-486.

261. Qin, C.; Cheng, K.; Chen, K.; Hu, X.; Liu, Y.; Lan, X.; Zhang, Y.; Liu, H.; Xu, Y.; Bu, L.; Su, X.; Zhu, X.; Meng, S.; Cheng, Z., Tyrosinase as a multifunctional reporter gene for Photoacoustic/MRI/PET triple modality molecular imaging. *Scientific Reports* **2013,** *3*, 1490.

262. Hersi, H. M.; Raulf, N.; Gaken, J.; Folarin, N. d.; Tavassoli, M., MicroRNA-9 inhibits growth and invasion of head and neck cancer cells and is a predictive biomarker of response to plerixafor, an inhibitor of its target CXCR4. *Molecular Oncology* **2018,** *12* (12), 2023-2041.

263. Zheng, H. F.; Zhou, L.; Shi, Y. R.; Tian, J.; Wang, F., Tyrosinase-Based Reporter Gene for Photoacoustic Imaging of MicroRNA-9 Regulated by DNA Methylation in Living Subjects. *Mol Ther-Nucl Acids* **2018,** *11*, 34-40.

264. Buchanan, M. R.; Ofosu, F. A.; Brister, S. J., *ThrombinIts Key Role in Thrombogenesis-Implications for Its Inhibition*. CRC Press: 1994.

265. Brill-Edwards, P.; Ginsberg, J. S.; Johnston, M.; Hirsh, J., Establishing a Therapeutic Range for Heparin Therapy. *Annals of Internal Medicine* **1993,** *119* (2), 104-109.

266. Reilly, B. M.; Raschke, R. A., New method to predict patients' intravenous heparin dose requirements. *Journal of General Internal Medicine* **1996,** *11* (3), 168-173.

267. Liveris, A.; Bello, R. A.; Friedmann, P.; Duffy, M. A.; Manwani, D.; Killinger, J. S.; Rodriquez, D.; Weinstein, S., Anti-Factor Xa Assay Is a Superior Correlate of Heparin Dose Than Activated Partial Thromboplastin Time or Activated Clotting Time in Pediatric Extracorporeal Membrane Oxygenation*. *Pediatric Critical Care Medicine* **2014,** *15* (2), e72-e79.

268. Zmuda, K.; Neofotistos, D.; Ts' ao, C.-h., Effects of unfractionated heparin, low-molecular-weight heparin, and heparinoid on thromboelastographic assay of blood coagulation. *American journal of clinical pathology* **2000,** *113* (5), 725-731.

269. Despotis, G.; Joist, J.; Hogue Jr, C.; Alsoufiev, A.; Kater, K.; Goodnough, L.; Santoro, S.; Spitznagel, E.; Rosenblum, M.; Lappas, D., The impact of heparin concentration and activated clotting time monitoring on blood conservation: a prospective, randomized evaluation in patients undergoing cardiac operation. *The Journal of thoracic and cardiovascular surgery* **1995,** *110* (1), 46-54.

270. Arimura, J.; Poole, R. L.; Jeng, M.; Rhine, W.; Sharek, P., Neonatal heparin overdose-a multidisciplinary team approach to medication error prevention. *The journal of pediatric pharmacology and therapeutics : JPPT : the official journal of PPAG* **2008,** *13* (2), 96-8.

271. Wang, X.; Xie, X.; Ku, G.; Wang, L. V.; Stoica, G., Noninvasive imaging of hemoglobin concentration and oxygenation in the rat brain using high-resolution photoacoustic tomography. *Journal of biomedical optics* **2006,** *11* (2), 024015.

272. Wang, J.; Jeevarathinam, A. S.; Humphries, K.; Jhunjhunwala, A.; Chen, F.; Hariri, A.; Miller III, B. R.; Jokerst, J. V., A Mechanistic Investigation of Methylene Blue and Heparin Interactions and Their Photoacoustic Enhancement. *Bioconjugate chemistry* **2018,** *29* (11), 3768-3775.

273. Springer, M. L.; Sievers, R. E.; Viswanathan, M. N.; Yee, M. S.; Foster, E.; Grossman, W.; Yeghiazarians, Y., Closed-chest cell injections into mouse myocardium guided by high-resolution echocardiography. *Am J Physiol-Heart C* **2005,** *289* (3), H1307-H1314.

274. Rodriguez-Porcel, M.; Gheysens, O.; Chen, I. Y.; Wu, J. C.; Gambhir, S. S., Image-guided cardiac cell delivery using high-resolution small-animal ultrasound. *Mol Ther* **2005,** *12* (6), 1142-1147.

275. Bara, C.; Ghodsizad, A.; Niehaus, M.; Makoui, M.; Piechaczek, C.; Martin, U.; Warnecke, G.; Karck, M.; Gams, E.; Klein, H. M.; Haverich, A.; Ruhparwar, A., In vivo echocardiographic imaging of transplanted human adult stem cells in the myocardium labeled with clinically applicable CliniMACS nanoparticles. *J Am Soc Echocardiog* **2006,** *19* (5), 563-568.

276. Hartanto, J.; Jokerst, J. V., Nanoparticles for Ultrasound-Guided Imaging of Cell Implantation. In *Design and Applications of Nanoparticles in Biomedical Imaging*, Bulte, J. W. M.; Modo, M. M. J., Eds. Springer International Publishing: Cham, 2017; pp 299-314.

277. Jokerst, J. V.; Khademi, C.; Gambhir, S. S., Intracellular aggregation of multimodal silica nanoparticles for ultrasound-guided stem cell implantation. *Science Translational Medicine* **2013,** *5* (177), 177ra35.

278. Bulte, J. W. M.; Daldrup-Link, H. E., Clinical Tracking of Cell Transfer and Cell Transplantation: Trials and Tribulations. *Radiology* **2018,** *289* (3), 604-615.

279. Frangioni, J. V.; Hajjar, R. J., In vivo tracking of stem cells for clinical trials in cardiovascular disease. *Circulation* **2004,** *110* (21), 3378-83.

280. Wang, J.; Jokerst, J. V., Stem Cell Imaging: Tools to Improve Cell Delivery and Viability. *Stem Cells Int* **2016,** *2016*, 9240652.

281. Lemaster, J. E.; Jokerst, J. V., What is new in nanoparticle-based photoacoustic imaging? *Wiley Interdisciplinary Reviews: Nanomedicine and Nanobiotechnology* **2017,** *9* (1), e1404-n/a.

282. Cui, W.; Tavri, S.; Benchimol, M. J.; Itani, M.; Olson, E. S.; Zhang, H.; Decyk, M.; Ramirez, R. G.; Barback, C. V.; Kono, Y.; Mattrey, R. F., Neural progenitor cells labeling with microbubble contrast agent for ultrasound imaging in vivo. *Biomaterials* **2013,** *34* (21), 4926-35.

283. Pysz, M. A.; Willmann, J. K., Targeted contrast-enhanced ultrasound: an emerging technology in abdominal and pelvic imaging. *Gastroenterology* **2011,** *140* (3), 785-790.

284. Kempen, P. J.; Greasley, S.; Parker, K. A.; Campbell, J. L.; Chang, H.-Y.; Jones, J. R.; Sinclair, R.; Gambhir, S. S.; Jokerst, J. V., Theranostic Mesoporous Silica Nanoparticles Biodegrade after Pro-Survival Drug Delivery and Ultrasound/Magnetic Resonance Imaging of Stem Cells. *Theranostics* **2015,** *5* (6), 631-642.

285. Chen, F.; Ma, M.; Wang, J.; Wang, F.; Chern, S. X.; Zhao, E. R.; Jhunjhunwala, A.; Darmadi, S.; Chen, H.; Jokerst, J. V., Exosome-like silica nanoparticles: a novel ultrasound contrast agent for stem cell imaging. *Nanoscale* **2017,** *9* (1), 402-411.

286. Foroutan, F.; Jokerst, J. V.; Gambhir, S. S.; Vermesh, O.; Kim, H.-W.; Knowles, J. C., Sol–Gel Synthesis and Electrospraying of Biodegradable (P2O5)55–(CaO)30–(Na2O)15 Glass Nanospheres as a Transient Contrast Agent for Ultrasound Stem Cell Imaging. *ACS Nano* **2015,** *9* (2), 1868-1877.

287. Kuliszewski, M. A.; Fujii, H.; Liao, C.; Smith, A. H.; Xie, A.; Lindner, J. R.; Leong-Poi, H., Molecular imaging of endothelial progenitor cell engraftment using contrast-enhanced ultrasound and targeted microbubbles. *Cardiovasc Res* **2009,** *83* (4), 653-662.

288. Bourdeau, R. W.; Lee-Gosselin, A.; Lakshmanan, A.; Farhadi, A.; Kumar, S. R.; Nety, S. P.; Shapiro, M. G., Acoustic reporter genes for noninvasive imaging of microorganisms in mammalian hosts. *Nature* **2018,** *553* (7686), 86-+.

289. Lakshmanan, A.; Lu, G. J.; Farhadi, A.; Nety, S. P.; Kunth, M.; Lee-Gosselin, A.; Maresca, D.; Bourdeau, R. W.; Yin, M.; Yan, J.; Witte, C.; Malounda, D.; Foster, F. S.; Schroder, L.; Shapiro, M. G., Preparation of biogenic gas vesicle nanostructures for use as contrast agents for ultrasound and MRI. *Nature Protocols* **2017,** *12* (10), 2050-2080.

290. Shapiro, M. G.; Goodwill, P. W.; Neogy, A.; Yin, M.; Foster, F. S.; Schaffer, D. V.; Conolly, S. M., Biogenic gas nanostructures as ultrasonic molecular reporters. *Nature Nanotechnology* **2014,** *9* (4), 311-316.

291. Jokerst, J. V.; Thangaraj, M.; Kempen, P. J.; Sinclair, R.; Gambhir, S. S., Photoacoustic imaging of mesenchymal stem cells in living mice via silica-coated gold nanorods. *ACS Nano* **2012,** *6* (7), 5920-30.

292. Wang, C.; Ma, X.; Ye, S.; Cheng, L.; Yang, K.; Guo, L.; Li, C.; Li, Y.; Liu, Z., Protamine Functionalized Single-Walled Carbon Nanotubes for Stem Cell Labeling and In Vivo Raman/Magnetic Resonance/Photoacoustic Triple-Modal Imaging. *Advanced Functional Materials* **2012,** *22* (11), 2363-2375.

293. Donnelly, E. M.; Kubelick, K. P.; Dumani, D. S.; Emelianov, S. Y., Photoacoustic Image-Guided Delivery of Plasmonic-Nanoparticle-Labeled Mesenchymal Stem Cells to the Spinal Cord. *Nano Lett* **2018,** *18* (10), 6625-6632.

294. Nam, S. Y.; Ricles, L. M.; Suggs, L. J.; Emelianov, S. Y., In vivo Ultrasound and Photoacoustic Monitoring of Mesenchymal Stem Cells Labeled with Gold Nanotracers. *Plos One* **2012,** *7* (5).

295. Kim, T.; Lemaster, J. E.; Chen, F.; Li, J.; Jokerst, J. V., Photoacoustic Imaging of Human Mesenchymal Stem Cells Labeled with Prussian Blue-Poly(l-lysine) Nanocomplexes. *ACS Nano* **2017,** *11* (9), 9022-9032.

296. Lemaster, J. E.; Chen, F.; Kim, T.; Hariri, A.; Jokerst, J. V., Development of a Trimodal Contrast Agent for Acoustic and Magnetic Particle Imaging of Stem Cells. *ACS Applied Nano Materials* **2018,** *1* (3), 1321-1331.

297. Lin, C. Y.; Chen, F.; Hariri, A.; Chen, C. J.; Wilder-Smith, P.; Takesh, T.; Jokerst, J. V., Photoacoustic Imaging for Noninvasive Periodontal Probing Depth Measurements. *J Dent Res* **2018,** *97* (1), 23-30.

298. Lemaster, J. E.; Wang, Z.; Hariri, A.; Chen, F.; Hu, Z.; Huang, Y.; Barback, C. V.; Cochran, R.; Gianneschi, N. C.; Jokerst, J. V., Gadolinium Doping Enhances the Photoacoustic Signal of Synthetic Melanin Nanoparticles: A Dual Modality Contrast Agent for Stem Cell Imaging. *Chemistry of Materials* **2019,** *31* (1), 251-259.

299. Yin, C.; Wen, G. H.; Liu, C.; Yang, B. G.; Lin, S. E.; Huang, J. W.; Zhao, P. C.; Wong, S. H. D.; Zhang, K. Y.; Chen, X. Y.; Li, G.; Jiang, X. H.; Huang, J. P.; Pu, K. Y.; Wang, L. D.; Bian, L. M., Organic Semiconducting Polymer Nanoparticles for Photoacoustic Labeling and Tracking of Stem Cells in the Second Near-Infrared Window. *Acs Nano* **2018,** *12* (12), 12201-12211.

300. Nystrom, N. N.; Yip, L. C. M.; Carson, J. J. L.; Scholl, T. J.; Ronald, J. A., A human photoacoustic imaging reporter gene using the clinical dye indocyanine green. *bioRxiv* **2019**, 537100.

301. Zeiderman, M. R.; Morgan, D. E.; Christein, J. D.; Grizzle, W. E.; McMasters, K. M.; McNally, L. R., Acidic pH-Targeted Chitosan-Capped Mesoporous Silica Coated Gold Nanorods Facilitate Detection of Pancreatic Tumors via Multispectral Optoacoustic Tomography. *ACS Biomaterials Science & Engineering* **2016,** *2* (7), 1108-1120.

302. Jiang, Y.; Pu, K., Molecular Fluorescence and Photoacoustic Imaging in the Second Near-Infrared Optical Window Using Organic Contrast Agents. *Advanced Biosystems* **2018,** *2* (5), 1700262.

303. Smith, A. M.; Mancini, M. C.; Nie, S., Bioimaging: second window for in vivo imaging. *Nature nanotechnology* **2009,** *4* (11), 710.

304. Roach, W.; Johnson, T.; Rockwell, B., Proposed maximum permissible exposure limits for ultrashort laser pulses. *Health physics* **1999,** *76* (4), 349-354.

305. Park, J.-E.; Kim, M.; Hwang, J.-H.; Nam, J.-M., Golden Opportunities: Plasmonic Gold Nanostructures for Biomedical Applications based on the Second Near-Infrared Window. *Small Methods* **2017,** *1* (3), 1600032.

306. Homan, K.; Kim, S.; Chen, Y.-S.; Wang, B.; Mallidi, S.; Emelianov, S., Prospects of molecular photoacoustic imaging at 1064 nm wavelength. *Optics letters* **2010,** *35* (15), 2663-2665.

307. Sun, Y.; Ding, M.; Zeng, X.; Xiao, Y.; Wu, H.; Zhou, H.; Ding, B.; Qu, C.; Hou, W.; Er-Bu, A., Novel bright-emission small-molecule NIR-II fluorophores for in vivo tumor imaging and image-guided surgery. *Chemical science* **2017,** *8* (5), 3489-3493.

308. Jathoul, A. P.; Laufer, J.; Ogunlade, O.; Treeby, B.; Cox, B.; Zhang, E.; Johnson, P.; Pizzey, A. R.; Philip, B.; Marafioti, T., Deep in vivo photoacoustic imaging of mammalian tissues using a tyrosinase-based genetic reporter. *Nature Photonics* **2015,** *9* (4), 239.

309. Peters, L.; Weidenfeld, I.; Klemm, U.; Loeschcke, A.; Weihmann, R.; Jaeger, K.-E.; Drepper, T.; Ntziachristos, V.; Stiel, A. C., Phototrophic purple bacteria as optoacoustic in vivo reporters of macrophage activity. *Nature Communications* **2019,** *10* (1), 1191.

310. Bhaskar, V.; Chan, H.-L.; MacEachern, M.; Kripfgans, O. D., Updates on ultrasound research in implant dentistry: a systematic review of potential clinical indications. *Dentomaxillofacial Radiology* **2018,** *47* (6), 20180076.

311. David, C. M.; Tiwari, R., Ultrasound in maxillofacial imaging: A review. *Journal of Medicine, Radiology, Pathology and Surgery* **2015,** *1* (4), 17-23.

312. Evirgen, Ş.; Kamburoğlu, K., Review on the applications of ultrasonography in dentomaxillofacial region. *World journal of radiology* **2016,** *8* (1), 50.

313. Hall, A.; Girkin, J., A review of potential new diagnostic modalities for caries lesions. *Journal of Dental Research* **2004,** *83* (1_suppl), 89-94.

314. Kocasarac, H. D.; Angelopoulos, C., Ultrasound in dentistry: toward a future of radiation-free imaging. *Dental Clinics of North America* **2018,** *62* (3), 481-489.

315. Musu, D.; Rossi-Fedele, G.; Campisi, G.; Cotti, E., Ultrasonography in the diagnosis of bone lesions of the jaws: a systematic review. *Oral surgery, oral medicine, oral pathology and oral radiology* **2016,** *122* (1), e19-e29.

316. Sharma, S.; Rasila, D.; Singh, M.; Mohan, M., Ultrasound as a diagnostic boon in Dentistry a review. *Int J Sci Stud* **2014,** *2* (2).

317. Singh, G. P.; Dogra, S.; Kumari, E., Ultrasonography: maxillofacial applications. *Ann Dent Spec* **2014,** *2* (3), 104-7.

318. Marotti, J.; Heger, S.; Tinschert, J.; Tortamano, P.; Chuembou, F.; Radermacher, K.; Wolfart, S., Recent advances of ultrasound imaging in dentistry – a review of the literature. *Oral Surgery, Oral Medicine, Oral Pathology and Oral Radiology* **2013,** *115* (6), 819-832.

319. Zhou, Y.; Yao, J.; Wang, L. V., Tutorial on photoacoustic tomography. *Journal of Biomedical Optics* **2016,** *21* (6), 1-14, 14.

320. Wang, L. V.; Hu, S., Photoacoustic tomography: in vivo imaging from organelles to organs. *science* **2012,** *335* (6075), 1458-1462.

321. Rich, L. J.; Seshadri, M., Photoacoustic imaging of vascular hemodynamics: validation with blood oxygenation level–dependent MR imaging. *Radiology* **2014,** *275* (1), 110-118.

322. Hariri, A.; Wang, J.; Kim, Y.; Jhunjhunwala, A.; Chao, D. L.; Jokerst, J. V., In vivo photoacoustic imaging of chorioretinal oxygen gradients. *Journal of biomedical optics* **2018,** *23* (3), 036005.

323. Mehrmohammadi, M.; Joon Yoon, S.; Yeager, D.; Y Emelianov, S., Photoacoustic imaging for cancer detection and staging. *Current molecular imaging* **2013,** *2* (1), 89-105.

324. Borg, R. E.; Rochford, J., Molecular Photoacoustic Contrast Agents: Design Principles & Applications. *Photochemistry and Photobiology* **2018,** *94* (6), 1175-1209.

325. Lemaster, J. E.; Jokerst, J. V., What is new in nanoparticle-based photoacoustic imaging? *Wiley Interdiscip Rev Nanomed Nanobiotechnol* **2017,** *9* (1), 10.1002/wnan.1404.

326. Swierczewska, M.; Lee, S.; Chen, X., Inorganic Nanoparticles for Multimodal Molecular Imaging. *Molecular Imaging* **2011,** *10* (1), 7290.2011.00001.

327. Jiang, Y.; Pu, K., Advanced Photoacoustic Imaging Applications of Near-Infrared Absorbing Organic Nanoparticles. *Small* **2017,** *13* (30), 1700710.

328. Weissleder, R., A clearer vision for in vivo imaging. *Nature Biotechnology* **2001,** *19*, 316.

329. Darling, C. L.; Huynh, G.; Fried, D., Light scattering properties of natural and artificially demineralized dental enamel at 1310 nm. *Journal of biomedical optics* **2006,** *11* (3), 034023.

330. Fried, D.; Glena, R. E.; Featherstone, J. D.; Seka, W., Nature of light scattering in dental enamel and dentin at visible and near-infrared wavelengths. *Applied optics* **1995,** *34* (7), 1278-1285.

331. Spitzer, D.; Ten Bosch, J., The absorption and scattering of light in bovine and human dental enamel. *Calcified tissue research* **1975,** *17* (2), 129-137.

332. Abou Neel, E. A.; Aljabo, A.; Strange, A.; Ibrahim, S.; Coathup, M.; Young, A. M.; Bozec, L.; Mudera, V., Demineralization-remineralization dynamics in teeth and bone. *International journal of nanomedicine* **2016,** *11*, 4743-4763.

333. Fried, D.; Featherstone, J. D. B.; Darling, C. L.; Jones, R. S.; Ngaotheppitak, P.; Bühler, C. M., Early Caries Imaging and Monitoring with Near-Infrared Light. *Dental Clinics of North America* **2005,** *49* (4), 771-793.

334. Harris, D. M.; Fried, D., *Pulsed Nd:YAG laser selective ablation of surface enamel caries: I. Photoacoustic response and FTIR spectroscopy*. SPIE: 2000; Vol. 3910.

335. Rajian, J. R.; Carson, P. L.; Wang, X., Quantitative photoacoustic measurement of tissue optical absorption spectrum aided by an optical contrast agent. *Optics Express* **2009,** *17* (6), 4879-4889.

336. El-Sharkawy, Y. H.; El Sherif, A. F., Photoacoustic diagnosis of human teeth using interferometric detection scheme. *Optics & Laser Technology* **2012,** *44* (5), 1501-1506.

337. El-Sharkawy, Y. H.; Badr, Y.; Gadallah, M.; El-Sherif, A. F. In *Diagnostic of human teeth using photoacoustic response*, Lasers in Dentistry XII, International Society for Optics and Photonics: 2006; p 613701.

338. Kim, K.; Witte, R.; Koh, I.; Ashkenazi, S.; O'Donnell, M. In *Early detection of dental caries using photoacoustics*, Photons Plus Ultrasound: Imaging and Sensing 2006: The Seventh Conference on Biomedical Thermoacoustics, Optoacoustics, and Acousto-optics, International Society for Optics and Photonics: 2006; p 60860G.

339. Li, T.; Dewhurst, R. In *Photoacoustic Non-Destructive Evaluation and Imaging of Caries in Dental Samples*, AIP Conference Proceedings, AIP: 2010; pp 1574-1581.

340. Li, T.; Dewhurst, R. In *Photoacoustic imaging in both soft and hard biological tissue*, Journal of Physics: Conference Series, IOP Publishing: 2010; p 012028.

341. Cheng, R.; Shao, J.; Gao, X.; Tao, C.; Ge, J.; Liu, X., Noninvasive Assessment of Early Dental Lesion Using a Dual-Contrast Photoacoustic Tomography. *Scientific Reports* **2016,** *6*, 21798.

342. Koyama, T.; Kakino, S.; Matsuura, Y. In *Photoacoustic imaging of hidden dental caries by using a fiber-based probing system*, Biomedical Imaging and Sensing Conference, International Society for Optics and Photonics: 2017; p 1025119.

343. Wang, S.; Tao, C.; Yang, Y.; Wang, X.; Liu, X., Theoretical and experimental study of spectral characteristics of the photoacoustic signal from stochastically distributed particles. *IEEE Transactions on Ultrasonics, Ferroelectrics, and Frequency Control* **2015,** *62* (7), 1245-1255.

344. Rao, B.; Cai, X.; Favazza, C.; Yao, J.; Li, L.; Duong, S.; Liaw, L.-H.; Holtzman, J.; Wilder-Smith, P.; Wang, L. V. In *Photoacoustic microscopy of human teeth*, Lasers in Dentistry XVII, International Society for Optics and Photonics: 2011; p 78840U.

345. Periyasamy, V.; Rangaraj, M.; Pramanik, M. In *Photoacoustic imaging of teeth for dentine imaging and enamel characterization*, Lasers in Dentistry XXIV, International Society for Optics and Photonics: 2018; p 1047309.

346. Hughes, D.; Sampathkumar, A.; Longbottom, C.; Kirk, K. In *Imaging and detection of early stage dental caries with an all-optical photoacoustic microscope*, Journal of Physics: Conference Series, IOP Publishing: 2015; p 012002.

347. Park, K.; Kim, J. Y.; Lee, C.; Jeon, S.; Lim, G.; Kim, C. Handheld Photoacoustic Microscopy Probe *Scientific reports* [Online], 2017, p. 13359. PubMed. (accessed 2017/10//).

348. Yamada, A.; Kakino, S.; Matsuura, Y., Detection of photoacoustic signals from blood in dental pulp. *Optics and Photonics Journal* **2016,** *6* (09), 229.

349. Mombelli, A.; Müller, N.; Cionca, N., The epidemiology of peri-implantitis. *Clinical Oral Implants Research* **2012,** *23* (s6), 67-76.

350. Naveau, A.; Shinmyouzu, K.; Moore, C.; Avivi-Arber, L.; Jokerst, J.; Koka, S., Etiology and Measurement of Peri-Implant Crestal Bone Loss (CBL). *Journal of Clinical Medicine* **2019,** *8* (2), 166.

351. Lee, D.; Park, S.; Kim, C., *Dual-modal photoacoustic and ultrasound imaging of dental implants*. SPIE: 2018; Vol. 10494, p 5.

352. Lee, D.; Park, S.; Noh, W.-C.; Im, J.-S.; Kim, C., Photoacoustic imaging of dental implants in a porcine jawbone ex vivo. *Optics letters* **2017,** *42* (9), 1760-1763.

353. Schou, S.; Holmstrup, P.; Stoltze, K.; Hjørting-Hansen, E.; Fiehn, N. E.; Skovgaard, L. T., Probing around implants and teeth with healthy or inflamed peri-implant mucosa/gingiva: a histologic comparison in cynomolgus monkeys (Macaca fascicularis). *Clinical oral implants research* **2002,** *13* (2), 113-126.

354. McFall, W. T.; Bader, J. D.; Rozier, R. G.; Ramsey, D., Presence of periodontal data in patient records of general practitioners. *Journal of periodontology* **1988,** *59* (7), 445-449.

355. Cole, A.; McMichael, A., Audit of dental practice record-keeping: a PCT-coordinated clinical audit by Worcestershire dentists. *Primary Dental Care* **2009,** *16* (3), 85-93.

356. Fernandes, L. O.; Mota, C. C. B. O.; de Melo, L. S. A.; da Costa Soares, M. U. S.; da Silva Feitosa, D.; Gomes, A. S. L., In vivo assessment of periodontal structures and measurement of gingival sulcus with optical coherence tomography: a pilot study. *Journal of biophotonics* **2017,** *10* (6-7), 862-869.

357. Le, N. M.; Song, S.; Zhou, H.; Xu, J.; Li, Y.; Sung, C.-E.; Sadr, A.; Chung, K.-H.; Subhash, H. M.; Kilpatrick, L.; Wang, R. K., A noninvasive imaging and measurement using optical coherence tomography angiography for the assessment of gingiva: An in vivo study. *Journal of Biophotonics* **2018,** *11* (12), e201800242.

358. Lin, C.; Chen, F.; Hariri, A.; Chen, C.; Wilder-Smith, P.; Takesh, T.; Jokerst, J., Photoacoustic imaging for noninvasive periodontal probing depth measurements. *J. Dent. Res.* **2018,** *97* (1), 23-30.

359. Pirotte, T.; Veyckemans, F., Ultrasound-guided subclavian vein cannulation in infants and children: a novel approach. *British journal of anaesthesia* **2007,** *98* (4), 509-514.

360. Eke, P. I.; Dye, B. A.; Wei, L.; Thornton-Evans, G. O.; Genco, R. J., Prevalence of Periodontitis in Adults in the United States: 2009 and 2010. *Journal of Dental Research* **2012,** *91* (10), 914-920.

361. Inglehart, M. R.; Bagramian, R., *Oral health-related quality of life*. Quintessence Pub.: 2002.

362. Brennan, D. S.; Spencer, A. J.; Roberts-Thomson, K. F., Tooth loss, chewing ability and quality of life. *Quality of Life Research* **2008,** *17* (2), 227-235.

363. Sheiham, A., Oral health, general health and quality of life. *Bulletin of the World Health Organization* **2005,** *83* (9), 644-644.

364. Gomes, M. C.; de Almeida Pinto-Sarmento, T. C.; de Brito Costa, E. M. M.; Martins, C. C.; Granville-Garcia, A. F.; Paiva, S. M., Impact of oral health conditions on the quality of life of preschool children and their families: a cross-sectional study. *Health and quality of life outcomes* **2014,** *12* (1), 55.

365. Hollister, M.; Weintraub, J., The association of oral status with systemic health, quality of life, and economic productivity. *Journal of dental education* **1993,** *57* (12), 901-912.

366. Locker, D.; Matear, D.; Stephens, M.; Jokovic, A., Oral health-related quality of life of a population of medically compromised elderly people. *Community dental health* **2002,** *19* (2), 90-97.

367. Tonetti, M. S.; Dyke, T. E., Periodontitis and atherosclerotic cardiovascular disease: consensus report of the Joint EFP/AAP Workshop on Periodontitis and Systemic Diseases. *Journal of clinical periodontology* **2013,** *40* (s14).

368. Grossi, S. G.; Dunford, R. G.; Ho, A.; Koch, G.; Machtei, E. E.; Genco, R. J., Sources of error for periodontal probing measurements. *Journal of periodontal research* **1996,** *31* (5), 330-336.

369. Perry, D. A.; Beemsterboer, P. L.; Essex, G., *Periodontology for the dental hygienist*. Elsevier Health Sciences: 2015.

370. Singh, R. S.; Culjat, M. O.; Grundfest, W. S.; Brown, E. R.; White, S. N., Tissue mimicking materials for dental ultrasound. *The Journal of the Acoustical Society of America* **2008,** *123* (4), EL39-EL44.

371. Vandana, K. L.; Gupta, I., The location of cemento enamel junction for CAL measurement: A clinical crisis. *J Indian Soc Periodontol* **2009,** *13* (1), 12-15.

372. Nguyen, K. C. T.; Duong, D. Q.; Almeida, F. T.; Major, P. W.; Kaipatur, N. R.; Pham, T. T.; Lou, E. H. M.; Noga, M.; Punithakumar, K.; Le, L. H., Alveolar Bone Segmentation in Intraoral Ultrasonographs with Machine Learning. *Journal of Dental Research* **2020,** *99* (9), 1054-1061.

373. Tattan, M.; Sinjab, K.; Lee, E.; Arnett, M.; Oh, T. J.; Wang, H. L.; Chan, H. L.; Kripfgans, O. D., Ultrasonography for chairside evaluation of periodontal structures: a pilot study. *Journal of periodontology* **2020,** *91* (7), 890-899.

374. Chan, H.-L.; Kripfgans, O. D., Ultrasonography for diagnosis of peri-implant diseases and conditions: a detailed scanning protocol and case demonstration. *Dentomaxillofacial Radiology* **2020,** *49* (7), 20190445.

375. Chifor, R.; Badea, A. F.; Chifor, I.; Mitrea, D.-A.; Crisan, M.; Badea, M. E., Periodontal evaluation using a non-invasive imaging method (ultrasonography). *Med Pharm Rep* **2019,** *92* (Suppl No 3), S20-S32.

376. Chan, H. L.; Sinjab, K.; Chung, M. P.; Chiang, Y. C.; Wang, H. L.; Giannobile, W. V.; Kripfgans, O. D., Non-invasive evaluation of facial crestal bone with ultrasonography. *PLoS One* **2017,** *12* (2), e0171237.

377. Chifor, R.; Badea, M. E.; Hedesiu, M.; Serbanescu, A.; Badea, A. F., Experimental model for measuring and characterisation of the dento-alveolar system using high frequencies ultrasound techniques. *Med Ultrason* **2010,** *12* (2), 127-32.

378. Nguyen, K.-C. T.; Le, B. M.; Li, M.; Almeida, F. T.; Major, P. W.; Kaipatur, N. R.; Lou, E. H. M.; Punithakumar, K.; Le, L. H., Localization of cementoenamel junction in intraoral ultrasonographs with machine learning. *Journal of Dentistry* **2021,** *112*, 103752.

379. Nguyen, K.-C. T.; Le, L. H.; Kaipatur, N. R.; Major, P. W., Imaging the Cemento-Enamel Junction Using a 20-MHz Ultrasonic Transducer. *Ultrasound in Medicine & Biology* **2016,** *42* (1), 333-338.

380. Sinjab, K.; Kripfgans, O. D.; Ou, A.; Chan, H.-L., Ultrasonographic evaluation of edentulous crestal bone topography: A proof-of-principle retrospective study. *Oral Surgery, Oral Medicine, Oral Pathology and Oral Radiology* **2021**.

381. Barootchi, S.; Tavelli, L.; Majzoub, J.; Chan, H.; Wang, H.; Kripfgans, O., Ultrasonographic Tissue Perfusion in Peri-implant Health and Disease. *Journal of Dental Research* **2021**, 00220345211035684.

382. Thöne-Mühling, M.; Kripfgans, O. D.; Mengel, R., Ultrasonography for noninvasive and real-time evaluation of peri-implant soft and hard tissue: a case series. *International Journal of Implant Dentistry* **2021,** *7* (1), 1-13.

383. Kwak, Y.; Nguyen, V.-H.; Hériveaux, Y.; Belanger, P.; Park, J.; Haïat, G., Ultrasonic assessment of osseointegration phenomena at the bone-implant interface using convolutional neural network. *The Journal of the Acoustical Society of America* **2021,** *149* (6), 4337-4347.

384. Mozaffarzadeh, M.; Moore, C.; Golmoghani, E. B.; Mantri, Y.; Hariri, A.; Jorns, A.; Fu, L.; Verweij, M. D.; Orooji, M.; de Jong, N., Motion-compensated noninvasive periodontal health monitoring using handheld and motor-based photoacoustic-ultrasound imaging systems. *Biomed. Opt. Express* **2021,** *12* (3), 1543-1558.

385. Caton, J. G.; Armitage, G.; Berglundh, T.; Chapple, I. L. C.; Jepsen, S.; Kornman, K. S.; Mealey, B. L.; Papapanou, P. N.; Sanz, M.; Tonetti, M. S., A new classification scheme for periodontal and peri-implant diseases and conditions - Introduction and key changes from the 1999 classification. *J Periodontol* **2018,** *89 Suppl 1*, S1-S8.

386. Chan, H.-L.; Wang, H.-L.; Fowlkes, J. B.; Giannobile, W. V.; Kripfgans, O. D., Non-ionizing real-time ultrasonography in implant and oral surgery: A feasibility study. *Clinical Oral Implants Research* **2017,** *28* (3), 341-347.

387. Schmidt, J. C.; Sahrmann, P.; Weiger, R.; Schmidlin, P. R.; Walter, C., Biologic width dimensions – a systematic review. *Journal of Clinical Periodontology* **2013,** *40* (5), 493-504.

388. Bahal, P.; Malhi, M.; Shah, S.; Ide, M., Managing the consequences of periodontal diseases/treatment: gingival recession. *Dental Update* **2019,** *46* (10), 966-977.

389. Tugnait, A.; Clerehugh, V., Gingival recession—its significance and management. *Journal of dentistry* **2001,** *29* (6), 381-394.

390. Nugala, B.; Kumar, B. S.; Sahitya, S.; Krishna, P. M., Biologic width and its importance in periodontal and restorative dentistry. *Journal of conservative dentistry: JCD* **2012,** *15* (1), 12.

391. Alves, P. H. M.; Alves, T. C. L. P.; Pegoraro, T. A.; Costa, Y. M.; Bonfante, E. A.; de Almeida, A. L. P. F., Measurement properties of gingival biotype evaluation methods. *Clinical Implant Dentistry and Related Research* **2018,** *20* (3), 280-284.

392. Ilhan, B.; Guneri, P.; Wilder-Smith, P., The contribution of artificial intelligence to reducing the diagnostic delay in oral cancer. *Oral Oncology* **2021,** *116*, 105254.

393. Daniels, K.; Gummadi, S.; Zhu, Z.; Wang, S.; Patel, J.; Swendseid, B.; Lyshchik, A.; Curry, J.; Cottrill, E.; Eisenbrey, J., Machine Learning by Ultrasonography for Genetic Risk Stratification of Thyroid Nodules. *JAMA Otolaryngology–Head & Neck Surgery* **2020,** *146* (1), 36-41.

394. Eke, P. I.; Dye, B.; Wei, L.; Thornton-Evans, G.; Genco, R., Prevalence of periodontitis in adults in the United States: 2009 and 2010. *Journal of dental research* **2012,** *91* (10), 914-920.

395. D'aiuto, F.; Nibali, L.; Parkar, M.; Patel, K.; Suvan, J.; Donos, N., Oxidative stress, systemic inflammation, and severe periodontitis. *Journal of dental research* **2010,** *89* (11), 1241-1246.

396. Darveau, R. P., Periodontitis: a polymicrobial disruption of host homeostasis. *Nature Reviews Microbiology* **2010,** *8* (7), 481.

397. Cochran, D. L., Inflammation and bone loss in periodontal disease. *Journal of periodontology* **2008,** *79* (8S), 1569-1576.

398. Karadottir, H.; Lenoir, L.; Barbierato, B.; Bogle, M.; Riggs, M.; Sigurdsson, T.; Crigger, M.; Egelberg, J., Pain experienced by patients during periodontal maintenance treatment. *Journal of periodontology* **2002,** *73* (5), 536-542.

399. Stewart, R.; West, M., Increasing evidence for an association between periodontitis and cardiovascular disease. Am Heart Assoc: 2016.

400. Leng, W.-D.; Zeng, X.-T.; Kwong, J. S.; Hua, X.-P., Periodontal disease and risk of coronary heart disease: An updated meta-analysis of prospective cohort studies. *Int. J. Cardiol.* **2015,** *201*, 469-472.

401. Michaud, D.; Kelsey, K.; Papathanasiou, E.; Genco, C.; Giovannucci, E., Periodontal disease and risk of all cancers among male never smokers: an updated analysis of the Health Professionals Follow-up Study. *Ann. Oncol.* **2016,** *27* (5), 941-947.

402. Lee, Y. T.; Lee, H. C.; Hu, C. J.; Huang, L. K.; Chao, S. P.; Lin, C. P.; Su, E. C. Y.; Lee, Y. C.; Chen, C. C., Periodontitis as a Modifiable Risk Factor for Dementia: A Nationwide Population-Based Cohort Study. *J. Am. Geriatr. Soc.* **2017,** *65* (2), 301-305.

403. Abbayya, K.; Puthanakar, N. Y.; Naduwinmani, S.; Chidambar, Y., Association between periodontitis and Alzheimer's disease. *North American journal of medical sciences* **2015,** *7* (6), 241.

404. Kornman, K. S., Mapping the pathogenesis of periodontitis: a new look. *Journal of periodontology* **2008,** *79* (8S), 1560-1568.

405. Mariotti, A.; Hefti, A. F. In *Defining periodontal health*, BMC oral health, BioMed Central: 2015; p S6.

406. Perry, D., *Periodontology for the dental hygienist*. 4 ed.; Elsevier: St. Louis, MO, 2014.

407. Larsen, C.; Barendregt, D. S.; Slot, D. E.; Van der Velden, U.; Van der Weijden, F., Probing pressure, a highly undervalued unit of measure in periodontal probing: a systematic review on its effect on probing pocket depth. *Journal of clinical periodontology* **2009,** *36* (4), 315-322.

408. Armitage, G. C.; Svanberc, G. K.; Löe, H., Microscopic evaluation of clinical measurements of connective tissue attachment levels. *Journal of clinical periodontology* **1977,** *4* (3), 173-190.

409. Koka, S., The implant-mucosal interface and its role in the long-term success of endosseous oral implants: a review of the literature. *The International journal of prosthodontics* **1999,** *11* (5), 421-32.

410. Schou, S.; Holmstrup, P.; Stoltze, K.; Hjørting-Hansen, E.; Fiehn, N.-E.; Skovgaard, L. T., Probing around implants and teeth with healthy or inflamed peri-implant mucosa/gingiva. *Clinical Oral Implants Research* **2002,** *13* (2), 113-126.

411. Giraldo, V. M.; Duque, A.; Aristizabal, A. G.; Hernández, R. D. M., Prevalence of Peri-implant Disease According to Periodontal Probing Depth and Bleeding on Probing: A Systematic Review and Meta-Analysis. *The International journal of oral & maxillofacial implants* **2018,** *33* (4), e89-e105.

412. Rakic, M.; Galindo-Moreno, P.; Monje, A.; Radovanovic, S.; Wang, H.-L.; Cochran, D.; Sculean, A.; Canullo, L., How frequent does peri-implantitis occur? A systematic review and meta-analysis. *Clinical oral investigations* **2018,** *22* (4), 1805-1816.

413. Lin, C.; Chen, F.; Hariri, A.; Chen, C.; Wilder-Smith, P.; Takesh, T.; Jokerst, J., Photoacoustic Imaging for Noninvasive Periodontal Probing Depth Measurements. *Journal of dental research* **2017**, 0022034517729820.

414. Stylogiannis, A.; Prade, L.; Buehler, A.; Aguirre, J.; Sergiadis, G.; Ntziachristos, V., Continuous wave laser diodes enable fast optoacoustic imaging. *Photoacoustics* **2018,** *9*, 31-38.

415. Beard, P., Biomedical photoacoustic imaging. *Interface focus* **2011**, rsfs20110028.

416. Deán-Ben, X. L.; Razansky, D., Optoacoustic signal excitation with a tone-burst of short pulses. *Photoacoustics* **2018,** *11*, 1-5.

417. Knieling, F.; Neufert, C.; Hartmann, A.; Claussen, J.; Urich, A.; Egger, C.; Vetter, M.; Fischer, S.; Pfeifer, L.; Hagel, A.; Kielisch, C.; Görtz, R. S.; Wildner, D.; Engel, M.; Röther, J.; Uter, W.; Siebler, J.; Atreya, R.; Rascher, W.; Strobel, D.; Neurath, M. F.; Waldner, M. J., Multispectral Optoacoustic Tomography for Assessment of Crohn's Disease Activity. *New England Journal of Medicine* **2017,** *376* (13), 1292-1294.

418. Jo, J.; Tian, C.; Xu, G.; Sarazin, J.; Schiopu, E.; Gandikota, G.; Wang, X., Photoacoustic tomography for human musculoskeletal imaging and inflammatory arthritis detection. *Photoacoustics* **2018**.

419. Masthoff, M.; Helfen, A.; Claussen, J.; et al., Use of multispectral optoacoustic tomography to diagnose vascular malformations. *JAMA Dermatology* **2018**.

420. Aguirre, J.; Hindelang, B.; Berezhnoi, A.; Darsow, U.; Lauffer, F.; Eyerich, K.; Biedermann, T.; Ntziachristos, V., Assessing nailfold microvascular structure with ultra-wideband raster-scan optoacoustic mesoscopy. *Photoacoustics* **2018,** *10*, 31-37.

421. Attia, A. B. E.; Chuah, S. Y.; Razansky, D.; Ho, C. J. H.; Malempati, P.; Dinish, U. S.; Bi, R.; Fu, C. Y.; Ford, S. J.; Lee, J. S.-S.; Tan, M. W. P.; Olivo, M.; Thng, S. T. G., Noninvasive real-time characterization of non-melanoma skin cancers with handheld optoacoustic probes. *Photoacoustics* **2017,** *7*, 20-26.

422. Vandenberghe, B.; Jacobs, R.; Bosmans, H., Modern dental imaging: a review of the current technology and clinical applications in dental practice. *European Radiology* **2010,** *20* (11), 2637-2655.

423. Barratt, D. C.; Chan, C. S.; Edwards, P. J.; Penney, G. P.; Slomczykowski, M.; Carter, T. J.; Hawkes, D. J., Instantiation and registration of statistical shape models of the femur and pelvis using 3D ultrasound imaging. *Medical image analysis* **2008,** *12* (3), 358-374.

424. Pekam, F. C.; Marotti, J.; Wolfart, S.; Tinschert, J.; Radermacher, K.; Heger, S., High-frequency ultrasound as an option for scanning of prepared teeth: an in vitro study. *Ultrasound in medicine & biology* **2015,** *41* (1), 309-316.

425. D., S. E.; S., G. G.; A., P., In vitro accuracy and reproducibility of automated and conventional periodontal probes. *Journal of Clinical Periodontology* **1997,** *24* (5), 340-345.

426. Savage, A.; Eaton, K. A.; Moles, D. R.; Needleman, I., A systematic review of definitions of periodontitis and methods that have been used to identify this disease. *Journal of clinical periodontology* **2009,** *36* (6), 458-467.

427. Fishman, E. K.; Ney, D. R.; Heath, D. G.; Corl, F. M.; Horton, K. M.; Johnson, P. T., Volume rendering versus maximum intensity projection in CT angiography: what works best, when, and why. *Radiographics* **2006,** *26* (3), 905-922.

428. Harris, E. F., Tooth-coding systems in the clinical dental setting. *Den Anthr* **2005,** *18* (2), 43-49.

429. Moran, C. M.; Pye, S. D.; Ellis, W.; Janeczko, A.; Morris, K. D.; McNeilly, A. S.; Fraser, H. M., A Comparison of the Imaging Performance of High Resolution Ultrasound Scanners for Preclinical Imaging. *Ultrasound in Medicine and Biology* **2011,** *37* (3), 493-501.

430. Liopo, A.; Su, R.; Oraevsky, A. A., Melanin nanoparticles as a novel contrast agent for optoacoustic tomography. *Photoacoustics* **2015,** *3* (1), 35-43.

431. Fan, Q.; Cheng, K.; Hu, X.; Ma, X.; Zhang, R.; Yang, M.; Lu, X.; Xing, L.; Huang, W.; Gambhir, S. S.; Cheng, Z., Transferring Biomarker into Molecular Probe: Melanin Nanoparticle as a Naturally

Active Platform for Multimodality Imaging. *Journal of the American Chemical Society* **2014,** *136* (43), 15185-15194.

432. L., V. K.; B., S., Thickness of gingiva in association with age, gender and dental arch location. *Journal of Clinical Periodontology* **2005,** *32* (7), 828-830.

433. Suri, L.; Gagari, E.; Vastardis, H., Delayed tooth eruption: Pathogenesis, diagnosis, and treatment. A literature review. *American Journal of Orthodontics and Dentofacial Orthopedics* **2004,** *126* (4), 432-445.

434. A., L. M., Periodontal probing: What does it mean? *Journal of Clinical Periodontology* **1980,** *7* (3), 165-176.

435. Newman, M. G.; Takei, H.; Klokkevold, P. R.; Carranza, F. A., *Carranza's clinical periodontology*. Elsevier health sciences: 2011.

436. Lehmann, T.; Troeltsch, E.; Spitzer, K., Image processing and enhancement provided by commercial dental software programs. *Dentomaxillofacial Radiology* **2002,** *31* (4), 264-272.

437. Nikoozadeh, A.; Chang, C.; Choe, J. W.; Bhuyan, A.; Lee, B. C.; Moini, A.; Khuri-Yakub, P. T. In *An integrated ring CMUT array for endoscopic ultrasound and photoacoustic imaging*, Ultrasonics Symposium (IUS), 2013 IEEE International, IEEE: 2013; pp 1178-1181.

438. Wang, S.; Liu, Y.; Fang, D.; Shi, S., The miniature pig: a useful large animal model for dental and orofacial research. *Oral diseases* **2007,** *13* (6), 530-537.

439. Tonetti, M. S.; Van Dyke, T. E., Periodontitis and atherosclerotic cardiovascular disease: consensus report of the Joint EFP/AAPWorkshop on Periodontitis and Systemic Diseases. *Journal of periodontology* **2013,** *84*, S24-S29.

440. Kornman, K. S., Mapping the pathogenesis of periodontitis: a new look. *Journal of periodontology* **2008,** *79*, 1560-1568.

441. Chan, H.-L.; Sinjab, K.; Chung, M.-P.; Chiang, Y.-C.; Wang, H.-L.; Giannobile, W. V.; Kripfgans, O. D., Non-invasive evaluation of facial crestal bone with ultrasonography. *PLoS One* **2017,** *12* (2), e0171237.

442. Nguyen, K.-C. T.; Le, L. H.; Kaipatur, N. R.; Major, P. W., Imaging the cemento-enamel junction using a 20-MHz ultrasonic transducer. *Ultrasound in medicine and biology* **2016,** *42* (1), 333-338.

443. Moore, C.; Jokerst, J. V., Photoacoustic Ultrasound for Enhanced Contrast in Dental and Periodontal Imaging. In *Dental Ultrasound in Periodontology and Implantology*, Springer: 2020; pp 215-230.

444. Lukashevich, P.; Zalesky, B.; Ablameyko, S., Medical image registration based on SURF detector. *Pattern Recognition and Image Analysis* **2011,** *21* (3), 519.

445. Sotiras, A.; Davatzikos, C.; Paragios, N., Deformable medical image registration: A survey. *IEEE transactions on medical imaging* **2013,** *32* (7), 1153-1190.

446. Wen, G.-J.; Lv, J.-j.; Yu, W.-x. J. I. T. o. G.; Sensing, R., A high-performance feature-matching method for image registration by combining spatial and similarity information. **2008,** *46* (4), 1266-1277.

447. Bay, H.; Tuytelaars, T.; Van Gool, L. In *Surf: Speeded up robust features*, European conference on computer vision, Springer: 2006; pp 404-417.

448. Lowe, D. G. J. I. j. o. c. v., Distinctive image features from scale-invariant keypoints. **2004,** *60* (2), 91-110.

449. Matas, J.; Chum, O.; Urban, M.; Pajdla, T. J. I.; computing, v., Robust wide-baseline stereo from maximally stable extremal regions. **2004,** *22* (10), 761-767.

450. Heinrich, M. P.; Jenkinson, M.; Bhushan, M.; Matin, T.; Gleeson, F. V.; Brady, M.; Schnabel, J. A. J. M. i. a., MIND: Modality independent neighbourhood descriptor for multi-modal deformable registration. **2012,** *16* (7), 1423-1435.

451. Heinrich, M. P.; Jenkinson, M.; Bhushan, M.; Matin, T.; Gleeson, F. V.; Brady, M.; Schnabel, J. A., MIND: Modality independent neighbourhood descriptor for multi-modal deformable registration. *Medical image analysis* **2012,** *16* (7), 1423-1435.

452. Buades, A.; Coll, B.; Morel, J.-M. In *A non-local algorithm for image denoising*, 2005 IEEE Computer Society Conference on Computer Vision and Pattern Recognition (CVPR'05), IEEE: 2005; pp 60-65.

453. Wang, Z.; Bovik, A. C.; Sheikh, H. R.; Simoncelli, E. P., Image quality assessment: from error visibility to structural similarity. *IEEE transactions on image processing* **2004,** *13* (4), 600-612.

454. Mozaffarzadeh, M.; Mahloojifar, A.; Orooji, M.; Kratkiewicz, K.; Adabi, S.; Nasiriavanaki, M., Linear-array photoacoustic imaging using minimum variance-based delay multiply and sum adaptive beamforming algorithm. *Journal of biomedical optics* **2018,** *23* (2), 026002.

455. Matrone, G.; Savoia, A. S.; Caliano, G.; Magenes, G., The delay multiply and sum beamforming algorithm in ultrasound B-mode medical imaging. *IEEE transactions on medical imaging* **2014,** *34* (4), 940-949.

456. Mozaffarzadeh, M.; Mahloojifar, A.; Orooji, M.; Adabi, S.; Nasiriavanaki, M., Double-stage delay multiply and sum beamforming algorithm: Application to linear-array photoacoustic imaging. *IEEE Transactions on Biomedical Engineering* **2017,** *65* (1), 31-42.

457. Mozaffarzadeh, M.; Hariri, A.; Moore, C.; Jokerst, J. V., The double-stage delay-multiply-and-sum image reconstruction method improves imaging quality in a led-based photoacoustic array scanner. *Photoacoustics* **2018,** *12*, 22-29.

458. Mozaffarzadeh, M.; Varnosfaderani, M. H.; Sharma, A.; Pramanik, M.; de Jong, N.; Verweij, M. D., Enhanced contrast acoustic-resolution photoacoustic microscopy using double-stage delay-multiply-and-sum beamformer for vasculature imaging. *Journal of biophotonics* **2019,** *12* (11), e201900133.

459. Hariri, A.; Alipour, K.; Mantri, Y.; Schulze, J. P.; Jokerst, J. V., Deep learning improves contrast in low-fluence photoacoustic imaging. *Biomed. Opt. Express* **2020,** *11* (6), 3360-3373.

460. Farnia, P.; Najafzadeh, E.; Hariri, A.; Lavasani, S. N.; Makkiabadi, B.; Ahmadian, A.; Jokerst, J. V., Dictionary learning technique enhances signal in LED-based photoacoustic imaging. *Biomed. Opt. Express* **2020,** *11* (5), 2533-2547.

461. Chen, H.; Zheng, R.; Lou, E.; Ta, D. In *Imaging Spinal Curvatures of AIS Patients using 3D US Free-hand Fast Reconstruction Method*, 2019 IEEE International Ultrasonics Symposium (IUS), IEEE: 2019; pp 1440-1443.

462. Hariri, A.; Chen, F.; Moore, C.; Jokerst, J. V., Noninvasive staging of pressure ulcers using photoacoustic imaging. *Wound Repair & Regeneration* **2019,** *27* (5), 488-496.

463. Mozaffarzadeh, M.; Soozande, M.; Fool, F.; Pertijs, M. A.; Vos, H. J.; Verweij, M. D.; Bosch, J. G.; de Jong, N., Receive/transmit aperture selection for 3D ultrasound imaging with a 2D matrix transducer. *Applied Sciences* **2020,** *10* (15), 5300.

464. van Knippenberg, L.; van Sloun, R. J.; Shulepov, S.; Bouwman, A.; Mischi, M. In *Towards flow estimation in the common carotid artery using free-hand cross-sectional doppler*, 2019 IEEE International Ultrasonics Symposium (IUS), IEEE: 2019; pp 1322-1325.

465. Chung, S.-W.; Shih, C.-C.; Huang, C.-C., Freehand three-dimensional ultrasound imaging of carotid artery using motion tracking technology. *Ultrasonics* **2017,** *74*, 11-20.

466. Mozaffari, M. H.; Lee, W.-S., Freehand 3-D ultrasound imaging: a systematic review. *Ultrasound in medicine & biology* **2017,** *43* (10), 2099-2124.

467. Solberg, O. V.; Lindseth, F.; Torp, H.; Blake, R. E.; Hernes, T. A. N., Freehand 3D ultrasound reconstruction algorithms—a review. *Ultrasound in medicine & biology* **2007,** *33* (7), 991-1009.

468. Wang, L. V., *Photoacoustic imaging and spectroscopy*. CRC press: 2017.

469. Moore, C.; Jokerst, J. V., Strategies for image-guided therapy, surgery, and drug delivery using photoacoustic imaging. *Theranostics* **2019,** *9* (6), 1550.

470. Vu, T.; Razansky, D.; Yao, J., Listening to tissues with new light: recent technological advances in photoacoustic imaging. *Journal of Optics* **2019,** *21* (10), 103001.

471. Frinking, P.; Segers, T.; Luan, Y.; Tranquart, F., Three decades of ultrasound contrast agents: a review of the past, present and future improvements. *Ultrasound in medicine & biology* **2020,** *46* (4), 892-908.

472. Ramirez, D. G.; Abenojar, E.; Hernandez, C.; Lorberbaum, D. S.; Papazian, L. A.; Passman, S.; Pham, V.; Exner, A. A.; Benninger, R. K., Contrast-enhanced ultrasound with sub-micron sized contrast agents detects insulitis in mouse models of type1 diabetes. *Nature communications* **2020,** *11* (1), 1-13.

473. Cox, B. T.; Laufer, J. G.; Beard, P. C.; Arridge, S. R., Quantitative spectroscopic photoacoustic imaging: a review. *Journal of biomedical optics* **2012,** *17* (6), 061202.

474. Moore, C.; Jokerst, J. V., Photoacoustic Ultrasound for Enhanced Contrast in Dental and Periodontal Imaging. In *Dental Ultrasound in Periodontology and Implantology*, Springer: 2021; pp 215-230.

475. de Leon, A.; Wei, P.; Bordera, F.; Wegierak, D.; McMillen, M.; Yan, D.; Hemmingsen, C.; Kolios, M. C.; Pentzer, E. B.; Exner, A. A., Pickering Bubbles as Dual-Modality Ultrasound and Photoacoustic Contrast Agents. *ACS Applied Materials & Interfaces* **2020,** *12* (19), 22308-22317.

476. Guggenheim, J. A.; Allen, T. J.; Plumb, A.; Zhang, E. Z.; Rodriguez-Justo, M.; Punwani, S.; Beard, P. C., Photoacoustic imaging of human lymph nodes with endogenous lipid and hemoglobin contrast. *Journal of biomedical optics* **2015,** *20* (5), 050504.

477. Zhou, Y.; Tripathi, S. V.; Rosman, I.; Ma, J.; Hai, P.; Linette, G. P.; Council, M. L.; Fields, R. C.; Wang, L. V.; Cornelius, L. A., Noninvasive determination of melanoma depth using a handheld photoacoustic probe. *The Journal of investigative dermatology* **2017,** *137* (6), 1370.

478. Manohar, S.; Gambhir, S., Clinical photoacoustic imaging. *Photoacoustics* **2020,** *19*.

479. Attia, A. B. E.; Balasundaram, G.; Moothanchery, M.; Dinish, U.; Bi, R.; Ntziachristos, V.; Olivo, M., A review of clinical photoacoustic imaging: Current and future trends. *Photoacoustics* **2019,** *16*, 100144.

480. Choi, W.; Park, E.-Y.; Jeon, S.; Kim, C., Clinical photoacoustic imaging platforms. *Biomedical engineering letters* **2018,** *8* (2), 139-155.

481. Huang, J.; Pu, K., Activatable Molecular Probes for Second Near-Infrared Fluorescence, Chemiluminescence, and Photoacoustic Imaging. *Angewandte Chemie* **2020,** *132* (29), 11813-11827.

482. Ou, H.; Li, J.; Chen, C.; Gao, H.; Xue, X.; Ding, D., Organic/polymer photothermal nanoagents for photoacoustic imaging and photothermal therapy in vivo. *Science China Materials* **2019,** *62* (11), 1740-1758.

483. Weissleder, R.; Mahmood, U., Molecular imaging. *Radiology* **2001,** *219* (2), 316-333.

484. López-Otín, C.; Bond, J. S., Proteases: multifunctional enzymes in life and disease. *The Journal of biological chemistry* **2008,** *283* (45), 30433.

485. Dominy, S. S.; Lynch, C.; Ermini, F.; Benedyk, M.; Marczyk, A.; Konradi, A.; Nguyen, M.; Haditsch, U.; Raha, D.; Griffin, C., Porphyromonas gingivalis in Alzheimer's disease brains: Evidence for disease causation and treatment with small-molecule inhibitors. *Science advances* **2019,** *5* (1), eaau3333.

486. Jiang, T.; Olson, E. S.; Nguyen, Q. T.; Roy, M.; Jennings, P. A.; Tsien, R. Y., Tumor imaging by means of proteolytic activation of cell-penetrating peptides. *Proceedings of the National Academy of Sciences* **2004,** *101* (51), 17867-17872.

487. Yan, R.; Ye, D., Molecular imaging of enzyme activity in vivo using activatable probes. *Science Bulletin* **2016,** *61* (21), 1672-1679.

488. Wang, L.; Yang, P.-P.; Zhao, X.-X.; Wang, H., Self-assembled nanomaterials for photoacoustic imaging. *Nanoscale* **2016,** *8* (5), 2488-2509.

489. Zhang, D.; Qi, G. B.; Zhao, Y. X.; Qiao, S. L.; Yang, C.; Wang, H., In situ formation of nanofibers from purpurin18-peptide conjugates and the assembly induced retention effect in tumor sites. *Advanced Materials* **2015,** *27* (40), 6125-6130.

490. Yan, R.; Hu, Y.; Liu, F.; Wei, S.; Fang, D.; Shuhendler, A. J.; Liu, H.; Chen, H.-Y.; Ye, D., ---- Activatable NIR Fluorescence/MRI Bimodal Probes for in Vivo Imaging by Enzyme-Mediated Fluorogenic Reaction and Self-Assembly. *Journal of the American Chemical Society* **2019,** *141* (26), 10331-10341.

491. Ye, D.; Shuhendler, A. J.; Cui, L.; Tong, L.; Tee, S. S.; Tikhomirov, G.; Felsher, D. W.; Rao, J., Bioorthogonal cyclization-mediated in situ self-assembly of small-molecule probes for imaging caspase activity in vivo. *Nature Chemistry* **2014,** *6* (6), 519-526.

492. Xia, X.; Yang, M.; Oetjen, L. K.; Zhang, Y.; Li, Q.; Chen, J.; Xia, Y., An enzyme-sensitive probe for photoacoustic imaging and fluorescence detection of protease activity. *Nanoscale* **2011,** *3* (3), 950-953.

493. Liu, C.; Li, S.; Gu, Y.; Xiong, H.; Wong, W.-t.; Sun, L., Multispectral photoacoustic imaging of tumor protease activity with a gold nanocage-based activatable probe. *Molecular imaging and biology* **2018,** *20* (6), 919-929.

494. Yang, K.; Zhu, L.; Nie, L.; Sun, X.; Cheng, L.; Wu, C.; Niu, G.; Chen, X.; Liu, Z., Visualization of protease activity in vivo using an activatable photo-acoustic imaging probe based on CuS nanoparticles. *Theranostics* **2014,** *4* (2), 134.

495. Morgounova, E.; Johnson, S. M.; Shao, Q.; Hackel, B.; Ashkenazi, S. In *Lifetime-based photoacoustic probe activation modeled by a dual methylene blue-lysine conjugate*, Photons Plus Ultrasound: Imaging and Sensing 2014, International Society for Optics and Photonics: 2014; p 89435F.

496. Li, Y.; Zhou, Y.; Yue, X.; Dai, Z., Cyanine conjugates in cancer theranostics. *Bioactive Materials* **2021,** *6* (3), 794-809.

497. Sun, W.; Guo, S.; Hu, C.; Fan, J.; Peng, X., Recent development of chemosensors based on cyanine platforms. *Chemical reviews* **2016,** *116* (14), 7768-7817.

498. Mishra, A.; Behera, R. K.; Behera, P. K.; Mishra, B. K.; Behera, G. B., Cyanines during the 1990s: a review. *Chemical reviews* **2000,** *100* (6), 1973-2012.

499. Benson, R. C.; Kues, H. A., Absorption and fluorescence properties of cyanine dyes. *Journal of Chemical and Engineering Data* **1977,** *22* (4), 379-383.

500. Kilian, H. I.; Kang, H.; Nyayapathi, N.; Fukuda, T.; Adluru, E.; Zhang, H.; Quinn, B.; Xia, J.; Choi, H. S.; Lovell, J. F., Facile formulation of a long-wavelength cyanine for optical imaging in the second near-infrared window. *Biomaterials Science* **2020,** *8* (15), 4199-4205.

501. Polom, K.; Murawa, D.; Rho, Y. s.; Nowaczyk, P.; Hünerbein, M.; Murawa, P., Current trends and emerging future of indocyanine green usage in surgery and oncology: a literature review. *Cancer* **2011,** *117* (21), 4812-4822.

502. Li, Y.; Zhou, Y.; Yue, X.; Dai, Z., Cyanine Conjugate-Based Biomedical Imaging Probes. *Advanced Healthcare Materials* **2020,** *9* (22), 2001327.

503. Zhao, X.; Fan, Z.; Qiao, Y.; Chen, Y.; Wang, S.; Yue, X.; Shen, T.; Liu, W.; Yang, J.; Gao, H.; Zhan, X.; Shang, L.; Yin, Y.; Zhao, W.; Ding, D.; Xi, R.; Meng, M., AIEgens Conjugation Improves the Photothermal Efficacy and Near-Infrared Imaging of Heptamethine Cyanine IR-780. *ACS Applied Materials & Interfaces* **2020,** *12* (14), 16114-16124.

504. Mokrousov, M. D.; Novoselova, M. V.; Nolan, J.; Harrington, W.; Rudakovskaya, P.; Bratashov, D. N.; Galanzha, E. I.; Fuenzalida-Werner, J. P.; Yakimov, B. P.; Nazarikov, G., Amplification of

photoacoustic effect in bimodal polymer particles by self-quenching of indocyanine green. *Biomed. Opt. Express* **2019,** *10* (9), 4775-4788.

505. Miranda, D.; Huang, H.; Kang, H.; Zhan, Y.; Wang, D.; Zhou, Y.; Geng, J.; Kilian, H. I.; Stiles, W.; Razi, A., Highly-soluble cyanine J-aggregates entrapped by liposomes for in vivo optical imaging around 930 nm. *Theranostics* **2019,** *9* (2), 381.

506. Hestand, N. J.; Spano, F. C., Expanded Theory of H- and J-Molecular Aggregates: The Effects of Vibronic Coupling and Intermolecular Charge Transfer. *Chemical Reviews* **2018,** *118* (15), 7069-7163.

507. West, W.; Pearce, S., The dimeric state of cyanine dyes. *The Journal of Physical Chemistry* **1965,** *69* (6), 1894-1903.

508. Kasha, M.; Rawls, H.; El-Bayoumi, M. A., The exciton model in molecular spectroscopy. *Pure and Applied Chemistry* **1965,** *11* (3-4), 371-392.

509. Geoghegan, K. F.; Rosner, P. J.; Hoth, L. R., Dye-Pair Reporter Systems for Protein− Peptide Molecular Interactions. *Bioconjugate chemistry* **2000,** *11* (1), 71-77.

510. Weissleder, R.; Tung, C.-H.; Mahmood, U.; Bogdanov, A., In vivo imaging of tumors with protease-activated near-infrared fluorescent probes. *Nature biotechnology* **1999,** *17* (4), 375-378.

511. Morales, J.; Pawle, R. H.; Akkilic, N.; Luo, Y.; Xavierselvan, M.; Albokhari, R.; Calderon, I. A. C.; Selfridge, S.; Minns, R.; Takiff, L.; Mallidi, S.; Clark, H. A., DNA-Based Photoacoustic Nanosensor for Interferon Gamma Detection. *ACS Sensors* **2019,** *4* (5), 1313-1322.

512. Zhang, L.; Lin, D.; Sun, X.; Curth, U.; Drosten, C.; Sauerhering, L.; Becker, S.; Rox, K.; Hilgenfeld, R., Crystal structure of SARS-CoV-2 main protease provides a basis for design of improved α-ketoamide inhibitors. *Science* **2020,** *368* (6489), 409-412.

513. Mellott, D. M.; Tseng, C.-T.; Drelich, A.; Fajtová, P.; Chenna, B. C.; Kostomiris, D. H.; Hsu, J.; Zhu, J.; Taylor, Z. W.; Kocurek, K. I., A Clinical-Stage Cysteine Protease Inhibitor blocks SARS-CoV-2 Infection of Human and Monkey Cells. *ACS chemical biology* **2021**.

514. Wang, J.; Chen, F.; Arconada-Alvarez, S. J.; Hartanto, J.; Yap, L.-P.; Park, R.; Wang, F.; Vorobyova, I.; Dagliyan, G.; Conti, P. S.; Jokerst, J. V., A Nanoscale Tool for Photoacoustic-Based Measurements of Clotting Time and Therapeutic Drug Monitoring of Heparin. *Nano Letters* **2016,** *16* (10), 6265-6271.

515. Boccia, A. C.; Lukeš, V.; Eckstein-Andicsová, A.; Kozma, E., Solvent- and concentration-induced self-assembly of an amphiphilic perylene dye. *New Journal of Chemistry* **2020,** *44* (3), 892-899.

516. Nişancı, B.; Daştan, A.; Bozdemir, Ö. A., Aromatic stacking of a perylenetetracarboxylic tetraester: Self-assembly in both water and chloroform. *Tetrahedron Letters* **2018,** *59* (39), 3558-3562.

517. Armbruster, D. A.; Pry, T., Limit of blank, limit of detection and limit of quantitation. *The Clinical biochemist. Reviews* **2008,** *29 Suppl 1* (Suppl 1), S49-S52.

518. Kaur, J.; Singh, P. K., Trypsin Detection Strategies: A Review. *Critical Reviews in Analytical Chemistry* **2020**, 1-19.

519. Kuramochi, H.; Nakata, H.; Ishii, S.-i., Mechanism of association of a specific aldehyde inhibitor, leupeptin, with bovine trypsin. *The Journal of Biochemistry* **1979,** *86* (5), 1403-1410.

520. Mukherjee, P.; Desai, P.; Ross, L.; White, E. L.; Avery, M. A., Structure-based virtual screening against SARS-3CL(pro) to identify novel non-peptidic hits. *Bioorg Med Chem* **2008,** *16* (7), 4138-4149.

521. Rut, W.; Groborz, K.; Zhang, L.; Sun, X.; Zmudzinski, M.; Pawlik, B.; Wang, X.; Jochmans, D.; Neyts, J.; Młynarski, W., SARS-CoV-2 M pro inhibitors and activity-based probes for patient-sample imaging. *Nature chemical biology* **2021,** *17* (2), 222-228.

522. Beutler, E.; Waalen, J., The definition of anemia: what is the lower limit of normal of the blood hemoglobin concentration? *Blood* **2006,** *107* (5), 1747-1750.

523. Robles, F. E.; Chowdhury, S.; Wax, A., Assessing hemoglobin concentration using spectroscopic optical coherence tomography for feasibility of tissue diagnostics. *Biomed. Opt. Express* **2010,** *1* (1), 310-317.

524. Guentsch, A.; Kramesberger, M.; Sroka, A.; Pfister, W.; Potempa, J.; Eick, S., Comparison of gingival crevicular fluid sampling methods in patients with severe chronic periodontitis. *J. Periodontol.* **2011,** *82* (7), 1051-1060.

525. Eke, P. I.; Dye, B. A.; Wei, L.; Slade, G. D.; Thornton-Evans, G. O.; Borgnakke, W. S.; Taylor, G. W.; Page, R. C.; Beck, J. D.; Genco, R. J., Update on Prevalence of Periodontitis in Adults in the United States: NHANES 2009 to 2012. *J. Periodontol.* **2015,** *86* (5), 611-622.

526. Listl, S.; Galloway, J.; Mossey, P.; Marcenes, W., Global economic impact of dental diseases. *J. Dent. Res.* **2015,** *94* (10), 1355-1361.

527. Hajishengallis, G., Periodontitis: from microbial immune subversion to systemic inflammation. *Nat. Rev. Immuno.* **2014,** *15*, 30.

528. Kuboniwa, M.; Lamont, R. J., Subgingival biofilm formation. *Periodontol. 2000* **2010,** *52* (1), 38-52.

529. Nazir, M. A., Prevalence of periodontal disease, its association with systemic diseases and prevention. *Int. J. Health Sci.* **2017,** *11* (2), 72-80.

530. Hajishengallis, G.; Lamont, R. J., Beyond the red complex and into more complexity: the polymicrobial synergy and dysbiosis (PSD) model of periodontal disease etiology. *Mol. Oral Microbiol.* **2012,** *27* (6), 409-419.

531. Byrne, S. J.; Dashper, S. G.; Darby, I. B.; Adams, G. G.; Hoffmann, B.; Reynolds, E. C., Progression of chronic periodontitis can be predicted by the levels of Porphyromonas gingivalis and Treponema denticola in subgingival plaque. *Oral Microbiology and Immunology* **2009,** *24* (6), 469-477.

532. Kinney, J. S.; Morelli, T.; Oh, M.; Braun, T. M.; Ramseier, C. A.; Sugai, J. V.; Giannobile, W. V., Crevicular fluid biomarkers and periodontal disease progression. *J. Clin. Periodontol.* **2014,** *41* (2), 113-120.

533. Graves, D. T.; Jiang, Y.; Genco, C., Periodontal disease: bacterial virulence factors, host response and impact on systemic health. *Curr. Opin. Infect. Dis.* **2000,** *13* (3), 227-232.

534. Imamura, T., The role of gingipains in the pathogenesis of periodontal disease. *J. Periodontol.* **2003,** *74* (1), 111-118.

535. Olsen, I.; Potempa, J., Strategies for the inhibition of gingipains for the potential treatment of periodontitis and associated systemic diseases. *J. Oral Microbiol.* **2014,** *6* (1), 24800.

536. Kataoka, S.; Baba, A.; Suda, Y.; Takii, R.; Hashimoto, M.; Kawakubo, T.; Asao, T.; Kadowaki, T.; Yamamoto, K., A novel, potent dual inhibitor of Arg-gingipains and Lys-gingipain as a promising agent for periodontal disease therapy. *The FASEB Journal* **2014,** *28* (8), 3564-3578.

537. Kadowaki, T.; Baba, A.; Abe, N.; Takii, R.; Hashimoto, M.; Tsukuba, T.; Okazaki, S.; Suda, Y.; Asao, T.; Yamamoto, K., Suppression of Pathogenicity of Porphyromonas gingivalis by Newly Developed Gingipain Inhibitors. *Mol. Pharmacol.* **2004,** *66* (6), 1599.

538. Dominy, S. S.; Lynch, C.; Ermini, F.; Benedyk, M.; Marczyk, A.; Konradi, A.; Nguyen, M.; Haditsch, U.; Raha, D.; Griffin, C.; Holsinger, L. J.; Arastu-Kapur, S.; Kaba, S.; Lee, A.; Ryder, M. I.; Potempa, B.; Mydel, P.; Hellvard, A.; Adamowicz, K.; Hasturk, H.; Walker, G. D.; Reynolds, E. C.; Faull, R. L. M.; Curtis, M. A.; Dragunow, M.; Potempa, J., Porphyromonas gingivalis in Alzheimer's disease brains: Evidence for disease causation and treatment with small-molecule inhibitors. *Science Advances* **2019,** *5* (1), eaau3333.

539. Nara, P. L.; Sindelar, D.; Penn, M. S.; Potempa, J.; Griffin, W. S. T., Porphyromonas gingivalis Outer Membrane Vesicles as the Major Driver of and Explanation for Neuropathogenesis, the Cholinergic Hypothesis, Iron Dyshomeostasis, and Salivary Lactoferrin in Alzheimer's Disease. *Journal of Alzheimer's Disease* **2021,** *82*, 1417-1450.

540. Alhogail, S.; Suaifan, G. A.; Bizzarro, S.; Kaman, W. E.; Bikker, F. J.; Weber, K.; Cialla-May, D.; Popp, J.; Zourob, M., On site visual detection of Porphyromonas gingivalis related periodontitis by using a magnetic-nanobead based assay for gingipains protease biomarkers. *Microchimica Acta* **2018,** *185* (2), 149.

541. Kaman, W. E.; Galassi, F.; de Soet, J. J.; Bizzarro, S.; Loos, B. G.; Veerman, E. C.; van Belkum, A.; Hays, J. P.; Bikker, F. J., A Highly Specific Protease-Based Approach for the Detection of Porphyromonas gingivalis in the Diagnosis of Periodontitis. *J. Clin. Microbiol.* **2011**, JCM. 05313-11.

542. Svärd, A.; Neilands, J.; Palm, E.; Svensäter, G.; Bengtsson, T.; Aili, D., Protein-Functionalized Gold Nanoparticles as Refractometric Nanoplasmonic Sensors for the Detection of Proteolytic Activity of Porphyromonas gingivalis. *ACS Applied Nano Materials* **2020,** *3* (10), 9822-9830.

543. Liu, S.; Wang, Y.-n.; Ma, B.; Shao, J.; Liu, H.; Ge, S., Gingipain-Responsive Thermosensitive Hydrogel Loaded with SDF-1 Facilitates In Situ Periodontal Tissue Regeneration. *ACS Applied Materials & Interfaces* **2021,** *13* (31), 36880-36893.

544. AlKahtani, R. N., The implications and applications of nanotechnology in dentistry: A review. *The Saudi Dental Journal* **2018,** *30* (2), 107-116.

545. Hannig, M.; Hannig, C., Nanomaterials in preventive dentistry. *Nature Nanotechnology* **2010,** *5* (8), 565-569.

546. Chan, H.-L. A.; Kripfgans, O. D., Dental Ultrasound in Periodontology and Implantology.

547. Joshi, B. P.; Zhou, J.; Pant, A.; Duan, X.; Zhou, Q.; Kuick, R.; Owens, S. R.; Appelman, H.; Wang, T. D., Design and Synthesis of Near-Infrared Peptide for in Vivo Molecular Imaging of HER2. *Bioconjugate Chemistry* **2016,** *27* (2), 481-494.

548. Trabuco, L. G.; Lise, S.; Petsalaki, E.; Russell, R. B., PepSite: prediction of peptide-binding sites from protein surfaces. *Nucleic acids research* **2012,** *40* (W1), W423-W427.

549. Eichinger, A.; Beisel, H.-G.; Jacob, U.; Huber, R.; Medrano, F.-J.; Banbula, A.; Potempa, J.; Travis, J.; Bode, W., Crystal structure of gingipain R: an Arg-specific bacterial cysteine proteinase with a caspase-like fold. *The EMBO Journal* **1999,** *18* (20), 5453-5462.

550. http://www.mimotopes.com.

551. Potempa, J.; Nguyen, K. A., Purification and characterization of gingipains. *Current Protocols in Protein Science* **2007,** *49* (1), 21.20. 1-21.20. 27.

552. Ashimoto, A.; Chen, C.; Bakker, I.; Slots, J., Polymerase chain reaction detection of 8 putative periodontal pathogens in subgingival plaque of gingivitis and advanced periodontitis lesions. *Oral microbiology and immunology* **1996,** *11* (4), 266-273.

553. Petsalaki, E.; Stark, A.; García-Urdiales, E.; Russell, R. B., Accurate Prediction of Peptide Binding Sites on Protein Surfaces. *PLOS Computational Biology* **2009,** *5* (3), e1000335.

554. Moore, C.; Borum, R. M.; Mantri, Y.; Xu, M.; Fajtová, P.; O'Donoghue, A. J.; Jokerst, J. V., Activatable Carbocyanine Dimers for Photoacoustic and Fluorescent Detection of Protease Activity. *ACS Sens.* **2021,** *6* (6), 2356-2365.

555. Jung, Y.-J.; Jun, H.-K.; Choi, B.-K., Porphyromonas gingivalis suppresses invasion of Fusobacterium nucleatum into gingival epithelial cells. *J. Oral Microbiol.* **2017,** *9* (1), 1320193.

556. Jayaprakash, K.; Khalaf, H.; Bengtsson, T., Gingipains from Porphyromonas gingivalis play a significant role in induction and regulation of CXCL8 in THP-1 cells. *BMC Microbiology* **2014,** *14* (1), 1-9.

557. Houle, M.-A.; Grenier, D.; Plamondon, P.; Nakayama, K., The collagenase activity of Porphyromonas gingivalis is due to Arg-gingipain. *FEMS Microbiol. Lett.* **2003,** *221* (2), 181-185.

558. Park, S.; Park, K.; Na, H. S.; Chung, J.; Yang, H., Washing- and Separation-Free Electrochemical Detection of Porphyromonas gingivalis in Saliva for Initial Diagnosis of Periodontitis. *Analytical Chemistry* **2021,** *93* (13), 5644-5650.

559. Skottrup, P. D.; Leonard, P.; Kaczmarek, J. Z.; Veillard, F.; Enghild, J. J.; O'Kennedy, R.; Sroka, A.; Clausen, R. P.; Potempa, J.; Riise, E., Diagnostic evaluation of a nanobody with picomolar affinity toward the protease RgpB from Porphyromonas gingivalis. *Analytical Biochemistry* **2011,** *415* (2), 158-167.

560. Mozaffarzadeh, M.; Moore, C.; Golmoghani, E. B.; Mantri, Y.; Hariri, A.; Jorns, A.; Fu, L.; Verweij, M. D.; Orooji, M.; de Jong, N.; Jokerst, J. V., Motion-compensated noninvasive periodontal health monitoring using handheld and motor-based photoacoustic-ultrasound imaging systems. *Biomedical Optics Express* **2021,** *12* (3), 1543-1558.

561. Grenier, D.; Dang La, V., Proteases of Porphyromonas gingivalis as important virulence factors in periodontal disease and potential targets for plant-derived compounds: a review article. *Curr. Drug Targets* **2011,** *12* (3), 322-331.

562. Nakanishi, H.; Nonaka, S.; Wu, Z., Microglial Cathepsin B and Porphyromonas gingivalis Gingipains as Potential Therapeutic Targets for Sporadic Alzheimer's Disease. *CNS & Neurological Disorders-Drug Targets (Formerly Current Drug Targets-CNS & Neurological Disorders)* **2020,** *19* (7), 495-502.

563. Ryder, M. I., Porphyromonas gingivalis and Alzheimer disease: recent findings and potential therapies. *J. Periodontol.* **2020,** *91*, S45-S49.

564. Haditsch, U.; Roth, T.; Rodriguez, L.; Hancock, S.; Cecere, T.; Nguyen, M.; Arastu-Kapur, S.; Broce, S.; Raha, D.; Lynch, C. C., Alzheimer's disease-like neurodegeneration in Porphyromonas gingivalis infected neurons with persistent expression of active gingipains. *Journal of Alzheimer's Disease* **2020,** *75* (4), 1361-1376.

565. Stahl, T.; Allen, T.; Beard, P. In *Characterization of the thermalisation efficiency and photostability of photoacoustic contrast agents*, Photons Plus Ultrasound: Imaging and Sensing 2014, International Society for Optics and Photonics: 2014; p 89435H.

566. Kaman Wendy, E.; Galassi, F.; de Soet Johannes, J.; Bizzarro, S.; Loos Bruno, G.; Veerman Enno, C. I.; van Belkum, A.; Hays John, P.; Bikker Floris, J., Highly Specific Protease-Based Approach for Detection of Porphyromonas gingivalis in Diagnosis of Periodontitis. *Journal of Clinical Microbiology* **2012,** *50* (1), 104-112.

567. McElfresh, C.; Harrington, T.; Vecchio, K. S., Application of a novel new multispectral nanoparticle tracking technique. *Measurement Science and Technology* **2018,** *29* (6), 065002.

568. Lemaster, J. E.; Jeevarathinam, A. S.; Kumar, A.; Chandrasekar, B.; Chen, F.; Jokerst, J. V., Synthesis of Ultrasmall Synthetic Melanin Nanoparticles by UV Irradiation in Acidic and Neutral Conditions. *ACS Applied Bio Materials* **2019,** *2* (10), 4667-4674.

569. Singh, P.; Bodycomb, J.; Travers, B.; Tatarkiewicz, K.; Travers, S.; Matyas, G. R.; Beck, Z., Particle size analyses of polydisperse liposome formulations with a novel multispectral advanced nanoparticle tracking technology. *International journal of pharmaceutics* **2019,** *566*, 680-686.

570. Mehta, D.; Jackson, R.; Paul, G.; Shi, J.; Sabbagh, M., Why do trials for Alzheimer's disease drugs keep failing? A discontinued drug perspective for 2010-2015. *Expert opinion on investigational drugs* **2017,** *26* (6), 735-739.

571. Rosenblum, W. I., Why Alzheimer trials fail: removing soluble oligomeric beta amyloid is essential, inconsistent, and difficult. *Neurobiology of aging* **2014,** *35* (5), 969-974.

572. Toyn, J., What lessons can be learned from failed Alzheimer's disease trials? Taylor & Francis: 2015.

573. Gursky, O.; Aleshkov, S., Temperature-dependent β-sheet formation in β-amyloid Aβ1–40 peptide in water: uncoupling β-structure folding from aggregation. *Biochimica et Biophysica Acta (BBA) - Protein Structure and Molecular Enzymology* **2000,** *1476* (1), 93-102.

574. Pryor, N. E.; Moss, M. A.; Hestekin, C. N., Unraveling the early events of amyloid-β protein (Aβ) aggregation: techniques for the determination of Aβ aggregate size. *International journal of molecular sciences* **2012,** *13* (3), 3038-3072.

575. Bartolini, M.; Naldi, M.; Fiori, J.; Valle, F.; Biscarini, F.; Nicolau, D. V.; Andrisano, V., Kinetic characterization of amyloid-beta 1–42 aggregation with a multimethodological approach. *Analytical biochemistry* **2011,** *414* (2), 215-225.

576. Janssen, L.; Sobott, F.; De Deyn, P. P.; Van Dam, D., Signal loss due to oligomerization in ELISA analysis of amyloid-beta can be recovered by a novel sample pre-treatment method. *MethodsX* **2015,** *2*, 112-123.

577. Pujol-Pina, R.; Vilaprinyó-Pascual, S.; Mazzucato, R.; Arcella, A.; Vilaseca, M.; Orozco, M.; Carulla, N., SDS-PAGE analysis of Aβ oligomers is disserving research into Alzheimer s disease: appealing for ESI-IM-MS. *Scientific reports* **2015,** *5*, 14809.

578. Xue, C.; Lin, T. Y.; Chang, D.; Guo, Z., Thioflavin T as an amyloid dye: fibril quantification, optimal concentration and effect on aggregation. *Royal Society open science* **2017,** *4* (1), 160696-160696.

579. Iadanza, M. G.; Jackson, M. P.; Hewitt, E. W.; Ranson, N. A.; Radford, S. E., A new era for understanding amyloid structures and disease. *Nature Reviews Molecular Cell Biology* **2018**, 1.

580. Liberta, F.; Loerch, S.; Rennegarbe, M.; Schierhorn, A.; Westermark, P.; Westermark, G. T.; Hazenberg, B. P.; Grigorieff, N.; Fändrich, M.; Schmidt, M., Cryo-EM fibril structures from systemic AA amyloidosis reveal the species complementarity of pathological amyloids. *Nature communications* **2019,** *10* (1), 1104.

581. Radamaker, L.; Lin, Y.-H.; Annamalai, K.; Huhn, S.; Hegenbart, U.; Schönland, S. O.; Fritz, G.; Schmidt, M.; Fändrich, M., Cryo-EM structure of a light chain-derived amyloid fibril from a patient with systemic AL amyloidosis. *Nature communications* **2019,** *10* (1), 1103.

582. Gallagher-Jones, M.; Glynn, C.; Boyer, D. R.; Martynowycz, M. W.; Hernandez, E.; Miao, J.; Zee, C.-T.; Novikova, I. V.; Goldschmidt, L.; McFarlane, H. T., Sub-ångström cryo-EM structure of a prion protofibril reveals a polar clasp. *Nature structural & molecular biology* **2018,** *25* (2), 131.

583. Brar, S. K.; Verma, M., Measurement of nanoparticles by light-scattering techniques. *TrAC Trends in Analytical Chemistry* **2011,** *30* (1), 4-17.

584. Mahl, D.; Diendorf, J.; Meyer-Zaika, W.; Epple, M., Possibilities and limitations of different analytical methods for the size determination of a bimodal dispersion of metallic nanoparticles. *Colloids and Surfaces A: Physicochemical and Engineering Aspects* **2011,** *377* (1-3), 386-392.

585. Tomaszewska, E.; Soliwoda, K.; Kadziola, K.; Tkacz-Szczesna, B.; Celichowski, G.; Cichomski, M.; Szmaja, W.; Grobelny, J., Detection limits of DLS and UV-Vis spectroscopy in characterization of polydisperse nanoparticles colloids. *Journal of Nanomaterials* **2013,** *2013*.

586. Ban, T.; Morigaki, K.; Yagi, H.; Kawasaki, T.; Kobayashi, A.; Yuba, S.; Naiki, H.; Goto, Y., Real-time and single fibril observation of the formation of amyloid β spherulitic structures. *Journal of Biological Chemistry* **2006,** *281* (44), 33677-33683.

587. Ban, T.; Yamaguchi, K.; Goto, Y., Direct Observation of Amyloid Fibril Growth, Propagation, and Adaptation. *Accounts of Chemical Research* **2006,** *39* (9), 663-670.

588. Filipe, V.; Hawe, A.; Jiskoot, W., Critical evaluation of Nanoparticle Tracking Analysis (NTA) by NanoSight for the measurement of nanoparticles and protein aggregates. *Pharmaceutical research* **2010,** *27* (5), 796-810.

589. Yang, D. T.; Lu, X.; Fan, Y.; Murphy, R. M., Evaluation of Nanoparticle Tracking for Characterization of Fibrillar Protein Aggregates. *AIChE J* **2014,** *60* (4), 1236-1244.

590. Hlaing, M.; Gebear-Eigzabher, B.; Roa, A.; Marcano, A.; Radu, D.; Lai, C.-Y., Absorption and scattering cross-section extinction values of silver nanoparticles. *Optical Materials* **2016,** *58*, 439-444.

591. Satinover, S. J.; Dove, J. D.; Borden, M. A., Single-Particle Optical Sizing of Microbubbles. *Ultrasound in Medicine & Biology* **2014,** *40* (1), 138-147.

592. Stetefeld, J.; McKenna, S. A.; Patel, T. R., Dynamic light scattering: a practical guide and applications in biomedical sciences. *Biophysical Reviews* **2016,** *8* (4), 409-427.

593. Tian, X.; Nejadnik, M. R.; Baunsgaard, D.; Henriksen, A.; Rischel, C.; Jiskoot, W., A Comprehensive Evaluation of Nanoparticle Tracking Analysis (NanoSight) for Characterization of Proteinaceous Submicron Particles. *Journal of Pharmaceutical Sciences* **2016,** *105* (11), 3366-3375.

594. Krueger, A. B.; Carnell, P.; Carpenter, J. F., Characterization of factors affecting nanoparticle tracking analysis results with synthetic and protein nanoparticles. *Journal of pharmaceutical sciences* **2016,** *105* (4), 1434-1443.

595. Zagorski, M. G.; Yang, J.; Shao, H.; Ma, K.; Zeng, H.; Hong, A., Methodological and chemical factors affecting amyloid-β peptide amyloidogenicity. In *Methods in enzymology*, Elsevier: 1999; Vol. 309, pp 189-204.

596. Finder, V. H.; Glockshuber, R., Amyloid-β aggregation. *Neurodegenerative Diseases* **2007,** *4* (1), 13-27.

597. Gross, J.; Sayle, S.; Karow, A. R.; Bakowsky, U.; Garidel, P., Nanoparticle tracking analysis of particle size and concentration detection in suspensions of polymer and protein samples: Influence of experimental and data evaluation parameters. *European Journal of Pharmaceutics and Biopharmaceutics* **2016,** *104*, 30-41.

598. Parthasarathy, R., Rapid, accurate particle tracking by calculation of radial symmetry centers. *Nature Methods* **2012,** *9* (7), 724-726.

599. Walker, J. G., Improved nano-particle tracking analysis. *Measurement Science and Technology* **2012,** *23* (6), 065605.

600. Berglund, A. J., Statistics of camera-based single-particle tracking. *Physical Review E* **2010,** *82* (1), 011917.

601. Michalet, X., Mean square displacement analysis of single-particle trajectories with localization error: Brownian motion in an isotropic medium. *Physical Review E* **2010,** *82* (4), 041914.

602. Michalet, X.; Berglund, A. J., Optimal diffusion coefficient estimation in single-particle tracking. *Physical Review E* **2012,** *85* (6), 061916.

603. Hartman, J.; Kirby, B., Decorrelation correction for nanoparticle tracking analysis of dilute polydisperse suspensions in bulk flow. *Physical Review E* **2017,** *95* (3), 033305.

604. Ryan, T. M.; Caine, J.; Mertens, H. D.; Kirby, N.; Nigro, J.; Breheney, K.; Waddington, L. J.; Streltsov, V. A.; Curtain, C.; Masters, C. L., Ammonium hydroxide treatment of Aβ produces an aggregate free solution suitable for biophysical and cell culture characterization. *PeerJ* **2013,** *1*, e73.

605. Rambaldi, D. C.; Zattoni, A.; Reschiglian, P.; Colombo, R.; De Lorenzi, E., In vitro amyloid Aβ1-42 peptide aggregation monitoring by asymmetrical flow field-flow fractionation with multi-angle light scattering detection. *Analytical and Bioanalytical Chemistry* **2009,** *394* (8), 2145-2149.

606. Schmit, J. D.; Ghosh, K.; Dill, K., What Drives Amyloid Molecules To Assemble into Oligomers and Fibrils? *Biophysical Journal* **2011,** *100* (2), 450-458.

607. Amin, S.; Barnett, G. V.; Pathak, J. A.; Roberts, C. J.; Sarangapani, P. S., Protein aggregation, particle formation, characterization & rheology. *Current Opinion in Colloid & Interface Science* **2014,** *19* (5), 438-449.

608. Liu, J.; Nguyen, M. D. H.; Andya, J. D.; Shire, S. J., Reversible Self-Association Increases the Viscosity of a Concentrated Monoclonal Antibody in Aqueous Solution. *Journal of Pharmaceutical Sciences* **2005,** *94* (9), 1928-1940.

609. Nicoud, L.; Lattuada, M.; Yates, A.; Morbidelli, M., Impact of aggregate formation on the viscosity of protein solutions. *Soft Matter* **2015,** *11* (27), 5513-5522.

610. He, F.; Becker, G. W.; Litowski, J. R.; Narhi, L. O.; Brems, D. N.; Razinkov, V. I., High-throughput dynamic light scattering method for measuring viscosity of concentrated protein solutions. *Analytical Biochemistry* **2010,** *399* (1), 141-143.

611. Moore, K. A.; Pate, K. M.; Soto-Ortega, D. D.; Lohse, S.; van der Munnik, N.; Lim, M.; Jackson, K. S.; Lyles, V. D.; Jones, L.; Glassgow, N.; Napumecheno, V. M.; Mobley, S.; Uline, M. J.; Mahtab, R.; Murphy, C. J.; Moss, M. A., Influence of gold nanoparticle surface chemistry and diameter upon Alzheimer's disease amyloid-β protein aggregation. *Journal of Biological Engineering* **2017,** *11* (1), 5.

612. Jameson, L. P.; Smith, N. W.; Dzyuba, S. V., Dye-binding assays for evaluation of the effects of small molecule inhibitors on amyloid (aβ) self-assembly. *ACS Chem Neurosci* **2012,** *3* (11), 807-819.

613. Bieschke, J.; Russ, J.; Friedrich, R. P.; Ehrnhoefer, D. E.; Wobst, H.; Neugebauer, K.; Wanker, E. E., EGCG remodels mature α-synuclein and amyloid-β fibrils and reduces cellular toxicity. *Proceedings of the National Academy of Sciences* **2010,** *107* (17), 7710-7715.

614. Palhano, F. L.; Lee, J.; Grimster, N. P.; Kelly, J. W., Toward the molecular mechanism (s) by which EGCG treatment remodels mature amyloid fibrils. *Journal of the American Chemical Society* **2013,** *135* (20), 7503-7510.

615. Churches, Q. I.; Caine, J.; Cavanagh, K.; Epa, V. C.; Waddington, L.; Tranberg, C. E.; Meyer, A. G.; Varghese, J. N.; Streltsov, V.; Duggan, P. J., Naturally occurring polyphenolic inhibitors of amyloid beta aggregation. *Bioorganic & Medicinal Chemistry Letters* **2014,** *24* (14), 3108-3112.

616. Hoover, B. M.; Murphy, R. M., Evaluation of nanoparticle tracking analysis for the detection of rod-shaped particles and protein aggregates. *Journal of pharmaceutical sciences* **2020,** *109* (1), 452-463.

617. Vestad, B.; Llorente, A.; Neurauter, A.; Phuyal, S.; Kierulf, B.; Kierulf, P.; Skotland, T.; Sandvig, K.; Haug, K. B. F.; Øvstebø, R., Size and concentration analyses of extracellular vesicles by nanoparticle tracking analysis: a variation study. *Journal of extracellular vesicles* **2017,** *6* (1), 1344087.

618. Kim, A.; Bernt, W.; Cho, N.-J., Improved Size Determination by Nanoparticle Tracking Analysis: Influence of Recognition Radius. *Analytical Chemistry* **2019,** *91* (15), 9508-9515.